Contribution to the study of microstructured optical fibres : numerical methods and physical results

G. Renversez

Contribution à l'étude des fibres optiques microstructurées : méthodes numériques et résultats physiques

Contribution to the study of microstructured optical fibres : numerical methods and physical results

Gilles RENVERSEZ
Institut Fresnel (UMR CNRS 6133) & Université Paul Cézanne Aix-Marseille III

Mémoire présenté pour l'obtention
de l'habilitation à diriger des recherches
mémoire soutenu publiquement le 9 décembre 2008
à l'Université de Provence Aix-Marseille I
devant le jury composé de

Frédérique DEFORNEL	Directrice de recherche	Institut Carnot de Bourgogne
John DUDLEY	Professeur, rapporteur	Université de Besançon et IUF
Albert FERRANDO	Professeur	Université de Valence, Espagne
Hugues GIOVANNINI	Professeur	Université Paul Cézanne
Marie HOUSSIN	Professeur, rapporteur	Université de Provence
Ross MCPHEDRAN	Professeur, rapporteur	Université de Sydney, Australie
Gérard TAYEB	Professeur	Université Paul Cézanne
Frédéric ZOLLA	Professeur	Université de Provence

Table des matières

Table des figures

Liste des tableaux

Avant-propos

Ce mémoire est issu des travaux effectués au sein de l'Institut Fresnel depuis mon recrutement à l'Université Paul Cézanne en tant que maître de conférences. Je n'y aborde donc pas du tout mes recherches effectuées lors de mon DEA de Physique théorique sur les vortex dans l'hélium superfluide, ni celles liées à ma thèse sur la modélisation biologiquement réaliste de neurones isolés ou en réseaux, ni celles sur la modélisation du cytosquelette cellulaire réalisées lors de mon post-doc. C'est très certainement parce que j'ai déjà changé plusieurs fois de thématiques de recherches en quelques années que, par contrecoup, je me suis consacré quasiment exclusivement à l'étude des fibres optiques microstructurées depuis mon arrivée à l'Institut Fresnel. Ce sujet de recherche très ciblé est en fait, dans le détail des travaux réalisés, nettement plus varié qu'il ne le semble au premier abord. En effet, il couvre au moins trois aspects qui me semblent tout aussi pertinents les uns que les autres et qui se fécondent mutuellement.

En premier lieu la partie élaboration de méthodes numériques pour l'étude des fibres microstructurées (ou de tout autre guide d'ondes invariant par translation suivant un axe principal) est certainement celle à laquelle j'ai consacré le plus de temps et d'efforts. Il ne pouvait en être autrement pour deux raisons. L'équipe de recherche de l'Institut Fresnel à laquelle j'ai la chance d'appartenir, à savoir l'équipe CLARTE, a une très solide réputation dans la modélisation des phénomènes électromagnétiques depuis les travaux conduits dans les années soixante-dix sur les réseaux de diffraction au sein du Laboratoire d'Optique Électromagnétique. La seconde raison est qu'il n'y avait pas à mon arrivée à l'Institut Fresnel de méthode satisfaisante pour étudier les fibres optiques microstructurées et que l'étude de guides d'onde éventuellement aussi complexes ne peut pas s'envisager avec une unique méthode numérique.

Le second aspect de cette thématique de recherches est l'étude des propriétés physiques de ces fibres d'un nouveau type. Les résultats acquis n'auraient bien évidemment pas pu l'être sans le développement des méthodes numériques et leurs efficaces programmations informatiques.

Le dernier aspect concerne la conception de profils de fibres ayant des propriétés particulièrement intéressantes pour les applications, que ces dernières soient dans le domaine des télécoms ou dans le moyen infrarouge. Cet aspect est celui qui m'a permis d'interagir le plus fortement avec des équipes d'expérimentateurs capables de fabriquer et de caractériser ces fibres microstructurées. Là encore, les avancées réalisées n'ont pu l'être que grâce aux résultats plus fondamentaux acquis auparavant sur les propriétés physiques de ces fibres. Ces études plus appliquées ont elles-mêmes généré des questions s'intégrant complètement dans l'aspect précédent.

Ces mouvements de va-et-vient font qu'il est difficile de trouver une présentation linéaire idéale de ces travaux de recherche. C'est donc une solution de compromis que j'espère être la meilleure possible que j'ai choisie, et qui est décrite dans la table des matières. Cet ordre de présentation est celui que j'avais choisi pour les parties que j'avais rédigées pour notre ouvrage collectif *Foundations of Photonic Crystal Fibres* publié par Imperial College Press en 2005. Ce mémoire est en partie basé sur ce travail mais de nombreux progrès réalisés depuis y sont incorporés, je pense notamment aux nouvelles méthodes numériques disponibles, aux résultats sur les fibres de type ARROW, à la généralisation du diagramme de transition du second mode, ou à l'obtention d'une fibre à cœur creux à bandes photoniques interdites en verre de haut indice pour les grandes longueurs d'ondes. Par ailleurs, quelques petites erreurs ou imprécisions ont été corrigées. Une autre approche assez répandue dans ce type de document aurait été de rédiger une courte synthèse des travaux de recherche effectués. Ce n'est pas celle que j'ai suivie ici pour deux raisons. La première est que n'ayant pas rédigé de thèse en optique guidée ni même dans un quelconque thème de la photonique, j'ai souhaité rédiger un mémoire relativement complet, qui puisse (me) servir de référence. La seconde est l'existence de notre ouvrage collectif. J'y ai passé beaucoup de temps, peut-être trop du point de vue de l'efficacité administrativo-universitaire, tout d'abord en mettant en forme nos résultats précédents et en effectuant des travaux que je n'ai pas publiés dans des articles mais qui me semblait indispensables à l'ouvrage. Maintenant que le livre est sorti depuis trois ans, et que de nouvelles méthodes ont été élaborées, que des résultats supplémentaires ont été obtenus, que des imprécisions ont été repérées, j'ai considéré comme nécessaire et opportun de rédiger ce mémoire sous cette forme.

Pour finir cet avant-propos, je tiens à signaler que tous le calculs associés aux figures présentées ont

été effectués par des codes numériques que j'ai programmés ou dont je dispose du code source pour les avoir conçus et pour avoir supervisé dans le détail leur réalisation par mes doctorants ou post-doctorants[1].

[1] Je ne parle bien évidemment pas là des bibliothèques de calcul scientifiques comme PETSc, Lapack, Linpack, AMOS, ...

Remerciements et petit historique

Les travaux présentés dans ce mémoire n'auraient certainement pas pu prendre leur forme actuelle sans l'impulsion décisive de Daniel Maystre qui m'a permis d'encadrer la thèse de Boris Kuhlmey sur les fibres optiques microstructurées dans la période 2000-2003. En effet c'est lors de cette thèse qu'a été élaborée la méthode multipolaire, que sa programmation en langage structuré a été faite au laboratoire, et que finalement un bon nombre des résultats acquis a été obtenu. Dans notre communauté, rares sont les personnes qui ne connaissent pas les immenses compétences scientifiques de Daniel Maystre en électromagnétisme théorique sous toutes ses formes. Je ne peux que confirmer sa réputation, et je le remercie de l'aide qu'il a pu me fournir dans ces premières années que j'ai consacrées à l'étude des fibres optiques microstructurées. Daniel a ensuite pris avec le succès que l'on sait le virage des métamatériaux. Le déroulement de mes travaux de recherche lors de ces années d'apprentissage et de découverte de l'électromagnétisme[2] n'aurait pas eu le même succès sans les remarquables qualités scientifiques et humaines de Boris Kuhlmey. Il a allié à la fois une grande maîtrise calculatoire, un solide sens physique, et une facilité exceptionnelle dans la programmation. Boris est maintenant lecturer au sein du CUDOS (Center of Ultrahigh Bandwith Devices for Optical Systems) de l'Université de Sydney, et j'en suis très heureux même si j'aurais préféré pour la recherche de notre pays qu'un tel physicien puisse trouver des opportunités équivalentes quelque part dans l'hexagone.

Puisque j'en suis arrivé à la belle ville de Sydney, il est grand temps de mentionner des chercheurs de grand talent notamment Ross McPhedran, Professeur à l'Université de Sydney, et Lyndsay Botten, Professeur à l'Université Technologique de Sydney. La thèse de Boris s'est effectuée en cotutelle entre l'Université Paul Cézanne et l'Université de Sydney avec pour encadrant australien Ross McPhedran et avec une aide initiale cruciale de Lyndsay Botten. Dans le même temps, plusieurs financements successifs issus du CNRS et de l'Australian Research Council nous ont permis de renouveler une vieille collaboration entre l'équipe CLARTE et l'équipe de Ross McPhedran qui avait pris forme dans les années soixante-dix et qui s'était nettement ralentie. J'ai ainsi pu passer plusieurs mois à la School of Physics de l'Université de Sydney puis au CUDOS entre 2000 et 2005. Ces séjours et les visites régulières de Ross dans notre laboratoire ont toujours été extrêmement fructueux tant sur les aspects scientifiques que culturels car Ross est un érudit et pas uniquement dans les fonctions de Green et de Bessel. Il a aussi plusieurs fois clarifié et amélioré des manuscrits peu accessibles. Les séjours les plus longs et le plus formateurs à l'Université de Sydney ont eu lieu lors de mes deux années de délégation au CNRS attribuées par sa section 8. C'est aussi lors de cette période en délégation que j'ai eu le temps de rédiger ma contribution à notre ouvrage collectif *Foundations of Photonic Crystal Fibres* publié par Imperial College Press en 2005. Ce mémoire est en partie basé sur ce que j'ai écrit pour ce livre.

Par la suite, j'ai encadré la thèse de Philippe Boyer avec Michel Nevière et Evgueni Popov. La période faste des débuts de l'étude des fibres microstructurées étaient alors terminée et le nombre d'équipes travaillant sur le domaine nettement plus important. Néanmoins grâce à la rigueur et à la ténacité de Philippe Boyer, plusieurs résultats intéressants ont été obtenus. Il faut commencer par mentionner l'élaboration et la validation complète à partir de la méthode différentielle couplée à la factorisation rapide de Fourier d'une nouvelle méthode de recherche et de suivi des modes à pertes des fibres microstructurées. On peut aussi citer le travail sur les fibres optiques microstructurées de type ARROW. Philippe après un post-doc à l'XLim est maintenant ATER au sein de l'Institut National Polytechnique de Grenoble. Il a toutes les qualités pour poursuivre une carrière universitaire que je lui souhaite d'entamer rapidement. Au cours de sa thèse, j'ai pu discuter à de nombreuses reprises avec Evgueni Popov des problèmes rencontrés, il a su chaque fois apporter sa réponse rapide et efficace. Je tenais à cette occasion à le remercier d'avoir accepter ma participation à l'encadrement de cette thèse.

Depuis septembre 2005, j'encadre avec André Nicolet, la thèse de Fabien Drouart sur l'étude des solutions nonlinéaires dans des fibres microstructurées, ou non, en présence d'un terme de type effet Kerr optique en tenant compte de la section de la fibre et de la constante de propagation contrairement à ce qui se fait usuellement. Ce travail délicat, et qui a désormais abouti pour la description du problème

[2]Pour ces deux mots, leurs deux acceptations sont pleinement valables puisque dans le même temps où je faisais mes premières recherches et publications en optique guidée j'enseignais l'électromagnétisme en DEUG.

scalaire, se fait en étroite collaboration avec le Professeur Christophe Geuzaine de l'Université de Liège. C'est un réel plaisir que de travailler avec ces deux ressortissants belges (André et Christophe sont tous deux sujets du Royaume de Belgique) avec trois maîtres mots : créativité, pertinence et humour. Fabien va soutenir sa thèse le 10 novembre 2008, et nous disposons maintenant d'un code numérique, basé sur la méthode des éléments finis et un algorithme novateur, capable de déterminer les solutions nonlinéaires auto-cohérentes dans un grand nombre de structures nonlinéaires. Je constate donc que pour le moment j'ai eu beaucoup de chance dans les thèses que j'ai pu co-encadrer : que cela soit avec mes collègues de l'équipe CLARTE ou les avec trois doctorants concernés tout s'est très bien passé que cela soit pendant ou après la thèse. J'espère qu'il en sera toujours ainsi.

D'autres membres de l'équipe m'ont rendu de grands services depuis mon arrivée au laboratoire, que cela soit pour la partie recherche de mon activité ou pour celle liée à l'enseignement. Je dois citer Gérard Tayeb et Patrick Vincent qui m'ont, à de très nombreuses reprises, aidé que cela soit en électromagnétisme, en calcul numérique (l'interface d'utilisation de la librairie AMOS notamment), en programmation, en logistique informatique, et je dois certainement oublier certains domaines.

Une mention spéciale doit être attribuée à Frédéric Zolla qui m'a, à plusieurs reprises, encouragé, avec des mots justes, à rédiger ce mémoire. Je crois que sans lui ce document n'en serait encore qu'à l'état de brouillon.

Je craignais en arrivant dans ce laboratoire que mon intégration soit difficile car, comme je l'ai déjà écrit, je représentais alors un élément doublement exogène. Du point de vue thématique de recherche même si je connaissais déjà bien les fonctions de Bessel et d'autres fonctions spéciales et même si je disposais déjà d'une solide formation en physique fondamentale et d'une certaine expérience en calcul scientifique, mes connaissances en électromagnétisme étaient limitées. Et du point de vue relationnel, je n'avais jamais travaillé avec l'un des membres du laboratoire avant mon recrutement. Mais quelques années plus tard, je crois pouvoir écrire que je partage avec les membres de CLARTE la même conception de notre travail de recherche et d'enseignement et que j'ai acquis une certaine expertise dans mon domaine de recherche.

Première partie

Contribution à l'étude des fibres optiques microstructurées : méthodes numériques et résultats physiques

Contribution to the study of microstructured optical fibres : numerical methods and physical results

Table des matières

Chapitre 1

Introduction à l'étude des fibres optiques microstructurées

Sommaire

1.1 Un aperçu des fibres optiques microstructurées

Les fibres optiques microstructurées sont constituées d'un arrangement d'inclusions d'indice optique différent de celui de la matrice dans laquelle elles se trouvent. Ces inclusions peuvent être circulaires ou non, d'indice optique plus élevé ou non que celui de la matrice. Leur arrangement peut correspondre à un sous ensemble d'un réseau périodique ou au contraire être disposé aléatoirement. Le nombre de ces inclusions peut être de seulement trois à plusieurs centaines. On comprend donc bien que les fibres microstructurées sont des guides d'onde d'une très grande variété et que leurs propriétés de guidage de la lumière vont pouvoir être ajustées de façon précise du fait de l'étendue de l'espace des paramètres les décrivant.

1.2 Les modes à pertes dans les fibres optiques microstructurées

1.2.1 Introduction

Une des caractéristiques essentielles des fibres optiques microstructurées est que leurs modes sont des modes à pertes. C'est-à-dire que la constante de propagation des ces modes n'est pas purement réelle mais possède une partie imaginaire non-nulle. Cette propriété a d'importantes conséquences aussi bien sur les méthodes numériques permettant de les étudier que sur les propriétés physiques de ces mêmes fibres.

Afin de détailler ce caractère à pertes des modes des fibres microstructurées, nous allons introduire un type de fibre microstructurée très commun, celui des fibres microstructurées faites d'inclusions de bas indice dans une matrice de haut indice et dont le coeur est constitué d'une région de la matrice : on parle usuellement de fibres microstructurées à coeur plein (on verra ultérieurement que cette appellation est incomplète). Pour simplifier la présentation nous considérerons que la zone regroupant un nombre limité d'inclusions, appelée gaine optique, est de taille finie. Au delà cette zone, la matrice s'étend jusqu'à une éventuelle gaine.

Si l'on considère que la gaine est placée loin de la gaine optique et du coeur de la fibre, et que l'on peut par conséquent négliger son influence, le guidage dans le coeur est alors uniquement dû au nombre fini d'inclusions de bas indices plongées dans une matrice infinie de haut indice. *A priori*, la zone d'inclusions n'isole pas parfaitement le coeur de la fibre du reste de la matrice puisque les inclusions ne forment pas un ensemble connexe permettant ainsi une connexion entre la matrice extérieure et celle du coeur. Physiquement, on peut imaginer que la lumière fuit du coeur vers la matrice extérieure au travers des portions de matrice existant entre les inclusions, et par conséquent, on peut s'attendre à l'existence de pertes de confinement.

Dans le cas d'une interprétation par un guidage par réflexion totale interne modifiée, dans laquelle la gaine optique contenant les inclusions est remplacée par un matériau homogène ayant un indice de réfraction inférieur à celui de la matrice (et donc du coeur), le coeur est complètement isolé de la matrice extérieure. Il n'y a plus de connexion directe entre eux. Cependant, l'étendue spatiale de cette région annulaire de bas indice est finie, et par conséquent des pertes par effet "tunnel" sont inévitables.

Que l'on suive le premier ou le second raisonnement, on arrive à la même conclusion : pour un nombre fini d'inclusions, des pertes doivent se produire lors de la propagation du mode dans la fibre microstructurée. Nous appellerons ces pertes : pertes de guidage ou pertes de confinement ou encore pertes géométriques.

1.2.2 Modes à pertes d'un guide d'onde

Les pertes de confinement étant inévitables, les modes d'une fibre microstructurée décroissent lors de la propagation. Ils ne sont donc plus appelés modes guidés mais modes à pertes. Ces modes ne sont pas exclusifs des fibres microstructurées puisqu'ils apparaissent dans les fibres optiques conventionnelles sous certaines conditions [1, 2]. Les équations vérifiées par les champs électromagnétiques étant linéaires, les pertes sont proportionnelles à l'intensité des champs. Des calculs simples montrent que dans ce cas la décroissance des champs doit être exponentielle le long de la direction de propagation. Ceci se traduit par le fait que la constante de propagation du mode concerné, usuellement notée β, acquière une partie imaginaire non nulle. Dans le cas des guides d'onde invariants le long de leur axe principal (usuellement z), on sait que les modes sont caractérisés par une distribution des champs transverses invariante selon la coordonnée z, qui est modulée par un facteur de phase de la forme $\exp(i\beta z)$. Pour les modes à pertes, $\beta \in \mathbb{C}$, et le facteur phase s'écrit : $\exp(i\Re e(\beta)z)\exp(i\Im e(\beta)z)$ ($\Re$ et $\Im m$ étant respectivement la partie réelle et la partie imaginaire). Pour qu'un mode décroisse dans la direction de propagation il faut que les parties réelle et imaginaire de β soient de même signe.

La prise en compte d'une partie imaginaire non nulle dans la constante de propagation afin de décrire la décroissance des champs n'est qu'un des aspects des modes à pertes (et certainement le plus accessible). En effet l'utilisation d'une partie imaginaire complexe entraîne un certain nombre de difficulté s. Tout d'abord, β étant complexe, la valeur de la norme de la composante tranverse du vecteur d'onde, notée $k_\perp$, est elle aussi complexe puisqu'on a la relation : $k_\perp^2 + \beta^2 = n^2 k_0^2$ dans laquelle n est l'indice de réfraction au point où la relation est considérée. Ceci a deux conséquences : la première est que cela complique le choix de la racine carrée dans la relation précédente, c'est-à-dire qu'il faudra définir la bonne coupure dans le plan complexe. La seconde est que les champs deviennent divergents à grandes distances du coeur. Ceci entraîne que les champs ne sont plus de carré intégrable ce qui nous sort du cadre confortable des fonctions de $L^2(\mathbb{R}^2)$. Une autre conséquence est que les modes à pertes ne sont plus orthogonaux entre eux au sens usuel[3], et que la complétude n'est plus assurée[2]. Ces conséquences semblent réduire la pertinence de la notion de modes puisque la non-orthogonalité des modes génère un couplage entre eux.

Par ailleurs, comme il n'y a pas de relation d'ordre dans $\mathbb{C}$, on ne pourra pas aisément classer les modes à pertes comme on a peut le faire pour les modes guidés. Comme ces modes à pertes vont intervenir régulièrement au sein de ce document et que nous ne disposons pas encore d'une théorie parfaitement achevée ou que cette dernière est encore inconnue du rédacteur, nous allons adopter une approche heuristique afin de mieux cerner ces modes et leurs propriétés.

1.2.3 Approche heuristique des propriétés physiques des modes à pertes

Pour comprendre les propriétés inhabituelles des modes à pertes il faut garder à l'esprit que les modes sont définis pour une fibre qui est infiniment longue. La décroissance exponentielle du mode pour les z croissants étant équivalente à une croissance exponentielle pour les z décroissants, les champs modaux divergent donc quand z tend vers $-\infty$. Nous allons montrer que cela implique que les champs doivent diverger radialement dans le plan de section de la fibre.

Pour des raisons de simplicité, nous considérons une fibre à saut d'indice composé d'un coeur ayant un indice de réfraction n_{co}, d'une gaine optique d'indice n_{CL} elle-même entourée d'une matrice d'indice optique égal à celui du coeur c-a-d n_{co} (voir la figure 1.1). Dans une telle fibre tous les modes sont à pertes du fait des pertes par effet "tunnel"[4, 5]. Intéressons nous au mode fondamental (à pertes), se propageant

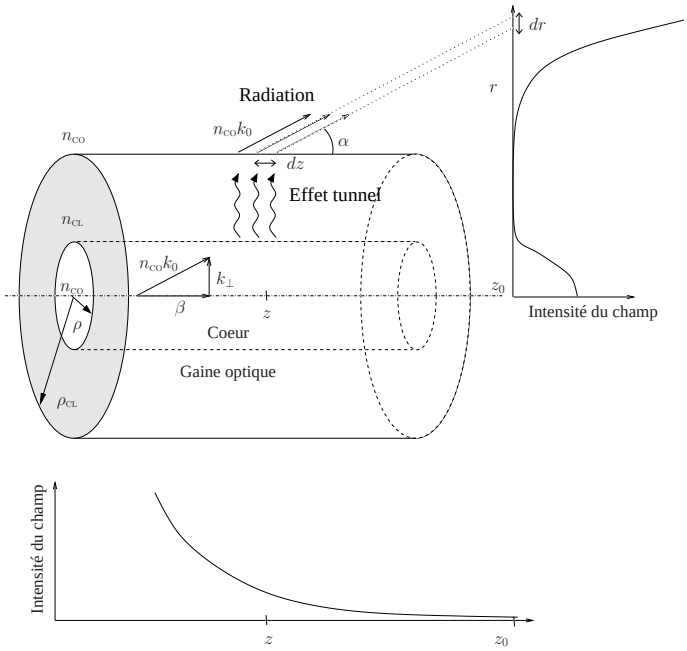

FIG. 1.1 – Modes à pertes et divergence radiale des champs.

vers les z croissants, de cette structure. Dans le coeur, la distribution spatiale de la densité de puissance est similaire à celle du mode fondamental d'un fibre à saut d'indice sans pertes. Elle est centro-symétrique avec un maximum au centre du coeur. Dans la gaine optique, les champs sont évanescents, et la densité d'énergie décroît exponentiellement avec la distance au coeur de la fibre. La constante de propagation et la norme du vecteur d'onde étant la même dans le coeur et dans la matrice entourant la gaine optique, la quantité de puissance, qui a atteint le bord extérieur de la gaine optique, rayonne vers l'extérieur en faisant un angle α avec ce bord :

$$\alpha = \cos^{-1}\left(\frac{\Re e(\beta)}{n_{\mathrm{CO}}k_0}\right) . \tag{1.1}$$

En termes de rayons optiques, un rayon originaire du bord de la gaine optique en z va parvenir à la côte de référence $z_0 > z$ à une distance radiale $r(z)$ du centre du coeur telle que :

$$r(z) = \rho_{\mathrm{CL}} + (z_0 - z)\tan\alpha \tag{1.2}$$

Toute la puissance émise du bord extérieur de la gaine optique dans un cylindre de longueur infinitésimale dz situé en z se retrouve, à la côte z_0, dans la section annulaire de rayon $r(z)$ et de largeur $dr = dz\tan\alpha$. La puissance émise dans cette couronne est par conséquent la puissance totale émise à la côté z par dz divisé par l'aire de la couronne $2\pi r dr$. La puissance totale rayonnée par le cylindre infinitésimale étant proportionnelle à la densité totale à la côte z et par conséquent à $\exp(-2\Im m(\beta)z)dz$[1], en dehors de la

[1]Le facteur 2 dans l'exponentielle provient de la puissance qui est une fonction quadratique des champs.

gaine optique la densité de puissance $S(r)$ est proportionnelle à :

$$S(r) \propto \frac{1}{r \tan \alpha} \exp \left[-2\Im m(\beta) \left(z_0 - \frac{r - \rho_{\mathrm{CL}}}{\tan \alpha} \right) \right]. \tag{1.3}$$

La densité de puissance au centre du coeur en $r = 0$ en z_0 étant proportionnelle à $\exp(-2\Im m(\beta) z_0)$, la densité de puissance normalisée évaluée dans la matrice en z_0 est donnée par :

$$\frac{S(r)}{S(0)} \propto \frac{1}{r \tan \alpha} \exp \left[2\Im m(\beta) \left(\frac{r - \rho_{\mathrm{CL}}}{\tan \alpha} \right) \right]. \tag{1.4}$$

$\Im m(\beta)$ étant positive, on voit que la puissance diverge exponentiellement avec la distance radiale à l'axe de la fibre.

Ce résultat peut sembler contre-intuitif mais cette divergence exponentielle de la puissance aux grandes valeurs de r est une des propriétés fondamentales des modes à pertes. Dans la pratique une telle distribution de la puissance et des champs associés n'est pas réalisable. Les fibres réelles sont toujours de taille finie et par conséquent, un raisonnement équivalent à celui qui vient d'être fait ci-dessus doit être limité par la valeur de z_s de z à laquelle la fibre débute. Si on tient compte de cette modification, on trouve encore une croissance exponentielle de la puissance dans la section de la fibre, mais elle cesse en $r(z_s)$, et elle devient nulle pour des valeurs de r supérieures à $r(z_s)$. La puissance totale passant au travers de la section de la fibre pour tous les z possibles est égale à celle entrant en z_s. La croissance exponentielle dans le section de la fibre n'est pas en contradiction avec la conservation de l'énergie : elle en est une conséquence directe. Ceci reste valable dans le cas d'un fibre infiniment longue, mais le flux de puissance au travers de la section totale est alors infini quelque soit z.

1.2.4 Mise en garde mathématique

Dans l'exemple décrit précédemment, on a considéré au moins implicitement que les pertes par effet tunnel étaient petites, et que leurs effets sur le mode devaient rester faibles. On a en quelque sorte adapté les modes guidés ($\Im m(\beta) = 0$) de la fibre conventionnelle pour les transformer en modes à pertes en permettant à la constante de propagation β d'avoir une petite partie imaginaire. Mathématiquement cela reviendrait à modifier le problème avec des conditions aux limites sans pertes en un problème avec des conditions aux limites avec de faibles pertes sans pour autant reformuler tout le problème. Mais, ce type de problème usuellement référencé comme un problème avec des conditions aux limites ouvertes ('open boundary conditions' en anglais) n'est pas facile à manipuler du point de vue mathématique.

Encore récemment, la seule manière rigoureuse de traiter les problèmes de ce type était de les éviter : au lieu de considérer le système comme étant composé du coeur de la fibre et de la gaine optique avec des conditions aux limites ouvertes au delà, nous aurions à considérer le système composé du coeur de la gaine et du reste de l'univers de manière à préserver la conservation de l'énergie. Le défaut principal de ce type d'approche est que les solutions sont alors associées à un continuum de valeurs réelles de β. Les modes à pertes, qui nous permettent d'analyser la physique des fibres ayant des gaines optiques finies ou infinies ne sont pas les solutions naturelles du problème physique incluant la fibre et tout son milieu extérieur.

Mais les solutions des véritables problèmes ayant des conditions aux limites ouvertes sont les modes à pertes. Cependant, avec ces conditions, le système d'intérêt pratique (le coeur de la fibre, ou le coeur et sa gaine optique) ne satisfait plus la conservation de l'énergie. Les opérateurs mathématiques à employer ne sont plus alors hermitiens, ce qui les rend nettement plus difficiles à étudier. Premièrement, les fonctions propres de ces opérateurs non-hermitiens ne forment plus une base orthogonale complète, mais un ensemble de fonctions non-orthogonales entre elles qui peut être complète ou incomplète. Par conséquent, décomposer un champ sur cet ensemble n'est pas immédiat, et les outils usuels faisant intervenir la décomposition modale (*i.e.* la majorité des techniques employées en optique guidée) ne sont plus utilisables. Deuxièmement, l'obtention de manière rigoureuse des solutions du problème physique fait apparaître des difficultés. Les travaux présentés dans cette habilitation n'en sont pas exempts : ainsi

dans l'établissement de l'une des trois méthodes numériques développées pour étudier les fibres microstructurées, à savoir la méthode multipolaire[2], l'établissement de la méthode multipolaire n'est pas mathématiquement rigoureuse puisque une des étapes n'est pas justifiée. En effet, dans l'obtention de l'identité de Wijngaard (détaillée dans la partie 1 de l'annexe B de la référence [6]), on fait appel à la fonction de Green :

$$G_e = -\frac{i}{4} H_0^{(1)}(k_\perp^{\mathrm{M}} r). \tag{1.5}$$

La valeur $k_\perp^{\mathrm{M}}$ n'est pas déterminée à cette étape de la démonstration, mais pour des modes à pertes $k_\perp^{\mathrm{M}}$ sera complexe avec une partie imaginaire positive entraînant que la fonction de Green utilisée n'est plus de carré intégrable. La convolution avec cette fonction de Green faite dans la suite de l'établissement de la méthode n'est donc plus mathématiquement justifiée. L'établissement de la méthode multipolaire pour les modes guidés est bien rigoureuse pour les modes guidés, elle ne l'est plus, dans sa forme actuelle en tout cas, pour les modes à pertes. On rencontrera des difficultés mathématiques liées elles-aussi aux modes à pertes dans les sections relatives à la méthode de type éléments finis qui sera exposée dans le chapitre2 dédié aux méthodes numériques pour l'étude fibres microstructurées.

Alors que la méthode multipolaire et la méthode éléments finis sont construites de manière totalement différente : les deux fournissent des résultats dont l'accord est excellent pour de très nombreuses configurations. Ceci nous rassure *a posteriori* sur la validité de nos approches en attendant qu'une clarification mathématique ne soit fournie par nos collègues mathématiciens.

Ce travail de fond semble être en cours puisque l'étude des systèmes aux conditions aux limites ouvertes est un sujet actuel de recherche. On peut citer notamment les travaux de P.T. Leung et K.M. Wang [7–14]. Ces travaux semblent suggérer[3] qu'un ensemble de modes à pertes d'une classe au moins de problèmes aux conditions aux limites ouvertes, similaire à ceux qui nous intéressent, forme une base complète et orthogonale si l'espace fonctionnel employé et son produit scalaire sont correctement définis. Dans les travaux mentionnés ci-dessus, les solutions du problème ne constituent pas un continuum mais un ensemble discret et complet de modes à pertes. Il n'est pas encore clairement établi que la modélisation des fibres microstructurées avec leurs modes à pertes rentre exactement dans le cadre mathématique déterminé par Leung *et al.* mais c'est certainement ce type de travaux qui nous apportera les justifications qui nous font défaut actuellement en terme de rigueur mathématique.

[2] Ceci ne signifie pas que les autres méthodes présentées dans ce mémoire en sont exemptes.

[3] Les précautions prises dans cette formulation sont volontaires et ne sont dues qu'à la compréhension partielle des travaux mentionnés par l'auteur de ce mémoire.

Chapitre 2

Two numerical methods to study microstructured optical fibres

Sommaire

2.1 Introduction

2.2 The multipole method

2.2.1 Introduction

We will now present the *Multipole Method* which has been used to study microstructured optical fibers (MOFs) since 2001. The multipole method presented here [15, 16] is a generalization to mode searching in conical mounting of a previous multipole method already developed a few years earlier [17] at the Fresnel Institute. In fact, these multipole methods are natural extension of the usual method used to find the modes in step-index optical fibres (we will clarify this in the following sections). This method has five advantages which have proved to be useful in the investigation of MOF properties.

- The longitudinal or axial propagation constant of the mode β may be complex, and this is crucial since the imaginary part of the propagation constant β is not null due to the leaky nature of the MOF modes (See the section 1.2 on leaky modes in the introduction p. 5).
- The angular frequency ω, related to the free space wavenumber by $\omega = k_0 c$, is an input parameter and β is given by the calculations. The method is hence well suited for computations involving material dispersion.
- As the MOF represents a new type of waveguide, MOF research needs methods that can deal with a wide variety of structures, allowing systematic studies of MOF properties to be performed. It appears that this is partially the case for the Multipole Method : it can be used on a wide range (several orders of magnitude) of wavelengths relative to MOF dimensions.
- It can deal with the two main types of MOF : solid core MOF and air core photonic crystal fibres. core MOF.
- The last advantage comes from McIsaac's theoretical work [18, 19] on the symmetry properties of waveguide modes according to waveguide symmetries. These powerful theoretical results are well suited to MOF due to the usual structure of their inclusions (generally a subset of a triangular lattice, see Fig. 2.1). These symmetry properties permit us to reduce the number of numerical computations, which is useful for the systematic study of MOF, and they will be described more precisely in the following sections of this chapter.

2.2.2 The multipole formulation

In order to make the Multipole Method intuitive and to avoid an overload of notation and calculus, which can be quite tedious, we start with a *simplified approach* [20]. First of all, we have to define the geometry of the microstructured optical fiber to be studied and we have to fix the choice of the propagating electromagnetic fields.

The geometry of the modelled microstructured optical fiber

In this chapter we will limit our study to MOF models involving non-overlapping *circular inclusions*. This restriction to circular inclusions is not fundamental for the formulation but it allows more straightforward computations. On the contrary, the fact that the inclusions are *non-overlapping* is a fundamental hypothesis of our method (the justification comes from the necessity to fulfill the hypotheses of Graf's theorems). The other fundamental hypothesis is the longitudinal invariance of the MOF model. The geometry we are dealing with is described in Fig. 2.2, which represents a transverse xy cross section of the fibre (the z axis being along the fiber axis). This shows a silica matrix of refractive index n_e, perforated with a finite number N_i of inclusions indexed by j and of diameter d_j, whose centers are specified by

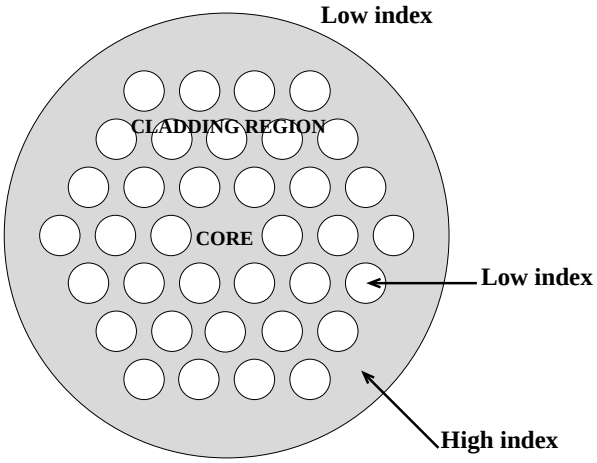

FIG. 2.1 – Cross section of a typical microstructured optical fiber. The inclusions have a lower refractive index than the background medium, or matrix. The inclusions are arranged following a subset of a triangular lattice. In this example, there are three rings of inclusions. The solid core consists of one missing inclusion at the center of the structure. We call the region containing the inclusions the *cladding region* .

$\mathbf{c}_j$. The refractive index of inclusion j is n_j. Outside this hole region, the MOF is enclosed in a *jacket* (radius $r > R_0$, region *(d)* in Fig. 2.2), the index n_0 of which may be complex. One possibility is to take a jacket with refractive index equal to unity, simulating a MOF in air or vacuum.

The choice of the propagating electromagnetic fields

We characterize in the complex representation the electric and magnetic fields $\boldsymbol{\mathcal{E}}$ and $\boldsymbol{\mathcal{H}}$ in the MOF by specifying the components $\mathcal{E}_z$ and $\mathcal{H}_z$ along the fibre axis, with transverse fields following from Maxwell's equations [2]. In fact, it is convenient to work with *scaled magnetic fields* : $\boldsymbol{\mathcal{K}} = Z\boldsymbol{\mathcal{H}}$, where $Z = (\mu_0/\varepsilon_0)^{1/2}$ denotes the *impedance of free space*. Each mode is characterized by its *propagation constant* β, and the transverse dependence of the fields is such that

$$\boldsymbol{\mathcal{E}}(r,\theta,z,t) = \mathbf{E}(r,\theta)e^{i(\beta z-\omega t)}\,, \tag{2.1}$$

$$\boldsymbol{\mathcal{K}}(r,\theta,z,t) = \mathbf{K}(r,\theta)e^{i(\beta z-\omega t)}\,, \tag{2.2}$$

with ω denoting the angular frequency, related to the free space wavenumber by $\omega = kc$. Note that β is complex for leaky modes, the imaginary part of β accounting for attenuation along the z axis. Here we will use the mode *effective index*, which is related to β by $n_{\text{eff}} = \beta/k$.

Each of the fields ($V = E_z$ or $V = K_z$) satisfies the *Helmholtz equation*

$$(\triangle + (k_\perp^{\mathrm{M}})^2)V = 0 \tag{2.3}$$

in the matrix, where $k_\perp^{\mathrm{M}} = \sqrt{k^2 n_{\mathrm{M}}^2 - \beta^2}$, and

$$(\triangle + (k_\perp^{i})^2)V = 0 \tag{2.4}$$

in inclusion i, where $k_\perp^{i} = \sqrt{k^2 n_i^2 - \beta^2}$. Care is required when computing the complex square roots [21].

A simplified approach of the Multipole Method

The multipole method simply results from considering the balance of incoming and outgoing fields. Its aim is to solve the problem of scattering from a system consisting of multiple inclusions. In this section we go through each step of the multipole method in a very simplified manner, with simplified notations, to extract the physics behind the Multipole Method.

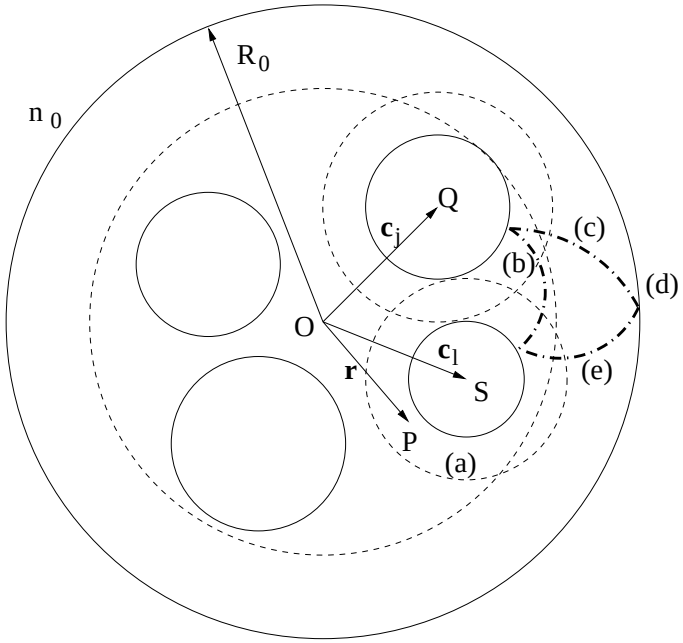

FIG. 2.2 – Geometry of the MOF considered, together with the contributions to the fields just outside a generic hole i. Regions of convergence of multipole expansions are indicated by dashed lines. Note that $\mathbf{QP}$ is $\mathbf{r}_j$ in (2.22), while $\mathbf{SP}$ is $\mathbf{r}_l$ and $\mathbf{OP}$ is $\mathbf{r}$. Solid lines indicate physical boundaries, dashed lines indicate regions of convergence (see section 2.2.2 for a complete description).

Fourier-Bessel Series We consider a single inclusion in the matrix (see the hashed region in Fig. 2.3), with its center at the origin of the coordinate system O. In cylindrical coordinates a field $V(r,\theta)$ is 2π periodic along the angular coordinate ($V(r,\theta+2\pi)=V(r,\theta)$). In any homogeneous annulus around the inclusion (the grey region delimited by the two dashed circles in Fig. 2.3), for fixed r, $V(r,\theta)$ is a regular and 2π-periodic function of θ, so that we can expand $V(r,\theta)$ in a Fourier series :

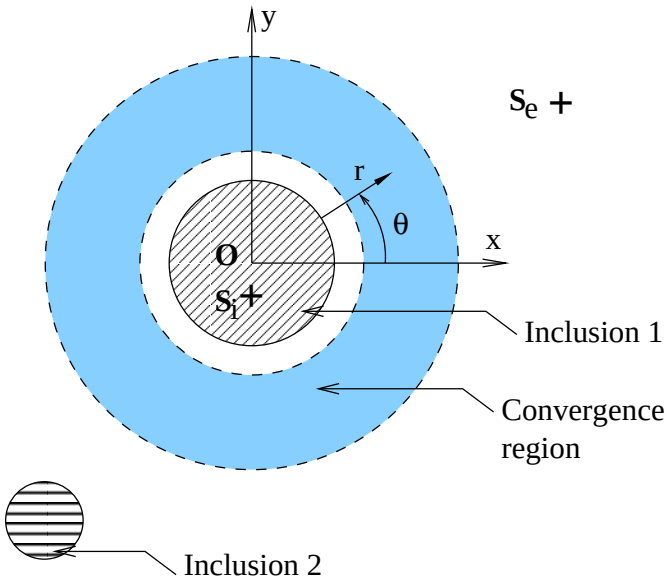

FIG. 2.3 – Scheme for the simplified approach of the multipole method. The first inclusion is the hashed disk in the matrix, with center at the origin O. The dashed circles represent the borders of an homogenous annulus (grey region) around the inclusions, this region is also called the convergence region. S_i is a source localized inside the inclusion and S_e represents a source outside the convergence region. The second inclusion is the small hashed disk in the lower part of the schematic diagram.

$$V(r,\theta) = \sum_{n\in\mathbb{Z}} f_n(r)\exp(in\theta). \tag{2.5}$$

Note that since $V(r,\theta)$ is regular in the annulus, the Fourier coefficients $f_n(r)$ are regular functions of r. Using the Fourier expansion in the Helmholtz equation Eq. 2.3, the following identity is obtained :

$$\sum_{n\in\mathbb{Z}} \left[\frac{d^2 f_n(r)}{dr^2} + \frac{1}{r}\frac{df_n(r)}{dr} + \left((k_\perp^{\mathrm{M}})^2 - \frac{n^2}{r^2}\right) f_n(r)\right] \exp(in\theta) = 0\,. \tag{2.6}$$

By making use of the uniqueness of the Fourier expansion, we are led to an equation valid for all n

$$\frac{d^2 f_n(r)}{dr^2} + \frac{1}{r}\frac{df_n(r)}{dr} + \left((k_\perp^{\mathrm{M}})^2 - \frac{n^2}{r^2}\right) f_n(r) = 0\,. \tag{2.7}$$

With a linear change of variables $u = k_\perp^{\mathrm{M}} r$ this equation becomes

$$\frac{d^2 f_n(u)}{du^2} + \frac{1}{u}\frac{df_n(u)}{du} + \left(1 - \frac{n^2}{u^2}\right) f_n(u) = 0\,. \tag{2.8}$$

Eq. 2.8 is the *Bessel differential equation* of order n [22]. The functions $f_n(u)$ are therefore linear combinations of Bessel functions of the first and second kind of order n ($J_n(u)$ and $Y_n(u)$ respectively), or, equivalently, of Bessel and Hankel functions of the first kind of order n, the latter being defined by $H_n^{(1)}(u) = J_n(u) + iY_n(u)$:

$$f_n(u) = A_n J_n(u) + B_n H_n^{(1)}(u)\,. \tag{2.9}$$

Replacing $f_n(r)$ in the Fourier expansion Eq. 2.5, we have

$$V(r,\theta) = \sum_{n\in\mathbb{Z}} \left(A_n J_n(k_\perp^{\mathrm{M}} r) + B_n H_n^{(1)}(k_\perp^{\mathrm{M}} r)\right) \exp(in\theta)\,. \tag{2.10}$$

The expansion of the field V in Eq. 2.10 is called a *Fourier-Bessel series*. Any function which is regular and satisfies the Helmholtz equation in an annulus can be expressed as a Fourier-Bessel series.

Physical Interpretation of Fourier-Bessel Series (no inclusion) The Fourier-Bessel series can be split into two very different parts : the Bessel functions of the first kind are regular everywhere, whereas the Hankel functions have a singularity at 0 where they diverge. Furthermore, Hankel functions of the first kind satisfy the outgoing wave equation, whereas Bessel functions of the first kind do not.

To understand the meaning of the two parts of the Fourier-Bessel function, we consider the same annulus as above, but without the inclusion. The whole space is now homogeneous. If a source is placed inside the inner circle of the annulus (S_i in Fig. 2.3), the field it radiates has a singularity inside the inner circle of the annulus, and it satisfies the outgoing wave condition. In the annulus, it consequently cannot be represented by a Bessel series, but only by a superposition of Hankel functions. Conversely, a source placed beyond the outer ring of the annulus (S_e in Fig. 2.3) radiates a field which is regular in the annulus and in the region delimited by the inner circle of the annulus. Its field expansion in the annulus cannot therefore contain Hankel functions, but only Bessel functions.

Eq. 2.10 can be written as

$$V(r,\theta) = \mathcal{R}(r,\theta) + \mathcal{O}(r,\theta) \tag{2.11}$$

with

$$\mathcal{R}(r,\theta) = \sum_{n\in\mathbb{Z}} A_n J_n(k_\perp^{\mathrm{M}} r)\exp(in\theta) \tag{2.12}$$

$$\mathcal{O}(r,\theta) = \sum_{n\in\mathbb{Z}} B_n H_n^{(1)}(k_\perp^{\mathrm{M}} r)\exp(in\theta)\,. \tag{2.13}$$

$\mathcal{R}$ is the *regular* part of V. It describes fields radiated from sources situated beyond the outer circle of the annulus. $\mathcal{O}$ is the *singular* part of V. It describes fields radiated from sources situated inside the inner circle of the annulus. Note that if a source is placed inside the annulus, the field it radiates has a singularity in the annulus. A field radiated by a source inside the annulus cannot therefore be described by a Fourier-Bessel series in that annulus.

Change of Basis In the local coordinate system with origin in S_e, the field radiated by S_e is an outgoing, singular field. In an annulus surrounding S_e, the radiated field is described by a series of Hankel functions $\mathcal{O}_s(r_s, \theta_s)$, with (r_s, θ_s) being the local coordinates associated with S_e. In the coordinate system with center O, the same field is regular and incident into the annulus surrounding O defined by the two dashed circles in Fig. 2.3 : the nature of the field depends on the system of coordinates. We can construct a linear operator associating the outgoing field in one coordinate system with the resulting incoming field in another coordinate system. We define the operator $\mathcal{H}$ by

$$\mathcal{R} = \mathcal{H}\mathcal{O}_s \,, \tag{2.14}$$

where $\mathcal{R}$ is the regular field in an annulus around O (Eq. 2.13). In practice, operator $\mathcal{H}$ will be represented by a matrix linking the Fourier-Bessel coefficients A_n of $\mathcal{R}$ to the Fourier-Bessel coefficients B_n of $\mathcal{O}_e$. The coefficients of the matrix are well known, and given by Graf's theorem, as will be shown later in the mathematical derivation of the Multipole Method (see section 2.2.2).

Fourier-Bessel Series and one Inclusion : Scattering Operator We now put the inclusion back in the annulus, and consider fields originating outside the annulus, *e.g.* from S_e. In the annulus, the field radiated from S_e is regular and follows from Eq. 2.14. The field reaching the inclusion will be scattered. The scattered field radiates away from the inclusion : there are now sources inside the region delimited by the inner circle of the annulus. The scattered field is hence described in the annulus by an outgoing field $\mathcal{O}$ while the incoming field is associated with $\mathcal{R}$. Since we only consider linear scattering, $\mathcal{R}$ and $\mathcal{O}$ are linked by a *linear scattering operator*, $\mathcal{S}$, defined by

$$\mathcal{O} = \mathcal{S}\mathcal{R} \,. \tag{2.15}$$

Once $\mathcal{H}$ and $\mathcal{S}$ are known, we can compute the scattered field using Eq. 2.14 and 2.15. In practice, the scattering operator is represented by a matrix linking the Fourier-Bessel coefficients A_n of $\mathcal{R}$ and B_n of $\mathcal{O}$. For simple geometries of inclusions (*e.g.* circular inclusions), the coefficients of the matrix can be expressed in exact analytic form. For inclusions with arbitrary geometry, the matrix can be computed numerically[23, 24].

Fourier-Bessel Series and Two Inclusions : The Multipole Method We now consider two inclusions (1 and 2), and a source S_e exterior to both inclusions. $\mathcal{R}_1$, the incoming regular field for inclusion 1 now results from the superposition of the field $\mathcal{O}_s$ radiated from S_e and the scattered field $\mathcal{O}_2$ from inclusion 2. Using the change of basis operators $\mathcal{H}_{s,1}$ and $\mathcal{H}_{2,1}$ defined as in Eq. 2.14, we have

$$\mathcal{R}_1 = \mathcal{H}_{2,1}\mathcal{O}_2 + \mathcal{H}_{s,1}\mathcal{O}_s \,. \tag{2.16}$$

Similarly, $\mathcal{R}_2$, the regular incoming field for inclusion 2 is given by

$$\mathcal{R}_2 = \mathcal{H}_{1,2}\mathcal{O}_1 + \mathcal{H}_{s,2}\mathcal{O}_s \,. \tag{2.17}$$

The two equations above simply make it explicit that the incoming field on one inclusion results from the superposition of the field radiated by the other inclusion and the source. Using the scattering operators $\mathcal{S}_1$ and $\mathcal{S}_2$ for inclusions 1 and 2 respectively, we have

$$\begin{cases} \mathcal{O}_1 = \mathcal{S}_1(\mathcal{H}_{2,1}\mathcal{O}_2 + \mathcal{H}_{s,1}\mathcal{O}_s) \\ \mathcal{O}_2 = \mathcal{S}_2(\mathcal{H}_{1,2}\mathcal{O}_1 + \mathcal{H}_{s,2}\mathcal{O}_s) \,. \end{cases} \tag{2.18}$$

This linear system of equations links the two unknown scattered fields $\mathcal{O}_1$ and $\mathcal{O}_2$ to the known source field $\mathcal{O}_s$ through change of basis and scattering operators. Once the scattering and change of basis operators are computed, one can deduce the fields scattered from the system constituted of both cylinders through solving Eq. 2.18. It is straightforward to generalize the technique used here to more than two cylinders.

In practice, all operators are represented by matrices and the fields $\mathcal{O}$ and $\mathcal{R}$ by the vectors consisting of the Fourier-Bessel coefficients of the fields. The matrices are readily computed, so that given the Fourier-Bessel expansion of a source field $\mathcal{O}_s$, the Fourier-Bessel coefficients describing $\mathcal{O}_1$ and $\mathcal{O}_2$ follow from solving the matrix equations equivalent to Eq. 2.18. Once $\mathcal{O}_1$ and $\mathcal{O}_2$ are known, the regular part of the field around inclusions 1 and 2 can be deduced *e.g.* from the scattering matrices through Eq. 2.15. The fields are then known in any homogeneous annulus surrounding the inclusions. In fact it appears that the superposition of outgoing fields $\mathcal{O}_s$, $\mathcal{O}_1$ and $\mathcal{O}_2$ describes the field accurately everywhere.

Using change of basis operators, we have converted the computation of the field scattered from a complex system consisting of several inclusions to the computation of scattering operators of single inclusions. Guided modes of a structure consisting of several inclusions correspond to non-zero fields around the inclusion in the absence of any exterior sources. To find modes, one therefore has to find inclusion-parameters for which Eq. 2.18 has solutions with non-zero $\mathcal{O}_1$ and $\mathcal{O}_2$ in the absence of the $\mathcal{O}_s$ term. This definition of a mode for a guiding structure is essentially the same as that which can be used to compute the modes of an ordinary step index optical fiber [1].

In the next few subsections we describe the multipole method more rigorously, explicitly defining all required fields, operators and vectors, and detailing the domains of validity of the expansions. Furthermore, we adapt the method to the case in which the matrix containing the inclusions is surrounded by a jacket.

Rigorous Formulation of the Field Identities

In the vicinity of the l^{th} cylindrical inclusion (see Fig. 2.2), we represent the fields in the matrix in local coordinates $\mathbf{r}_l = (r_l, \theta_l) = \mathbf{r} - \mathbf{c}_l$ and express the fields in Fourier-Bessel series. With $J_m(z)$ and $H_m^{(1)}(z)$ being the usual Bessel function of order m and the Hankel function of the first kind of order m respectively, we have for the electric field

$$E_z = \sum_{m\in\mathbb{Z}} \left[A_m^{\mathrm{E}l} J_m(k_\perp^{\mathrm{M}} r_l) + B_m^{\mathrm{E}l} H_m^{(1)}(k_\perp^{\mathrm{M}} r_l) \right] e^{im\theta_l} \tag{2.19}$$

and similarly for the z-component of the scaled magnetic field K_z, but with coefficients $A_m^{\mathrm{K}l}$ and $B_m^{\mathrm{K}l}$. In 2.19 the J_m terms represent the regular incident part[1] $\mathcal{R}^{\mathrm{E}l}$ of the field E_z for cylinder l since it is finite everywhere, including inside the inclusion, while the $H_m^{(1)}$ terms represent the outgoing wave part[2] $\mathcal{O}^{\mathrm{E}l}$ of the field, associated with a source inside the cylinder. We thus have $E_z = \mathcal{R}^{\mathrm{E}l} + \mathcal{O}^{\mathrm{E}l}$.

Local expansion 2.19 is valid only in an annulus extending from the surface of the cylinder to the nearest cylinder or source (region (a) in Fig. 2.2). The same expression may be used around the jacket boundary which we designate by the superscript 0 (region d in Fig. 2.2).

Another description of the fields is originally due to Wijngaard [25]. He reasoned that a field in a region can be written as a superposition of outgoing waves from all source bodies in the region. If the waves originate outside the region, their expansion is in terms of J-type waves, which are source free. Of course this physical argument can be supplemented by rigorous mathematical arguments [25–27], as discussed in Appendix A.1. For MOFs, the *Wijngaard expansion* takes the form

$$\begin{aligned} E_z = \sum_{l=1}^{\mathrm{N}_i} \sum_{m\in\mathbb{Z}} B_m^{\mathrm{E}l} H_m^{(1)}(k_\perp^{\mathrm{M}} |\mathbf{r}_l|) e^{im\arg(\mathbf{r}-\mathbf{c}_l)} \\ + \sum_{m\in\mathbb{Z}} A_m^{\mathrm{E}0} J_m(k_\perp^{\mathrm{M}} r) e^{im\theta} \,, \end{aligned} \tag{2.20}$$

[1] The Bessel functions J_m are continuous and finite in a bounded domain, so the field they describe must therefore have its origin in sources outside that domain.

[2] Hankel functions $H_m^{(1)}$ satisfy the outgoing wave condition and diverge at 0; their contribution to the field in an annulus surrounding an inclusion is therefore associated with fields originating in sources in or on the inclusion, and radiating away from it.

and is valid everywhere in the matrix. Each term of the first m series is an outgoing wave field with a source at cylinder l, while the final term, indexed by 0, is the regular field originating at the jacket boundary.

Equating 2.19 and 2.20, thus enforcing consistency, yields, in the vicinity of cylinder l,

$$\sum_{m\in\mathbb{Z}} A_m^{\mathrm{E}l} J_m(k_\perp^{\mathrm{M}} r_l) e^{im\theta_l} = \sum_{\substack{j=1\\ j\neq l}}^{N} \sum_{m\in\mathbb{Z}} B_m^{\mathrm{E}j} H_m^{(1)}(k_\perp^{\mathrm{M}} r_j) e^{im\theta_j} + \sum_{m\in\mathbb{Z}} A_m^{\mathrm{E}0} J_m(k_\perp^{\mathrm{M}} r) e^{im\theta}, \tag{2.21}$$

since the $H_m^{(1)}(k_\perp^{\mathrm{M}} r_l)$ terms are common to both expansions. Note that the sum on the left hand side of Eq. 2.21 is associated with the regular incident field for inclusion l, while the double sum on the right hand side is associated with the outgoing field originating from all other inclusions ($j \neq l$), and the last sum represents the field coming from the jacket. Hence Eq. 2.21 simply results from considering in detail the origin of the field incident on inclusion l.

Evaluating Eq. 2.21 is not straightforward since different terms refer to different origins. We therefore use the Graf's addition theorem [22] which lets us transform the cylindrical waves between different origins. A full discussion is given in Appendix A.2, where we show that it may be viewed as a change of basis transformation. For example the contribution to the local regular field in the vicinity of cylinder l due to cylinder j (line b, Fig. 2.2) is

$$\sum_{n\in\mathbb{Z}} A_n^{\mathrm{E}lj} J_n(k_\perp^{\mathrm{M}} r_l) e^{in\arg(\mathbf{r}_l)} = \sum_{m\in\mathbb{Z}} B_m^{\mathrm{E}j} H_m^{(1)}(k_\perp^{\mathrm{M}} r_j) e^{im\arg(\mathbf{r}_j)}\,, \tag{2.22}$$

where

$$A_n^{\mathrm{E}lj} = \sum_{m\in\mathbb{Z}} \mathcal{H}_{nm}^{lj} B_m^{\mathrm{E}j}\,, \tag{2.23}$$

$$\mathcal{H}_{nm}^{lj} = H_{n-m}^{(1)}(k_\perp^{\mathrm{M}} c_{lj}) e^{-i(n-m)\arg(\mathbf{c}_{lj})}\,, \tag{2.24}$$

and $\mathbf{c}_{lj} = \mathbf{c}_j - \mathbf{c}_l$, as shown in Appendix A.2.1. The physics behind Eq. 2.22 is quite intuitive, and corresponds to the *Change of Basis* paragraph in Sec. 2.2.2 : the right hand term is associated with an outgoing wave originating from sources inside inclusion j. In any annulus not intersecting or including inclusion j, and in particular in an annulus centered on inclusion l, this field is regular and satisfies the Helmholtz equation. It can hence be expressed in terms of a series of Bessel functions, which is exactly what Eq. 2.22 does.

At this point we introduce the notation $\mathbf{A}^{\mathrm{E}lj} = [A_n^{\mathrm{E}lj}]$, which lets us generate vectors of mathematical objects. A similar notation is used for matrices, *i.e.*, $\boldsymbol{\mathcal{H}}^{lj} = [\mathcal{H}_{nm}^{lj}]$. In matrix form, then, we represent the basis change 2.23 as

$$\mathbf{A}^{\mathrm{E}lj} = \boldsymbol{\mathcal{H}}^{lj} \mathbf{B}^{\mathrm{E}j}. \tag{2.25}$$

Similarly, the contribution to the regular incident field at cylinder l due to the jacket (line e, Fig. 2.2) is

$$\sum_{n\in\mathbb{Z}} A_n^{\mathrm{E}l0} J_n(k_\perp^{\mathrm{M}} r_l) e^{in\arg(\mathbf{r}_l)} = \sum_{m\in\mathbb{Z}} A_m^{\mathrm{E}0} J_m(k_\perp^{\mathrm{M}} r) e^{im\theta}\,, \tag{2.26}$$

where the change of basis (derived in Appendix A.2.2) is

$$\mathbf{A}^{\mathrm{E}l0} = \boldsymbol{\mathcal{J}}^{l0} \mathbf{A}^{\mathrm{E}0}\,, \tag{2.27}$$

with

$$\boldsymbol{\mathcal{J}}^{l0} = \left[\mathcal{J}_{nm}^{l0}\right] = \left[(-1)^{(n-m)} J_{n-m}(k_\perp^{\mathrm{M}} c_l) e^{i(m-n)\arg(\mathbf{c}_l)}\right]. \tag{2.28}$$

Accumulating these contributions for all cylinders and the jacket we have, in the annulus (a) around cylinder l (see Fig. 2.2)

$$\mathbf{A}^{\mathrm{E}l} = \sum_{\substack{j=1 \\ j\neq l}}^{\mathrm{N}_i} \mathbf{A}^{\mathrm{E}lj} + \mathbf{A}^{\mathrm{E}l0} = \sum_{\substack{j=1 \\ j\neq l}}^{\mathrm{N}_i} \boldsymbol{\mathcal{H}}^{lj}\mathbf{B}^{\mathrm{E}j} + \boldsymbol{\mathcal{J}}^{l0}\mathbf{A}^{\mathrm{E}0}, \tag{2.29}$$

a result that holds for both the E_z and K_z fields.

In a similar way, the outgoing field in the vicinity of the jacket boundary due to cylinder j (line c, Fig. 2.2) is

$$\sum_{n\in\mathbb{Z}} B_n^{\mathrm{E}0j} H_n^{(1)}(k_\perp^{\mathrm{M}} r) e^{in\theta} = \sum_{m\in\mathbb{Z}} B_m^{\mathrm{E}j} H_m^{(1)}(k_\perp^{\mathrm{M}} r_j) e^{im\arg(\mathbf{r}_j)}\,, \tag{2.30}$$

with the change of basis represented by

$$\mathbf{B}^{\mathrm{E}0j} = \boldsymbol{\mathcal{J}}^{0j}\mathbf{B}^{\mathrm{E}j}\,, \tag{2.31}$$

where

$$\boldsymbol{\mathcal{J}}^{0j} = \left[\mathcal{J}_{nm}^{0j}\right] = \left[J_{n-m}(k_\perp^{\mathrm{M}} c_j) e^{-i(n-m)\arg(\mathbf{c}_j)}\right]\,, \tag{2.32}$$

as shown in Appendix A.2.3.

By adding the contributions for all cylinder sources we reexpress the first term on the right-hand side of the Wijngaard expansion 2.20 in a form valid just inside the jacket (region d)

$$\sum_{l=1}^{\mathrm{N}_i} \mathcal{O}^{\mathrm{E}l} = \sum_{n\in\mathbb{Z}} B_n^{\mathrm{E}0} H_n^{(1)}(k_\perp^{\mathrm{M}} r) e^{in\theta} = \mathcal{O}^{\mathrm{E}0}\,, \tag{2.33}$$

where

$$\mathbf{B}^{\mathrm{E}0} = \sum_{l=1}^{\mathrm{N}_i} \mathbf{B}^{\mathrm{E}0l} = \sum_{l=1}^{\mathrm{N}_i} \boldsymbol{\mathcal{J}}^{0l}\mathbf{B}^{\mathrm{E}l}, \tag{2.34}$$

a result that also holds for both E_z and K_z.

Boundary Conditions and Field Coupling

While the field identities of the previous section apply individually to each field component, cross coupling between them occurs at boundaries. In what follows, it is most convenient to formulate the boundary conditions in terms of cylindrical reflection coefficients as derived in Appendix A.3. For circular inclusions, for the reflected fields outside each cylinder we have

$$\begin{aligned} B_n^{\mathrm{E}l} &= R_n^{\mathrm{EE}l} A_n^{\mathrm{E}l} + R_n^{\mathrm{EK}l} A_n^{\mathrm{K}l}\,, \\ B_n^{\mathrm{K}l} &= R_n^{\mathrm{KE}l} A_n^{\mathrm{E}l} + R_n^{\mathrm{KK}l} A_n^{\mathrm{K}l}\,, \end{aligned} \tag{2.35}$$

where the expression for the reflection coefficients are given in Eqs A.29 in Appendix A.3. The reflection matrices are derived for each inclusion treated in isolation, and are thus known in closed form for circular inclusions, in which case they are diagonal. For non-circular inclusions, they could be replaced by either analytic expressions for other special cases, or numerical estimates from a differential or integral equation treatment [17, 23]. In these cases they generally also have off-diagonal elements.

Equations (2.35) can be written as

$$\begin{bmatrix} \mathbf{B}^{\mathrm{E}l} \\ \mathbf{B}^{\mathrm{K}l} \end{bmatrix} = \begin{bmatrix} \mathbf{R}^{\mathrm{EE}l} & \mathbf{R}^{\mathrm{EK}l} \\ \mathbf{R}^{\mathrm{KE}l} & \mathbf{R}^{\mathrm{KK}l} \end{bmatrix} \begin{bmatrix} \mathbf{A}^{\mathrm{E}l} \\ \mathbf{A}^{\mathrm{K}l} \end{bmatrix}\,, \tag{2.36}$$

or

$$\tilde{\mathbf{B}}^l = \tilde{\mathbf{R}}^l \tilde{\mathbf{A}}^l\,, \tag{2.37}$$

with $\mathbf{R}^{\mathrm{EE},l} = \mathrm{diag}(R_n^{\mathrm{EE}l})$ and similar definitions for the other reflection matrices. We also need an interior form at the jacket boundary (point d in Fig. 2.2),

$$\tilde{\mathbf{A}}^0 = \tilde{\mathbf{R}}^0 \tilde{\mathbf{B}}^0 \tag{2.38}$$

where $\tilde{\mathbf{A}}^0$, $\tilde{\mathbf{B}}^0$ and $\tilde{\mathbf{R}}^0$ are defined as in Eqs. 2.36–2.37, and the coefficients of $\tilde{\mathbf{R}}^0$ are given by Eqs. A.25. In this form the outgoing field ($\tilde{\mathbf{B}}^0$) generated by all inclusions (line c) is reflected by the jacket to generate the regular field ($\tilde{\mathbf{A}}^0$), which feeds into the incident field for inclusion l (line e in Fig. 2.2). It is straightforward to adapt $\tilde{\mathbf{R}}^0$ to cases where multiple films surround the hole region.

Derivation of the Rayleigh Identity

With the structure of the field coupling derived in Section 2.2.2, we now form field identities applying to the vector components $\tilde{\mathbf{A}}^l$ and $\tilde{\mathbf{B}}^l$. From Eq. 2.29 we have

$$\tilde{\mathbf{A}}^l = \sum_{\substack{j=1 \\ j\neq l}}^{\mathrm{N}_i} \tilde{\boldsymbol{\mathcal{H}}}^{lj} \tilde{\mathbf{B}}^j + \tilde{\boldsymbol{\mathcal{J}}}^{l0} \tilde{\mathbf{A}}^0 \,, \tag{2.39}$$

where $\tilde{\boldsymbol{\mathcal{H}}}^{lj} = \mathrm{diag}(\boldsymbol{\mathcal{H}}^{lj}, \boldsymbol{\mathcal{H}}^{lj})$, and $\tilde{\boldsymbol{\mathcal{J}}}^{l0} = \mathrm{diag}(\boldsymbol{\mathcal{J}}^{l0}, \boldsymbol{\mathcal{J}}^{l0})$. Equation 2.39 is the representation of the regular incident field at cylinder l in terms of outgoing components $\tilde{\mathbf{B}}^j$ from all other cylinders and an incident field contribution $\tilde{\mathbf{A}}^0$ from the jacket.

Combining Eq. 2.39 for all cylinders $l = 1 \ldots \mathrm{N}_i$ and introducing $\boldsymbol{\mathcal{A}} = \left[\tilde{\mathbf{A}}^l\right]$ and $\boldsymbol{\mathcal{B}} = \left[\tilde{\mathbf{B}}^l\right]$, we derive

$$\boldsymbol{\mathcal{A}} = \tilde{\boldsymbol{\mathcal{H}}} \boldsymbol{\mathcal{B}} + \tilde{\boldsymbol{\mathcal{J}}}^{\mathrm{B0}} \tilde{\mathbf{A}}^0 \,, \tag{2.40}$$

where $\tilde{\boldsymbol{\mathcal{H}}} = \left[\tilde{\boldsymbol{\mathcal{H}}}^{lj}\right]$ for $l, j = 1 \ldots \mathrm{N}_i$ with $\tilde{\boldsymbol{\mathcal{H}}}^{ll} \equiv \mathbf{0}$ and

$$\tilde{\boldsymbol{\mathcal{J}}}^{\mathrm{B0}} = \left[\tilde{\boldsymbol{\mathcal{J}}}^{l0}\right] = \left[(\tilde{\boldsymbol{\mathcal{J}}}^{10})^T, \quad (\tilde{\boldsymbol{\mathcal{J}}}^{20})^T, \quad \cdots, \quad (\tilde{\boldsymbol{\mathcal{J}}}^{\mathrm{N}_i 0})^T\right]^T, \tag{2.41}$$

where the T indicates the transpose. Similarly, the vector outgoing field in the vicinity of the jacket due to all the cylinders is given by

$$\tilde{\mathbf{B}}^0 = \sum_{j=1}^{\mathrm{N}_i} \tilde{\boldsymbol{\mathcal{J}}}^{0l} \tilde{\mathbf{B}}^l = \tilde{\boldsymbol{\mathcal{J}}}^{0\mathrm{B}} \boldsymbol{\mathcal{B}} \tag{2.42}$$

from Eq.2.34. Here

$$\tilde{\boldsymbol{\mathcal{J}}}^{0\mathrm{B}} = \left[\tilde{\boldsymbol{\mathcal{J}}}^{0l}\right] = \left[\tilde{\boldsymbol{\mathcal{J}}}^{01}, \quad \tilde{\boldsymbol{\mathcal{J}}}^{02}, \quad \cdots \quad \tilde{\boldsymbol{\mathcal{J}}}^{0\mathrm{N}_i}\right] . \tag{2.43}$$

Combining Eqs. 2.37, Eqs. 2.38, 2.40 and 2.42 and eliminating $\tilde{\mathbf{A}}^0$ and $\tilde{\mathbf{B}}^0$ we form a homogeneous system of equations (which represents the *Rayleigh identity*, which we will also call the *field identity*) in the source coefficients

$$\left[\mathbf{I} - \boldsymbol{\mathcal{R}}\left(\tilde{\boldsymbol{\mathcal{H}}} + \tilde{\boldsymbol{\mathcal{J}}}^{\mathrm{B0}} \tilde{\mathbf{R}}^0 \tilde{\boldsymbol{\mathcal{J}}}^{0\mathrm{B}}\right)\right] \boldsymbol{\mathcal{B}} \equiv \boldsymbol{\mathcal{M}} \boldsymbol{\mathcal{B}} = \mathbf{0}, \tag{2.44}$$

where the right-hand side indicates the absence of external sources, and

$$\boldsymbol{\mathcal{R}} = \mathrm{diag}\left[\tilde{\mathbf{R}}^1, \tilde{\mathbf{R}}^2, \cdots, \tilde{\mathbf{R}}^{\mathrm{N}_i}\right] . \tag{2.45}$$

Non-trivial solutions to the homogeneous system (2.44) correspond to non-zero fields propagating in the z-direction. The solutions represent a non-zero field existing without any exterior source of energy, in other words propagating (possibly leaky) fibre modes. We will see in the next Chapter how this equation can be solved to obtain the modes of a MOF structure.

2.2.3 Symmetry properties of MOF

Symmetry properties of modes

In the previous section, we use a generalization of the study carried out by Lord Rayleigh [28] more than a century ago. In the following we will use the formalization of a work initiated in the same period, *i.e.* in 1894, by Pierre Curie [29] concerning symmetry properties in electromagnetics.

This formalization was realized by P. McIsaac in two seminal articles [18, 19]. All the theoretical results presented here can be found in much more detail in these two articles.

Using group representation theory, he classified the electromagnetic modes of waveguide structures, according to the symmetry properties of the configuration. Due to the symmetry properties exhibited by the structure of most MOF, his results are very useful for classifying, before any computation, the modes existing in the studied MOF.

A structure which possesses only rotationnal symmetry with no reflection symmetry, and for which $2\pi/n$ (n being an integer) is the smallest angle associated with a symmetry operation is said to possess[3] the symmetry group C_n of order n. Fig. 2.4 shows the cross sections of several structures with C_n symmetry. If a structure has an n-fold rotation symmetry together with at least one plane of relection

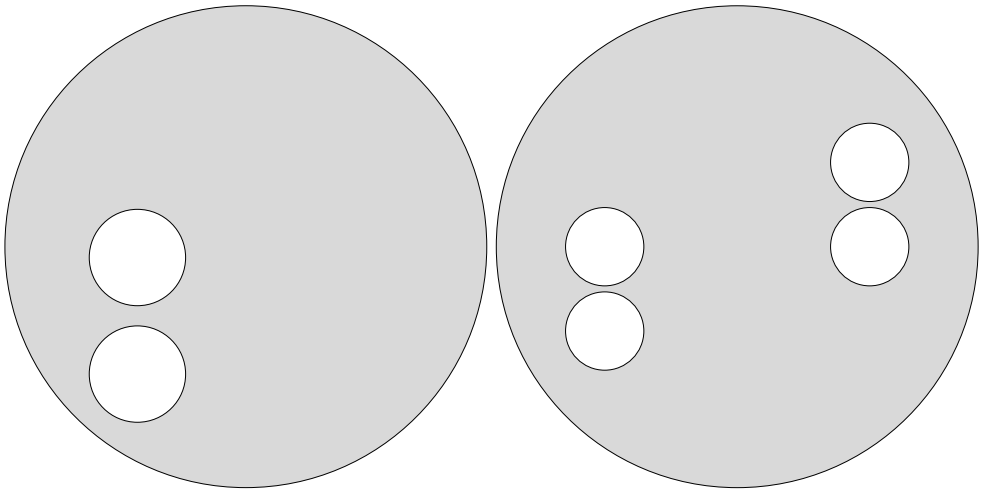

(a) C_1 symmetry (b) C_2 symmetry

FIG. 2.4 – Two examples of a structure with a C_n symmetry. The structure is invariant through a rotation of $2\pi/n$ and there is no reflection symmetry.

symmetry, then there are exactly n planes of reflection symmetry. All these planes intersect along the axis of the rotational symmetry and the angular space between them is equal to π/n. The symmetry group for this kind of structure is called C_{nv} (see Fig. 2.5).

McIsaac assigned the modes of a waveguide to classes depending on the azimuthal symmetry of the modal fields patterns, and he called these classes *mode classes*. Each mode class contains an infinite number of modes. For a waveguide with C_n symmetry there are n different mode classes, and for a waveguide with C_nv symmetry there are $n+1$ distinct mode classes if n is odd and $n+2$ classes if n is even. In each class, all the modes are either non-degenerate or two-fold degenerate (see table 2.1).

The special case of $C_{\infty v}$ which corresponds to the limiting case $n \to \infty$ is also treated in McIsaac's study [18, 19].

In his nomenclature, McIsaac labels the two mode classes containing nondegenerate modes as the first and the second mode classes (p=1,2). The two remaining mode classes containing nondegenerate modes existing if n is even are placed at the end of the list (p=n+1,n+2). In each class of symmetry, modes have different symmetry properties which can be used to simplify the computation of the modal fields and propagation constants. Indeed, McIsaac showed that for each symmetry class these computations

[3] A structure with the C_1 symmetry has actually no symmetry.

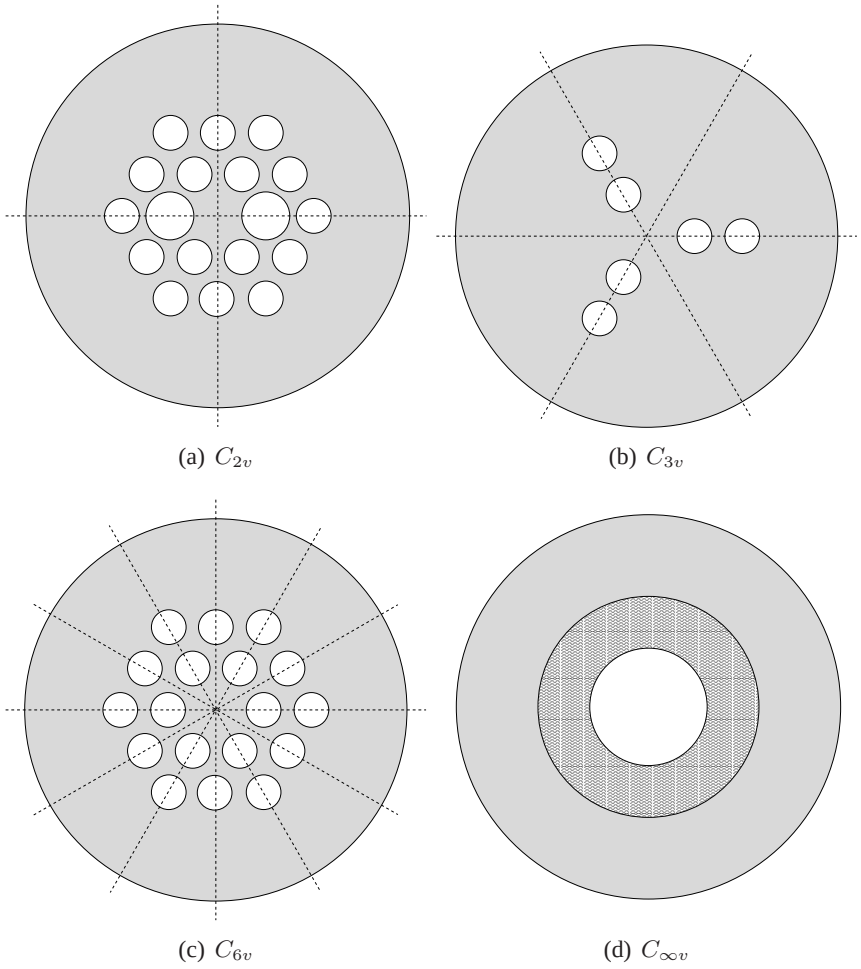

(a) C_{2v} (b) C_{3v}

(c) C_{6v} (d) $C_{\infty v}$

FIG. 2.5 – Four examples of a structure with a C_{nv} symmetry. The structure is invariant through a rotation of $2\pi/n$ and there is a least one reflection symmetry. The dashed lines represent the symmetry planes. The $C_{\infty v}$ symmetry is the limit case $n \to \infty$.

need to take into account only a limited angular sector, the minimal sector, with vertex at the center of the waveguide and appropriate boundary conditions along the edges of the sector.

It must be noted that only the nondegenerate modes satisfy all the symmetries of the waveguide, and on the contrary the degenerate modes will possess only a subgroup of the symmetries. We now focus on C_{nv} waveguides (the C_n case being also treated in McIsaac's articles) since this point group is the most frequently encountered group in MOF studies. Both the angle of the minimal sector of each mode class and the boundary conditions are prescribed by the theory. Two kinds of boundary conditions are defined : the short-circuit boundary condition, *i.e.* the tangential electric field has to vanish at the boundary, and the open-circuit boundary condition, *i.e.* the tangential magnetic field has to vanish at the boundary. The boundary lines of the minimal sector must coincide with two of the planes of reflection symmetry of the waveguide. In Fig. 2.6, we give the minimal sectors for waveguides with C_{6v} symmetry. For this point group, there are 8 mode classes. For non-degenerate mode classes $p = 1, 2, 7, 8$ the angle of the minimal sector is equal to $\pi/6$, and for the four degenerate mode classes $p = 3, 4$ and $p = 5, 6$ the angle is equal to $\pi/2$.

In Fig. 2.7, we give the minimal sectors for waveguides with C_{4v} symmetry. For this point group, there are 6 mode classes. For non-degenerate mode classes $p = 1, 2, 5, 6$ the angle of the minimal sector is equal to $\pi/4$, and for the two degenerate mode classes $p = 3, 4$ the angle is equal to $\pi/2$.

In Fig. 2.8, we give the minimal sectors for waveguides with C_{3v} symmetry. For this point group, there are 4 mode classes, two being non-degenerate with an minimal geometrical sector equal to $\pi/2$ and the two others being degenerate with an angle of the minimal sector equals to π.

n	Number of non-degenerate mode classes	Number of pairs of two-fold degenerate mode classes	Total number of mode classes
odd	2	(n-1)/2	n+1
even	4	(n-2)/2	n+2

TAB. 2.1 – Table of mode classes and degeneracies for uniform waveguides with C_{nv} symmetry.

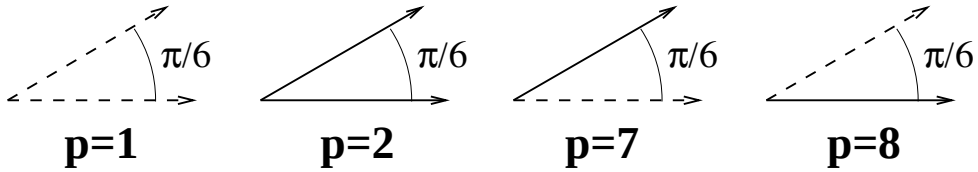

(a) Mode classes $p = 1, 2, 7$ and 8 are non-degenerate.

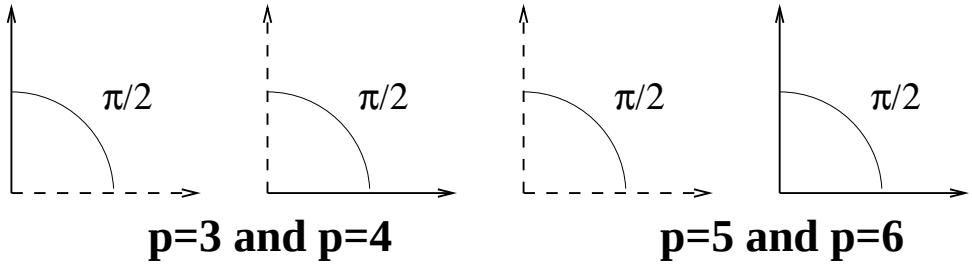

(b) Mode classes $p = 3, 4$ and $p = 5, 6$ are two-fold degenerate.

FIG. 2.6 – Minimal sectors for waveguides with C_{6v} symmetry. Solid lines indicate zero tangential electric field, and dashed lines indicate zero tangential magnetic field.

In Fig. 2.9, we give the minimal sectors for waveguides with C_{2v} symmetry. For this point group, there are 4 mode classes, all of them being non-degenerate. The angle of the minimal sector is equal to $\pi/2$ for the 4 mode classes.

The application of McIsaac's theoretical results for C_{6v} MOFs has already been used to show that the fundamental mode of these fibres is degenerate [30]. Consequently, these perfect fibers are not birefringent. Clear illustrations of this property will be given in section 2.2.6.

2.2.4 Implementation

In this section, we discuss the implementation of the Multipole Method to find the modes and dispersion characteristics of a given fibre structure. The homogeneous equation 2.44 corresponds to a non-trivial field vector $\boldsymbol{\mathcal{B}}$ only if the determinant of the matrix $\boldsymbol{\mathcal{M}}$ is effectively zero. Once the structure and wavelength are given, the matrix $\boldsymbol{\mathcal{M}}$ depends only on β, or, equivalently, its effective index n_{eff}. The search for modes therefore becomes a matter of finding zeros of the complex function $\det(\boldsymbol{\mathcal{M}})$ of the complex variable n_{eff}. To investigate this numerically, field expansions such as Eq. 2.19 must be truncated, say with m running from $-M$ to M. M will be called the *truncation order parameter*.

We know from the previous section on symmetry properties, that the modes of fibres with a C_{nv} symmetry are either nondegenerate or doubly degenerate. Since $\det(\boldsymbol{\mathcal{M}})$ is the product of the eigenvalues of $\boldsymbol{\mathcal{M}}$, we must look for minima in which one or two of the eigenvalues have magnitudes that are substantially smaller than the others. However, a minimum of the determinant may also correspond to an artefact resulting from many eigenvalues being small simultaneously (which we call a false minimum). To distinguish these from genuine solutions, we consider the singular values [31] of $\boldsymbol{\mathcal{M}}$, which, for our case, correspond to the magnitudes of the eigenvalues. False minima can be distinguished by a singular value decomposition at the putative minimum.

The null vectors corresponding to small singular values are approximate solutions to the field identity 2.44. For non-degenerate modes, the null vector is unique to within an arbitrary multiplicative constant. For a two-fold degenerate mode, we let the basis states be prescribed by symmetry proper-

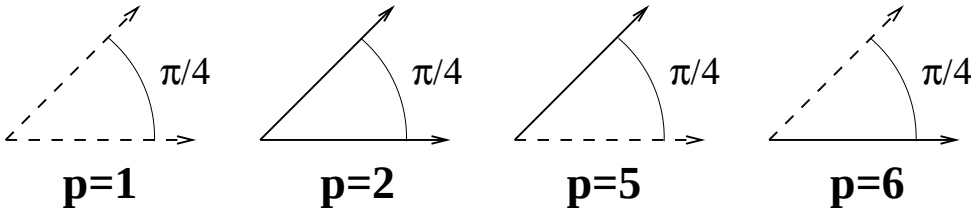

(a) Mode classes $p = 1, 2, 5$ and 6 are non-degenerate.

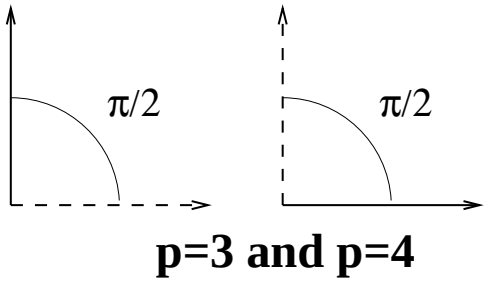

(b) Mode classes $p = 3, 4$ are two-fold degenerate.

FIG. 2.7 – Minimal sectors for waveguides with C_{4v} symmetry. Solid lines indicate zero tangential electric field, and dashed lines indicate zero tangential magnetic field.

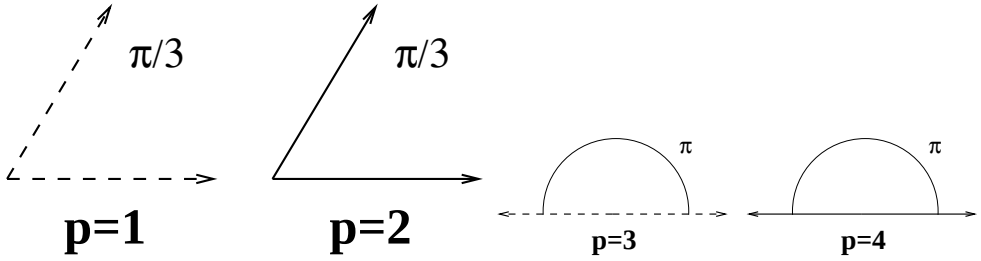

(a) Mode classes $p = 1, 2$ are non-degenerate.

(b) Mode classes $p = 3, 4$ are degenerate.

FIG. 2.8 – Minimal sectors for waveguides with C_{3v} symmetry. Solid lines indicate zero tangential electric field, and dashed lines indicate zero tangential magnetic field.

ties (see Section 2.2.3), though any linear combination of these is equally justified.

Finding modes

For this task we need an algorithm aimed at finding all the zeros of the determinant of $\mathcal{M}$ in a region of the complex n_{eff} plane. The algorithm should be economical in function calls as each evaluation of the determinant is computationally very expensive for large structures. As it can be seen in Fig. 2.10, the zeros are very sharp, so that a very accurate first estimate of the zero is necessary for most simple root-finding routines. More specific algorithms for finding zeros of analytic or meromorphic functions [32, 33] have good convergence for simple structures (with six cylinders for example) but fail for more complex structures, even with good initial guesses. The present approach to root finding seems computationally efficient. We first compute a map of the modulus of the determinant over the region of interest, and then use the local minima of this map as initial points for a mixed zooming and modified Broyden [34] algorithm (an iterative minimization algorithm, guaranteed to converge for parabolic minima).

The initial scanning region has to be chosen in accordance with the physical problem studied : if the fibre is air cored and air guided modes are sought, we choose $\Re e(n_{\text{eff}}) < 1$, whereas if the fibre has a solid core we usually choose to search for modes in a region where $\Re e(n_{\text{eff}})$ is between the optical indices of the inclusions and the matrix. In the latter case hundreds of modes may exist for small $\Re e(n_{\text{eff}})$ which are of little interest because of their high losses. We therefore often concentrate on a smaller n_{eff} scanning

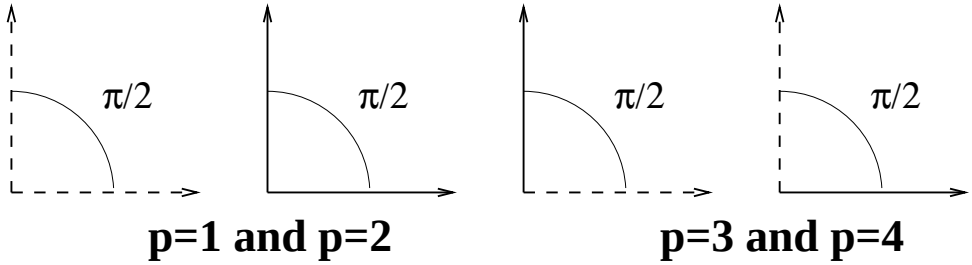

FIG. 2.9 – Minimal sectors for waveguides with C_{2v} symmetry. Mode classes $p = 1, 2, 3$ and 4 are non-degenerate. Solid lines indicate zero tangential electric field, and dashed lines indicate zero tangential magnetic field.

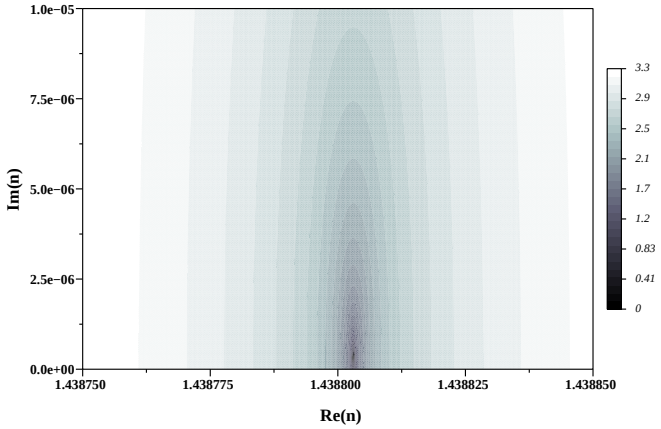

FIG. 2.10 – Map of the logarithm of the magnitude of the determinant of $\mathcal{M}$ versus the real and the imaginary parts of the complex refractive index n. The minimum (in the black region) is associated with the fundamental mode of the test MOF described in section 2.2.5.

region near the highest index of the structure. A scanning region for $\Im m(n_{\text{eff}})$ giving good results in almost any case is $10^{-12} < \Im m(n_{\text{eff}}) < 10^{-3}$.

Dispersion characteristics

The above process of finding modes is carried out for a specific wavelength. We could reiterate the search for modes for many different wavelengths to obtain dispersion characteristics, but this process would be quite laborious. We have found two alternative methods to be of value. One computes and identifies the modes for three or four different wavelengths, then uses a spline interpolation to estimate the n_{eff} values for other wavelengths and refines the estimate with the mixed zooming and Broyden algorithm. Each newly determined point of the $n_{\text{eff}}(\lambda)$ curve can be used to enhance the spline estimate. The second (and often more efficient) method is to compute the modes for only one wavelength λ_0, then slightly perturb the wavelength to get $n_{\text{eff}}(\lambda_0 + \delta_\lambda)$ using $n_{\text{eff}}(\lambda_0)$ as a first guess, and then use a first order estimate of n_{eff} at the next wavelength. One can then compute $n_{\text{eff}}(\lambda + m\delta_\lambda)$ using a first order estimate computed from the two preceding values. For both methods, the wavelength step has to be chosen to be very small : For small steps more points are necessary to compute the dispersion characteristics in a given wavelength range, but for large steps the first order guess becomes inaccurate and the convergence of the zooming and the Broyden algorithm becomes unacceptably slow. Having small steps and therefore numerous numerical values on the dispersion curve is also of benefit when evaluating second order derivatives, as is necessary when computing the group velocity dispersion.

Material dispersion can be included easily by changing the optical indices according to the current

wavelength at each step using, for example, Sellmeier approximation [35] for silica.

The method described here can be adapted to study the change of n_{eff} of a mode for any continuously varying parameter, for example cylinder radius, cylinder spacing or optical index. One problem that can occur when following the evolution of a mode with a continously varying parameter is mode crossing. This results in wrong data, but can easily be detected in most cases through a discontinuity of derivatives, and can also easily be eliminated by restarting the algorithm with the correct mode on the other side of the crossing. The correct choice for δ_λ strongly depends on wavelength and structure, so that no general advice can be given.

Using the symmetries within the Multipole Method

The incorporation of field symmetry in the multipole formulation has two benefits. Firstly, it enables definitive statements to be made about the degeneracies of modes, even in the presence of the accidental degeneracies which arise when normally distinct modal trajectories cross each other. Secondly, it greatly reduces computational burdens, enabling accurate answers for quite large MOF structures to be obtained rapidly on PC's.

In applying the multipole formulation to large C_{6v} MOFs, it is highly advantageous to exploit the symmetry properties in Fig. 2.5(c) to reduce the size of the matrix $\boldsymbol{\mathcal{M}}$. This can be achieved since only multipole coefficients for inclusions lying in the minimal sector indicated in Fig. 2.6 need be specified ; those for holes outside the minimal sector can be obtained by multiplying by the appropriate geometric phase factor (related to $\exp(2\pi i/6)$). The resulting reduction in the order of the matrix $\boldsymbol{\mathcal{M}}$ depends on the type of the mode, being maximal for the non-degenerate modes in Fig. 2.6(a), and still being around 3.5 for degenerate modes (see Fig. 2.6(b)), leading to considerable reductions in processing time.

Another way to obtain $\Im m(\beta)$

One of the challenges of MOF consists in finding leaky modes with losses as small as possible. We are thus faced with a practical problem. The real part of β ($\Re e(\beta)$) is of the same magnitude as k_0 whereas its imaginary part ($\Im m(\beta)$) can be extraordinary smaller, say $10^{-15}\, k_0$! In such circumstances, how can we obtain $\Im m(\beta)$ with a sufficiently good precision ? For this purpose, the losses cannot be determined directly via the poles of the scattering matrix. The fact that we are unable to do this is, of course, linked with the computer precision. We are therefore "doomed" to adopt a new strategy by making use of an energy conservation criterion. More precisely, let us consider the closed surface depicted in Fig. 2.11. If we assume that we will only be dealing with lossless materials, we have the following identity ;

$$\int_{\Sigma} \Re e\{\underset{\sim}{\boldsymbol{S}}\} \cdot \mathbf{n}_{|\Sigma}\, ds = 0 \tag{2.46}$$

where $\boldsymbol{\mathcal{S}}$ is the complex Poynting vector, namely $\boldsymbol{\mathcal{S}} = \frac{1}{2}\boldsymbol{\mathcal{E}} \times \overline{\boldsymbol{\mathcal{H}}}$. As a result, $\boldsymbol{\mathcal{S}}$ can be expressed as follows :

$$\underset{\sim}{\boldsymbol{S}}(x,y,z) = \boldsymbol{S}(x,y)e^{-2\Im m(\beta)z} \tag{2.47}$$

with $\boldsymbol{S} = \frac{1}{2}\boldsymbol{E} \times \overline{\boldsymbol{H}}$. The equation 2.46 can be recast as per :

$$\begin{aligned} \int_{\Sigma_1} \Re e\{\boldsymbol{S}\} \cdot (-\boldsymbol{e}^z)\rho\, d\rho d\theta \quad &+ \quad e^{-2\Im m(\beta)z_0} \int_{\Sigma_2} \Re e\{\boldsymbol{S}\} \cdot (\boldsymbol{e}^z)\rho\, d\rho d\theta \\ \int_{\Sigma_R} \Re e\{\boldsymbol{S}\} e^{-2\Im m(\beta)z} \cdot (\boldsymbol{e}^r) R\, d\theta dz \quad &= \quad 0 \end{aligned} \tag{2.48}$$

If we let $S_z = \boldsymbol{S} \cdot \boldsymbol{e}^z$ and $S_r = \boldsymbol{S} \cdot \boldsymbol{e}^r$, we are led to :

$$\begin{aligned} (e^{-2\Im m(\beta)z_0} - 1) \int_{(\theta,\rho)\in[0,2\pi[\times[0,R]} \Re e\{S_z\}\rho\, d\rho d\theta \quad &+ \\ \left(\int_0^{z_0} e^{-2\Im m(\beta)z}\, dz\right) R \int_0^{2\pi} \Re e\{S_r\}\, d\theta \quad &= \quad 0\,. \end{aligned} \tag{2.49}$$

Now $\int_0^{z_0} e^{-2\Im m(\beta)z}\,dz = -\frac{1}{2\Im m(\beta)}(e^{-2\Im m(\beta)z_0} - 1)$, therefore $\Im m(\beta)$ can be expressed as follows :

$$\Im m(\beta) = \frac{R\int_0^{2\pi} \Re e\{S_r\}\,d\theta}{\int_{(\theta,\rho)\in[0,2\pi[\times[0,R]} \Re e\{S_z\}\rho\,d\rho d\theta} \tag{2.50}$$

Via the previous identity, we then deduce the imaginary part of n_{eff} by

$$\Im m(n_{\text{eff}}) = \frac{\Im m(\beta)}{k_0}\,. \tag{2.51}$$

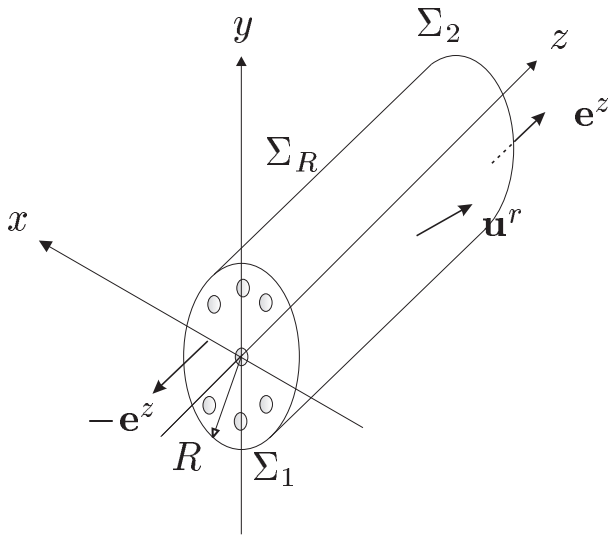

FIG. 2.11 – Scheme used to compute indirectly the losses. The surface Σ is defined as the boundary of a "slice" of a circular cylinder of radius R and length z. Σ is also defined in the following way : $\Sigma = \Sigma_1 \cup \Sigma_2 \cup \Sigma_R$, where $\Sigma_1 = \{(r,\theta,z) \in \mathbb{R}^3, r \leq R, \theta \in [0,2\pi[, z = 0\}$, $\Sigma_2 = \{(r,\theta,z) \in \mathbb{R}^3, r \leq R, \theta \in [0,2\pi[, z = z_0\}$ and $\Sigma_R = \{(r,\theta,z) \in \mathbb{R}^3, r = R, \theta \in [0,2\pi[, z \in [0,z_0]\}$

Software and Computational Demands

We have developed a FORTRAN 90 code to exploit the above considerations. For symmetric structures the suggested optimizations are used and the software can therefore deal, even on PC's, with large structures (modes for fibres with 180 holes have so far been computed on current personal computers). Once the structure has been defined, the software is able to find automatically all the modes within a given region of the complex plane for n_{eff} and can optionally track a mode as a function of wavelength to obtain dispersion characteristics. Material dispersion can be included, if desired.

Computational demands are relatively modest : the complete set of modes with the truncation order parameter $M = 5$ in the region of interest $1.4 < \Re e(n_{\text{eff}}) < 1.45$ for the structure (with a silica matrix) used in Fig. 2.15 can be computed on a current personal computer in less than one minute using less than 2Mb of memory. Of course the load rises for larger structures, but the complete set of modes for a structure having three layers of holes in a hexagonal arrangement takes less than a quarter of an hour (and about 15Mb memory) on a workstation. dispersion curves can be computationally more expensive : the loss curves in Chapter 7 took from about half an hour (for $d/\Lambda = 0.075$ where we used $M = 5$) to several hours (for $d/\Lambda = 0.7$ where $M = 7$ was needed for accuracy).

2.2.5 Validation of the Multipole Method

Even though the Multipole Method is mathematically rigorous, the computed results must be validated. Indeed, the computations are numerical, not analytic and the implementation itself could be

erroneous. This validation will be realized in two steps : first the numerical convergence and the self-consistency of the method will be checked, and finally we will compare results obtained from the Multipole Method with those compused using other numerical methods.

Convergence and self-consistency

The main approximation used in numerical computations via the Multipole Method is the truncation of the Fourier-Bessel series used to described the electromagnetic fields. In order to check the convergence of the numerical results, the effective indices of the computed modes must converge as M , the truncation order parameter (see section 2.2.4), is increased. Our test configuration will be the following : The MOF has a C_{6v} symmetry, the distance between the centres of a pair of adjacent holes Λ, called the pitch, is equal to 6.75 μm, the hole diameter d is fixed at 5.0 μm, and $\lambda = 1.55\,\mu m$. The silica matrix is considered as infinite and its relative permittivity is taken from the Sellmeier expansion at the corresponding wavelength [35] (ε_r = 2.0852042). As can be seen in the first three columns of table 2.2, the convergence of n_{eff} with respect to M is indeed verified. The data are plotted in figure 2.12. For $M < 17$, the determinant is always below 1.0e-10, and for $M \geq 17$ the determinant is greater than 2.0e-9. This means that a value of M that is too high can lead to a bad determination of the effective index due to cumulative numerical errors in matrix computations. An other example of the convergence of the Multipole Method can be found in the following publication [16].

TAB. 2.2 – Convergence of n_{eff} with the truncation order parameter M. Results are for the p=3 fundamental mode of the test MOF described in section 2.2.5. $W^E_{l,m}$ is also defined in this section : it measures the accuracy of the equality between the local and the global expansions of the z-component of the electric field.

M	$\Re e(n_{\text{eff}})$	$\Im m(n_{\text{eff}})$	$W^E_{1,1}$	$W^E_{2,1}$
3	1.43880301866122	3.3100275e-07	0.1329E-01	0.4563E-01
4	1.43877685791377	3.8506149e-08	0.5049E-02	0.8909E-02
5	1.43877422802377	4.2758291e-08	0.4549E-02	0.7941E-02
6	1.43877411171115	4.3250423e-08	0.1890E-02	0.3811E-02
7	1.43877411102638	4.3251229e-08	0.3527E-03	0.7641E-03
8	1.43877410938293	4.3257450e-08	0.2330E-03	0.4270E-03
9	1.43877410904527	4.3258245e-08	0.1574E-03	0.3146E-03
10	1.43877410903106	4.3258173e-08	0.4535E-04	0.9578E-04
11	1.43877410902931	4.3258227e-08	0.1086E-04	0.2190E-04
12	1.43877410902817	4.3258264e-08	0.1132E-04	0.2290E-04
13	1.43877410902807	4.3258229e-08	0.4683E-05	0.9681E-05
14	1.43877410902806	4.3258211e-08	0.8615E-06	0.1803E-05
15	1.43877410902810	4.3258235e-08	0.7263E-06	0.1504E-05
16	1.43877410902803	4.3258193e-08	0.4118E-06	0.8553E-06
17	1.43877410902643	4.3259535e-08	0.1005E-06	0.1869E-06

In the multipole formulation we have two different expansions for the field around each inclusion, the local one (Eq. 2.19) and the global one also called the Wijngaard expansion (Eq. 2.20). These two representations coincide only for untruncated Fourier-Bessel series so their numerical difference can be used as an accurate indicator of truncation errors and of the precision of the mode location. We introduce for the z-component of the electric field, the quantity $W^E_{l,k}$ defined by :

$$W^E_{l,k} = \frac{\int_{C_{l,k}} |E_z^{\text{local}}(\theta_{l,k}) - E_z^{\text{Wijngaard}}(\theta_{l,k})| d\theta_{l,k}}{\int_{C_{l,k}} |E_z^{\text{Wijngaard}}(\theta_{l,k})| d\theta_{l,k}}. \tag{2.52}$$

The doublet l, k stands for the l^{th} cylinder of the k^{th} elementary sector of the MOF structure. A similar quantity can be defined for the scaled magnetic field. As can be seen in table 2.2 or in figures 2.12(b) and 2.13(b) $W^E_{l,k}$ decreases while n_{eff} stabilises, as expected.

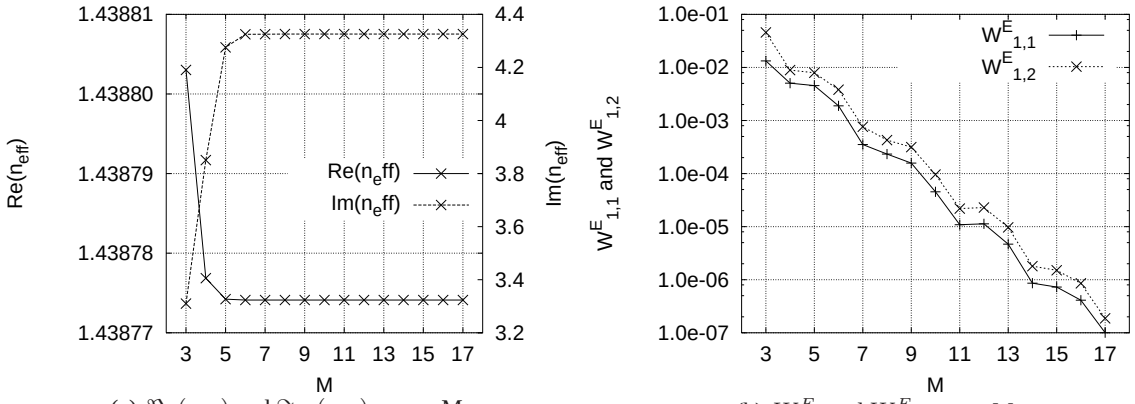

(a) $\Re e(n_{\text{eff}})$ and $\Im m(n_{\text{eff}})$ versus M (b) $W^E_{1,1}$ and $W^E_{1,2}$ versus M

FIG. 2.12 – Convergence of n_{eff} and of W^E with respect to M. The data are the same as in table 2.2. ($1.0e-0N$ means $1.0\,10^{-0N}$).

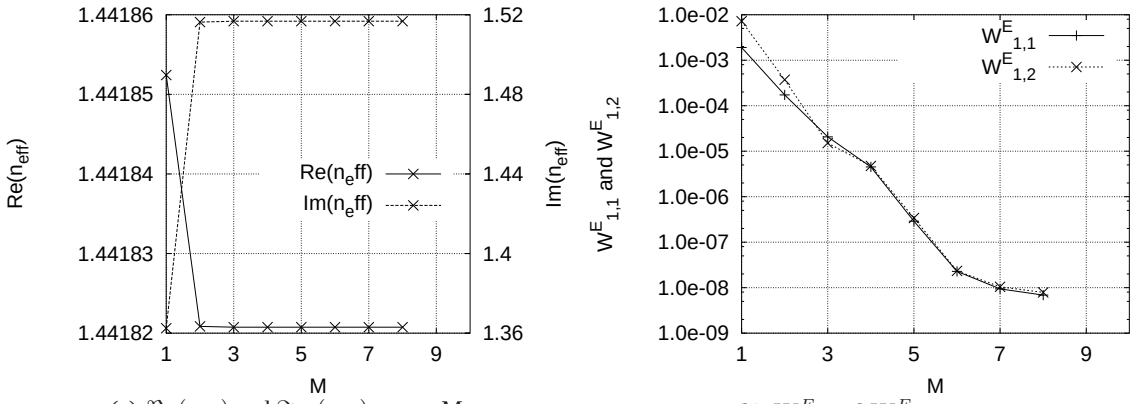

(a) $\Re e(n_{\text{eff}})$ and $\Im m(n_{\text{eff}})$ versus M (b) $W^E_{1,1}$ and $W^E_{1,2}$ versus M

FIG. 2.13 – Convergence of n_{eff} and of W^E with M, the MOF is the same as in Fig. 2.12 except that the hole diameters are equal to 1.5 μm. ($1.0e-0N$ means $1.0\,10^{-0N}$)

.

From numerical simulations, we have found that the truncation order parameter M should be made larger by a factor of around 1.5 times the largest argument of the Bessel functions on the boundary of the inclusions. This empirical rule is clearly illustrated in Fig. 2.12 and Fig. 2.13 : in the first case where the hole diameter is equal to 5 μm, M=8 is required to get the correct n_{eff} with a 10^{-9} accuracy and in the second case where the hole diameter is equal to 1.5 μm, M=3 is enough.

Comparison with other methods

The results obtained by applying the Multipole Method to MOF were compared to one of the first results obtained through a finite element method [36]. The results are in very good agreement and the existing differences are mainly due to the limitations caused by the numerical implementation (the mesh does not follow the symmetry properties of the structure) of the finite element method [37]. Another numerical implementation of the same multipole method was successfully compared to a beam propagation method [38] and to a plane-wave method [30] (the two implementations of the Multipole Method giving the same results). For the last case, it was shown that if enough plane-waves (more than 2^{16}) are considered then the two methods give the same results concerning the fundamental mode degeneracy[4] for the simple MOF structure described in the beginning of the previous section.

[4]The plane-wave method is not able to take into account the mode losses, so the imaginary part of the mode effective index cannot be computed.

2.2.6 First numerical examples

We now illustrate the numerical implementation of the Multipole Method through several basic numerical examples. These examples will exhibit the most frequently encountered symmetries in MOF : C_{2v}, C_{4v} and C_{6v}. We will not follow an arithmetical order but start with the most pedagogical example : the C_{6v} six hole MOF.

A detailed C_{6v} example : the six hole MOF

The cross section of this MOF can be seen in Fig. 2.16. The geometrical parameters of the fibre are the same as the ones of the six hole MOF used in section 2.2.5 (Λ = 6.75 μm, d = 5.0 μm), and the wavelength is also the same : $\lambda = 1.55\,\mu m$, but the relative permittivity ε_r is set to 2.1025. M is equal to 8 in all the numerical simulations of this section. In table 2.3, we give the effective indices n_{eff} of the main modes of this C_{6v} MOF. It is easy to see that the modes labelled C3/4-a of mode classes 3 and 4 have both the highest real part of n_{eff} and the lowest imaginary part, *i.e.* the lowest losses. These modes correspond to the fundamental mode of the MOF. We already know from the results described in section 2.2.3 that the modes of mode classes 3 and 4 are two-fold degenerate in a C_{6v} structure : this is exactly what is found for the C_{6v} example. In Fig. 2.15, we give the moduli of the electromagnetic field longitudinal components E_z and H_z for the two mode classes 3 and 4. As expected, the fields of these two degenerate modes do not have all the symmetry properties of the MOF structure but only a subset. It can be easily checked that these fields fulfil the symmetry properties described in Fig. 2.6(b). The longitudinal component of the Poynting vector is shown in Fig. 2.14, and it is the same for the two degenerate modes whilst being well localized in the core of the MOF.

In order to complete the description of the degenerate fundamental mode, the transverse electromagnetic vector fields for the two mode classes are given in Fig. 2.16. Since in the Multipole Method the electromagnetic fields are complex (see Eqs. (2.2)), we must consider both the real part and the imaginary part of the fields $\mathbf{E}(r,\theta)$ and $\mathbf{K}(r,\theta)$ because of the factor $e^{i(\beta z-\omega t)}$ in the full expression of the propagating electromagnetic fields. This explains why they are both drawn in the vector field figures. Since the vector fields built from the real and the imaginary parts of $\mathbf{E}(r,\theta)$ (or $\mathbf{K}(r,\theta)$) are parallel in the MOF core, we conclude that the physical field, *i.e.* the real part of $\boldsymbol{\mathcal{E}}(r,\theta,z,t)$, is linearly polarized in the MOF core for the degenerate fundamental mode.

We now describe more briefly the main higher order modes of this six hole MOF. First of all we must recall that there is no order relation in $\mathcal{C}$, and consequently it is not possible *a priori* to classify the leaky higher order modes found in this structure with the definition used when the effective indices are purely real. If the imaginary part varied monotonicaly with respect to the real part, it would have been possible to keep a simple ordering for the modes. But as can be seen in Fig. 2.17, this is no longer the case after the sequence C3/4-a (fundamental mode), C2-a, C5/6-a, and C1-a. In the following pages we give for the higher order modes (C2-a, C5/6-a, and C1-a) the moduli of the electromagnetic fields and Poynting vector longitudinal components followed by the transverse electromagnetic vector fields. It has not yet been proven that this order (C2-a, C5/6-a, and C1-a) is conserved for all C_{6v} MOF[5].

Another useful issue is the possible correspondence between C_{6v} MOF and conventional $C_{\infty v}$ step-index optical fiber modes. Due to their different symmetry properties, it is not possible to follow completely for C_{6v} MOF modes the well known classification of guided modes in conventional step-index optical fiber : $HE_{\nu,m}$, $EH_{\nu,m}$, TE_m, TM_m. On one hand, in a $C_{\infty v}$ waveguide, the HE/EH classification uses modes such that the components E_z and H_z are given by a single Fourier-Bessel component when the center of the fiber is the origin of the coordinates. On the other hand, in a C_{6v} waveguide, several Fourier-Bessel components are required to described a mode (see Eq. 2.31 in section 2.2.2 and section A.2.2 in Appendix B). Consequently, if both E_z and H_z of a MOF mode can be approximated by a single Fourier-Bessel component then the correspondence with HE/EH modes is straightforward. Most of the time, however, this is not the case. Nevertheless for a few modes such correspondence can bo made, the results are given in the following table.

[5] mode crossing could appear between these MOF modes similarly as for conventional step-index optical fibre higher order modes (see Fig.12-4 of chapter 12 in reference [2]).

TAB. 2.3 – Mode class, degeneracy, and effective index for the main modes of the C_{6v} six hole MOF of section 2.2.5. The results are computed at $\lambda = 1.55\,\mu m$.

Mode class	Degeneracy	$\Re e(n_{\text{eff}})$	$\Im m(n_{\text{eff}})$	Label in Fig. 2.17
1	1	1.4307554	0.19457921E-05	C1-a
		1.4061823	0.88085482E-03	C1-b
2	1	1.4310182	0.70048952E-06	C2-a
		1.4041826	0.29291417E-03	C2-b
3, 4	2	1.4387741	0.43257457E-07	C3/4-a
		1.4211904	0.21562081E-04	C3/4-b
		1.4176892	0.46170513E-04	C3/4-c
5, 6	2	1.4308483	0.13214492E-05	C5/6-a
		1.4138932	0.17521791E-03	C5/6-b
		1.4025688	0.90274454E-04	C5/6-c
		1.4052517	0.51396894E-03	C5/6-d
7	1	1.4203103	0.11466473E-04	C7-a
8	1	1.4217343	0.29251040E-04	C8-a

TAB. 2.4 – Correspondence between the main four C_{6v} MOF modes for the six hole MOF example as defined in the text and conventional step-index fiber modes.

MOF		Conventional fibre
Symmetry class	Mode label	Mode
3/4	C3/4-a	$HE_{1,1}$
2	C2-a	TE_1
5/6	C5/6-a	$HE_{2,1}$
1	C1-a	TM_1

A more general analysis can be made by comparing the general forms of the HE and EH longitudinal components as presented in table 12-3 of chapter 12 in reference [2] with the expansions of the longitudinal components in terms of Fourier series given in table IV of reference [18]. Equating these expansions show that MOF modes of a given symmetry class may correspond to the superposition of specific HE/EH modes. Conversely, some EH/HE modes can only be of specific symmetry classes. Nevertheless as already stated no general one to one relationship can be deduced from these results.

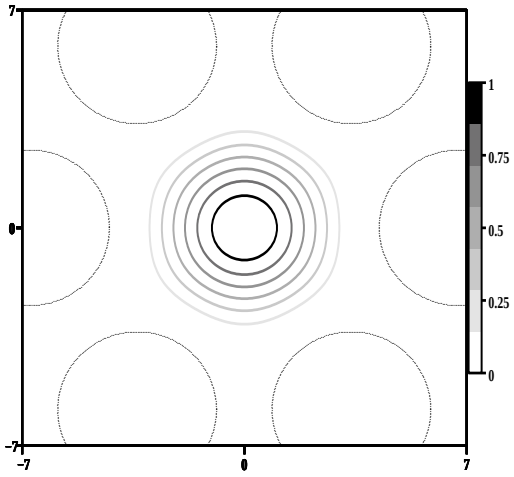

FIG. 2.14 – Modulus of the Poynting vector for the C_{6v} six hole MOF example : it is the same for the two symmetry classes p=3 and p=4. The modulus is normalized to unity.

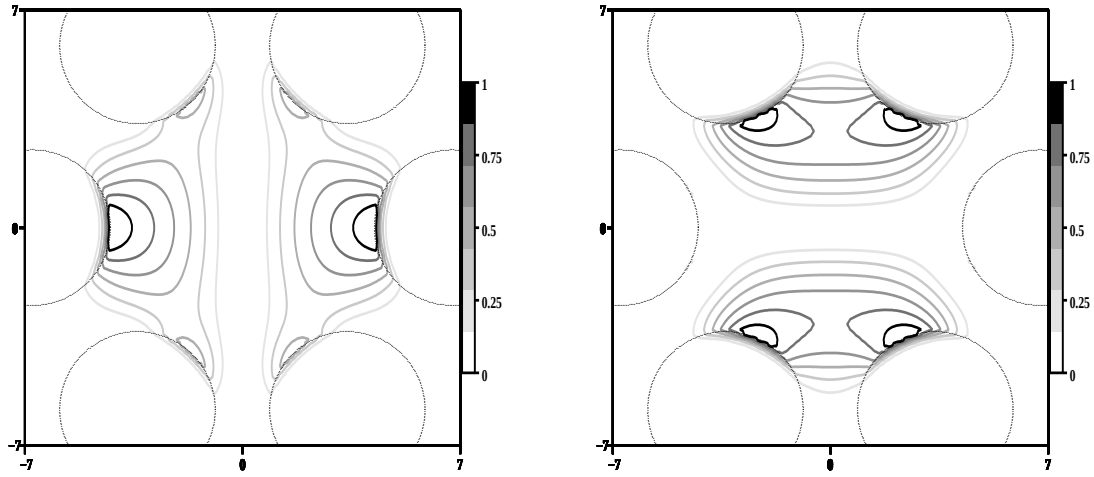

(a) $|E_z|$ for p=3

(b) $|K_z|$ for p=3

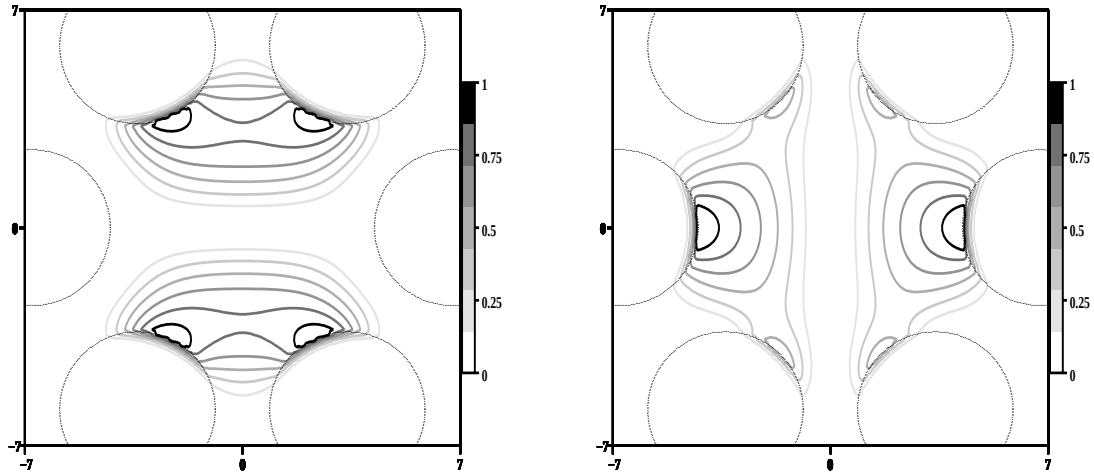

(c) $|E_z|$ for p=4

(d) $|K_z|$ for p=4

FIG. 2.15 – Moduli of electromagnetic field longitudinal components for the C_{6v} six hole MOF example, in the core region, for the degenerate fundamental mode which belongs to the symmetry classes p=3 and p=4, $n_{\text{eff}} = 1.4387741 + i\,0.4325745\,10^{-7}$. The field moduli are normalized to unity.

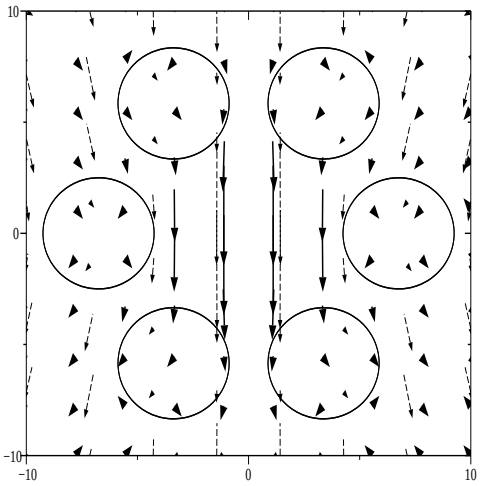

(a) Transverse E vector field for p=3

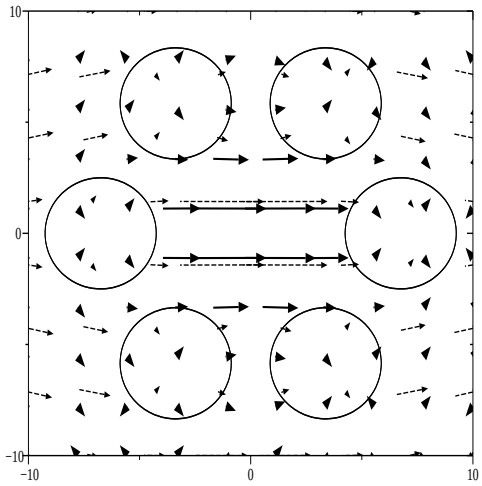

(b) Transverse K vector field for p=3

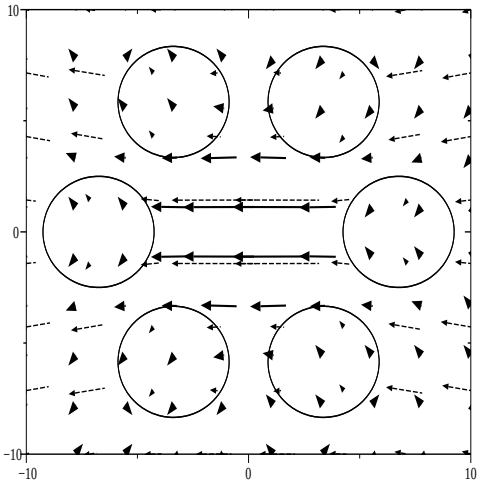

(c) Transverse E vector field for p=4

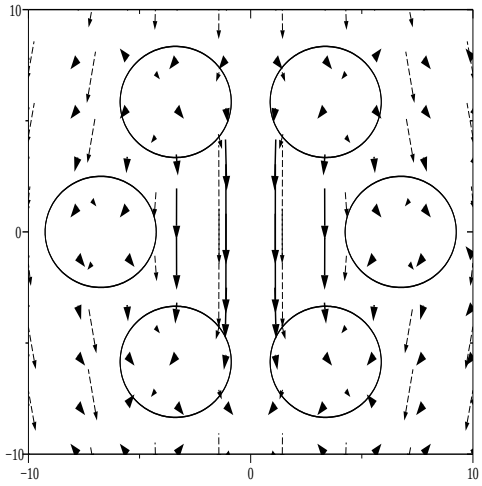

(d) Transverse K vector field for p=4

FIG. 2.16 – Transverse electromagnetic vector fields for the degenerate fundamental mode of the C_{6v} six hole MOF example. The real part of the field is represented by plain thick vectors and the imaginary part is represented by dashed thin vectors.

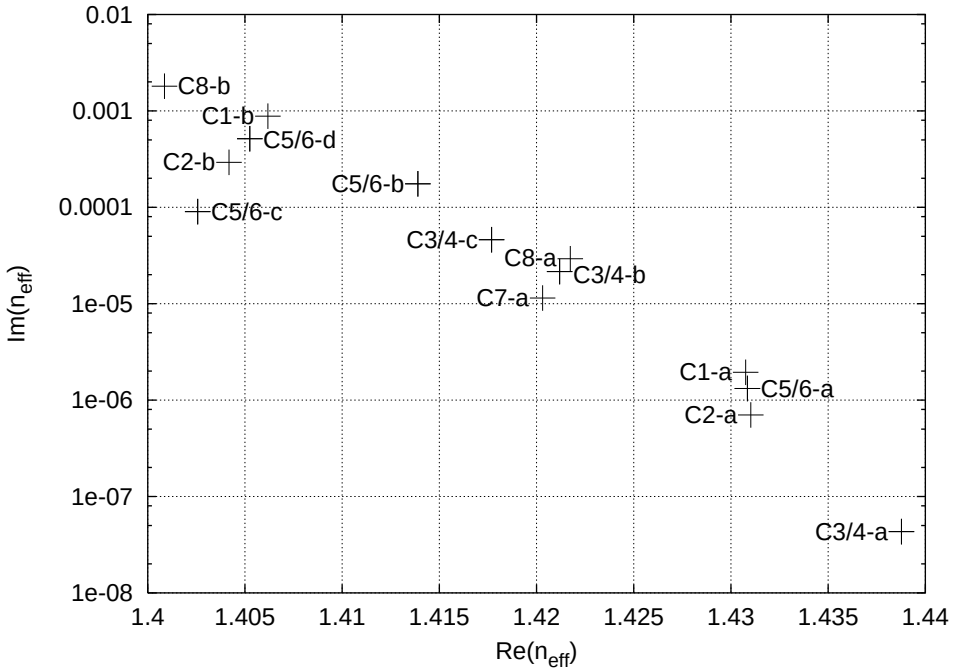

FIG. 2.17 – Imaginary part of n_{eff} versus its real part for the main modes given in table 2.3 for the C_{6v} six hole MOF of section 2.2.5. A log-scale is used for the imaginary part.

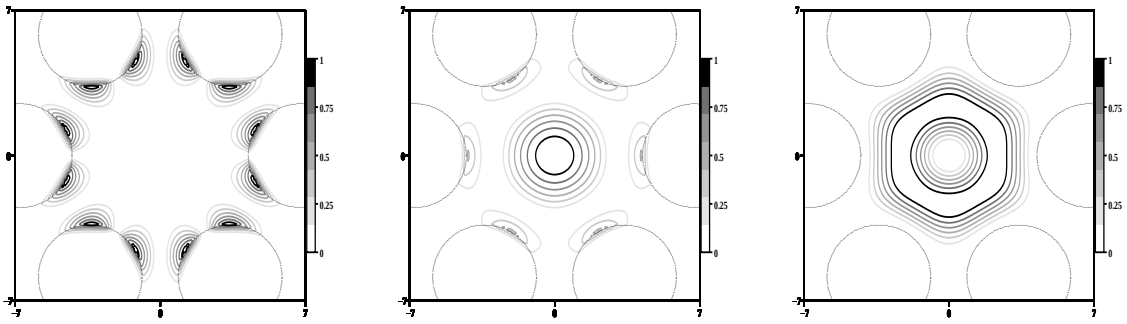

(a) $|E_z|$ (b) $|K_z|$ (c) $|S_z|$

FIG. 2.18 – Moduli of electromagnetic field and Poynting vector longitudinal components of the C_{6v} six hole MOF example, in the core region, for the higher order mode of symmetry class p=2 with the highest effective index real part, $n_{\text{eff}} = 1.4310182 + i\,0.70048952\,10^{-6}$. The maxima of the field moduli are normalized to unity.

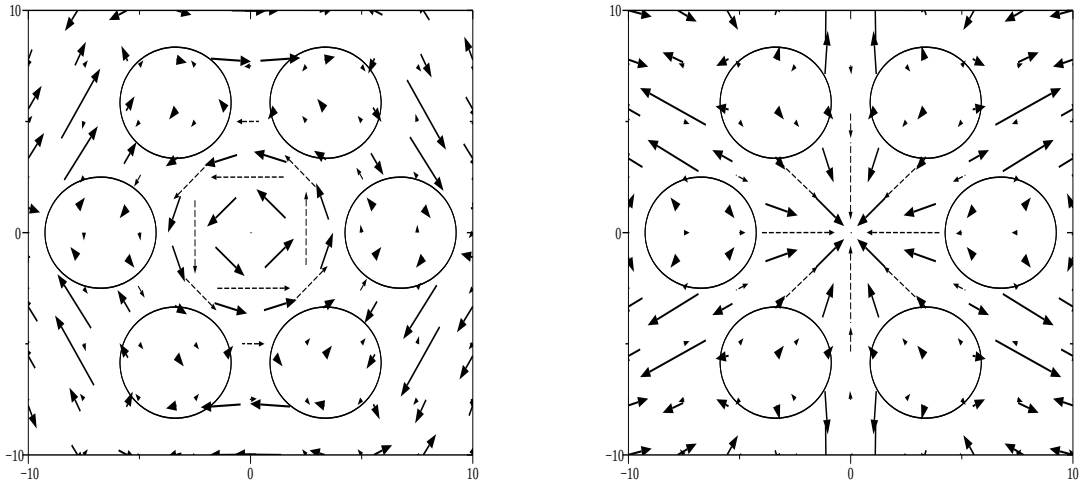

(a) Transverse E vector field

(b) Transverse K vector field

FIG. 2.19 – .
Transverse electromagnetic vector fields of the C_{6v} six hole MOF example, for the higher order mode of symmetry class p=2 with the highest effective index real part. The real part of the field is represented by plain thick vectors and the imaginary part is represented by dashed thin vectors.

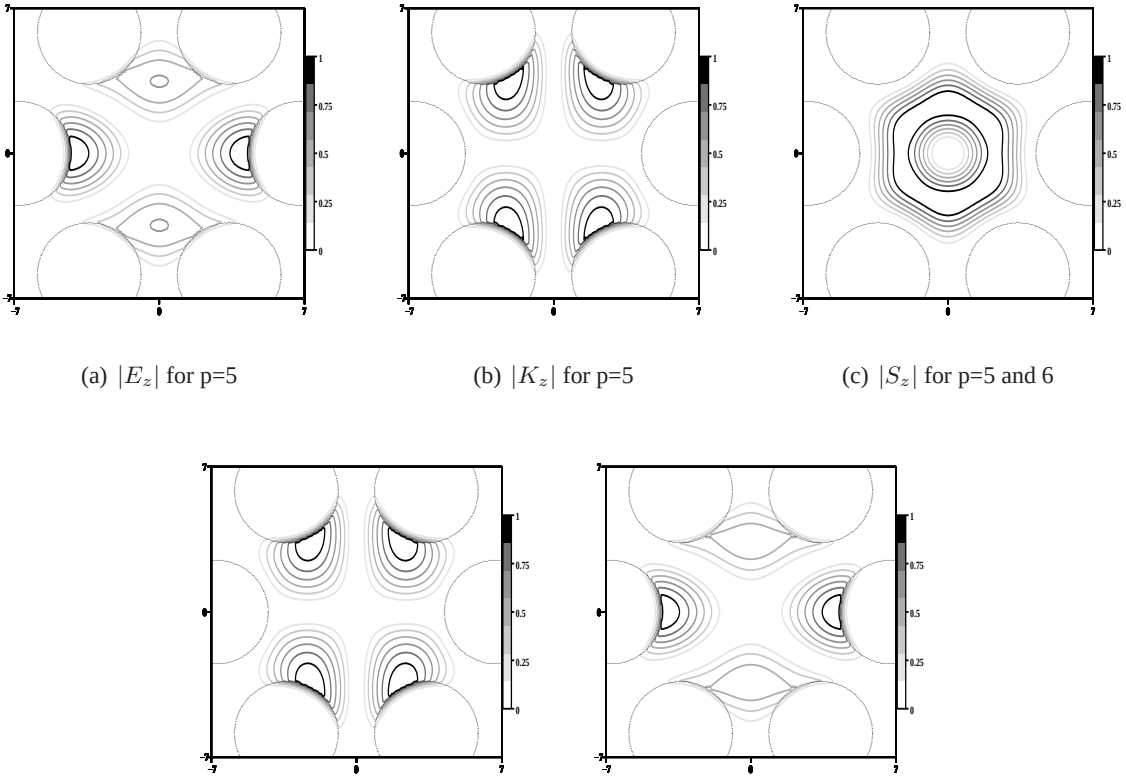

(a) $|E_z|$ for p=5 (b) $|K_z|$ for p=5 (c) $|S_z|$ for p=5 and 6

(d) $|E_z|$ for p=6 (e) $|K_z|$ for p=6

FIG. 2.20 – Moduli of electromagnetic field and Poynting vector longitudinal components of the C_{6v} six hole MOF example, in the core region, for the higher order modes of symmetry classes p=5 and p=6 with the highest effective index real part, $n_{\text{eff}} = 1.4308483 + i\,0.13214492\,10^{-5}$. The maxima of the field moduli are normalized to unity.

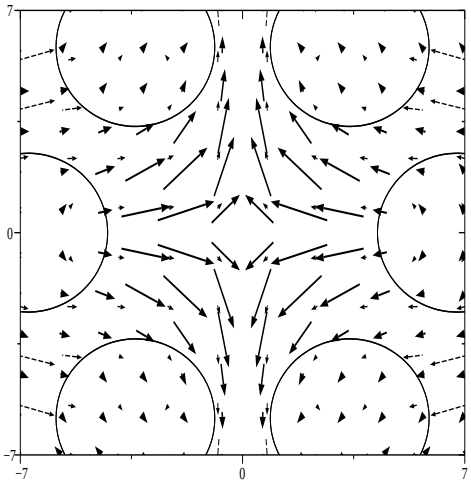

(a) Transverse E vector field for p=5

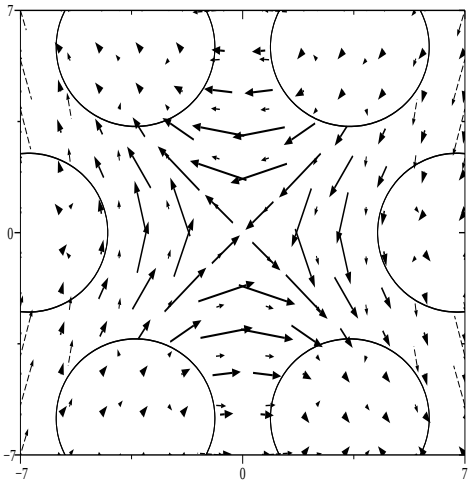

(b) Transverse K vector field for p=5

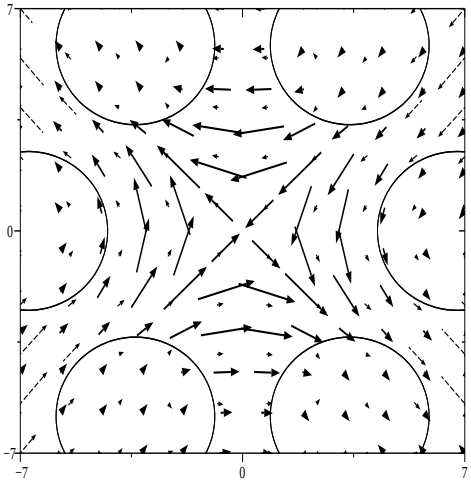

(c) Transverse E vector field for p=6

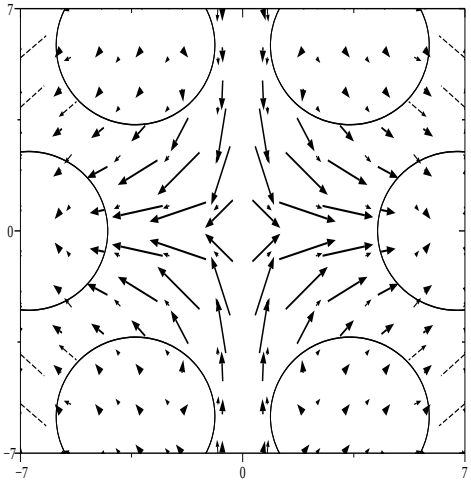

(d) Transverse K vector field for p=6

FIG. 2.21 – Transverse electromagnetic vector fields of the C_{6v} six hole MOF example, for the degenerate mode of symmetry classes p=5 and p=6. The real part of the field is represented by plain thick vectors and the imaginary part is represented by dashed thin vectors.

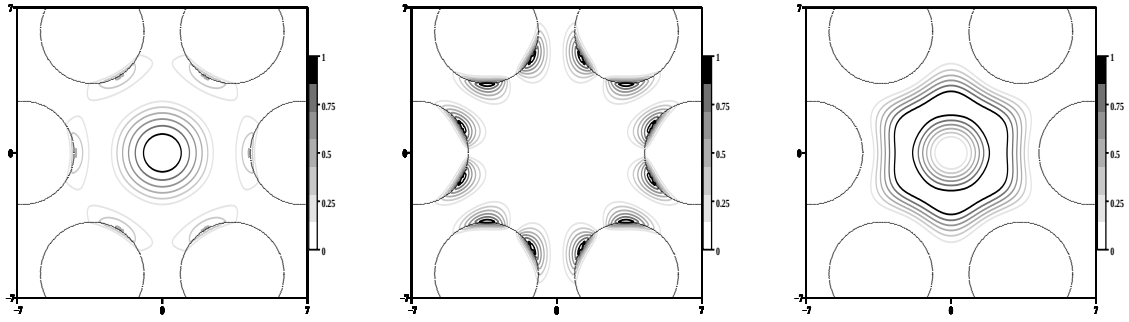

(a) $|E_z|$ (b) $|K_z|$ (c) $|S_z|$

FIG. 2.22 – Moduli of electromagnetic field and Poynting vector longitudinal components, in the core region, for the higher order mode of symmetry class p=1 with the highest effective index real part, $n_{\text{eff}} = 1.4307554 + i\,0.19457921\,10^{-5}$. The maxima of the field moduli are normalized to unity.

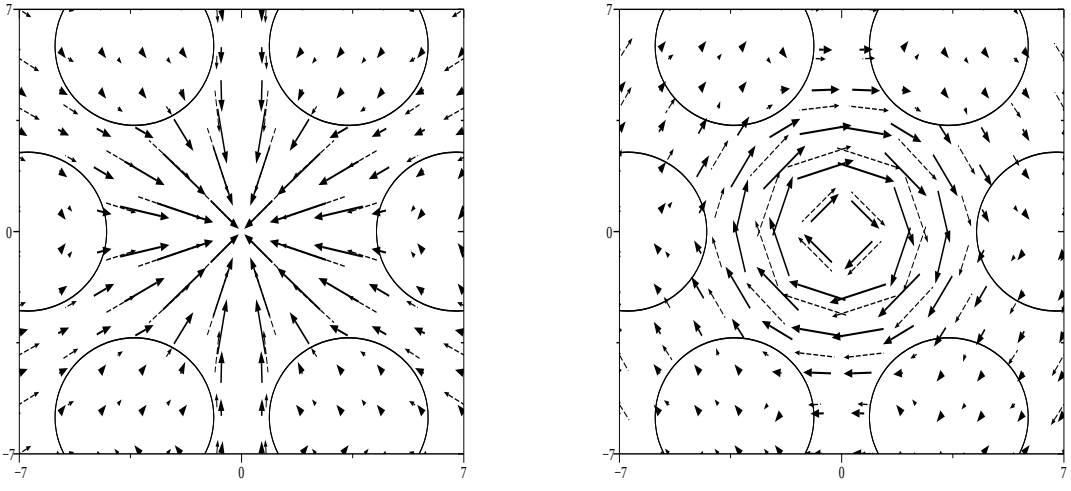

(a) Transverse E vector field (b) Transverse K vector field

FIG. 2.23 – Transverse electromagnetic vector fields for the higher order mode of symmetry class p=1 with the highest effective index real part. The real part of the field is represented by plain thick vectors and the imaginary part is represented by dashed thin vectors.

A C_{2v} example : a birefringent MOF

MOF have already been used to realize highly birefringent optical fibers [39] by means of the high index contrast and the numerous possible designs for the holes and their positions. In what follows we give a simple example which exibits a high birefringence : a C_{2v} six hole MOF with two types of hole. The MOF is nearly the same as that used in section 2.2.5 : $\Lambda = 6.75\ \mu m$, the diameters of the four small holes is fixed at 5.0 μm, but two symmetrically positioned small holes are now big holes of diameters equal to 7.0 μm, and we choose $\lambda = 1.55\,\mu m$ and ε_r = 2.0852042. M is equal to 8 in all the numerical simulations of this section. We already know from the results described in section 2.2.3 that none of the modes are degenerate. This is exactly what we found in table 2.5 where we give the effective indices n_{eff} of the main modes of this C_{2v} MOF.

TAB. 2.5 – Mode class, and effective index for the main modes of a C_{2v} six hole MOF. The results are obtained at $\lambda = 1.55\,\mu m$. According to McIsaac's theory none of the possible modes of this C_{2v} MOF can be degenerate.

Mode class	$\Re e(n_{\text{eff}})$	$\Im m(n_{\text{eff}})$	Label in Fig. 2.24
1	1.4245641	0.266614E-08	C1-a
	1.4302611	0.16786253E-05	C1-b
	1.4059800	0.4446967E-07	C1-c
	1.4096020	0.45426880E-03	C1-d
	1.3969515	0.30692507E-03	C1-e
2	1.4251917	0.125315E-08	C2-a
	1.4302577	0.6052240E-06	C2-b
	1.3992741	0.7157604E-06	C2-c
	1.4078141	0.15989247E-03	C2-d
	1.3970789	0.68785361E-04	C2-e
3	1.4373840	0.2127787E-07	C3-a
	1.4163151	0.56123303E-06	C3-b
	1.4189536	0.15076718E-04	C3-c
	1.4053802	0.16153919E-04	C3-d
	1.3946933	0.10998837E-02	C3-e
4	1.4375326	0.45399096E-07	C4-a
	1.4165924	0.93230300E-06	C4-b
	1.4194844	0.49669065E-04	C4-c
	1.4063350	0.23955853E-04	C4-d
	1.3982127	0.24979563E-02	C4-e

There are at least two interesting points concerning the modes in this C_{2v} si holes MOF. First of all, the determination of the fundamental mode is not straightforward : is it the mode labelled C2-a which has the lowest losses (see table 2.5 and Fig. 2.25) or the C4-a mode which have the highest real part of n_{eff}. We will describe a way to determine which one is the fundamental mode of the structure in the chapter 7, which is dedicated to MOF properties. The second point to consider is the lifting of the degeneracy of the C3/4-a mode described previously in the C_{6v} MOF into two distinct modes : C3-a and C4-b. The longitudinal components of these two modes are shown below in Fig. 2.26.

A C_{4v} example : a square MOF

We conclude the illustration of the ordinary symmetric structures in MOF with a C_{4v} example (the fiber contains eight identical holes of diameter 5.0 μm, the pitch is 6.75 μm, and $\varepsilon_r = 2.0852042$). In this case, only the classes 3 and 4 are degenerate as expected from McIsaac's theory. The fundamental mode belongs to these classes, and it is the mode labelled C3/4-a : the correponding longitudinal components are plotted in Fig. 2.28. The first modes of this structure are given in Table 2.6 and in Fig. 2.27.

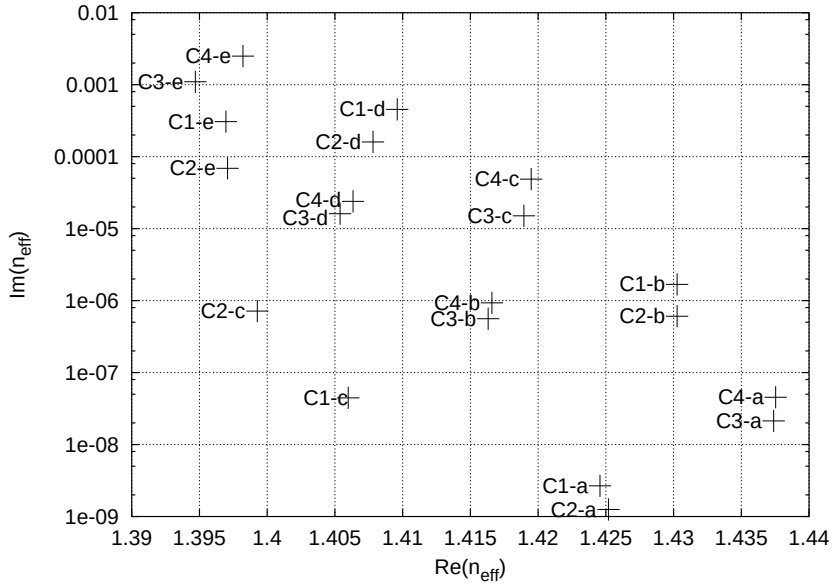

FIG. 2.24 – Imaginary part of n_{eff} versus its real part for the modes given in table 2.5 for the C_{2v} six hole MOF. A log-scale is used for the imaginary part.

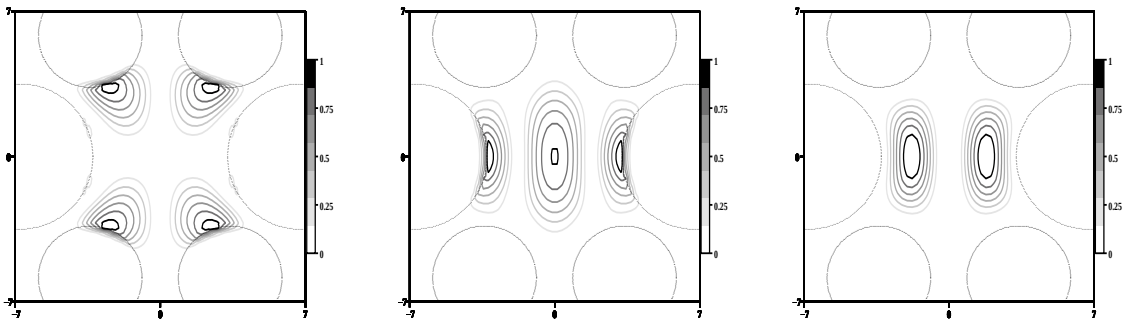

(a) $|E_z|$ (b) $|K_z|$ (c) $|S_z|$

FIG. 2.25 – Moduli of electromagnetic field and Poynting vector longitudinal components, in the core region of the C_{2v} six hole MOF example for the mode which belongs to the symmetry classes p=2, $n_{\text{eff}} = 1.4251917 + i\,0.12531510^{-8}$. The field moduli are normalized to unity.

2.2.7 Conclusion

In this long section, the Multipole Method has been explain in some detail. It appears that the symmetry properties of MOF modes obtained from McIsaac's theoretical work can be take into account naturally with this method. Only circular inclusions have been considered but more general inclusion shapes can be treated provided that the inclusions do not overlap. In this last case, the scattering matrix of each of the noncircular inclusions must be provided. Thanks to its speed and accuracy and to the way in which it can deal with material dispersion, the Multipole Method is the reference method to study finite size MOF properties including their losses when the fibers are made of circular inclusions.

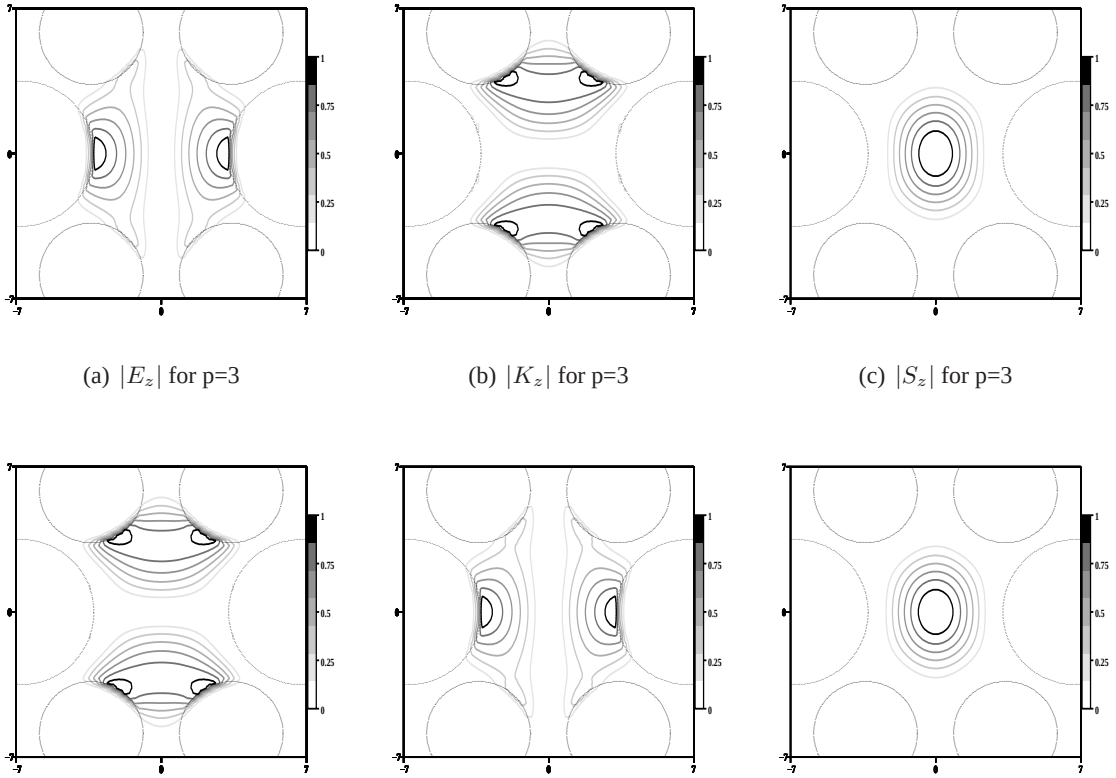

(a) $|E_z|$ for p=3 (b) $|K_z|$ for p=3 (c) $|S_z|$ for p=3

(d) $|E_z|$ for p=4 (e) $|K_z|$ for p=4 (f) $|S_z|$ for p=4

FIG. 2.26 – Moduli of electromagnetic field and Poynting vector longitudinal components, in the core region of the C_{2v} six hole MOF example for the modes of symmetry classes p=3 ($n_{\text{eff}} = 1.4373840 + i\,0.2127787\,10^{-7}$) and p=4 ($n_{\text{eff}} = 1.4375326\,10^{1} + i\,0.4539909\,10^{-7}$). The field moduli are normalized to unity.

TAB. 2.6 – Mode class, degeneracy, and effective index for the main modes of the square C_{4v} eight hole MOF. The results were computed at $\lambda = 1.55\,\mu m$.

Mode class	Degeneracy	$\Re e(n_{\text{eff}})$	$\Im m(n_{\text{eff}})$	Label in Fig. 2.27
1	1	1.433960	0.2984848E-06	C1-a
		1.423173	0.1387057E-04	C1-b
2	1	1.433891	0.2937135E-06	C2-a
		1.423461	0.1499999E-04	C2-b
		1.410688	0.6201385E-04	C2-c
3, 4	2	1.439607	0.8965050E-08	C3/4-a
		1.430761	0.1801941E-05	C3/4-b
		1.427466	0.5028845E-05	C3/4-c
		1.419888	0.2701725E-05	C3/4-d
		1.415520	0.8361918E-04	C3/4-e
		1.413382	0.8869551E-04	C3/4-f
5	1	1.433642	0.3221663E-06	C5-a
		1.423361	0.1371652E-04	C5-b
		1.411219	0.1878240E-03	C5-c
6	1	1.434133	0.2827584E-06	C6-a
		1.423380	0.1427653E-04	C6-b

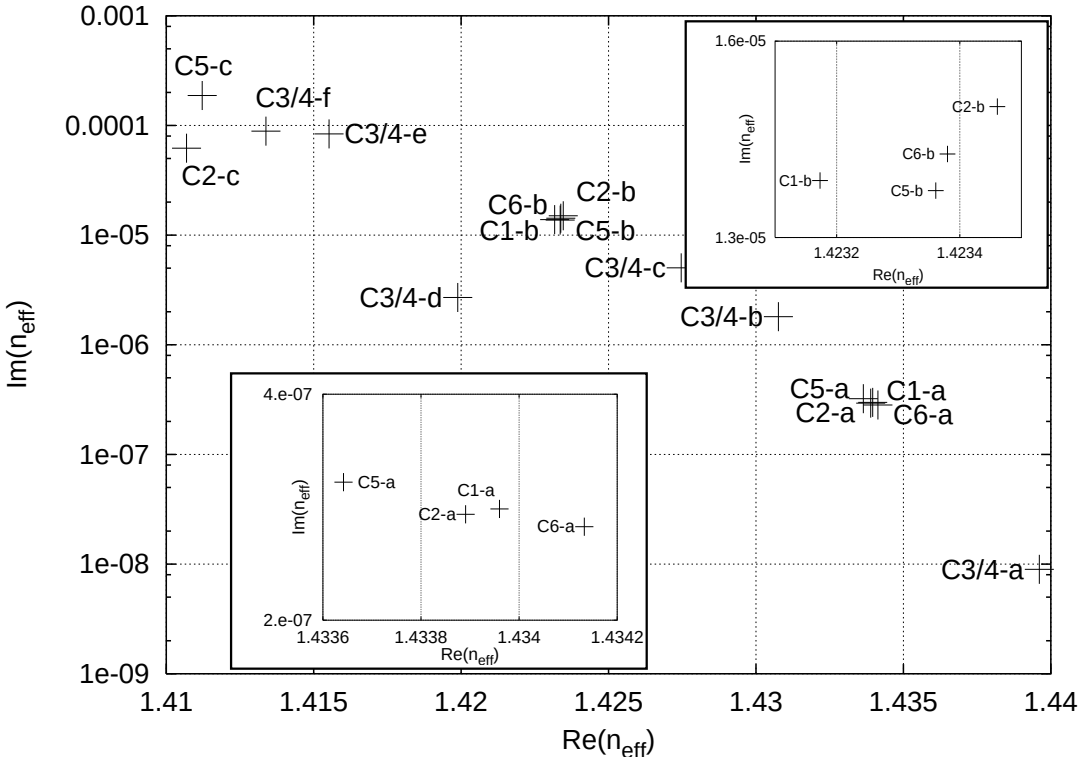

FIG. 2.27 – Imaginary part of n_{eff} versus its real part for the modes given in table 2.6 for the C_{4v} eight hole MOF. A log-scale is used for the imaginary part.The upper right inset is a zoom around the positions of C1-b and C-6b, the lower left inset is a zoom around the positions of C1-a and C-6a.

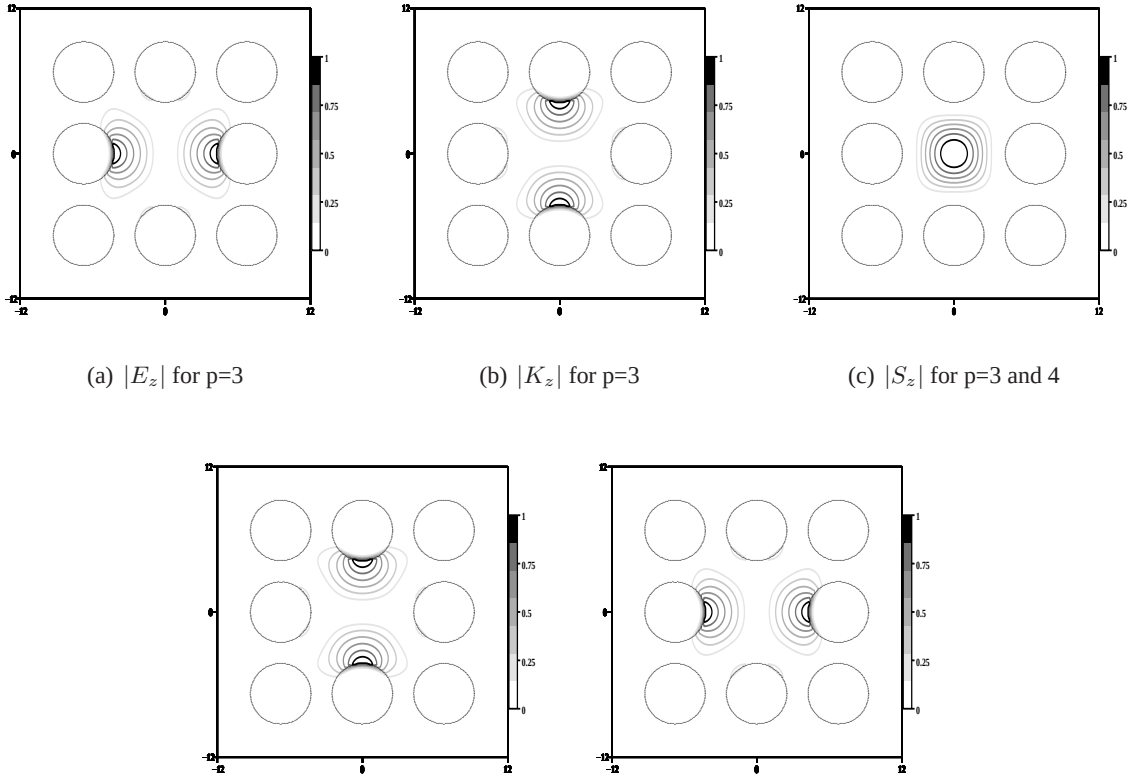

(a) $|E_z|$ for p=3 (b) $|K_z|$ for p=3 (c) $|S_z|$ for p=3 and 4

(d) $|E_z|$ for p=4 (e) $|K_z|$ for p=4

FIG. 2.28 – Moduli of electromagnetic field longitudinal components, in the core region for the degenerate fundamental mode which belongs to the symmetry classes p=3 and p=4, $n_{\text{eff}} = 1.4396074 + i\,0.8965065\,10^{-8}$. In (c) modulus of the Poynting vector : it is the same for the two symmetry classes p=3 and p=4. The field moduli are normalized to unity.

2.3 The differential method with the fast fourier factorization as a mode searching method

In order to concentrate on the modal problem and to avoid repeating what we have already published in articles dedicated to the Fast Fourier Factorization method (FFF)[40, 41], we refer to these references for the description of the FFF. We simply recall that the key point of the FFF is to rewrite the formulation of the linear relation between $\mathbf{E}$ and $\mathbf{D}$ in a truncated Fourier space. We found that, locally[40, 41] :

$$[D] = Q_\varepsilon [E] \tag{2.53}$$

in which the column matrices $[D]$ and $[E]$ are made up of three blocks, each of these blocks (r, θ, z) containing $2N+1$ Fourier components, and Q_ε is a square matrix. The size of this matrix is $3(2N+1)$ since it comprises the Toeplitz matrices : $[\![n_r^2]\!]$, $[\![n_r n_\theta]\!]$, $[\![n_\theta^2]\!]$, built from the extended unit vectors (denoted by $\mathbf{n}$) normal to the surfaces of the inclusions [40, 42]. The matrix Q_ε also contains the Toeplitz matrices $[\![\epsilon]\!]$ and $[\![1/\epsilon]\!]^{-1}$ arising from the application of the correct factorization rules, described by L. Li[43], used to reformulate the constitutive relation $\mathbf{D} = \epsilon \mathbf{E}$ in the truncated Fourier space (see section 4.7 of reference [44] and quoted references for the detailed properties of Toeplitz matrices).

$$Q_\epsilon = \begin{pmatrix} [\![\epsilon]\!][\![n_\theta^2]\!] + [\![\frac{1}{\epsilon}]\!]^{-1}[\![n_r^2]\!] & -\left([\![\epsilon]\!] - [\![\frac{1}{\epsilon}]\!]^{-1}\right)[\![n_r n_\theta]\!] & 0 \\ -\left([\![\epsilon]\!] - [\![\frac{1}{\epsilon}]\!]^{-1}\right)[\![n_r n_\theta]\!] & [\![\epsilon]\!][\![n_r^2]\!] + [\![\frac{1}{\epsilon}]\!]^{-1}[\![N_\theta^2]\!] & 0 \\ 0 & 0 & [\![\epsilon]\!] \end{pmatrix} \tag{2.54}$$

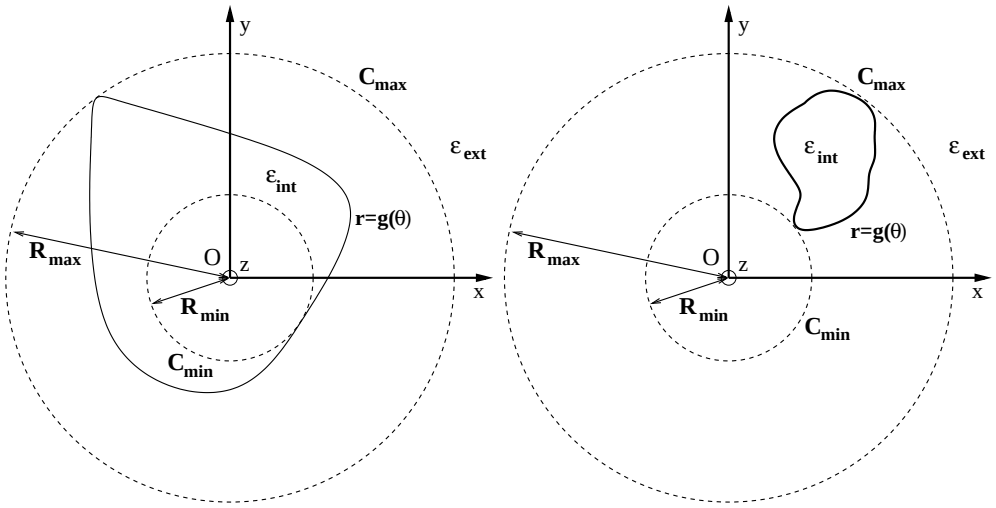

(a) Cylindrical object including the origin (b) Cylindrical object centered outside the origin

FIG. 2.29 – Modulated area with the used notations in the differential method.

This rewriting of the constitutive relation is used explicitly in a region called the "modulated area" (see Figures2.29). This area which lies between the inscribed circular cylinder C_{min} with radius R_{min} and the circumscribed circular cylinder C_{max} with radius R_{max}, contains all the diffracting cylindrical objects. For MOFs, this region contains the inclusions which confine the electromagnetic fields. In the modulated area, Maxwell's equations are reduced to a set of first order differential equations written in a four block matrix form (one block for each field component used in the theory) :

$$\frac{d}{dr}\begin{bmatrix} [E_\theta] \\ [E_z] \\ [H_\theta] \\ [H_z] \end{bmatrix} = iM(r)\begin{bmatrix} [E_\theta] \\ [E_z] \\ [H_\theta] \\ [H_z] \end{bmatrix} \tag{2.55}$$

in which $M(r)$ is a square matrix, depending on the blocks of the matrix Q_ε, with dimension $4(2N+1)$ and whose general expression valid for anisotropic, lossless or lossy, and/or inhomogeneous media can be

found in reference[40]. the expression of $M(r)$ for the present case (z-invariance and isotropic medium) is given below and was found in reference[41].

$$M(r) = \begin{pmatrix} -\frac{1}{r}\alpha Q_{\epsilon,rr}^{-1} Q_{\epsilon,r\theta} + \frac{i}{r} I_d & -\frac{1}{r}\alpha Q_{\epsilon,rr}^{-1} Q_{\epsilon,rz} & \frac{\gamma_0}{\omega r}\alpha Q_{\epsilon,rr}^{-1} & \omega\mu_0 I_d - \frac{\alpha}{\omega r^2} Q_{\epsilon,rr}^{-1}\alpha \\ -\gamma_0 Q_{\epsilon,rr}^{-1} Q_{\epsilon,r\theta} & -\gamma_0 Q_{\epsilon,rr}^{-1} Q_{\epsilon,rz} & \frac{\gamma_0^2}{\omega} Q_{\epsilon,rr}^{-1} - \omega\mu_0 I_d & -\frac{\gamma_0}{r\omega} Q_{\epsilon,rr}^{-1}\alpha \\ \omega\left(Q_{\epsilon,\theta\theta} - Q_{\epsilon,\theta r} Q_{\epsilon,rr}^{-1} Q_{\epsilon,r\theta}\right) - \frac{\gamma_0}{\mu_0\omega r}\alpha & \frac{\alpha^2}{\mu_0\omega r^2} + \omega\left(Q_{\epsilon,zr} Q_{\epsilon,rr}^{-1} Q_{\epsilon,rz} - Q_{\epsilon,zz}\right) & \frac{i}{r} I_d - \gamma_0 Q_{\epsilon,zr} Q_{\epsilon,rr}^{-1} & Q_{\epsilon,zr} Q_{\epsilon,rr}^{-1}\frac{\alpha}{r} \\ \omega\left(Q_{\epsilon,\theta\theta} - Q_{\epsilon,\theta r} Q_{\epsilon,rr}^{-1} Q_{\epsilon,r\theta}\right) - \frac{\gamma_0^2}{\mu_0\omega} I_d & \frac{\gamma_0}{\mu_0\omega r}\alpha + \omega\left(Q_{\epsilon,\theta z} - Q_{\epsilon,\theta r} Q_{\epsilon,rr}^{-1} Q_{\epsilon,rz}\right) & Q_{\epsilon,\theta r} Q_{\epsilon,rr}^{-1}\gamma_0 & -Q_{\epsilon,\theta r} Q_{\epsilon,rr}^{-1}\frac{\alpha}{r} \end{pmatrix} \tag{2.56}$$

The α matrix in $M(r)$ coefficients is a diagonal matrix such that $\alpha_{nm} = n\delta_{nm}$, it comes from the derivation according to θ. The $M(r)$ matrix depends only on the r-coordinate and its size is $(4(2N+1))^2$. The equations (2.55-2.56) are a new formulation of both the Maxwell's equations and the constitutive relations in cylindrical coordinates in the truncated Fourier space.

2.3.1 First Approach

Modes are homogeneous solutions of Maxwell's equations solutions, of the form $f(r,\theta)\exp(i(\beta z - \omega t))$, in which β is the modal propagation constant and ω is the angular frequency.

In a homogeneous and isotropic medium, the Fourier coefficients of the electromagnetic field components : $E_{z,n}$ and $H_{z,n}$ satisfy the propagation equation (see eq. (2.7), written in cylindrical coordinates. We simply slightly change the notations to adapt it to the description of this differential method :

$$(k_{t,j}r)^2 \frac{d^2 u_{z,n}}{d\left(k_{t,j}r\right)^2} + (k_{t,j}r)\frac{du_{z,n}}{d\left(k_{t,j}r\right)} + \left[(k_{t,j}r)^2 - n^2\right] u_{z,n} = 0 \tag{2.57}$$

with $u_{z,n} \in \{E_{z,n}, H_{z,n}\}$, $k_{t,j}^2 = k_j^2 - \beta^2$, $k_j^2 = \omega^2\mu_0\epsilon_j$, and $j \in \{int, ext\}$. The solutions are :

$$\begin{cases} H_{z,n} = A_{h,n}^{(j)} J_n\left(k_{t,j}r\right) + B_{h,n}^{(j)} H_n^+\left(k_{t,j}r\right) \\ E_{z,n} = A_{e,n}^{(j)} J_n\left(k_{t,j}r\right) + B_{e,n}^{(j)} H_n^+\left(k_{t,j}r\right). \end{cases} \tag{2.58}$$

In order to simplify the equations, we introduce the following column matrices with dimension $2(2N+1)$:

$$[A(r)] = \begin{bmatrix} \vdots \\ A_{e,n}^{(j)} J_n\left(k_{t,j}r\right) \\ \vdots \\ A_{h,n}^{(j)} J_n\left(k_{t,j}r\right) \\ \vdots \end{bmatrix} \text{ and } [B(r)] = \begin{bmatrix} \vdots \\ B_{e,n}^{(j)} H_n^+\left(k_{t,j}r\right) \\ \vdots \\ B_{h,n}^{(j)} H_n^+\left(k_{t,j}r\right) \\ \vdots \end{bmatrix} \tag{2.59}$$

We have omitted the j superscript in the left hand sides of eqs. (2.59). We recall that at $r = R_{min}$, $j = int$ and at $r = R_{max}$, $j = ext$. The scattering matrix S of the entire modulated area is defined by :

$$\begin{bmatrix} [B(R_{max})] \\ [A(R_{min})] \end{bmatrix} = S \begin{bmatrix} [B(R_{min})] \\ [A(R_{max})] \end{bmatrix} = \begin{bmatrix} S_{11} & S_{12} \\ S_{21} & S_{22} \end{bmatrix} \begin{bmatrix} [B(R_{min})] \\ [A(R_{max})] \end{bmatrix} \tag{2.60}$$

To avoid a divergence of the field at the origin ($H_n^+(r) \to \infty$ when $r \to 0$) we must have $B_{e,n}^{(int)} = 0$ and $B_{h,n}^{(int)} = 0\,\forall n$, *i.e.* $[B(R_{min})] = [0]$. In the external region, the amplitudes $B_{e,n}^{(ext)}$ and $B_{h,n}^{(ext)}$, which are the coefficients of Hankel functions, are associated with outgoing waves whereas the amplitudes $A_{e,n}^{(ext)}$ and $A_{h,n}^{(ext)}$, which are the multiplicative coefficients of Bessel functions, are associated with incident waves. Then, recalling that modes are homogeneous solutions of Maxwell's equations, we must have $A_{e,n}^{(ext)} = 0$ and $A_{h,n}^{(ext)} = 0\,\forall n$, *i.e.* $[A(R_{max})] = [0]$. Using eq. (2.60), we obtain that, for modal

fields, the column matrices $[A(R_{min})]$ and $[B(R_{max})]$ must be solutions of the following homogeneous set of equations :

$$S^{-1} \begin{bmatrix} [B(R_{max})] \\ [A(R_{min})] \end{bmatrix} = \begin{bmatrix} 0 \\ 0 \end{bmatrix} \tag{2.61}$$

Thus, the unknown amplitudes appear to be the eigenvectors associated with null eigenvalues of the inverse scattering matrix S^{-1}. Once determined, eq. (2.58) allows us to compute the fields.

2.3.2 Improved Approach in the S-matrix Propagation Algorithm with the Z-Matrix

In most cases, numerical instabilities do not permit us to integrate the differential set (2.55) directly from $r = R_{min}$ to $r = R_{max}$; that is why we use the S-matrix propagation algorithm[45]. In fact, for a fixed value of the argument $k_{t,int}R_{min}$ (see eq. 2.58), the spatial extension of the divergence due to the singularity of the Hankel functions at $r = 0$ spreads out along the r axis when the Bessel order n increases towards its maximum value fixed by the truncation order N. Consequently, the initial vectors of the integration evaluated at $r = R_{min}$ and calculated from the eq.(34) of reference[40], may contain high values which grow during the integration process and can make some blocks of the transmission matrix T ill-conditioned. We recall the reader that the T-matrix links the fields at $r = R_{min}$ and the fields at $r = R_{max}$. In order to avoid this numerical contamination, the principle of the S-matrix propagation algorithm is to split the modulated area in L slices. For each slice (s) limited by the circular cylinders with radius r_s and r_{s+1} ($r_1 = R_{min}$ and $r_{L+1} = R_{max}$), the differential set (2.55) is integrated. At $r = r_s$ for $s \in [2, L]$, we add for each interface an infinite thin homogeneous layer with permittivity ϵ_{ext}. Consequently, the column matrices defined by expression (2.59) can be generalized to the interfaces within the modulated area (see also Fig. 6 of reference[40]). We obtain the corresponding T-matrix denoted $T^{(s)}$ of the (s) slice which links the fields at r_s and the fields at r_{s+1}. We use the S-matrix of the (s) interface $r = r_s$, denoted $S^{(s)}$, and fully defined in eq. (40) of reference[40]. The S-matrix $S^{(s)}$ was defined in order to be better conditioned than the T-matrix $T^{(s)}$. We recall that the S_{22} block is such that :

$$S_{22}^{(s+1)} = S_{22}^{(s)} Z^{(s)} \tag{2.62}$$

with

$$Z^{(s)} = \{T_{11}^{(s)} + T_{12}^{(s)} S_{12}^{(s)}\}^{-1}. \tag{2.63}$$

At the end of the S-matrix propagation algorithm process, we obtain the S-matrix at the $(L+1)$ interface. This matrix is simply the required S matrix associated with the whole modulated area (see eq. (2.60)).

The modal problem initially described by equation (2.61), with the large $4(2N + 1)$ square matrix $S^{-}1$, may be performed using the benefits of the S-matrix propagation algorithm. From eq. (2.62), we deduce $\{S_{22}^{(s)}\}^{-1} = Z^{(s)}\{S_{22}^{(s+1)}\}^{-1}$. Then we multiply each side by the same vector $[A(R_{min})]$:

$$\{S_{22}^{(s)}\}^{-1} [A(R_{min})] = Z^{(s)}\{S_{22}^{(s+1)}\}^{-1} [A(R_{min})] . \tag{2.64}$$

Using eq.(40) of reference[40] or eq.(3.74) page 65 of reference [46] and identifying the left and right hand terms in eq. (2.64) we obtain :

$$[A(r_s)] = Z^{(s)} [A(r_{s+1})] . \tag{2.65}$$

In order to complete the field expansion at the interface r_s, we use again the equation (40) of reference[40], and we get :

$$[B(r_s)] = S_{12}^{(s)} [A(r_s)] . \tag{2.66}$$

For the L^{th} slice, using eq. (2.65) we note that the modal fields at the L^{th} interface are solution of :

$$[A(r_L)] = Z^{(L)} [0] \text{ or equivalently} \tag{2.67}$$

$$\{Z^{(L)}\}^{-1} [A(r_L)] = [0] \tag{2.68}$$

and the fields at the others interfaces are deduced through an iterative method by equations (2.65) and (2.66).

Equation (2.68) is a new formulation of the modal problem. Solving this equation presents two important advantages. First, the block $\{Z^{(L)}\}^{-1} = T_{11}^{(L)} + T_{12}^{(L)} S_{12}^{(L)}$ (see eq. (2.63)) is well-conditioned by definition if the number of slices in the S-matrix propagation algorithm is sufficient. The $\{Z^{(L)}\}^{-1}$ matrix is better conditioned than the S^{-1}-matrix and its size is halved. These properties allow us to study waveguides with a microstructured region, *i.e.* a modulated region in the FFF terminology, more extended along the r variable than the simple formulation we proposed previously[41]. We illustrate this improvement in section 2.3.4. Mode details concerning the different approaches we developed previously in the frame of the differential method to solve the modal problem can be found in the first section of chapter 6 of reference [46]. We can note that, as in section 2.3.1, the fields can be computed in the entire device cross section from the eigenvectors of the $\{Z^{(L)}\}^{-1}$ matrix associated with a null eigenvalue using eqs (2.65,2.66). In what follows, we will simply denote the $\{Z^{(L)}\}^{-1}$ matrix by Z^{-1} and we will denote the FFF based mode searching method we develop the FFF-MS.

The search algorithm we use within the FFF-MS is similar to the one detailed in the chapter 5 of reference[6]. However, since the computation of the S^{-1} scattering matrix of the whole MOF is more time consuming with this method than with the Multipole Method, we reduce as much as possible the number of evaluations of the Z^{-1} matrix even if this slightly reduces the capability of the algorithm to find automatically the modes of a given structure.

2.3.3 Modes and symmetries

Device with Sub-periodicity According to the Angular Variable θ

Typical MOF cross sections have often a sub-periodicity with respect to the angular variable θ, at least as a first approximation (see section 2.2.3). Nearly all the MOFs already realized fulfill the C_{nv} symmetry, *i.e.* a sub-periodicity of $2\pi/n$ with symmetry planes ($n \in \mathbb{N}^*$); most of them belong to the C_{6v} one. This property and the useful and general work of McIsaac[18, 19] relating waveguide symmetry properties and mode classification, using a group-theoretic approach, have already motivated the exploitation of the putative sub-periodicity according to θ within the Multipole Method. To use the symmetry properties of the structures studied has the following advantages : it allows a clear mode classification according to McIsaac's results. In addition, by reducing the size of the matrices in the numerical implementation of the method, it reduces the computation time and it avoids the loss of accuracy induced by the increase of the number of numerical operations when the matrix size is increased. For the already mentioned multipole method, all these benefits have already been obtained[6, 16, 47]. It is then obvious that such an improvement should be obtained in the framework of the FFF-MS. It is worth mentioning that both the MM and Finite Element Method[6] deal with the real space. Consequently, the symmetry relations are defined and used in this space. Bai and Li have established a formulation of the differential method for diffraction problems of crossed-gratings using Cartesian coordinates using the structure symmetries[48, 49]. In our work, the FFF method is formulated in the Fourier space for cylindrical coordinates (see section 3 of reference [40]), and symmetry properties have to be found in the Fourier space using angular periodicities of microstructured optical fibres.

The sub-periodicity in θ directly implies some properties for the Fourier expansions of the optogeometric quantities ($\bar{\bar{\epsilon}}$, n_r, n_θ, ...) used by the FFF, and then induce a splitting of the differential set into several independent sub-sets as we show in the following.

First, let us define the Fourier expansion of a geometrical quantity denoted $w(\theta)$ with sub-period T such that $N_T T = 2\pi$ where N_T is the number of sub-periodicity (for a C_{6v} structure, we have $N_T = 6$). On the 2π-period, the Fourier expansion of $w(\theta)$ is written :

$$w(\theta) = \sum_{n=-\infty}^{\infty} w_n e^{in\theta} \text{ with } w_n = \frac{1}{2\pi} \int_0^{2\pi} w(\theta) e^{-in\theta} d\theta. \tag{2.69}$$

The Fourier expansion of $w(\theta)$ on the sub-period T is written :

$$w(\theta) = \sum_{n=-\infty}^{\infty} w'_n e^{in\frac{2\pi}{T}\theta} \text{ with } w'_n = \frac{1}{T}\int_0^T w(\theta) e^{-in\frac{2\pi}{T}\theta} d\theta. \tag{2.70}$$

After a few calculations, we obtain the known result :

$$\forall n \in \mathbb{Z}, \begin{cases} \text{if } n \neq mN_T, m \in \mathbb{Z} \text{ then } w_n = 0, \\ \text{if } n = mN_T, m \in \mathbb{Z} \text{ then } w_n = w_{mN_T} = w'_m \end{cases} \tag{2.71}$$

The Fourier spectrum of $w(\theta)$ on the 2π-range is the Fourier spectrum of $w(\theta)$ on the sub-period T with an enlargement of factor N_T. Let us illustrate the consequences of this property (2.71) on a simple example in which $N_T = 3$. The Fourier coefficients of $w(\theta)$ in the T-range called (w'_n) are $\{..., w'_{-4}, w'_{-3}, w'_{-2}, w'_{-1}, w'_0, w'_1, w'_2, w'_3, w'_4, ...\}$ and, according to the property (2.71), the Fourier coefficients of w on the 2π-range called (w_n) are $\{..., 0, 0, w'_{-2}, 0, 0, w'_{-1}, 0, 0, w'_0, 0, 0, w'_1, 0, 0, w'_2, 0, 0, ...\}$. Consequently, the Toeplitz matrix of $w(\theta)$ denoted $[\![w]\!]$ (see section 4.7 of reference [44] and quoted references for the detailed properties of Toeplitz matrices) on the 2π-period contains non-null diagonals regularly separated by $(N_T - 1)$ null diagonals.

Moreover, when we invert such a matrix, as $[\![w]\!]$, or multiply two such matrices, the matrix structure is preserved even if the matrix obtained is not usually a Toeplitz matrix.

The blocks of the integration matrix $M(r)$ in eq. (2.55) are not Toeplitz matrices since some of them contain the matrix α and the blocks of the matrix Q_ϵ[40], nevertheless these blocks keep the diagonal structure of the matrix $[\![w]\!]$. Consequently, the differential set (2.55) is split into $N_T = 3$ independent differential sub-sets which link the Fourier coefficients of the field components (E_θ, E_z, H_θ or H_z) among the following classes of expansion orders : $\{-4, -1, 2\}$,$\{-3, 0, 3\}$ and $\{-2, 1, 4\}$.

To conclude, when we consider a sub-periodicity with N_T sub-periods, the differential set (2.55) is split into N_T independent and different sub-sets. However each block of the Q_ϵ matrix contains the same terms for all the differential sub-sets. The computational time depends approximatively on the cube of the matrix integration size, equal to $4(2N + 1)$, whereas the size of the integration matrix of each sub-set is $4(2N + 1)/N_T$ or less. So the duration of an integration for all the differential sub-sets scales as $N_T(4(2N + 1)/N_T)^3 = (4(2N + 1))^3/N_T^2$, while the computational time of the global differential set scales as $(4(2N+1))^3$. Hence taking into account the sub-periodicity permits us to reduce approximatively the computation time by a factor N_T^2 (36 for a C_{6v} structure).

Using the Mode Symmetries within the FFF-MS

In the previous section, we have shown that these sub-periodicities imply the splitting of the Fourier coefficient set of the modal electromagnetic fields into N_T independent sub-sets, all these sub-sets being required to compute the modal fields. In the present section, we first show that it is sufficient to study one or two sub-sets to describe completely the modal field of a $C_{N_T v}$ structures. This result is related to the exhaustive description of symmetry classes and field expressions of waveguide modes established by McIsaac[18, 19] and improved by Fini[47]. Secondly, we explain explicitly how the modal fields (Fourier amplitudes) are computed in the FFF-MS using the improved approach in the S-matrix propagation algorithm.

For a sub-periodicity order N_T, we choose to note I_i the N_T sub-sets of Fourier coefficient orders in the following way :

$$I_i = \{nN_T + i - 1, n \in \mathbb{Z}\} \text{ with } i \in [1, N_T]\,. \tag{2.72}$$

We only consider a $C_{N_T v}$ symmetry MOF, the C_{N_T} case can be found in a similar way. When N_T is odd, we know from McIsaac's work that there are $N_T + 1$ mode classes. The number of non-degenerate mode classes is equal to 2 and the number of pairs of two-fold degenerate mode classes is $(N_T - 1)/2$. When N_T is even, the number of non-degenerate mode classes is equal to 4 and the number of pairs of two-fold degenerate mode classes is $((N_T - 2)/2)$. We complete the three first columns given in Table IV of reference[18] with the sub-sets of Fourier coefficients needed to describe the fields in the FFF-MS for

each mode class (see Table (2.7)). We notice that some mode classes (C_k and C_{k+1}) need two sub-sets of Fourier coefficients. In Table (2.8), we illustrate the splitting of the Fourier coefficients into sub-sets for a $C_{N_T v}$ symmetry waveguide for N_T from 1 to 8. In Table (2.8), we illustrate the splitting of the Fourier

N_T	Mode class p	E_{zpq}	FFF-MS Fourier coefficients sub-sets
even odd	1	$\sum_{n=0}^{n=+\infty} F_{1qn}(r)\cos(N_T n\theta)$	I_1
even odd	2	$\sum_{n=0}^{n=+\infty} G_{1qn}(r)\sin(N_T n\theta)$	I_1
even odd	k	$\sum_{n=0}^{n=+\infty}\left\{F_{kqn}(r)\cos\left[(N_T n-\frac{k-1}{2})\theta\right]+P_{kqn}(r)\cos\left[(N_T n+\frac{k-1}{2})\theta\right]\right\}$	$I_{\frac{1+k}{2}}, I_{N_T+\frac{3-k}{2}}$
even odd	k+1	$\sum_{n=0}^{n=+\infty}\left\{G_{(k+1)qn}(r)\sin\left[(N_T n-\frac{k-1}{2})\theta\right]+R_{(k+1)qn}(r)\sin\left[(N_T n+\frac{k-1}{2})\theta\right]\right\}$	$I_{\frac{1+k}{2}}, I_{N_T+\frac{3-k}{2}}$
even	N_T+1	$\sum_{n=0}^{n=+\infty} F_{(N_T+1)qn}(r)\cos\left[N_T\left(n+\frac{1}{2}\right)\theta\right]$	$I_{1+\frac{N_T}{2}}$
even	N_T+2	$\sum_{n=0}^{n=+\infty} G_{(N_T+2)qn}(r)\sin\left[N_T\left(n+\frac{1}{2}\right)\theta\right]$	$I_{1+\frac{N_T}{2}}$

TAB. 2.7 – Fourier series representations of the longitudinal electric field for waveguides with $C_{N_T v}$ symmetry (the first three columns come from Table IV in reference[18]). Like in this reference, the q subscript indicates the q^{th} mode of the considered mode class. See eq. (2.72) for the definition of the I_i.

coefficients into sub-sets for a $C_{N_T v}$ symmetry waveguide for N_T from 1 to 8.

$N_T \rightarrow$ Mode class p $\downarrow$	1	2	3	4	5	6	7	8
1	I_1	I_1	I_1	I_1	I_1	I_1	I_1	I_1
2	I_1	I_1	I_1	I_1	I_1	I_1	I_1	I_1
3	-	I_2	I_2,I_3	I_2,I_4	I_2,I_5	I_2,I_6	I_2,I_7	I_2,I_8
4	-	I_2	I_2,I_3	I_2,I_4	I_2,I_5	I_2,I_6	I_2,I_7	I_2,I_8
5	-	-	-	I_3	I_3,I_4	I_3,I_5	I_3,I_6	I_3,I_7
6	-	-	-	I_3	I_3,I_4	I_3,I_5	I_3,I_6	I_3,I_7
7	-	-	-	-	-	I_4	I_4,I_5	I_4,I_6
8	-	-	-	-	-	I_4	I_4,I_5	I_4,I_6
9	-	-	-	-	-	-	-	I_5
10	-	-	-	-	-	-	-	I_5

TAB. 2.8 – Sub-sets of the Fourier coefficients in the FFF-MS associated with the different mode classes as defined by McIsaac for a $C_{N_T v}$ waveguide for several values of N_T.

In the previous paragraph, we determine the FFF-MS sub-sets of Fourier coefficients that describe each mode class for $C_{N_T v}$ waveguides. Now, we express the Fourier amplitudes of the FFF-MS modal fields w'_n given by equation (2.70) by comparison with the Fourier expansion expressions given by the third column of Table (2.7), distinguishing non-degenerate mode classes and degenerate mode classes. For a $C_{N_T v}$ symmetry waveguide, we notice that a couple of successive mode classes ($p = 1$ and 2 ; k and $k+1$; N_T+1 and N_T+2) need the same FFF-MS Fourier coefficient sub-sets (for example I_1 for $p = 1$ and 2). Thus, we limit the following discussion to even values of N_T ; the odd case can be deduced immediately by eliminating the mode classes N_{T+1} et N_{T+2}.

Fields expansions in Table (2.7) are expressed in a cosine or sine function basis ($\cos(N_T n\theta)$ and $\sin(N_T n\theta)$), and the Fourier amplitudes $F_{pqn}(r)$, $G_{pqn}(r)$, $P_{pqn}(r)$, and $R_{pqn}(r)$ are real numbers. Using the Euler formula, we find the Fourier expansion of the FFF-MS expressed on the exponential function basis ($e^{iN_T n\theta}$) in equation (2.70) and the corresponding Fourier amplitudes (w'_n) are complex numbers. Consequently, we deduce from the cosine function that Fourier amplitudes $F_{pqn}(r)$ and $P_{pqn}(r)$ satisfy : $w'_{-m} = w'_m$ with $m \geq 0$ for mode classes $p = 1$, k and N_T+1, and we deduce from the sine

function that Fourier amplitudes $G_{pqn}(r)$ and $R_{pqn}(r)$, satisfy : $w'_{-m} = -w'_m$ with $m \geq 0$ for mode classes $p = 2$, $k+1$ and $N_T + 2$.

Now we can come back to the link between the Z-matrix and the above results. We start with the two pairs of non-degenerate mode classes ($p = 1$ and 2 ; $N_T + 1$ and $N_T + 2$). The determinant map of the Z^{-1} sub-matrix associated with the sub-sets (I_1 or $I_{1+\frac{N_T}{2}}$) provides the effective index of both mode classes. On one hand, the modal fields (*i.e.* the eigenvectors associated with a null eigenvalue, see equation (2.68)) corresponding to a Fourier expansion expressed only with cosine functions (mode classes $p = 1$ and $N_T + 1$), contain Fourier amplitudes with identical signs as shown above. On the other hand, the modal fields corresponding to a Fourier expansion expressed only with sine functions (mode classes $p = 2$ and $N_T + 2$), contain Fourier amplitudes with opposite signs.

We now consider the case of degenerate mode classes ($p = k$ and $k+1$) : the determinant map of the Z^{-1} sub-matrix associated with the sub-sets ($I_{\frac{1+k}{2}}$ or $I_{N_T+\frac{3-k}{2}}$) provides the same effective index. The Fourier coefficients of the modal fields are linear combinations of eigenvectors (associated with a null-eigenvalue) of the Z^{-1} sub-matrix corresponding to the subsets $I_{\frac{1+k}{2}}$ and $I_{N_T+\frac{3-k}{2}}$. Before combining the eigenvectors, we must normalize them. We choose to normalize through the value of the smallest order Fourier coefficient. The linear combination becomes a summation when the Fourier expansions are expressed with a cosine function (mode class $p = k$) and a difference when the Fourier expansions are expressed with a sine function (mode class $p = k + 1$).

As an example, we consider a waveguide with C_{6v} symmetry (seventh column of Table (2.8)). The Fourier expansion of E_{zpq} is written for the mode class $p = 1$ (first line of Table (2.7)) :

$$E_{z1q} = \sum_{n=0}^{+\infty} F_{1qn}(r) \cos\left(N_T n\theta\right). \tag{2.73}$$

Identifying with equation (2.70), we finally obtain :

$$E_{z1q} = \sum_{n=-\infty}^{+\infty} w'_n e^{iN_T n\theta} \text{ with } w'_m = w'_{-m} = \frac{F_{1qm}(r)}{2} \, (m \geq 0). \tag{2.74}$$

The eigenvector deduced from the equation (2.68) and corresponding to the sub-set I_1 contains these Fourier coefficients w'_n. We can compute the E_{zpq} Fourier expansion for the other mode classes in the same way.

2.3.4 Validation of the FFF based mode searching method by comparison with the Multipole Method results

In order to validate the FFF-MS as a modal method for studying MOFs we use the MM as a reference method since it is the most accurate method currently available in the case of circular and homogeneous inclusions due to the fact that it is then partially analytic[6]. Our first test system is the C_{6v}, one ring solid core MOF described in reference [6] ; the hole diameter d is equal to 1 μm, the pitch Λ is equal to 2.3 μm, the matrix index $n_{mat} = 1.4439035654$ (the number of significant digits given here has no relation to the accuracy with which the refractive index of silica is known at that wavelength, the given values are the ones used in the numerical simulations), and the cylinder index $n_{cyl} = 1$. The second test structure is a C_{2v} six-hole solid core MOF. It is worth mentioning that all the results computed with the FFF shown in this section and the following ones are obtained on a desktop computer with reasonable computation times.

A C_{6v} MOF

The MM finds an effective index value n_{eff} for the fundamental mode such that $n_{\text{eff}} = 1.4207845 + i\,7.20952\,10^{-4}$ for $\lambda = 1.56\,\mu$m for a value of the parameter M, which controls the number of coefficients in the Fourier-Bessel expansion, equal to 12 (*i.e.*$2M + 1$ coefficients). For $N = 60$, our mode searching algorithm finds $n_{\text{eff}} = 1.42078315 + i\,7.20465\,10^{-4}$. In this case the relative error between

FFF-MS and MM for the effective index modulus is around 10^{-6}. We test the convergence capability of theFFF-MS according the Fourier expansion order N ; this is done in Fig. 2.30 for the fundamental mode of our test structure. If the correct factorization rules used for the description of the constitutive relation linking $\mathbf{E}$ and $\mathbf{D}$ are not included, we are no longer in the frame of the FFF but within the classical differential method (CDM)[50]. It has already been shown that in this case the convergence is much slower and even not attainable (see Fig. 6 and 10 of reference [42]) for diffraction problems in TM polarization. The results shown in Fig. 2.30 clearly demonstrate that the effective index computed using the FFF-MS converges toward the value obtained from the MM when the Fourier expansion order N is increased. As expected, we can also state that, in a modal problem, the FFF-MS convergence is much faster than that of the similar mode searching method based on the classical differential method (denoted CDM-MS below).

In order to quantify these convergences, we compute the relative error between the FFF-MS results and the MM ones and also the relative error between the CDM-MS and the MM results. Since n_{eff} is a complex number we use the normalized modulus of the difference between the two values. As can be seen in Fig. 2.31, as soon as $N = 60$, the relative error for the FFF-MS is around 10^{-6} for $N = 60$ and reduces to $3.\,10^{-7}$ for $N = 162$. The fall of the relative error obtained for 35 slices in the S-matrix propagation algorithm between $N = 84$ and N about 100 is due to the FFF-MS values crossing the MM value. This fall shows that only the global behavior of the convergence curves must be considered. The field maps of the fundamental mode found with the FFF-MS naturally fulfill the symmetry properties (see section 2.3.3) as shown in Fig. 2.32, and these maps are identical to those obtained with the MM.

Since we have solved the issue of the numerical instabilities occuring in the previous formulation of the FFF-MS applied to mode searching[41], we can now study structures with more than one ring of inclusions, as is proven below. For a two-ring MOF with the same optogeometric parameters as the one ring MOF described above, the MM gives $n_{\text{eff}} = 1.4210361 + i\,2.38070\,10^{-5}$ for $M = 12$ at $\lambda = 1.56\,\mu$m. In this case, the FFF-MS gives $n_{\text{eff}} = 1.42103506 + i\,2.36453\,10^{-5}$ for $N = 60$ and $L = 45$ and $n_{\text{eff}} = 1.421036081 + i\,2.37984\,10^{-5}$ for $N = 150$ and $L = 105$. Consequently, the relative error is $1.3\,10^{-6}$ for the real part of the effective index and $6.8\,10^{-3}$ for the imaginary part for the first set of convergence parameters, and the relative error decreases to $1.3\,10^{-8}$ for the real part of n_{eff} and to $3.6\,10^{-4}$ for its imaginary part for the second set of parameters.

For a three-ring MOF at the same wavelength, the MM gives $n_{\text{eff}} = 1.4210465 + i\,8.118\,10^{-7}$ for $M = 12$ whereas the FFF-MS gives $n_{\text{eff}} = 1.4210445 + i\,7.928\,10^{-7}$ for $N = 60$ and $L = 70$ and $n_{\text{eff}} = 1.4210465 + i\,8.117\,10^{-7}$ for $N = 150$ and $L = 160$. The L values have been chosen in order to describe each inclusion layer, in the two MOFS, with the same number of layers in the S-algorithm. The relative error on the effective index is $1.4\,10^{-6}$ for the real part and $2.3\,10^{-2}$ for the imaginary part for the first set of convergence parameters, and the relative error decreases to $1.1\,10^{-8}$ for the real part, and to $1.7\,10^{-3}$ for the imaginary part for the second set of parameters.

We can conclude that the FFF-MS is now able to find accurately the effective indices of MOFs made of several rings of inclusions. It is worth mentioning that three ring MOFs are not only academic test fibers but also fabricated fibers as shown in reference[51].

As shown theoretically in the previous sections, the FFF-MS is also able to deal with the other symmetry classes. As an example we give the results for two higher order modes of our test MOF. The first one we consider belongs to the symmetry class $p = 2$. The effective index obtained with the MM for $M = 12$ is $1.3873312 + i\,4.2278502\,10^{-3}$ whereas with the FFF-MS we obtained a value of $1.38732918 + i\,4.22616\,10^{-3}$ for $N = 60$. The convergence test for the FFF-MS is shown in Fig. 2.33 and the computed field map of this mode is depicted in Fig. 2.34. The third mode we study belongs to the symmetry class $p = 1$. The effective index found with the MM for $M = 12$ is $1.3889179 + i\,5.7618884\,10^{-3}$, with the FFF-MS we obtained a value of $1.38891464 + i\,5.75947\,10^{-3}$ for $N = 60$. We can identify two properties when we compare the results for these two modes (see Fig. 2.35). First, for both modes the convergence of the FFF-MS is much faster than that of the CDM-MS. Second, the CDM-MS convergence is slower for the $p = 1$ mode (TM like) than for the $p = 2$ mode (TE like) and this is not the case for the FFF-MS results (note the logarithmic y scale) . These properties clearly illustrate the improvement ensured by the FFF ; this recent method being initially proposed to solve the

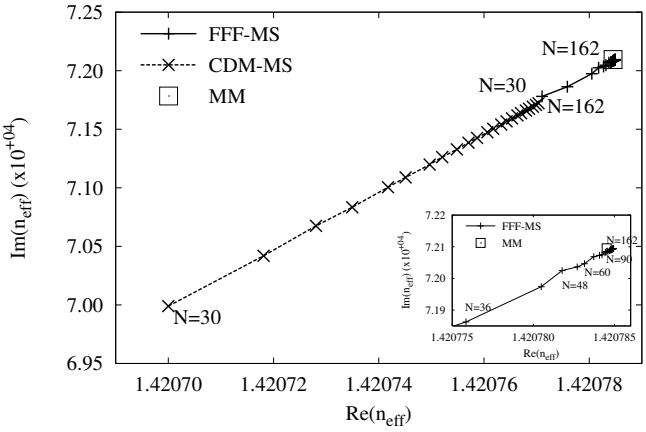

FIG. 2.30 – Convergence tests for the FFF-MS and CDM-MS for the effective index of the fundamental mode of the C_{6v} one ring test MOF described in the text versus the Fourier expansion order N. Inset : zoom of FFF-MS results and MM value.

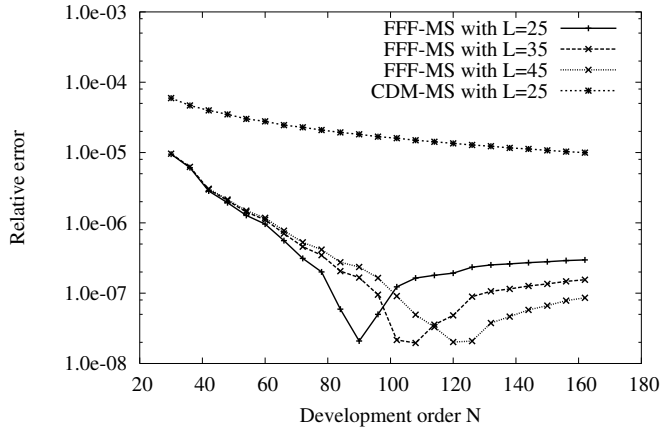

FIG. 2.31 – Modulus of the relative difference between the effective indices n_{eff} computed with the FFF-MS for 25, 35 and 45 slices in the S-algorithm, and with the MM result, versus the Fourier expansion order N (for the MM the number of Fourier-Bessel coefficients is equal to 12).

convergence problem of the CDM in diffraction studies for the TM polarization case [45].

In Table 2.9 we recapitulate the comparisons between the effective indices obtained with the FFF-MS and the MM for the one ring MOF. As can be seen, for all the possible mode classes of the C_{6v} MOF the FFF-MS provides accurate results. To complete the validation of the FFF-MS and to prove its usefulness in MOF studies, we also compare the modal dispersion computed with the two numerical methods for the fundamental mode of the two ring MOF already studied. As can be seen in Fig. 2.36, the agreement between the two methods is excellent both for the real part and the imaginary part of the effective index.

In table 2.10, we give the resources needed on the same computer needed by the MM and the FFF-MS in order to find the fundamental mode of several MOF configurations. As expected, the MM is much more rapid than the FFF-MS since the MM involves less numerical computations. Nevertheless, it can be seen that for complex structures which are not treatable by the MM, the duration and the memory required by the FFF-MS are similar to the ones it requires for the C_{6v} homogeneous case. It is also worth mentioning that the program for the MM has been optimized several times from its first version in 2001, this is not yet the case for the FFF-MS program which is a recent one. This difference can enhance the gap, due to methods themselves, seen in the computational durations observed in table 2.10.

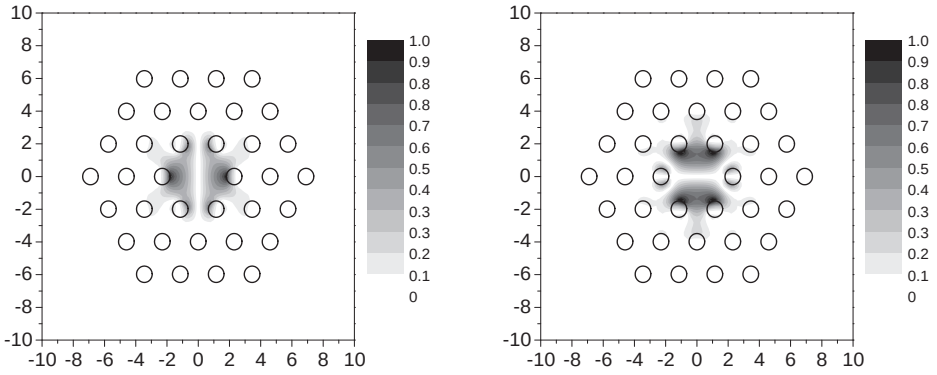

(a) $|E_z|$ for $p = 3$ (b) $|H_z|$ for $p = 3$

FIG. 2.32 – [Moduli of electromagnetic field longitudinal components for the fundamental mode, in the core region for the degenerate fundamental mode which belongs to the symmetry class $p = 3$, $n_{\text{eff}} = 1.4210465 + i\,8.117\,10^{-7}$ for $N = 150$. The field moduli are normalized to unity.

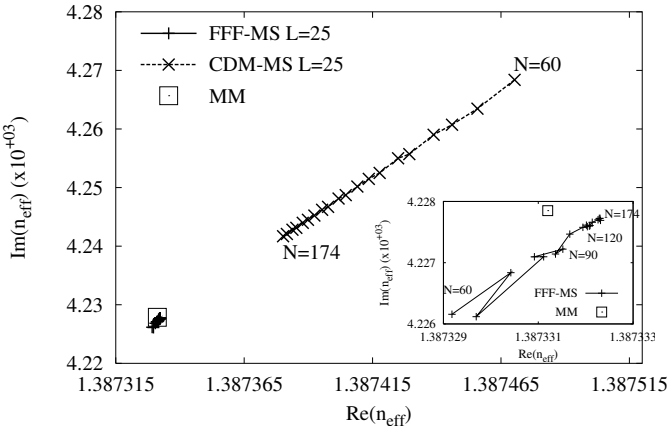

FIG. 2.33 – Convergence tests for the CDM-MS and FFF-MS versus the Fourier expansion order N for the effective index of the higher mode of symmetry class $p = 2$ with the highest effective index real part. The studied MOF is the six-hole test MOF described in the text. Inset : zoom of FFF-MS results and MM value.

A C_{2v} six-hole MOF

To conclude our tests of the FFF-MS method and its numerical implementation for calculating leaky modes in MOFs, we now consider a C_{2v} six-hole MOF similar to the one described in reference[6]. The MOF profile is a C_{2v} six-hole MOF with two types of holes. The pitch $\Lambda = 2.3\,\mu$m and the diameter of the four small holes is set to 1 μm and two symmetrically positioned small holes are now big holes of diameters equal to 1.4 μm. Due to their symmetry, there are only four symmetry classes (instead of eight in the C_{6v} case) none of them being degenerate[6]. Two core localized modes without nodes can be identified with the fundamental modes of the fibre, they belong respectively to the symmetry classes $p = 3$ and $p = 4$. The real part for the effective index of this $p = 4$ mode is bigger than that of the $p = 3$ mode whereas it is the contrary for the imaginary part. With the FFF-MS for $N = 60$, we obtain $n_{\text{eff}}(p = 3) = 1.41792219 + i\,5.11104\,10^{-4}$ and $n_{\text{eff}}(p = 4) = 1.41845587 + i\,5.27561\,10^{-4}$ instead of $n_{\text{eff}}(p = 3) = 1.4179265 + i\,5.11457\,10^{-4}$ and $n_{\text{eff}}(p = 4) = 1.418460 + i\,5.27845\,10^{-4}$ with the MM for $M = 12$. The good agreement between these results clearly shows that the FFF-MS can deal with other symmetries than the usual C_{6v} one, and can still reach a high accuracy.

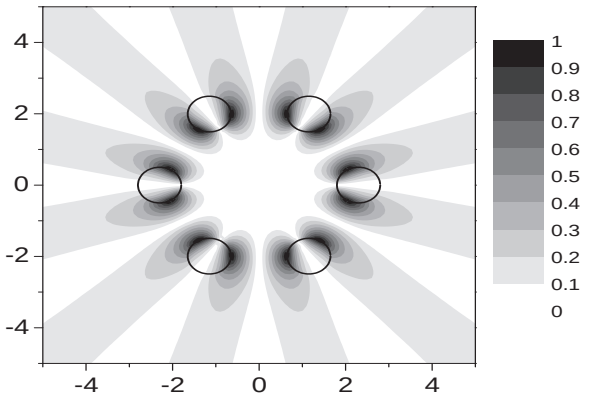

FIG. 2.34 – Modulus of electric field, in the core region for the higher order mode of symmetry class $p = 2$ with the highest effective index real part, $n_{\text{eff}} = 1.38732918 + i\,4.22616\,10^{-3}$ for $N = 60$. The field modulus is normalized to unity.

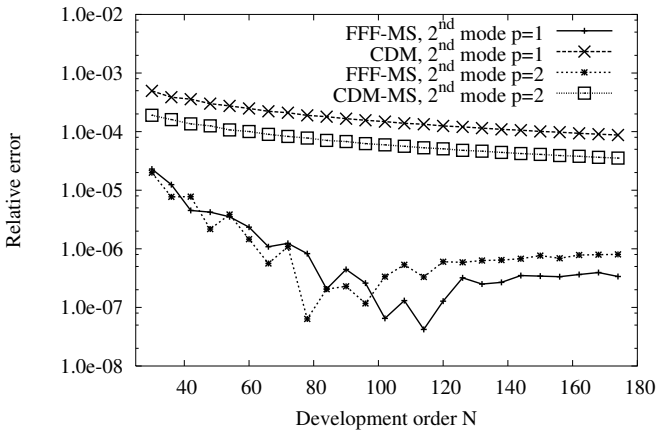

FIG. 2.35 – Comparisons of the effective index relative error versus the Fourier expansion order N, for the higher modes of symmetry classes $p = 1$ and $p = 2$ with the highest effective index real part. The results for the FFF-MS and the CDM-MS are shown. The studied MOF is the six-hole test MOF described in the text.

2.3.5 Sectorial MOFs

To illustrate the capabilities of the FFF-MS to study the modal properties of MOFs with arbitrary profiles that are not treatable by the multipole method extended[52] or not, we now describe some properties of sectorial MOFs. This type of MOF can be encountered when an extrusion process is used to build the fibre instead of the more conventional stack and draw technique[53, 54].
This structure with sectorial inclusions described in cylindrical coordinates is similar to lamellar gratings in Cartesian coordinates[45] since the cross section profile is invariant according to the integration variable r (the lamellar grating profile is invariant according to the integration variable commonly chosen as y). For both cases, the Q_ϵ matrix (see eq. (2.53) and ref. [40]) is independent of the integration variable (r or y). In addition the integration matrix M also becomes independent of y for lamellar gratings. In this case, the Rigorous Coupled-Wave (RCW) method is preferentially used (see chapter 6 in reference [45] and also reference [55]) : the solutions of the differential set are explicitly known through the eigenvalues and eigenvectors of the integration matrix. To the contrary, the RCW method cannot be used in cylindrical coordinates with sectorial inclusions since the integration matrix $M(r)$ remains dependent on r owing to the terms $\frac{1}{r}$ and $\frac{1}{r^2}$ (see equations (7-9) in reference[41]). Consequently, the

Mode class	MM $\Re e(n_{\text{eff}})$	MM $\Im m(n_{\text{eff}})$	FFF-MS $\Re e(n_{\text{eff}})$	FFF-MS $\Im m(n_{\text{eff}})$	Relative error on $\Re e(n_{\text{eff}})$	Relative error on $\Im m(n_{\text{eff}})$
1	1.388917884	$5.7618884\,10^{-3}$	1.388918390	$5.7616371\,10^{-3}$	$3.6\,10^{-7}$	$4.4\,10^{-5}$
2	1.387331199	$4.2278502\,10^{-3}$	1.387332286	$4.2277231\,10^{-3}$	$7.8\,10^{-7}$	$3.0\,10^{-5}$
3, 4	1.420784521	$7.2095221\,10^{-4}$	1.420784943	$7.2094414\,10^{-4}$	$3.0\,10^{-7}$	$1.1\,10^{-5}$
5, 6	1.386872247	$5.0376883\,10^{-3}$	1.386873053	$5.0374468\,10^{-3}$	$5.8\,10^{-7}$	$4.8\,10^{-5}$
7	1.332197539	$1.9429823\,10^{-2}$	1.332198974	$1.9428629\,10^{-2}$	$1.1\,10^{-6}$	$6.1\,10^{-5}$
8	1.351325880	$2.1553168\,10^{-2}$	1.351326338	$2.1552000\,10^{-2}$	$4.0\,10^{-7}$	$5.4\,10^{-5}$

TAB. 2.9 – Comparison between the FFF-MS and the MM for the first modes of each symmetry class of the C_{6v} MOF described in the text. The results are computed at $\lambda = 1.56\mu m$. For the MM the number of Fourier-Bessel coefficients is equal to 12, for the FFF-MS the number N of Fourier coefficients is set to 162. The relative error is computed from the normalized modulus of the difference between the two effective index values. The symmetry classes 3 and 4 are degenerate ; so are the classes 5 and 6.

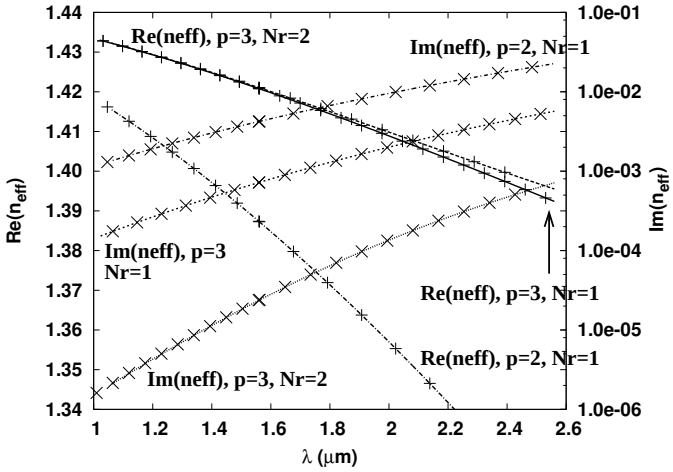

FIG. 2.36 – Comparison between the FFF-MS (lines) and the MM (crosses) for the dispersion of the degenerate fundamental mode (p=3 or 4) for the one ($Nr = 1$) and two ring ($Nr = 2$) C_{6v} MOFs described in the text, and for the modal dispersion of the second mode (p=2) for the same one ring MOF. For the MM the number of Fourier-Bessel coefficients is equal to 12, and for the FFF-MS N is set to 60.

staircase approximation[56] which is based on the use of the RCW method cannot be used. Nevertheless, for sectorial inclusions, the θ component of the normal vector to the inclusion surface is equal to unity along a radial axis of the modulated area : $r \in [R_{min}, R_{max}]$, $[\![n_\theta^2]\!] = I_d$ and $[\![n_\theta^2]\!] = [\![n_\theta n_r]\!] = 0$. This property allows us to reduce the matrix Q_ϵ to :

Configuration	MM time	MM RAM	FFF-MS time	FFF-MS RAM
homogeneous C_{6v}	(M=12) 10s	(M=12) 9Mo	(N=60) 191s (N=162) 2700s	(N=60) 16 Mo (N=162) 50 Mo
inhomogeneous C_{6v}	-	-	(N=60) 210s	16 Mo
sectorial C_{3v}	-	-	(N=60) 1062s	16 Mo

TAB. 2.10 – Computer resources needed, on the same computer, by the FFF-MS and the MM to compute, the fundamental mode for different MOF profiles. Note that several MOF structures can not be treated by the Multipole Method. The number of coefficients in the Fourier-Bessel expansion in the MM is equal to $(2M + 1)$, and the number of coefficients in the Fourier expansion in the FFF-MS is equal to $(2N + 1)$. The considered sectorial C_{3v} MOF is described in section 2.3.5 and the considered inhomogeneous C_{6v} MOF is described in section 2.3.6.

$$Q_\epsilon = \begin{bmatrix} [\![\epsilon]\!] & 0 & 0 \\ 0 & [\![\frac{1}{\epsilon}]\!]^{-1} & 0 \\ 0 & 0 & [\![\epsilon]\!] \end{bmatrix} \tag{2.75}$$

This matrix clearly illustrates the use of the inverse factorization rules[43] on the normal component of $\mathbf{D}$ to the considered surface, *i.e.* D_θ. The one-ring C_{nv} sectorial MOF geometry is described by the following geometric parameters : θ_m, the angle associated with one sector, R_{min}, the minimal sector radius, R_{max}, the maximum sector radius, and n the number of sectors. We start with the last validation test of our method : a C_{3v} sectorial MOF studied in reference [57]. We choose this example because the inclusions are not circular and it illustrates symmetry properties not yet studied in the previous sections of the present work. It has also the advantage that the results (Table 2 in reference [57]) are obtained with two different methods : a finite element method with transparent boundary conditions (FEM-TBC) and a Fourier decomposition method with adjustable boundary conditions (FDM-ABC)[58]. The sectorial MOF parameters are : $\lambda = 1.55\mu m$, $R_{min} = 1\mu$m, $R_{max} = 2\mu$m, $\theta_m = 54^o$, $n_{matrix} = 1$, and $n_{sector} = 1.44402362$.

n_{eff}	degenerate fundamental mode (p=3,4)	second mode (p=2)
FDM-ABC	$1.35584 + i5\ 10^{-5}$	$1.23957 + i5.09\ 10^{-4}$
FEM-TBC	(p=3) $1.35581 + i4.96\ 10^{-5}$ (p=4) $1.35580 + i4.95\ 10^{-5}$	$1.23950 + i5.67\ 10^{-4}$
FFF-MS $N = 60$	$1.3558867 + i5.012\ 10^{-5}$	$1.239615 + i5.138\ 10^{-4}$
FFF-MS $N = 150$	$1.3558863 + i5.011\ 10^{-5}$	$1.239619 + i5.140\ 10^{-4}$

TAB. 2.11 – Comparison between the FFF-MS, the FDM-ABC and the FEM-TBC for the effective index of the fundamental mode of the one ring C_{3v} MOF described in the text.

As can be seen from Table 2.11, the variation of the real part of n_{eff} for the fundamental mode of the one ring C_{3v} MOF between $N = 60$ and $N = 150$ is equal to $4\,10^{-7}$ and the three methods give quite similar results. The extent of the modulated area is 1 μm, as in the C_{6v} one ring MOF studied in section 2.3.4 and the wavelength is also similar. Besides as pointed out in the previous paragraph, sectorial inclusions allow us to use the simpler expression given by eq. (2.75) for the matrix Q_ϵ than that of circular inclusions. Hence we can expect that the accuracy of the computed results of this sectorial MOF for $N = 150$ is at least equal to the one obtained for the circular inclusion MOF, i.e., around $3\,10^{-7}$ for the real part of n_{eff}. We can use a similar argument for the imaginary part. Consequently, the accuracy obtained with the FFF-MS is better than that given with the FDM-ABC and the FEM-TBC in reference [57]. We also notice that the degeneracy of the fundamental mode, theoretically predicted for C_{3v} structures by McIsaac's work[18] (see Fig. 2.8 page 24), is obtained directly by the formalism detailed in section 2.3.3 for the FFF-MS unlike for the FEM-TBC in which a non degenerate fundamental mode is found (see Table 2.11). The field maps computed with the FFF-MS for the longitudinal component of the electric field are shown in Fig. 2.37. As shown by the theory the irreducible geometric angular sector where simple Dirichlet boundary condition apply for this field component, for the symmetry classes $p = 3$ or 4, is π and not $\pi/3$.

Part of the cross section of a six sectorial cylinder MOF is depicted in Fig. 2.38. We start our study by a MOF of this type with the same air filling fraction as the test example MOF we described in the section 2.3.4. We have $R_{min} = 1.8\,\mu$m, $R_{max} = 2.8\,\mu$m, and $\theta_m = 19.5652^o$. In this case, the effective index value is quite similar to the one already computed with the 6 circular hole MOF : we find $n_{\text{eff}} = 1.42050642 + i\,7.6390\,10^{-4}$ for $N = 60$. For $N = 120$, our search algorithm finds $n_{\text{eff}} = 1.42050887 + i\,7.6427\,10^{-4}$ for the fundamental mode of this sectorial MOF. Figure 2.39 shows the convergence test for this structure. The small loops which appear in the curve are not yet explained but they might be linked to the field expansions.

Going back to Fig. 2.38, we show the field map of the fundamental mode of a six sectorial cylinder MOF that can not be studied even with an extended version of the MM since the circles which include the inclusions are tangent. Mode searching in such structure is straightforward with the FFF-MS and does not require special treatment.

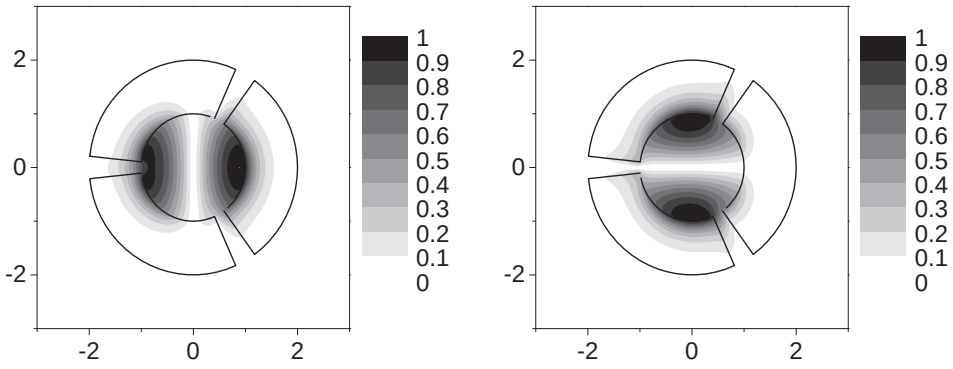

(a) $|E_z|$ for $p = 3$ (b) $|E_z|$ for $p = 4$

FIG. 2.37 – Moduli of electric field longitudinal component of the C_{3v} sectorial MOF described in the text for the degenerate fundamental mode, for the symmetry classes $p = 3$ and 4, $n_{\text{eff}} = 1.3558863 + i5.011\ 10^{-5}$ for $N = 150$. The field moduli are normalized to unity.

In Fig. 2.40, we give the trajectory in the complex plane of the sectorial MOF fundamental mode effective index as a function of its geometrical parameters. The decrease of the inner radius a induces an important decrease of $\Re e(n_{\text{eff}})$ without any significant change in the losses. This can be qualitatively understood as follows : the fields tend to spread over the low-index inclusions lowering the effective index. To the contrary, the increase of the outer radius b induces a fall in the losses, keeping nearly constant the real part of n_{eff}. This behaviour can also be explained ; the change on the structure does not modify the inner part of the confining region which controls the field shape and so consequently $\Re e(n_{\text{eff}})$, but this change isolates more deeply the fibre core from the outside region, reducing strongly $\Im m(n_{\text{eff}})$. The increase of the angle θ_m implies a decrease of both the real and the imaginary parts of n_{eff}. We can again explain this quite simply : this changes alters the inner shape of the core through an increase of the low-index region inducing a decrease of $\Re e(n_{\text{eff}})$, and in the same time it isolates the core from the outside (decrease of $\Im m(n_{\text{eff}})$).

2.3.6 Inhomogeneous MOFs

In this penultimate section, we illustrate the capability of the FFF-MS to deal with inhomogeneous inclusions. We start with a validation study using a single high index cylinder with a parabolic refractive index profile in a homogeneous matrix. Then we study a MOF made of six inhomogeneous inclusions.

The first device is studied with two different algorithms. The first one considers an inhomogeneous circular cylinder centered at the coordinate origin and does not use the FFF-MS but a semi-analytical calculus detailed below. In order to model a fibre with an inhomogenous radial index profile which is centered at the origin, the interior region of this fibre is split (in the same way as the modulated area in the S-matrix propagation algorithm) into P homogeneous layers. For each homogeneous layer (p) with $p \in [1, P]$ between the two circular cylinders with radius r_p and r_{p+1}, the corresponding refractive index is chosen as the average of the parabolic index profile between r_p and r_{p+1}. The higher the P value, the better the index profile is decribed, and the transmission matrix of all the P layers becomes the product of the P transmission matrices of the homogeneous layers. In fact, the transmission matrix (and the S-matrix) of a layer between two circular cylinders centered at the origin and filled with an homogeneous medium may be deduced directly from the explict expressions of the fields in such a medium (with the $\Psi^{(j)}(r)$ matrix in equation (34) of reference[40]) by writing the continuity of the fields at each interface. So, no integration is required and the differential set (2.55) is not used.

It is important to distinguish the present splitting of a radially inhomogeneous circular cylinder into P slices with the moot procedure invoking the staircase approximation[56]. With this last method, the arbitrary diffracting surface is split into several lamellar diffracting surfaces. However, the discretization

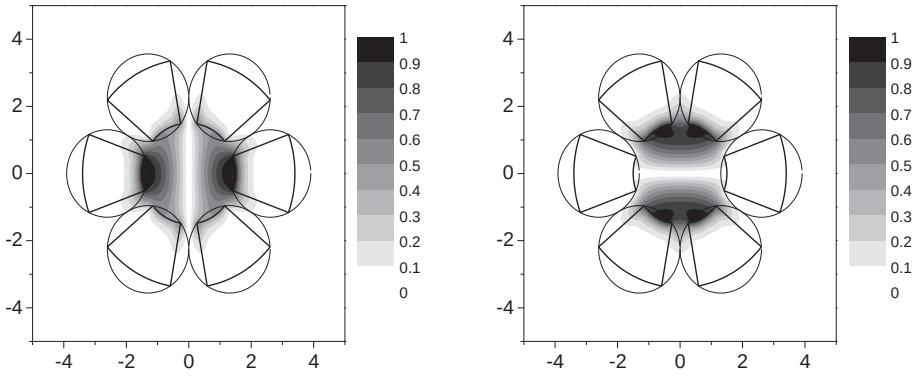

(a) $|E_z|$ for $p = 3$ (b) $|E_z|$ for $p = 4$

FIG. 2.38 – Modulus of electric field longitudinal component, for the degenerate fundamental mode which belongs to the symmetry classes $p = 3$ and $p = 4$ for the C_{6v} sectorial MOF with ($R_{min} = 1.5\,\mu$m, $R_{max} = 3.4\,\mu$m, and $\theta_m = 40°$, $n_{\text{eff}} = 1.4032977 + i\,2.9369\,10^{-6}$ for $N = 60$ and $L = 25$. The field moduli are normalized to unity. The thin circles correspond to the theoretical upper bound of the circle diameters for the MM.

of the smooth profile in a staircase form introduces edges leading to diverging fields and thus worsening the convergence rate. In our case, there is no diffracting surface but only fictitious surfaces created at the interfaces of the homogeneous layers. In other words, the splitting concerns the index profile and not a diffracting surface.

The second algorithm deals with the same inhomogeneous fibre but not centered at the coordinate origin, and it uses the complete FFF-MS described in the present work : the differential set (2.55) must be integrated numerically.

To describe the refractive index profile of both the test fiber of this paragraph and the MOF we consider below we write for $r \in [0, r_{max}]$: $n(r) = n_{cyl,cent} - (n_{cyl,cent} - n_{cyl,bord})(r/r_{max})^2$ in which $n_{cyl,cent}$ is the minimal refractive index at the inclusion center and $n_{cyl,bord}$ the refractive index at the inclusion boundary ($r = r_{max}$). For the test fibre we set : radius $r_{max} = 0.5\,\mu$m, $n_{cyl,cent} = 1.5$, $n_{cyl,bord} = n_{mat} = 1.47$, $\lambda = 0.4\,\mu$m, $n(r) = n_{cyl} - (n_{cyl} - n_{mat})(r/r_{max})^2$. For the fundamental mode HE_{11}, an approximate semi-analytical solution associated with an infinite parabolic profile is known[2]. It gives for the approximate effective index value $n_{\text{eff}} = 1.48727747$. It is important to notice that in the special case in which the center of the fibre corresponds to the coordinate origin we can use the first algorithm described in the beginning of this section. In this case, we obtain $n_{\text{eff}} = 1.48727514$ for $N = 1$ and $P = 200$. This accurate value will be our reference value for the next test. In order to validate the second algorithm associated with the FFF, we study the same inhomogeneous fibre but not centered at the origin (we set the fibre center position such as $R_{center} = 3\,\mu$m). In this case, the symmetry is broken ; thus more Fourier coefficients are needed to correctly describe the fields and we must use the algorithm of the FFF. The convergence test for this configuration is given in Fig. 2.41. We clearly see that The convergence is easily reached in this example ; we obtain $n_{\text{eff}} = 1.48727382$ for $N = 30$ and $L = 50$.

The MOF model we consider now is the one-ring MOF already described in section 2.3.4 but in the present case the refractive index profile of each inclusion follows a radial parabolic law. We recall that in the type of MOFs studied, the inclusion refractive index is lower than that of the matrix (in the previous paragraph the isolated fibre has a higher refractive index than the matrix one). We introduce $\Delta n_{cyl} = (n_{cyl,cent} - n_{cyl,bord})$ the refractive index gap of the inclusions (not the gap between the inclusion and the matrix indices). These parabolic profiles are depicted in Fig. 2.42. We may discuss the accuracy of the results according to the expansion order N, and to the number of integration steps (and the number of S-slices L). In the case of the homogeneous inclusions, we know that the higher the N value, the better the discontinuities of the ϵ, n_θ^2, n_r^2 and $n_\theta n_r$ functions are described according to θ. In

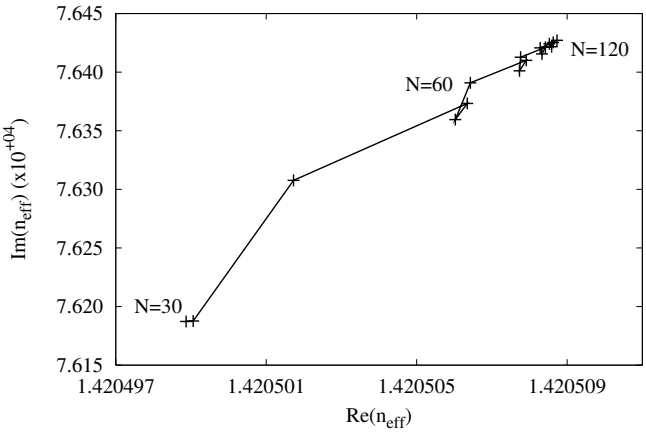

FIG. 2.39 – Convergence test for the effective index of the fundamental mode of the six sectorial inclusion MOF ($R_{min} = 1.8\,\mu$m, $R_{max} = 2.8\,\mu$m, and $\theta_m = 19.5652^o$) versus the Fourier expansion order N. The step in N is equal to 6. The number of slices in the S-algorithm L is set to 25.

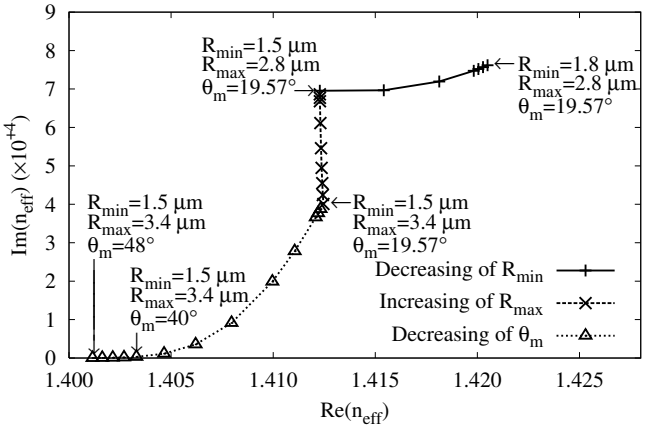

FIG. 2.40 – Evolution of the effective index n_{eff} as a function of the three geometrical parameters a, b, θ_m describing the C_{6v} sectorial MOF. The labels are written for the extremal values of the parameters.

the same way, the higher the number of integration steps, the better the radial refractive index profile is defined along a radial axis. For inhomogeneous inclusions in a matrix such that $n_{cyl,bord} = n_{mat}$, the refractive index profile becomes continuous in the whole space. This property explains why, in this case, the Gibbs phenomenon due to discontinuities with respect to θ does not occur. However, the shape of the parabolic refractive index profile requires more Fourier coefficients (higher value of N) but also more integration steps according to r, in order to describe accurately the structure compared to a homogeneous profile. For these reasons, we have observed that the accuracies obtained for a MOF with inhomogeneous inclusions but continuous refractive index profile remains of the same order of magnitude as those of a similar MOF with homogeneous inclusions when the N and L values are identical. In Fig. 2.43, we show the rebuilt profile of the whole MOF from the Fourier series used in the FFF-MS and not the theoretical profile. As can be seen, the resulting profile is regular, and fits well the parabolic law. In Fig. 2.44, we give the computed effective indices of the fundamental mode for the inclusion parabolic profiles described in Fig. 2.42. As expected both the real part and the imaginary part of the effective indices decrease when Δn_{cyl} increases.

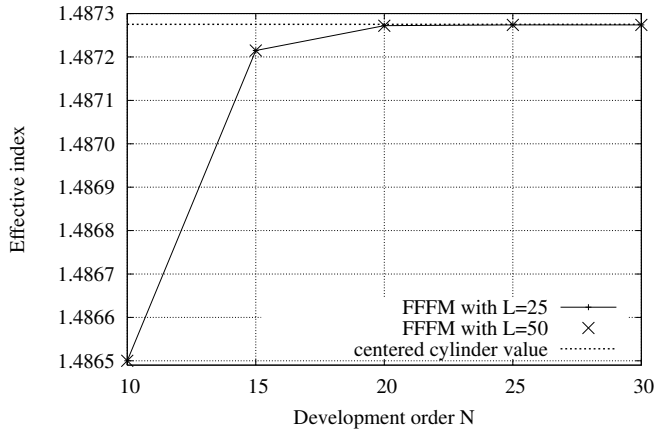

FIG. 2.41 – Convergence test for the inhomogeneous fibre not centered at the origin coordinates. L is the number of slices used in the S-algorithm.

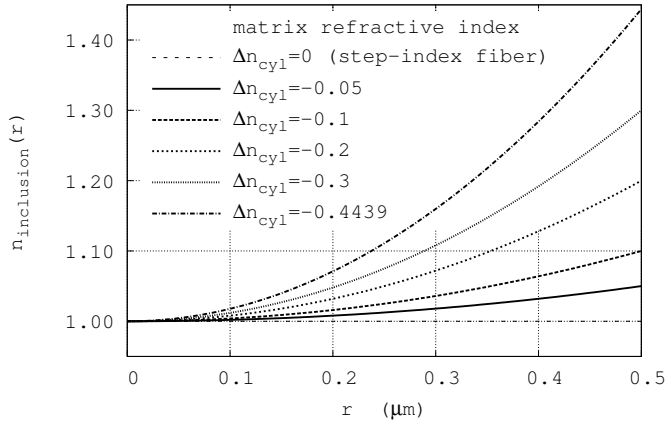

FIG. 2.42 – Chosen parabolic profile of the inhomogeneous inclusions for several values of the refractive index gap Δn_{cyl} between the inclusion center and the inclusion outer boundary. The analytic form of the refractive index profile is given in the text.

2.3.7 Conclusion

Thanks to various and complete comparisons with the multipole method and with more recent numerical methods, we can state that the FFF-MS, a mode searching method based on the differential method with the Fast Fourier Factorization, can find the different modes of solid core MOFs with a high accuracy both for the real part and the imaginary part of the effective index. This method can deal with both the fundamental mode and higher order modes. It can study arbitrary refractive index profile MOFs contrary to the multipole method. New results are given for C_{6v} sectorial MOFs and inhomogeneous MOFs. The counterpoints to the versatility of the developed method are its lower accuracy, which however is largely sufficient to compute accurately the modal dispersion, and its need for larger computer resources compared to the multipole method.

In the case of a profile periodic according to the angular variable, the symmetry properties of the modes are established, not in the real space as for the MM, but in Fourier space. The results given are valid both for all waveguides fulfilling C_n or C_{nv} symmetries, not just MOFs, and apply to all differential methods formulated using cylindrical coordinates (not just the FFF). These results allow both a clear mode classification and a large reduction of the necessary computational resources.

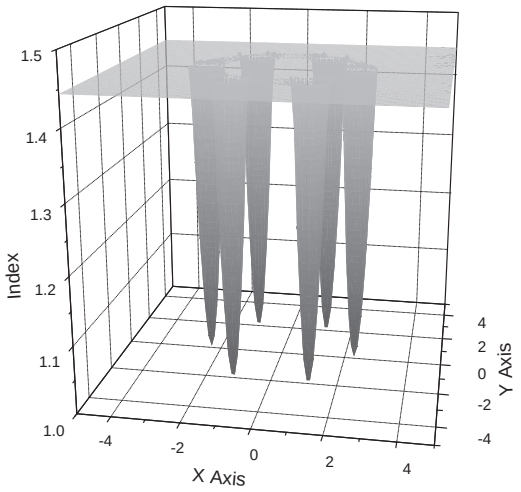

FIG. 2.43 – Refractive index profile of the one-ring C_{6v} inhomogeneous MOF described in the text, this profile is rebuilt from the Fourier series of the theoretical parabolic profile with $n_{cyl,bord} = n_{mat}$.

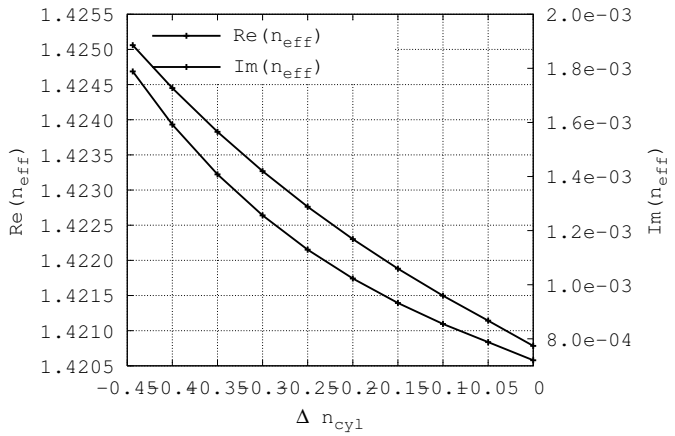

FIG. 2.44 – Effective index of the fundamental mode for the one-ring C_{6v} inhomogeneous MOF according to the inclusion refractive index gap Δn_{cyl} (see the text and Figures 2.42 and 2.43).

Chapitre 3

Main properties of microstructured optical fibres

Sommaire

3.1 Types of microstructured optical fibres or types of modes ?

Before dealing with type of microstructured optical fibres (MOFs) we must emphasize that a related crucial question is "What is the studied mode in the considered structure ?". Most of the time, the sought after mode is the fundamental mode of the fibre core that is to say the mode with the effective index with the highest real part in this particular region. In solid core MOFs made of low index inclusions in a high index matrix with a fibre core associated with a missing inclusion, the previous answer is easily checked but it is not the case in a hollow core MOF in which one may guide the light in the fibre core only for some specific range of wavelengths. In this last case, modes with an effective index, with a higher real part than the fundamental mode guided in the core by a photonic band gap, may exist in the structure but they are not located in the core but around it. In other words, most of the times when one describes the types of MOFs it is assumed that one particular mode (or a set of modes) are considered. As a consequence, we must define for each type of MOFs what is the studied mode. In the present chapter, we consider only the fundamental mode and the second order modes located in the core region (exception in sections 3.2.3 and 3.2.4). In what follows, we list the three main types of MOFs that can be found. Their guiding mechanisms are presented in their respective sections of this chapter. Furthermore, the main properties of each kind of the mentioned type of fibres are described in the corresponding section emphasizing especially solid core microstructured optical fibres with low index inclusions. More complex cases can be generated if more complicated cladding structures or core region are considered [59]. The three main types of MOFs we consider are :

1. solid core MOFs in section 3.2
2. hollow core MOFs or photonic crystal fibres in section 3.3
3. AntiResonant Reflecting Optical Waveguide MOFs (ARROW MOFs) in section 3.4

3.2 Main linear properties of modes in solid core microstructured optical fibres with low index inclusions

3.2.1 Solid core microstructured fibre with low index inclusions and band diagram point of view

This case is represented by solid core MOFs made of low index inclusions in a high index matrix with a fibre core associated with a set of missing inclusions forming the fibre core. In this kind of MOFs, the modes of interest are that located in the core and with the highest possible real part of the effective index together with the lowest imaginary part (which is linked to the losses, see section 3.1). We use this case to introduce the different points of view that can be used to get some physical insights concerning the properties of the MOF modes. One can use the homogenization technique to reduce the MOF to a conventional W-fibre in which the low index region represents the low index inclusion region of the MOF (see Figure 3.23 in section 3.2.4 and references[20, 60]). One can also consider the properties of the band diagram of the microstructured region, if this last is a subset of periodic lattice of inclusions, as will be shown.

In this paragraph, we focus on the guiding mechanism of solid core microstructured fibre with low index inclusions using a band diagram point of view that will also be used in the two subsequent sections (3.3 and 3.4). We start it by a brief survey of the band diagram description. The way we can compute band diagrams simitar to the scheme shown in Fig. 3.1, is briefly explained in Appendix B.

Several representations are possible : $(\lambda/\Lambda, \Re e(n_{eff}))$ used frequently in this dissertation (see Fig. 3.1), $(Re(\beta - k_0)\Lambda, k_0\Lambda)$ like in references [61–63], $(k_0\Lambda, Re(n_{eff}))$ like in reference [63–65], $(k_0\Lambda, Re(\beta)\Lambda)$ like in reference [66] (equivalent to the one used in Fig. 3.34).

At least two features must be underlined. First, as one can see in Fig. 3.1, the bandgap diagram exhibits three full finite photonic bandgaps which means that no mode exits in the periodic structure for these regions of the parameter space. Secondly, one mode of this structure is of particular interest since it represents an upper bound for the allowed effective indices of the modes of the periodic structure (see how it can be estimated using a simple but efficient fibre model in reference [67]).

As can be seen in Figure 3.2, the dispersion curve of the modes localized in the core of a finite size MOF (not the modes of the periodic structure used to compute the band diagram) are either above the upper mode allowed in the periodic microstructured cladding that is to say the so called the fundamental space filling mode, or inside the bandgaps.

As it will be discussed in sections 3.2.3 and 3.2.4, the existence of the second mode cut-off will be proved and described whereas that of the fundamental mode does not exist even if a partial delocalization occurs for it.

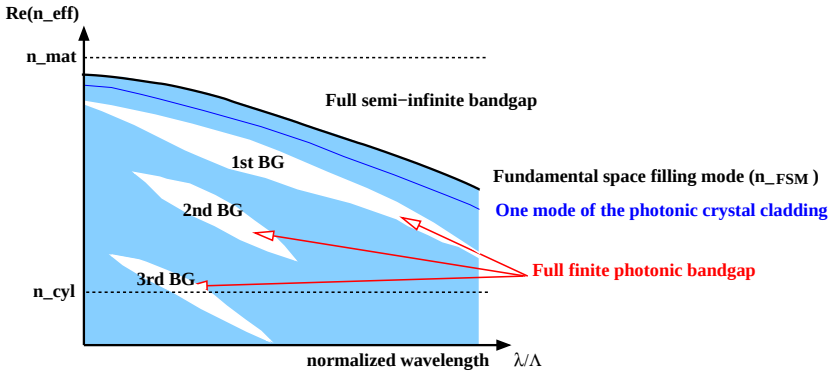

FIG. 3.1 – Schematic band diagram of a periodic array of inclusions of low refractive index n_{cyl} in a high refractive index matrix n_{mat}. The fundamental space filling mode is the mode of the periodic structure with the highest effective index (black thick curve). The semi-infinite photonic bandgap is the region in the plane $(\lambda/\Lambda, \Re e(n_{eff})/n_{mat})$ above the dispersion curve of the fundamental space filling mode. The three white regions below the fundamental space filling mode represent the parameter space in which no modes can propagates in the periodic structures, *i.e.* full finite photonic bandgaps.

This interpretation of the guiding mechanism is not complete and at least two warnings must be given. First, it is not valid when ones considers MOFS made of few inclusions since in this case it is hard to speak about a periodic structure (see the different examples described in section 2.2.6). Nevertheless, if the holes are big enough, the modes are confined with small losses in these small structures even in the six hole MOF. For some already fabricate MOFs [51], the number of hole rings is equal to three. In these case, the losses and the exact dispersion curves can not be computed directly and accurately if one considers an artificially periodized structure instead of the finite size one.

The second warning is related to an idea formulated as soon as 2000 by Ferrando[64]. In the frame of the band diagram point of view it is often argued that there are two fully distinct guiding mechanisms in MOFs : the modified total internal reflection one and the bandgap one. Nevertheless, when a MOF with a defect (relatively to the inclusions of the microstructured cladding region) located in the fibre core is considered two types of defect can be defined : a *donor* defect that is a low index inclusion with a smaller diameter or an *acceptor* defect *i.e.* an inclusion with a bigger diameter than the other inclusions[1][2]. In these two cases, the modes of the structures arise from the modes of the periodic structures : for the donor case they move upward to the semi-infinite bandgap for example, or to a lower bandgap whereas for the acceptor case, they move downward to the first bandgap for example. If we focus on a donor type MOF then one can obtain modes in the semi-infinite bandgap that arise from the first inter-band and modes in the first bandgap that come from the second inter-band. Both types of mode originated from the existence of a donor defect in the periodic structure. If the solid core MOF is seen as the limit case of a vanishing low index inclusion then it is difficult to split artificially the guiding mechanisms among the modes of the fibre between modified total internal reflexion (for the modes located in the semi-infinite photonic bandgap) and bandgap guidance (for the modes located in the finite photonic bandgaps). This remark and the first one involve that, even if it is quite convenient to split in two the guiding mechanisms

[1] These terms have been chosen so as to follow the ones in Solid State Physics due to the analogy that can be made between our problem and the one of electrons in potentials.

[2] We can also consider as a donor (resp. acceptor) defect an inclusion with a lower (rep. bigger) refractive index than that of the inclusions.

in MOFs to categorize them and to explain their properties, we must keep in mind that the intrinsic phenomenom is the complicated interaction of light with the finite number of inclusions around the fibre core.

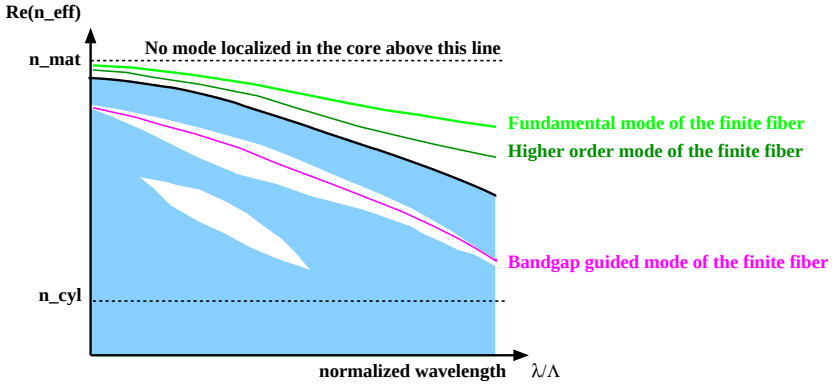

FIG. 3.2 – Schematic band diagram of a periodic array of inclusions of low refractive index n_{cyl} in a high refractive index matrix n_{mat} such that $n_{cyl} < n_{mat}$ together with the dispersion curves of several modes of a finite size MOF such that . As can be seen, forbidden bandgaps may exist for the microstructured cladding but they do not have any impact on the properties of the modes of the finite size MOF located in the semi-infinite bandgap.

The structure presented in Fig. 3.2 is a special case in which the fibre core has the same refractive index as that of the matrix of the cladding region ($n_{core} = n_{mat}$). If the core is for example a cylinder made of a refractive index such that $n_{cyl} < n_{core} < n_{mat}$ then the situation is more complex but understandable using the same diagram but with an added horizontal line associated with the n_{core} value (see Fig 3.3). With this particular configuration, even the fundamental mode will exhibit a cutoff like phenomena when the real part of its effective index becomes larger that of the low index core[3]. In both cases this mode is a leaky mode.

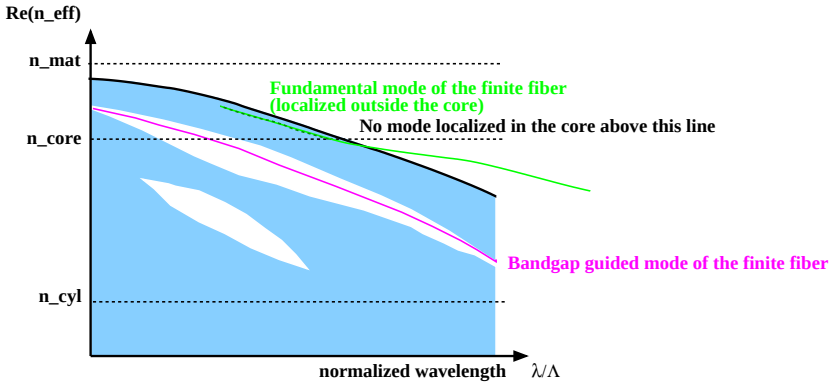

FIG. 3.3 – Schematic band diagram of a periodic array of inclusions of low refractive index n_{cyl} in a high refractive index matrix n_{mat} such that $n_{cyl} < n_{mat}$ together with the dispersion curve of the fundamental mode of the finite size MOF such that $n_{cyl} < n_{core} < n_{mat}$. In this case, the fundamental mode has a transition, it delocalizes from the low index core to the higher index region surrounding it when the wavelength decreases.

We start our description with the main linear properties of the fundamental mode of a solid core MOF based on a C_{6v} triangular lattice of low index circular inclusions (the optical indices of these inclusions n_i will be fixed to 1.0 in all this section). The second mode of this structure will also be studied in order to clarify the notion of single-modeness in MOF. We define transition regions for these two modes, so

[3]This phenomenon can be compared to the transition of the fundamental mode at the small wavelength edge of bangaps in PCF.

that it will be possible to determine the different operation regimes of solid core C_{6v} MOFs.

Finally, we study of the chromatic dispersion of the fundamental mode, and we show that chromatic dispersion in MOF can be fully managed in a useful way for practical applications using new MOF designs.

3.2.2 Basic properties of the losses

All the modes of the MOF structure that we considered in the previous chapter are leaky modes. The confinement losses (See section 1.2 of chapter 1.2 page 5) of these modes $\mathcal{L}$ (in decibel per meter) are related to the imaginary part of n_{eff} through the relation :

$$\mathcal{L} = \frac{40\pi}{\ln(10)\lambda}\Im m(n_{\text{eff}})10^6 \tag{3.1}$$

in which λ is given in micrometres. These losses are due to the finite number of air holes. It is worth mentioning that these losses occur even if the material absorption is fully neglected. The results given in this section concern the degenerate fundamental mode of solid core C_{6v} MOF such as that depicted in Fig.2.5(c). We limit the present study to the case of MOF cores composed of a single missing air hole in the finite size triangular lattice (See Fig. 3.4). The matrix is considered as infinite. When a silica matrix is considered, its permittivity is taken from the Sellmeier expansion at the corresponding wavelength [35] (ε_r = 2.0852042 for $\lambda = 1.55\,\mu m$ or equivalently $n_M = 1.444024$). When a high refractive index material is considered, we choose the value $n_M = 2.5$ which is representative of chalcogenide glasses[68–71].

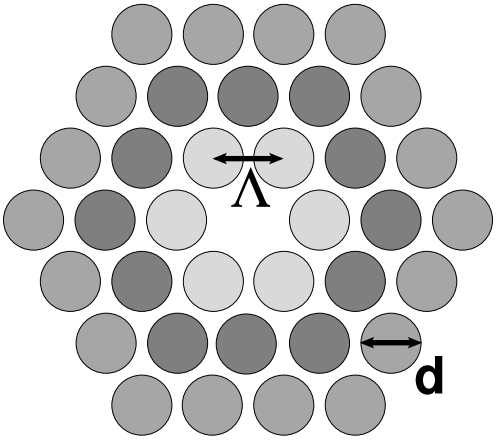

FIG. 3.4 – cross section of the modelled MOF with 3 rings of holes (holes are shown colored with different grey according to their ring number), $N_r = 3$. Λ is the pitch of the C_{6v} triangular lattice, and d is the hole diameter. The solid core is formed by one missing hole in the center of the structure.

In Fig. 3.5(a) we give the confinement losses, for a silica matrix, versus the ratio[4] d/Λ (d is the hole diameter and Λ is the pitch of the triangular lattice of inclusions) and the number N_r of hole rings surrounding the MOF core. The losses decrease monotonically with both the number of low-index inclusion rings and the ratio d/Λ [38]. We can notice that with the logarithmic scale for the losses the gap between successive values of N_r is nearly constant, and this means that for this kind of MOF the confinement losses decrease nearly exponentially with N_r[5]. In Fig. 3.5(b), we give the same confinement losses as in Fig. 3.5 but for an high index glass such that $n_M = 2.5$. We can observe that the behaviour is exactly the same but the loss level is lower for the MOF with the same geometry due to the higher refractive index contrast between the matrix and the inclusions.

To compare more quantitatively the impact of the refractive index, we introduce the ratio of the fundamental mode guiding losses $\mathcal{L}(m+1)$ for a microstructured fibre made of $N_r = m+1$ hole

[4] It is straightforward to see that this ratio d/Λ must be less than unity.

[5] The behaviour of the losses with N_r will be discussed in more detail in section 3.2.4.

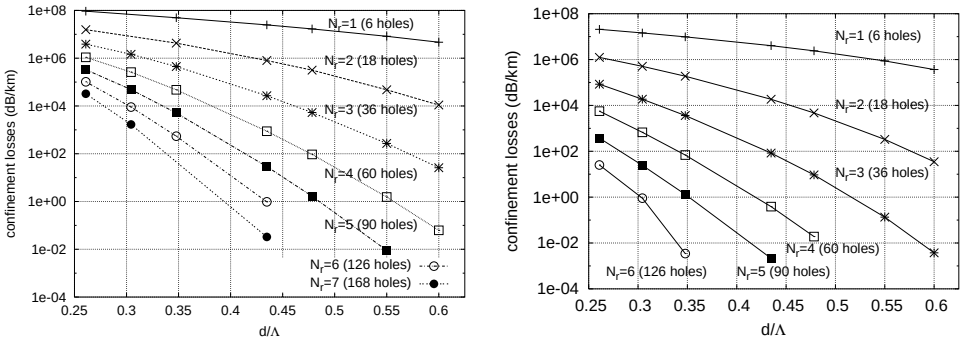

(a) For $n_M = 1.444024$ (b) For $n_M = 2.5$

FIG. 3.5 – Confinement losses (in dB/km with a log-scale) versus the ratio (d/Λ) and the number N_r of hole rings around the solid core. The MOF are based on a C_{6v} triangular lattice of air holes in an inifinite matrix. The pitch Λ is equal to 2.3 μm, and λ = 1.55 μm. N_r is the number of air hole rings surrounding the solid core.

rings over the fundamental mode losses $\mathcal{L}(m)$ for a $N_r = m$ fibre [51]. Slight variations of this ratio $\mathcal{L}(m+1)/\mathcal{L}(m)$ occur for different and small m values. In order to give an unique but meaningful value for this ratio, we compute its average, denoted $\alpha(N_r+1)/\alpha(N_r)$, for $m \in [1,4]$. In figure 3.6, we show this average ratio as a function of d/Λ for the two already studied refractive indices. The lower the loss ratio the more efficient the confining capacity of the fibre. As can be seen in this figure (note the y-axis logarithmic scale), the matrix refractive index $n = 2.5$ ensures a much stronger confinement than the n$= 1.444024$ matrix refractive index. Consequently, fewer rings of holes are needed to obtain the same guiding losses even for small values of d/Λ. It is worth mentioning that no material losses are taken into account in these numerical results.

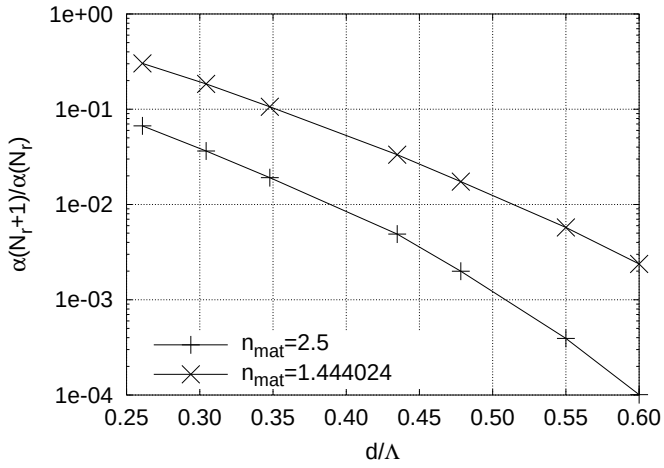

FIG. 3.6 – Average ratio of the losses of a $N_r = m+1$ MOF over the losses of $N_r = m$ (see the text for the definition of the average) for the fundamental mode as a function of d/Λ for two matrix refractive indices $n_M = 1.444024$ and $n_M = 2.5$.

In Fig. 3.7, we give the losses as a function of the pitch Λ for several values of the ratio d/Λ for a 3-ring silica MOF. For a fixed value of d/Λ, they decrease monotonically with the pitch Λ. It can also be seen in Fig. 3.5 and Fig. 3.7 that the MOF confinement losses can be made as low as 0.1 dB/km so the total losses in MOF can be limited by Rayleigh scattering and absorption rather that by the confinement losses [37].

The real part of the effective index $n_{\text{eff}} = \beta/k$ as a function of N_r the number of hole rings for several values of d/Λ is shown in Fig. 3.8. We see that $\Re e(n_{\text{eff}})$ increases with N_r and that the larger the ratio d/Λ the faster the limit value of $\Re e(n_{\text{eff}})$, corresponding to an infinite number of hole rings, is

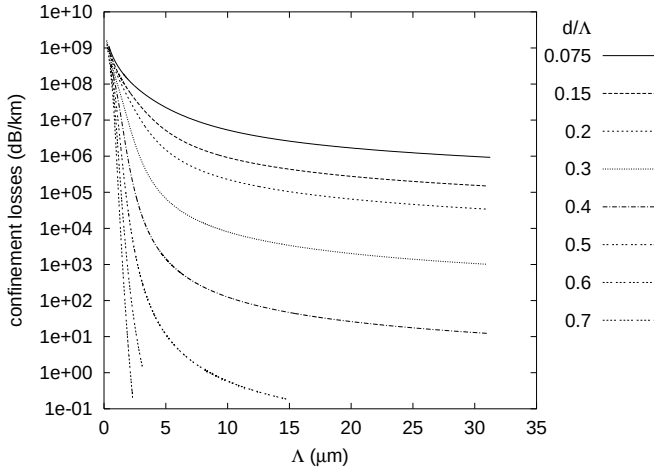

FIG. 3.7 – Confinement losses (in dB/km with a log-scale) versus the pitch Λ for several values of the ratio d/Λ for a 3-ring MOF. The MOF are based on a C_{6v} triangular lattice of air holes in silica (see the text). The wavelength λ is equal to 1.55 μm.

reached. This behaviour in a solid core MOF can be easily understood as follows : the larger the ratio d/Λ, the better the confinement of the mode is improved by N_r, and consequently the faster the real part of the effective index reaches its limit value. This dependency of $\Re e(n_{\text{eff}})$ with $\mathbb{N}_r$ has important consequences for the control of chromatic dispersion (see 3.2.5).

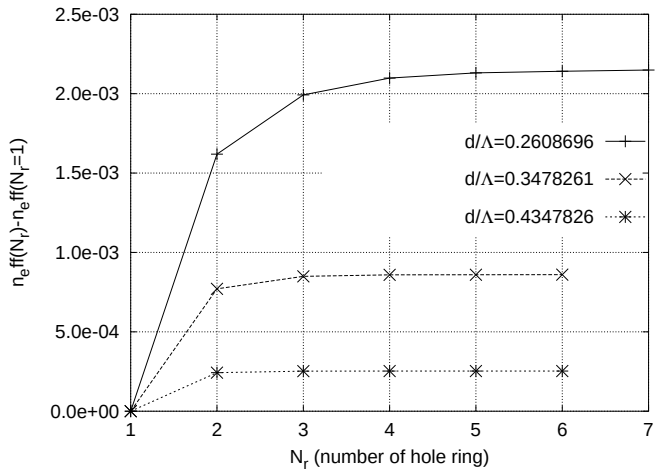

FIG. 3.8 – Real part of the effective index $n_{\text{eff}} = \beta/k$ as a function of N_r the number of hole rings around the MOF core for several values of d/Λ. The wavelength λ is equal to 1.55 μm, and the pitch Λ is equal to 2.3 μm. The diameter of the inclusions d is successively equal to 0.6, 0.8 and 1.0 μm, whilst the corresponding real part of the effective index associated with $N_r = 1$ is succesively equal to 1.427698 ,1.424475, and 1.421159.

3.2.3 Single-modedness of solid core C_{6v} MOF

One of the earliest known and most exciting properties of MOFs is that they can be *endlessly single-mode* [72]. However, as mentioned earlier, a MOF in which a finite number of rings of holes is solely responsible for the confinement of light carries an infinite number of modes, all of which are leaky. By using Fig. 3.9, it is possible to consider the relative losses of the modes : If the losses of the different modes of a MOF are such that after a given length of propagation all modes except for one have faded away, the MOF can be considered to be single-mode for that length of propagation. Such a definition

of single modedness is unsatisfactory in several ways : not only does it depend on the actual length of propagation, but it also depends on the pitch (see the losses of the three modes for small pitches in Fig. 3.9) and the number of rings of holes. Since the losses decrease with the number of rings of holes, for an infinite number of rings no MOF can be single-mode with such a definition.

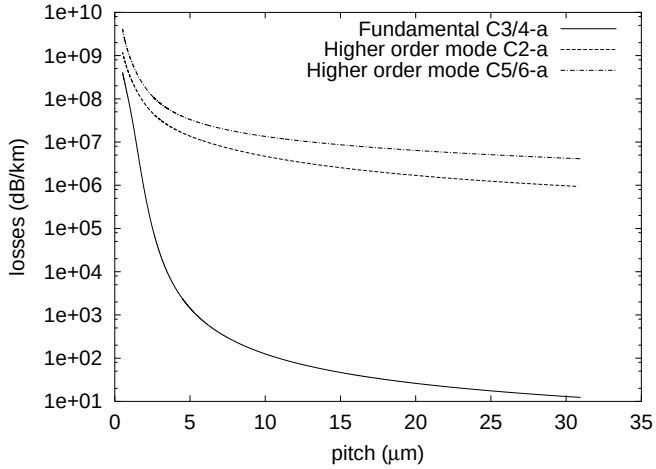

FIG. 3.9 – Losses for the fundamental mode and for two higher order modes, for a 3 ring MOF, as a function of the pitch. The wavelength λ is equal to 1.55 μm, and $d/\Lambda = 0.4$ (see section 2.2.6 page 30 for the used mode labels).

A cutoff for the second mode

This definition through the relative losses of the main modes is not satisfactory. To obtain a more definitive characterization of single-modeness one approach is to study the second mode of a C_{6v} MOF[6] as a function of MOF parameters. This kind of study was realized for the leaky modes of W-fibres by Maeda and Yamada [4] in the late seventies. In the case of MOF, the chosen parameter is the ratio λ/Λ, *i.e.* the normalized wavelength. The second mode properties will be studied at fixed d/Λ [74], and the ratio λ/Λ will be varied by changing the pitch Λ and keeping constant the wavelength λ at 1.55 μm. In doing so the refractive index of the silica matrix keeps a constant value $n_M = \sqrt{\varepsilon_M} = 1.444024$. Since λ is constant the confinement losses are directly proportional to the imaginary part of n_{eff}.

In Fig. 3.10, we give the losses as a function of λ/Λ for a MOF such that $d/\Lambda = 0.55$ for several values of the number of rings N_r. A transition in the loss curves can be observed for all studied N_r values, and the higher the N_r value the steeper the transition.

In fact, several parameters[7] can be used to observe this transition :

– the normalized effective radius R_{eff}/Λ where R_{eff} is defined by the following formula in which the function S_z is the real part of the longitudinal component of the Poynting vector :

$$R_{\text{eff}} = \frac{3}{2}\frac{\int S_z r^2 dr d\theta}{\int S_z r dr d\theta} \tag{3.2}$$

– the normalized effective area [35] A_{eff} defined as :

$$A_{\text{eff}} = \frac{(\int |E_z|^2 dr d\theta)^2}{\int |E_z|^4 dr d\theta} \tag{3.3}$$

[6] We define the second mode as the mode with the nearest real part to that of the fundamental one. See section 2.2.6 and ref. [73].

[7] For the two first parameters, the integrals are taken over the cladding region of the MOF because, as already stated, the associated fields diverge at infinity.

– the ratio of the magnetic field monopole coefficient (B_0^H) to the magnetic field dipole coefficient (B_1^H) for a cylinder in the first ring of the MOF.

$$\mathcal{M} = \frac{B_0^H}{B_1^H} \tag{3.4}$$

– the second derivative of the logarithm of the losses with respect to the logarithm of the pitch $\mathcal{Q}$ *i.e.* :

$$\mathcal{Q} = \frac{\partial^2[\log \Im m(n_{\text{eff}})]}{\partial[\log \Lambda]^2} \tag{3.5}$$

The most sensitive quantity was found to be $\mathcal{Q}$ [20, 60, 74] (this quantity will be called loss transition parameter). This exhibits a sharp negative minimum giving an accurate value of the transition position (see Fig. 3.10). Using this quantity, it can be shown that the width of the transition defined as the width of the $\mathcal{Q}$ minimum at mid-height tends to zero as N_r tends to infinity as shown in Fig. 3.12. To illustrate the transition we give in Fig. 3.11 the fields for the mode above, during and after the transition. When the mode is well confined in the MOF core, the losses decrease exponentially with the number of hole rings like in Fig. 3.5. On the contrary above the transition (*i.e.* at long normalized wavelength) the mode spreads into all the cladding region defined by the hole lattice and the mode loss follows approximately a power law as a function of N_r. In this latter case the mode is well described as a space-filling cladding resonance [67, 75, 76].

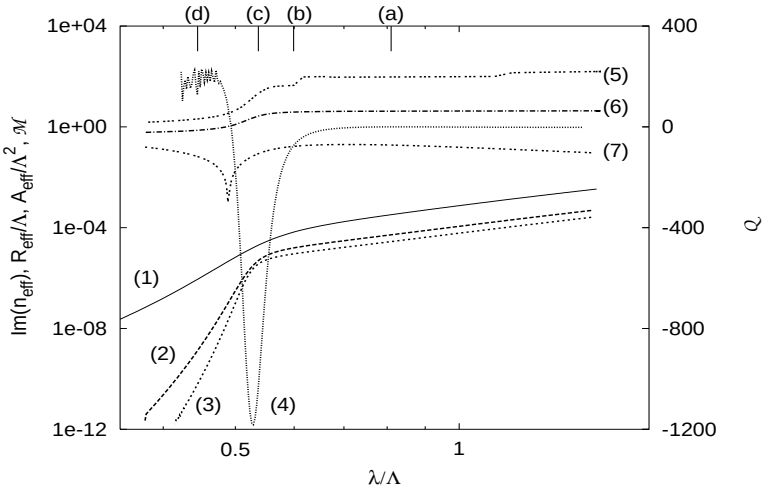

FIG. 3.10 – Variation of different physical quantities during the transition of the second mode, for a MOF with $d/\Lambda = 0.55$ used at $\lambda = 1.55$ μm. Curves (1) to (3) are $\Im m(n_{\text{eff}})$ for 4, 8 and 10 rings, curves (4) to (7) are $\mathcal{Q}$, A_{eff}/Λ^2, R_{eff}/Λ, and $\mathcal{M}$ as defined in the text, for $N_r = 8$. The points (a-d) indicate the positions of the field plots of Fig. 3.11.

This second mode is in fact a defect mode, the observed transition defined by the observed minimum of $\mathcal{Q}$ constituting a change from a confined state for high λ/Λ values to an extended state for low λ/Λ values [20]. We define the locus of this transition as the cutoff of the second mode. This cutoff is an intrinsic property of the mode and is not due to the finite size of the cladding region.

A phase diagram for the second mode

We have just defined the second mode cutoff in a MOF by varying λ/Λ at a fixed value of d/Λ. In this paragraph, we limit the study to an 8-ring MOF for a fixed value of n_M [20, 74], the dependencies according to N_r and n_M being discussed in the subsequent paragraph. In Fig. 3.13 we give the loss curves as a function of λ/Λ for several values of the geometrical parameter d/Λ. The transition between a localised mode and an extended mode remains sharp for $d/\Lambda > 0.45$, whereas for $d/\Lambda < 0.45$ the transition becomes more and more gradual, disappearing entirely around $d/\Lambda \simeq 0.4$.

In the $(d/\Lambda, \lambda/\Lambda)$ plane, the loci of the cutoffs define a curve which splits the MOF parameter space into two regions. Below this cutoff curve, the second mode is confined, and above it is extended or unconfined. The best fit of this limit curve obtained from finite size MOF studied with the Multipole Method is :

$$\frac{\lambda}{\Lambda} \simeq \alpha_{s.m.}(\frac{d}{\Lambda} - (\frac{d}{\Lambda})_{s.m.})^{\gamma_{s.m.}} \tag{3.6}$$

where $\alpha_{s.m.} = 2.8 \pm 0.12$, $\gamma_{s.m.} = 0.89 \pm 0.02$, and $(\frac{d}{\Lambda})_{s.m.} = 0.406 \pm 0.003$.

For $d/\Lambda < (d/\Lambda)_{s.m.}$, the second mode is always space filling, and consequently the fundamental mode is the only one to be potentially confined whatever the wavelength : the MOF is endlessly single-mode.

Using periodic boundary conditions in a plane wave basis and few points computed from the normalized effective area, Mortensen has obtained for the parameter $(d/\Lambda)_{s.m.}$ an approximate value of 0.45 [77]. From the experimental point of view, Folkenberg and his colleagues found that the above cutoff locus formula is in very good agreement with their experimental results obtained from high quality MOF [78]. On the theoretical side, Mortensen *et al.* have exhibited an adapted V-parameter for microstructured optical fibres which follows nicely Eq. (3.6) [79]. More recently, we used a simple self-referenced nondestructive method based on azimuthal analysis of the far-field pattern at the output of the tested fibre to measure the cutoff wavelength of the second mode [73]. The considered silica MOF had 5 rings of air holes (6 holes being missing in the last ring), and an average pitch of 2.6 μm and an average diameter of 1.43 μm. The measured cutoff wavelength was 1370 ± 10nm whereas the computed cutoff of the model fibre was around 1410 nm. This fairly good agreement is obtained while the criterion used for the experimental determination of the cutoff does not correspond exactly to the one based on $\mathcal{Q}$ minimum described in this section.

Towards a generalized phase diagram for the second mode

In this paragraph, we describe the influence of N_r on the position of the second mode transition and give results for both bigger and smaller valuer of n_M than that of silica [80]. We conclude with a generalized phase diagram for the second mode valid for a large range of matrix refractice indices [80].

As can be seen in Fig. 3.14, $\mathcal{Q}$ also have peaks for a high refractive index matrix ($n_M = 2.5$).

Furthermore, it appears that the behavior of the $\mathcal{Q}$ curves depends on N_r, as shown in Fig. 3.15 and 3.16. Fig. 3.15 shows $\mathcal{Q}$ as a function of the normalized wavelength for two different values of d/Λ, N_r ranging between 7 and 12, and $n_{\mathrm{mat}} = 2.5$. For the same matrix index the magnitude of the $\mathcal{Q}$ minima $|\mathcal{Q}_{\mathrm{min}}|$ as a function of N_r is shown on Fig. 3.16, for four different d/Λ ratios.

Depending on the value of d/Λ, two different behaviors can be distinguished : for d/Λ ratios greater than or equal to 0.425 the minimum of Q becomes narrower (complete study not shown) and deeper with increasing N_r. Fig. 3.16 shows that, in that case, $|\mathcal{Q}_{\mathrm{min}}|$ diverges with N_r, and as can be seen from the curve for $d/\Lambda = 0.43$ the rate at which $|\mathcal{Q}_{\mathrm{min}}|$ diverges increases quickly with d/Λ. The divergence of $|\mathcal{Q}_{\mathrm{min}}|$ implies that the cutoff transition becomes sharper with increasing number of rings, consistent with the fact that the cutoff should be infinitely sharp for infinite N_r (see Fig. 3.12 and reference [20]). Consequently the second mode does undergo a cutoff at finite wavelength for infinite solid core MOFs with $d/\Lambda \geq 0.425$.

On the contrary, for $d/\Lambda = 0.420$ and d/Λ ratios below this value, the minimum of Q vanishes slowly with increasing N_r. This behavior indicates that no transition should occur for the infinite solid core MOF, and therefore that the infinite solid core MOF is endlessly single mode for $d/\Lambda \leq 0.420$. The critical value $(d/\Lambda)_{\mathrm{S.M.}}$ below which the solid core MOF made of low index inclusions is endlessly single mode must therefore lie between 0.420 and 0.425.

We repeated this analysis for $n_{\mathrm{mat}} = 1.1$ and $n_{\mathrm{mat}} = 1.444024$ (Fig. 3.17). In all cases $(d/\Lambda)_{\mathrm{S.M.}}$ is strictly bounded by 0.420 and 0.425. Hence, $(d/\Lambda)_{\mathrm{S.M.}}$ can depend only very weakly on the matrix index. $(d/\Lambda)_{\mathrm{S.M.}}$ can be considered as a critical geometrical parameter associated with the second mode cutoff or similarly with the endlessly single mode behavior of MOFs.

Consequenlty, the results given in the previous paragraph are in fact only valid for the studied 8-ring and are not correct for infinite MOF.

Fig. 3.17 shows the phase diagram of the second mode (*ie* $(\lambda/\Lambda)_{\mathrm{S.M.}}$ as a function of d/Λ) for the three studied matrix indices, obtained for $N_r = 7$, along with the extrapolated phase diagram for the infinite solid core MOF with $n_{\mathrm{mat}} = 2.5$. The latter results from an extrapolation of the $(\lambda/\Lambda)_{\mathrm{S.M.}}$ data computed for several values of N_r, using a nonlinear least squares algorithm. Note that for values of d/Λ close to $(d/\Lambda)_{\mathrm{S.M.}}$ the cutoff curves for finite and infinite N_r differ substantially.

Increasing the index contrast shifts the cutoff curve towards longer wavelengths ; however, the limit of the endlessly single mode regime is conserved. Birks' analysis of scaling laws of photonic states with refractive index contrast[81] shows that if λ, Λ, n_M or nh vary, photonic states change so that quantity $\nu = 2\pi\Lambda(n_M^2 - n_{inclusion}^2)^{1/2}/\lambda$ remains invariant within the scalar approximation : for two structures with fixed d/Λ, but different n_M and $n_{inclusion}$ (say n_M and $n_{inclusion}$ and n'_M and $n'_{inclusion}$ respectively), the cutoff will occur at different wavelengths λ and λ' in order to keep ν constant at a value of $\nu_{\mathrm{S.M.}}$. Following this argument we have

$$(\lambda/\Lambda)'_{\mathrm{S.M.}} = (\lambda/\Lambda)_{\mathrm{S.M.}} \left(\frac{n_M'^2 - n_{inclusion}'^2}{n_M^2 - n_{inclusion}^2} \right)^{1/2} . \tag{3.7}$$

We can hence draw a unified phase diagram using quantity ν instead of λ/Λ (Fig. 3.17, grey curves) : MOFs with a ν value lying above the $\nu_{\mathrm{S.M.}}$ curve are multi-mode, whereas MOFs with a ν value below the $\nu_{\mathrm{S.M.}}$ curve are single-mode. As can be seen in Fig. 3.17, the $\nu_{\mathrm{S.M.}}$ curves for different n_M are surprisingly consistent keeping in mind that the scaling laws used are valid only within the scalar approximation.

In conclusion, we have shown that the ratio $(d/\Lambda)_{\mathrm{S.M.}}$ delimiting the endlessly single mode regime in MOFs is largely independent of the matrix refractive index, and can therefore be considered as a critical geometrical parameter for the second mode cutoff. We also observed that the differences between the behavior of finite and infinite structures are more pronounced near $(d/\Lambda)_{\mathrm{S.M.}}$.

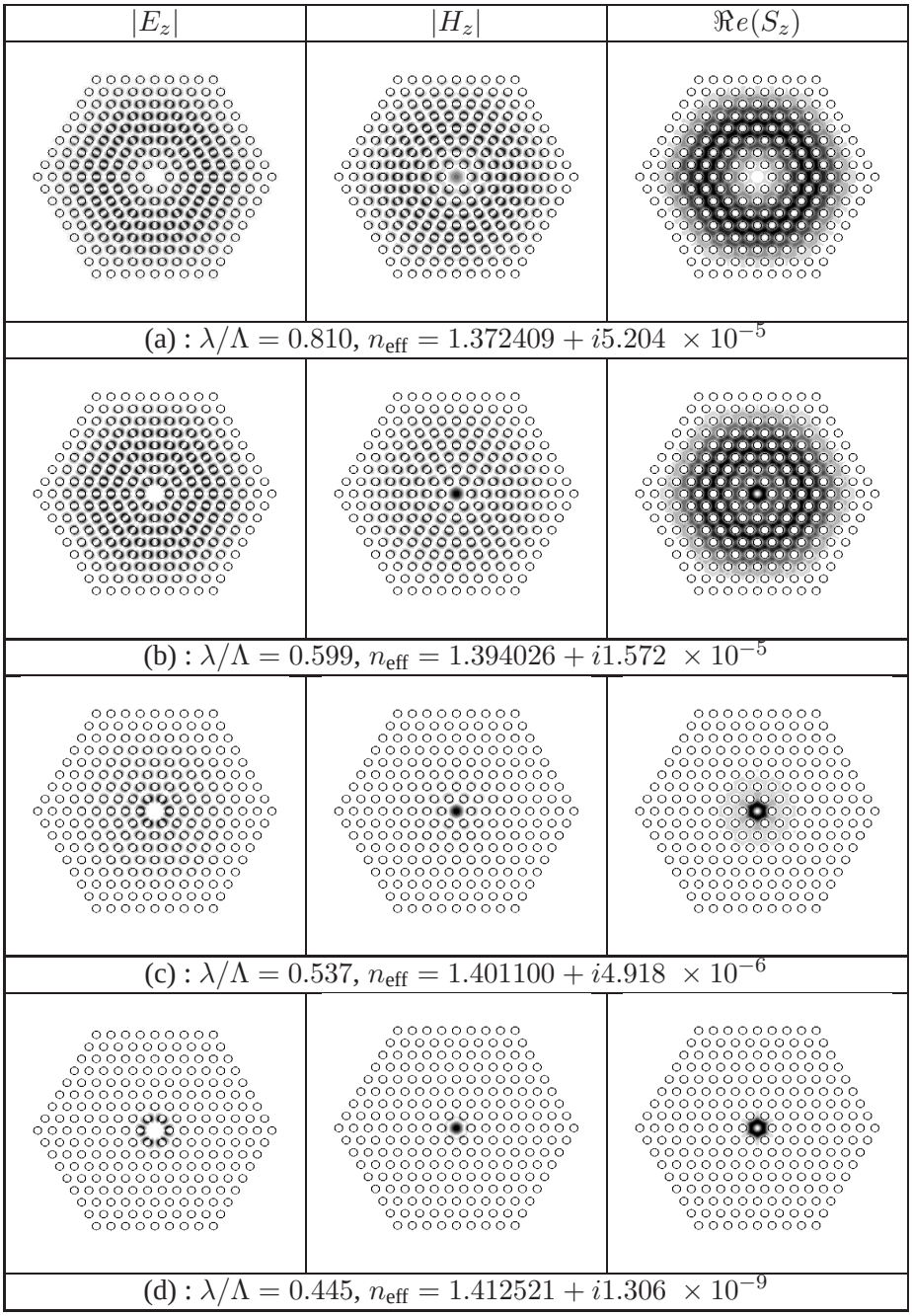

FIG. 3.11 – Field distributions of the second mode across the transition. The letters in brackets refer to the points marked on Fig. 3.10. For all structures $d/\Lambda = 0.55$, $\lambda = 1.55$ μm, and $N_r = 8$.

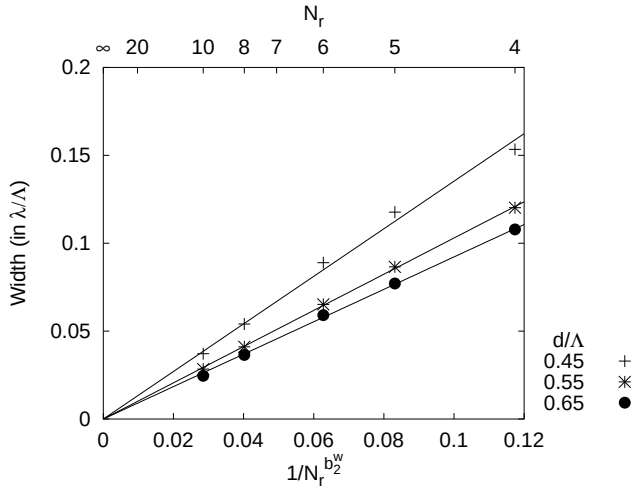

FIG. 3.12 – Width of the cutoff of the second mode as a function of the number of rings for three different values of d/Λ. The depicted quantity is the half-width of the $\mathcal{Q}$ peak as a function of $N_r^{-b_2^w}$. Here $b_2^w \simeq 1.55$. The width of the cutoff transition clearly goes to zero as the number of rings increases.

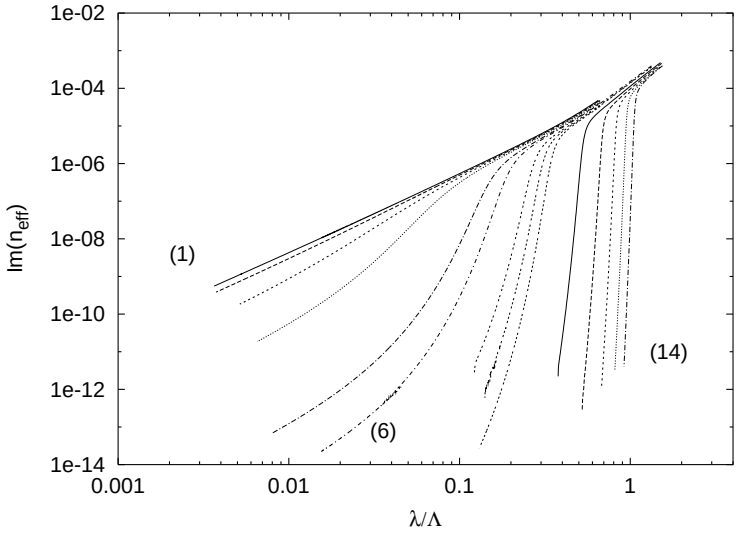

FIG. 3.13 – $\Im m(n_{\text{eff}})$ as a function of wavelength/pitch, for an 8 ring MOF at a wavelength of $\lambda = 1.55$ μm for several diameter-to-pitch ratios. $\Im m(n_{\text{eff}})$ decreases monotonically with increasing d/Λ, as this parameter takes the values 0.40 (1), 0.41, 0.42, 0.43, 0.45, 0.46 (6), 0.48, 0.49, 0.50, 0.55, 0.60, 0.65, 0.70, 0.75 (14).

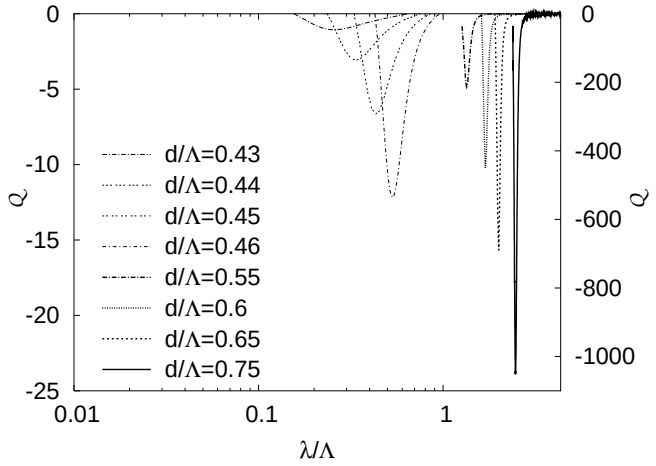

FIG. 3.14 – $\mathcal{Q}$ as a function of the normalized wavelength λ/Λ for eight d/Λ ratios for a 7-ring MOF made from a high index matrix ($n_{\rm mat} = 2.5$) with $\Lambda = 2.3\,\mu$m. The thin curves (left) are associated with the left-hand y-scale (lowest d/Λ and $|\mathcal{Q}|$ values), while the thick curves use the right y-scale.

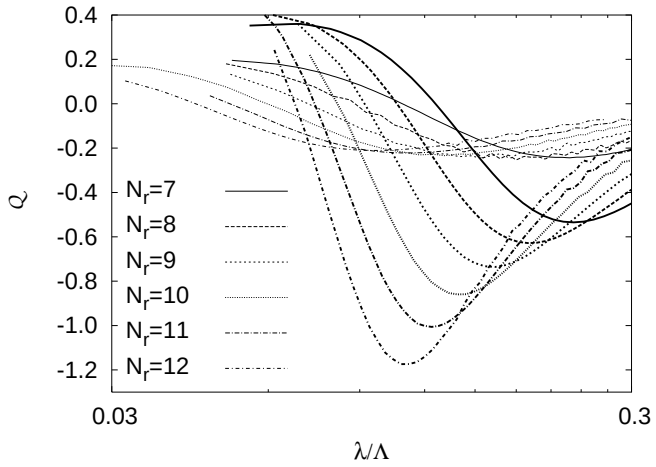

FIG. 3.15 – $\mathcal{Q}$ as a function of λ/Λ for $d/\Lambda = 0.42$ (thin curves) and for $d/\Lambda = 0.425$ (thick curves) for several values of N_r.

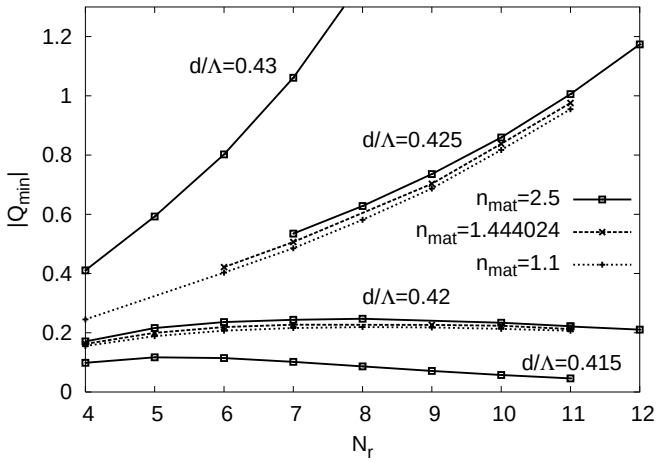

FIG. 3.16 – $|\mathcal{Q}_{\rm min}|$ as a function of N_r for three values of the matrix index $n_M = n_{\rm mat}$, for several close d/Λ values.

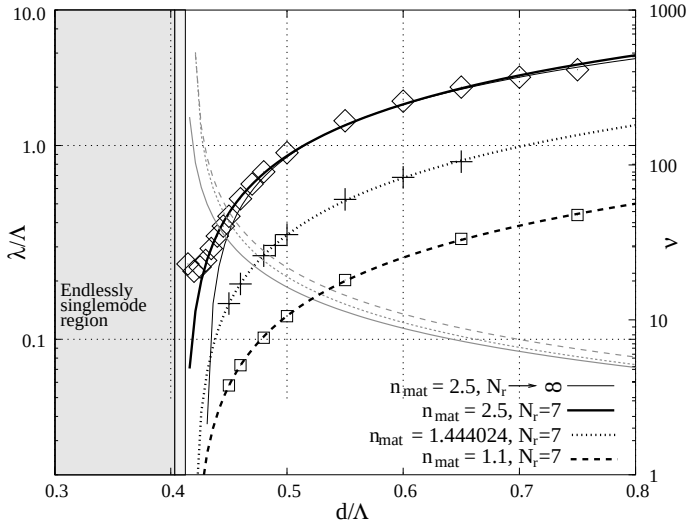

FIG. 3.17 – Phase diagram for the second mode. The points correspond to the computed values of $(\lambda/\Lambda)_{\mathrm{S.M.}}$ for the three matrix indices for $N_r = 7$; the thick black curves to the fits. The thin solid black curve is associated with the fit of the extrapolated results for $N_r \to \infty$ computed for $n_{\mathrm{mat}} = 2.5$. The grey region is the approximate "endlessly" single mode region valid for the three matrix indices for $N_r \geq 7$. Grey curves (right-hand scale) show the value of ν at cutoff for the same refractive indices as the corresponding black curves.

3.2.4 Modal transition without cutoff of the fundamental mode

It is well known that the fundamental mode of conventional optical fibres does not undergo any cutoff, but for W-fibres this is no longer true [4, 82]. Keeping in mind the useful analogies already drawn between these W-fibres and MOFs, it is a pertinent question to investigate the putative cutoff of the fundamental mode in MOF. In what follows we give some results concerning fundamental mode transition in MOF with a finite number N_r of hole inclusions.

Existence of a new kind of transition

The transition of the fundamental mode can be observed via a similar study as that conducted for the second mode. In Fig. 3.18, we give the variations of three physical quantities already described in the previous section, and once again these quantities are plotted as a function of λ/Λ. One can see that in a log-log plot the slope of the losses changes rapidly in a narrow region of the λ/Λ axis. As shown in Fig. 3.19, the change of $\Im m(n_{\text{eff}})$ is accompanied by a rapid variation in the field distributions. For large values of λ/Λ the mode has a large effective radius, *i.e.* it is cladding filling, and has high losses decreasing through a power law with respect to N_r. For small values of λ/Λ the mode is confined in the core and losses depend more strongly on the number of rings, they decrease exponentially with respect to N_r.

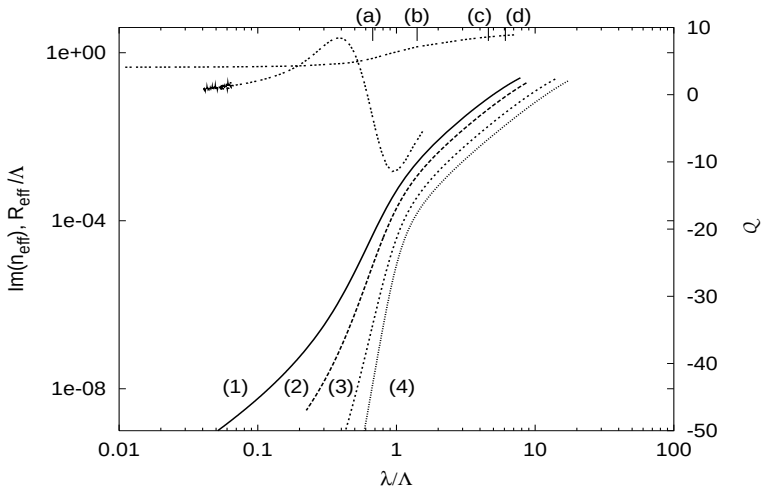

FIG. 3.18 – Variation of different physical quantities during the transition of the fundamental mode, for a MOF with $d/\Lambda = 0.3$ used at $\lambda = 1.55$ μm. Curves (1) to (4) are $\Im m(n_{\text{eff}})$ for 3, 4, 6 and 8 rings, curves (5) and (6) are R_{eff}/Λ and $\mathcal{Q}$ for $N_r = 3$ respectively. The points (a-d) indicate the positions of the field plots in Fig. 3.19.

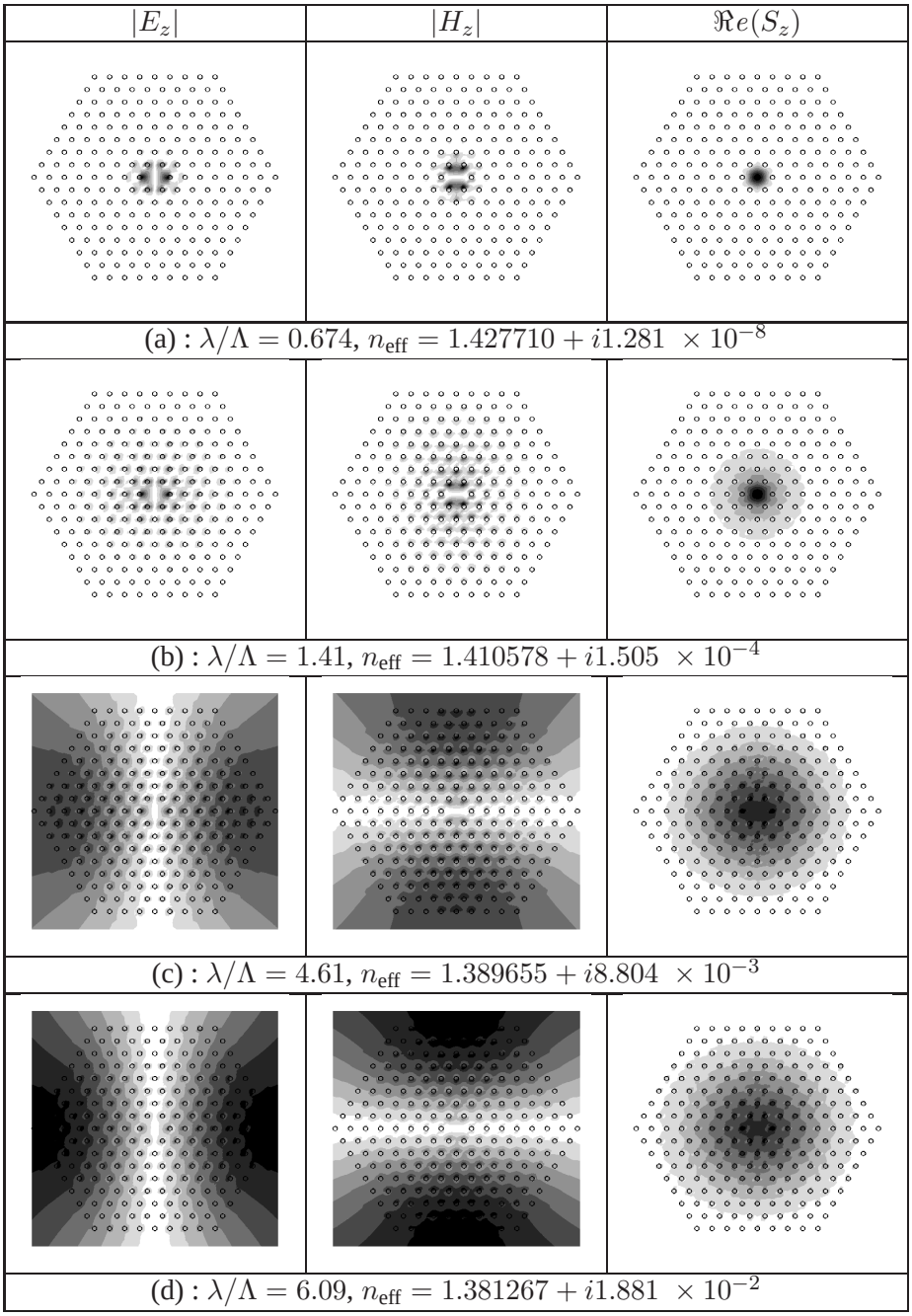

FIG. 3.19 – Field distributions of the fundamental mode across the transition. The letters in brackets refer to the points marked on Fig. 3.18. For all structures $d/\Lambda = 0.55$, and $\lambda = 1.55$ μm, and N_r=8. In plots (c) and (d), the fields diverge due to high losses of the associated leaky modes.

Even though the fundamental mode transition seems at first sight very similar to that for the second mode, they are not equivalent. The dependence of the locus of the negative $\mathcal{Q}$ peak on the number of rings is more important, and its width does not seem to become infinitely sharp with increasing N_r [60]. This second issue is addressed more quantitatively in Fig. 3.20 : the half-width of the negative $\mathcal{Q}$ peak converges with respect to N_r to a finite value at least for low enough d/Λ ratio (See also Fig. 3.12 concerning the width of the second mode cutoff, in which the width decreases to zero with increasing N_r).

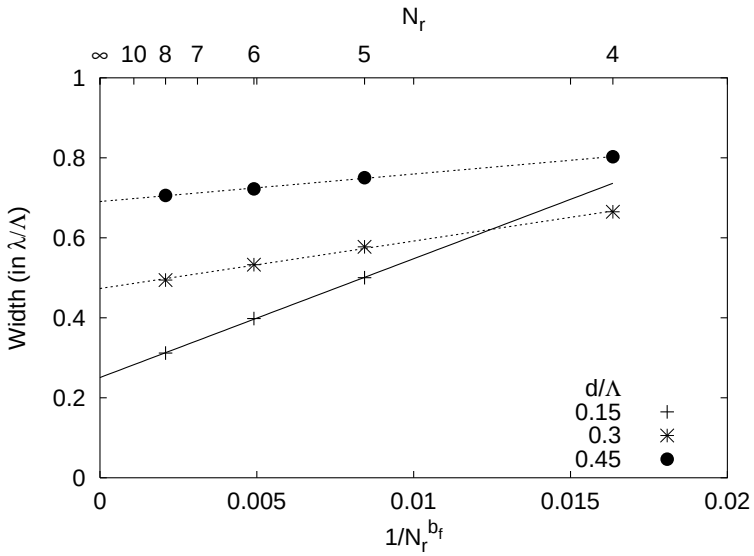

FIG. 3.20 – Half-width of the negative $\mathcal{Q}$ peak of the fundamental mode as a function of $1/N_r^{b_f}$. The width of the peak converges to a non-vanishing value. Here $b_f \simeq 2.97$. This figure must be compared to Fig. 3.12 obtained for the second mode.

Besides this, the loss transition parameter $\mathcal{Q}$ has a positive peak before the negative one. Consequently, instead of a transition point we must define a transition region. We define this transition region as the interval between the positive and the negative peak observed in the $\mathcal{Q}$ curve as illustrated in Fig. 3.21.

A crucial difference with the second mode transition (which can be seen as a cutoff as shown in the previous paragraphs) is the field localization. For the second mode as can be seen in Fig. 3.11, the z-component of the Poynting vector is no longer localized in the fibre core in the long wavelength regime. This is not the case for the fundamental mode, for which this longitudinal component does not vanish in the fibre core while the losses have already overcome the negative $\mathcal{Q}$ peak *i.e.* the beginning of the high loss regions. Since in all the considered cases in the present study the fundamental mode is a leaky mode, the fact that this mode does not fully leave the fibre core means that we can not speak about a cutoff for the fundamental mode as we did for the second mode but only a transition.

This lack of cutoff for the fundamental mode is not so surprising as it will be discussed int the paragraph "*Simple physical models below and above the transition region*" page 81.

A phase diagram for the fundamental mode

Using the same procedure as that described in section 3.2.3, one can establish the upper limit of the transition region (the $\mathcal{Q}$ minima in Fig 3.21). The associated curve (See the upper curve in Fig. 3.22) is obtained through the best fit of the computed $\mathcal{Q}$ minima values[8] for $N_r = 4$ using a similar function to that employed in Eq. (3.6).

[8] N_r=4 is the largest number of rings for which we could directly extract with the Multipole Method the locus of the minimum of $\mathcal{Q}$ for values of d/Λ up to 0.75 , for higher N_r, $\Im m(n_{\text{eff}})$ is smaller than the available numerical accuracy. The procedure described in section 2.2.4 page 26 was not used for the shown results. With it we can expect to increase the size of the largest studied structures.

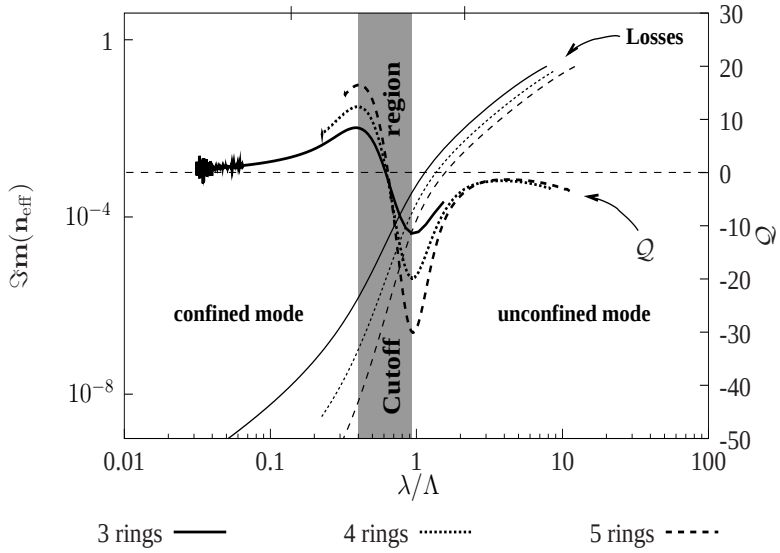

FIG. 3.21 – The different operation regions of a solid core C_{6v} MOF with low index inclusions. The curves show the fundamental mode losses and $\mathcal{Q}$ for MOF with $d/\Lambda = 0.3$ for $N_r = 3, 4$, and 5. The locus of $\mathcal{Q}$ extrema delimit the fundamental mode transition region (the grey region). The width of the transition region remains finite when $N_r \to \infty$.

$$\frac{\lambda}{\Lambda} \simeq \alpha_{f.u.}(\frac{d}{\Lambda} - (\frac{d}{\Lambda})_{f.u.})^{\gamma_{f.u.}} \tag{3.8}$$

where $\alpha_{f.u.} = 2.63 \pm 0.03$, $\gamma_{f.u.} = 0.83 \pm 0.02$, and $(\frac{d}{\Lambda})_{f.u.} \in]0; 0.06[$.

For λ/Λ above the limiting value defined by Eq. (3.8), the fundamental mode is always space filling (core and cladding), we will qualify it as unconfined but we recall that this is different from the second mode case (as explained in the previous paragraph). With increasing N_r, this upper limit of the transition region shifts slightly towards larger values of λ/Λ for $d/\Lambda \gtrsim 0.3$ and towards smaller values of λ/Λ for $d/\Lambda \lesssim 0.3$ [20].

The lower limit of the transition region represents the locus of the positive $\mathcal{Q}$ peaks (see the lower curve in Fig. 3.22). Due to numerical limitations relating to the smallest reachable $\Im m(n_{\text{eff}})$ (limitations described in section 2.2.4 page 23), the left side of the positive $\mathcal{Q}$ peak have been obtained only for $N_r = 3$ in a wide range of d/Λ with the current numerical implementation of the Multipole Method[9]. The upper and lower limits of the transition region split the MOF parameter space $(d/\Lambda, \lambda/\Lambda)$ in three regions : the unconfined fundamental mode region, the transition region, and the confined fundamental mode region.

Simple physical models below and above the transition region

We must stress that the fundamental mode transition diagram presented here (Fig. 3.22) has been obtained with finite (and relatively small) values of N_r, but as can be seen in Fig. 3.21, the upper and lower limits of the transition region along the λ/Λ axis depend only slightly on N_r. One must keep in mind that in all cases experimental MOF consist of a finite number of inclusion rings, so the results presented here retain their predictive value.

A more detailed study of the fundamental mode transition and a deep asymptotic analysis of this phenomenon can be found in references [20, 60, 83]. We give below only the main qualitative results. MOFs have already been modeled for short wavelengths as step index fibres with varying cladding index [72, 76, 84]. In the proposed approximate models, both the short and long normalized wavelength limits are treated : a W-fibre model called CF2 is used for short wavelengths, and a step-index fibre model called CF1 is used for long wavelengths. These models are depicted in Fig. 3.23.

[9] As already mentioned, this limit value of N_r can be increased using the procedure described section 2.2.4.

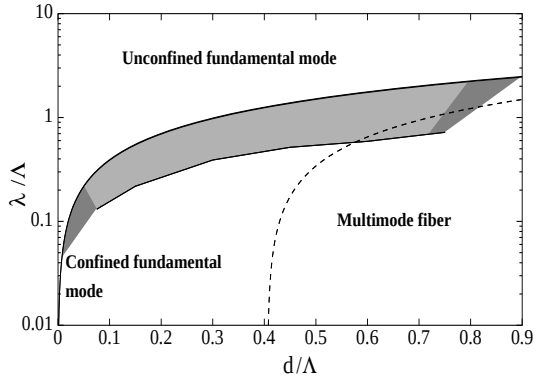

FIG. 3.22 – Diagram of the operation regimes of solid core C_{6v} MOFs with low index inclusions. The shaded grey region correspond to the fundamental mode transition region. The dashed line corresponds to the second mode transition locus as computed via Eq. (3.6).

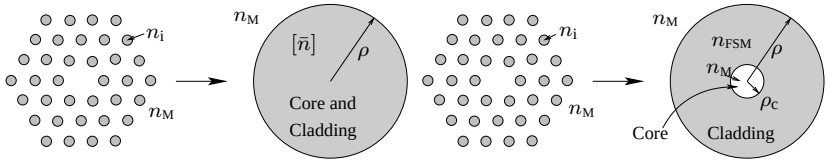

(a) CF1 model geometry : conventional step index fibre equivalent to a MOF at long wavelengths.

(b) CF2 model : Geometry of the conventional W-step index fibre equivalent to MOFs at short wavelengths.

FIG. 3.23 – Models of conventional optical fibres used for the asymptotic analysis of MOF in the long (CF1) and short (CF2) normalized wavelength limits. n_M is the matrix index and n_i is the inclusion index (See the text for more details).

At long normalized wavelengths, we have observed that the fundamental mode fills the entire confining region, *i.e.* the core and the cladding so we can consider a homogenized fibre with a core radius ρ equal to $N_r\Lambda + d/2$ and an average effective index $[\bar{n}]$ embedded in the matrix. This effective index is computed by means of homogenization argument [85] using the air filling fraction of the fibre. The modal index is calculated using the analytical formula given in table 12-12 of reference [2] concerning a step-index uniaxial fibre with a core radius equal to $N_r\Lambda + d/2$ surrounded by a matrix of index n_M. The agreement between the results given by this step-index model fibre and those given by the Multipole Method for the MOF are excellent for $\lambda/\Lambda \geq 0.5$. Thus in this regime, the mode properties only depend on the total fibre radius and on d/Λ. MOF modes are fairly lossy in this regime, since the effective indices in the core region of size $\rho = N_r\Lambda + d/2$ are smaller than the matrix index. The loss decreases with increasing N_r following a power law. Consequently, N_r has to be impractically large to obtain MOFs with acceptable losses for applications. Besides, some important quantities such as the chromatic dispersion depend on N_r [37]. At first sight, this regime of long normalized wavelength does not seem to be useful for practical applications.

In the short normalized wavelength region, we have observed that the fundamental mode is completely confined in the core region. Hence the fibre model is now a step-index W-fibre with a core made of silica of which the radius ρ_c is approximately[10] 0.64 Λ [36]. The intermediate region of the W-fibre is an annulus extending from the core radius to the end of the cladding region ($\rho = N_r\Lambda + d/2$). The index of this annulus is taken as n_{FSM}, the effective index of the fundamental space filling mode[11] (see section 3.2.1) [67, 72]. Using this CF2 model, it can be shown that the losses vary as $(\lambda/\Lambda)^2$ for a fixed

[10] This value of 0.64 Λ for the fibre core gives the best estimates for the actual value of the real part of the effective index of the fundamental mode given by more accurate methods (such as the finite element or multipole methods).

[11] n_{FSM} is the highest possible real effective index for a mode localized between the low index inclusions constituting a periodic lattice embedded in a high index infinite matrix.

number of ring N_r, and decrease exponentially with increasing N_r at fixed λ/Λ [20]. These behaviours are actually observed on the corresponding curves computed with the Multipole Method for the finite MOFs for $\lambda/\Lambda < 0.3$. In this regime, the real part of n_{eff} converges with increasing N_r and so does the chromatic dispersion.

Consequently, the small normalized wavelength region, or equivalently the regime in which the CF2 model is valid, is much more appropriate for practical MOF designs than the region associated with the CF1 model (long normalized wavelength). However, the further the CF2 region is penetrated toward short wavelength the stronger the analogy becomes between MOF and conventional optical fibres.

The region of the parameter space $(d/\Lambda, \lambda/\Lambda)$ between the regions in which the CF1 and CF2 models are valid is called the transition region. In this region, the properties of the fundamental mode change ; they depend on the MOF parameters $(d/\Lambda, N_r)$ and they differ from those of conventional step-index or W-profile fibres. This transition region seems to be fruitful for applications.

3.2.5 Chromatic dispersion

The chromatic dispersion, or equivalently the group velocity dispersion, plays a crucial role in conventional fibre optics [86] both in linear and nonlinear [35] phenomena. This key role is also present when microstructured optical fibres are considered [87–89]. Fairly early in MOF history, it became apparent that these new waveguides can exhibit peculiar and interesting dispersion properties and that they may be good candidates for dispersion management in optical systems [84, 90, 91].

The systematic study of chromatic dispersion in MOF [91] really began with the development of a vector simulation method with periodic boundary conditions [92]. Nevertheless we know from the previous section 3.2.4 that the MOF properties will converge with respect to N_r in the short normalized wavelength (λ/Λ) region of the operation regime diagram but that this is no longer true in the peculiar and promising transition regime. Therefore one must be able to take into account the finite cross section of MOF to describe accurately the chromatic dispersion and to compute their losses [37].

In this section, mixing the contents of several articles [37, 91, 93, 94] we describe how the chromatic dispersion can be managed in MOFs. We then show how it is possible using the great versatility of MOF design to get both ultraflattened chromatic dispersion and low losses.

Material and waveguide chromatic dispersion

The dispersion parameter D is computed through the usual formula from the real part of the effective index $\Re e(n_{\text{eff}})$ [86] :

$$D = -\frac{\lambda}{c}\frac{\partial^2 \Re e(n_{\mathtt{eff}})}{\partial \lambda^2} \tag{3.9}$$

D depends on λ, d, Λ, N_r, and also on n_M the matrix index[12]. Most of the time, for glasses, $n_M(\lambda)$ depends itself on λ (in dispersive media) [95].

To explain the procedures used to study the chromatic dispersion we must first recall a few results obtained for step-index optical fibres [86]. In a weakly guiding step index fibre, it can be shown that D is approximately composed of two components : one coming from the bulk material dispersion D_M and one coming from the waveguide itself D_W . So we have

$$D \simeq D_M + D_W \text{ with} \tag{3.10}$$

$$D_M = \frac{-\lambda}{c}\frac{d^2 n_M}{d\lambda^2} \tag{3.11}$$

$$D_W = -(\frac{\lambda}{c})\frac{\partial^2 [\Re e(n_{\mathtt{eff}})|_{n_M(\lambda)=constant}]}{\partial \lambda^2} \tag{3.12}$$

D_M can be easily computed using a Sellmeier type expansion for n_M [35, 95]. An explicit expression for D_W in terms of the usual step-index fibre parameters is available [86] but this is useless in the present

[12] In what follows we consider that the low index inclusions are simply holes of which the index is constant and equal to unity.

study which concerns MOF. We will assume that this splitting of the total chromatic dispersion D into two distinct terms is still approximately valid for MOF. it is worth mentioning that all the numerical simulations we did confirm the quality of this appromixation. It will be useful in understanding the global chromatic dispersion behavior in MOF[13].

In the case in which no material dispersion is taken into account *i.e.* $n_M(\lambda) = constant$, the effective index n_{eff} of a guided mode only explicitly depends on the pitch Λ of the inclusion lattice and the diameter d of these inclusions, and also on the wavelength λ. Hence as pointed out by Ferrando and his colleagues [91], that since n_{eff} is dimensionless, the dependence on the three above parameters can only occur through a dimensionless ratio. So, we can write the following when no material dispersion is involved :

$$n_{\text{eff}}(\lambda, d, \Lambda)|_{n_M(\lambda)=constant} = n_{\text{eff}}(d/\lambda, \Lambda/\lambda) \tag{3.13}$$

We now have to introduce a geometric transformation of the triangular inclusion lattice region of the MOF. Let us consider a set of inclusions defined by Λ_{ref} and d. We can build from this a new cladding with the same filling ratio $f = d/\Lambda_{\text{ref}}$ simply by rescaling both these quantities : Λ and $d(\Lambda/\Lambda_{\text{ref}})$. If we now realize a scale transformation of the wavelength and look for the resulting scaling properties of D_W, it can be shown using Eq.(3.13) that :

$$D_W(\lambda, \Lambda/\Lambda_{\text{ref}}, f) = \frac{\Lambda_{\text{ref}}}{\Lambda} D_W(\lambda\Lambda_{\text{ref}}/\Lambda, 1, f) \tag{3.14}$$

This scaling relation for waveguide dispersion allows us to compute straightforwardly the waveguide chromatic dispersion for all the rescaled MOF from the results obtained for the reference MOF : this is shown in Fig. 3.24. The scaling factor $\Lambda/\Lambda_{\text{ref}}$ can be used to modify the slopes of the chromatic dispersion curves : the higher the factor, the higher the absolute value of the slope. A $\Lambda/\Lambda_{\text{ref}}$ increase also induces an increase in the wavelength associated with zero D_W bounded by the first local maximum and the first local minimum of the waveguide dispersion (See Fig. 3.24).

On the other side, it is not possible to compute the D_W dependency on d/Λ using a similar argument : only numerical simulations will answer this question. Several curves are given for different filling ratios $f = d/\Lambda$ in Fig. 3.25. One can notice that the slope of the nearly linear part of these curves existing between the first local extrema is not really changed when the filling ratio is modified.

To achieve a specific total dispersion, one must compensate the material dispersion D_{mat} with D_W using the approximate relation Eq. (3.10). If the goal is to get flattened or ultraflattened chromatic dispersion in a target wavelength interval then one must control D_W to make it follow a trajectory parallel to that of $-D_{mat}$ in the target interval [91]. If this wavelength interval belongs to the interval in which the material dispersion behaves linearly (approximatively between 1.4 μm and 2.5 μm for silica) then a systematic approach can be used to obtain an initial MOF structure having an approximate ultraflattened dispersion curve.

We first have to adjust the slope of D_W using the scaling factor $\Lambda/\Lambda_{\text{ref}}$ in order to make it parallel to $-D_{mat}$. Then we can play with d/Λ to modify the average value of the total chromatic dispersion, the co-linearity of D_W and $-D_{mat}$ being nearly conserved in the studied wavelength interval. This scheme gives a first estimate MOF structure having the required total chromatic dispersion. Successive iterations of this process improve the quality of the results. To end the MOF design we must come back to the complete model : we have to take into account the material dispersion in our computation of chromatic dispersion curves. In some cases the gap between the complete model and the approximate one can be important compared to the required precision concerning the chromatic dispersion management.

This design scheme has also other important drawbacks. If the mean wavelength of the target interval is not included in the quasi-linear part of the waveguide dispersion then the scheme is no longer valid and only poor improvement can be obtained with sucessive iterations.

[13] We are not saying that this approximation will be used to compute the total chromatic dispersion in MOF (See section 2.2.4 page 25).

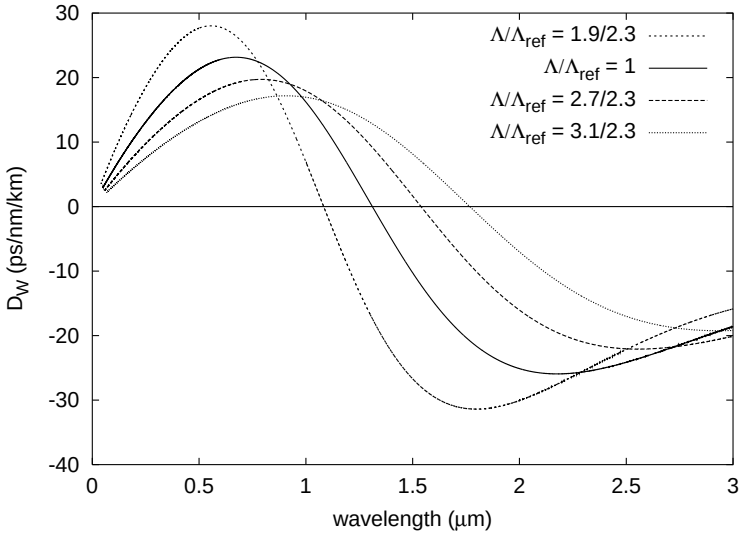

FIG. 3.24 – Waveguide chromatic dispersion curves obtained for a non-dispersive matrix ($n_M = 1.45$) for several values of the pitch Λ for a fixed filling ratio $f = d/\Lambda = 0.6/2.3$, and $N_r = 3$. The reference curve is obtained for $\Lambda_{\text{ref}} = 2.3\,\mu m$ with the Multipole Method and the other curves are obtained using the scaling law decribed by Eq. (3.14).

The influence of the number of rings N_r on chromatic dispersion

Another limitation of the design process described in the previous section is that the number of hole rings is not taken into account : we have worked with a fixed value for N_r, and as shown in section 3.2.4, depending on the position of the MOF in the phase diagram the MOF properties can depend strongly on N_r. This is exactly what we observe in the chromatic dispersion for several MOF configurations.

Directly linked to this issue are the losses. If one wants to practice chromatic dispersion management for applications using MOF the losses must be taken into account. A way to reduce the losses is to increase N_r as shown in the beginning of this chapter in section 3.2.2 and in Fig. 3.26(b), but we already know from section 3.2.4 that the behaviour of the losses with respect to N_r strongly depends on the values of λ/Λ and d/Λ.

The influence of the value of the refractive index on chromatic dispersion

As shown by Fig. 3.29, the magnitude of the refractive index has also a strong influence on the waveguide chromatic dispersion [96]. Its amplitude is increased both for its positive and negative peaks, and these two extrema are shifted to longer wavelengths. This properties could be useful to manage chromatic dispersion in the mid-infrared in chalcogenide MOFs since these glasses have a more negative material dispersion that is shifted to longer wavelengths than silica [68, 70, 97].

A more accurate MOF design procedure

In Fig. 3.30, we show the variation of the total chromatic dispersion with respect to the numbers of rings for six different MOF geometries, all located in the parameter region in which the MOF properties converge with increasing N_r. All the curves show a simple variation with N_r, which can be modeled accurately by an exponential form $D_1 \exp(-\kappa N_r) + D_{\text{lim}}$. Such a fitting form has three parameters $(D_1, \kappa, D_{\text{lim}})$, which can be determined accurately from the results of N_r =3 to 6. We have established that the exponential fit thereafter accurately describes the dispersion of much larger structures and even the limiting parameter D_{lim}, the dispersion of a mode pinned by a single defect in an infinite lattice. In fact, using the limiting dispersion D_{lim} determined numerically for a set of wavelengths λ, we can also determine $S_{\text{lim}} = \partial D_{\text{lim}}/\partial\lambda$, the limiting chromatic dispersion slope. These two quantities describe

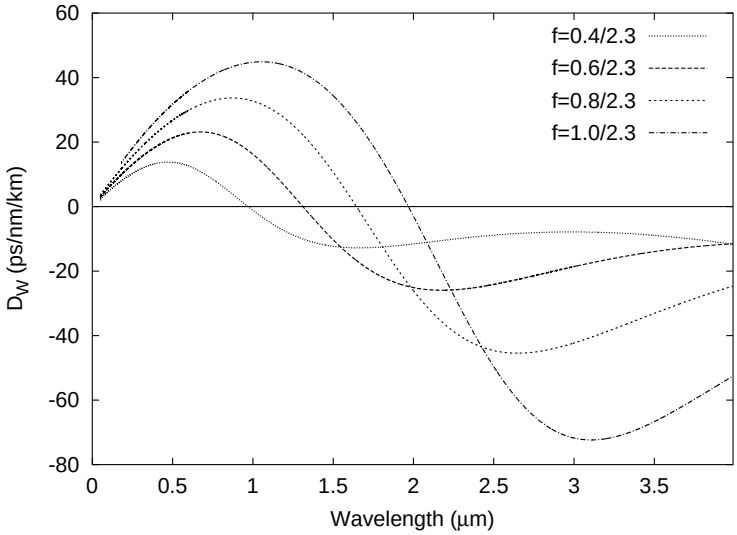

FIG. 3.25 – Waveguide chromatic dispersion curves obtained for a non dispersive matrix ($n_M = 1.45$) for several values of the filling ratio $f = d/\Lambda$ for a fixed value of the pitch Λ, and $N_r = 3$.

the chromatic dispersion of the defect mode for the infinite lattice, and naturally tell us the chromatic variation of dispersion for large MOF structures.

This procedure has important advantages since MOFs with relatively small numbers of rings are relatively quickly modeled, and it directly takes into account material dispersion. Actually, this procedure can be used as the second step of MOF design for dispersion management based on the scheme previously described. Its main drawback is that it is much more time consuming compared to the first step.

In Fig. 3.31 we show the variations of these important parameters D_{lim} and S_{lim} as a function of the hole diameter d for different pitches Λ. This figure illustrates well how one can isolate a MOF exhibiting a target dispersion value for a sufficiently large number of rings N_r, which is flat over an interval containing the chosen wavelength value. Indeed such a MOF will have the desired value of D_{lim} and simultaneously a value of S_{lim} close to zero. Note that the pitches exhibited in Fig. 3.31 were chosen carefully to exemplify this desirable behavior. We have also shown that, for the data of Fig. 3.31, the minima of S_{lim} as a function of d occur in the same diameter interval of $[0.65; 0.7]$ micrometres for all MOFs having $N_r \geq 6$. From Fig. 3.31, if one requires a positive nearly-zero flat chromatic dispersion then, using these curves, one should begin with its dispersion engineering with a MOF such that $\Lambda = 2.45\,\mu m$ and $d = 0.6\,\mu m$. Of course, Fig. 3.31 can be used to isolate MOF geometries having different characteristics, such as a prescribed slope with a fixed average value of dispersion over a given wavelength range. Note that, whereas the above designs have effectively a constant near zero chromatic dispersion for $N_r \geq 6$, their geometric losses impose much more stringent requirements on the number of rings, and the effective area of the fundamental mode $A_{\text{eff}} \simeq 36.5\,\mu m^2$ for $N_r = 6$: it requires $N_r \geq 18$ (1026 holes) to deliver losses below 1 dB/km at $\lambda = 1.55\mu$m. Even though some laboratories have already drawn 11-ring fibres [98] (containing around 396 holes), there is clearly a technological issue. To overcome these limitations of conventional MOF, innovative MOF designs have been proposed [94]. These consist of a solid core MOF in which the diameters of the inclusions increase with increasing distance from the fibre axis until the diameters reach a maximum value. With this new design and using three different hole diameters, it requires only seven rings (168 inclusions) to reach the $0.2\,dB/km$ level at $\lambda = 1.55\,\mu m$ with an amplitude of dispersion variation below $3.0\,10^{-2} ps.nm^{-1}.km^{-1}$ between $\lambda = 1.5\,\mu m$ and $\lambda = 1.6\,\mu m$.

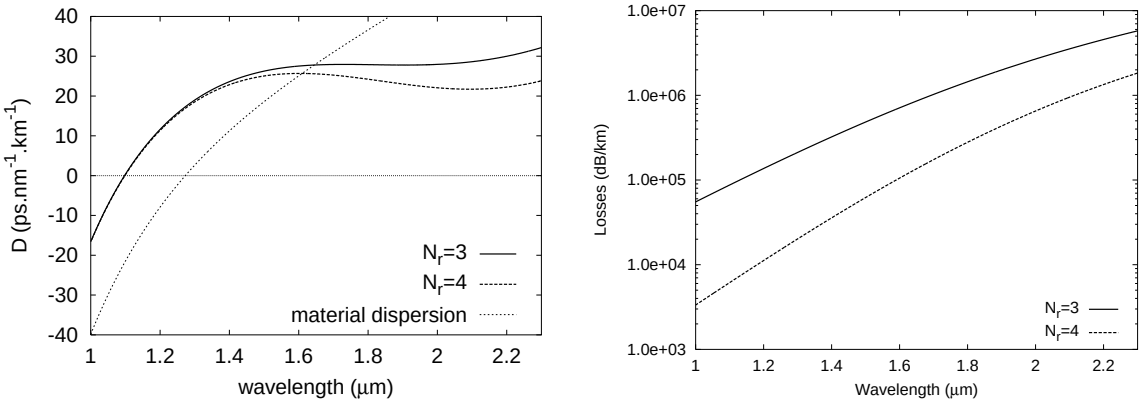

(a) Chromatic dispersion (b) Losses

FIG. 3.26 – Example of the crucial influence of N_r on chromatic dispersion for some MOF configurations : the flat chromatic dispersion obtained for $N_r = 3$ is lost for higher N_r. Dispersion and losses as a function of wavelength for several values of N_r. The material dispersion is also shown. The hole diameter d is equal to $0.8\,\mu m$.

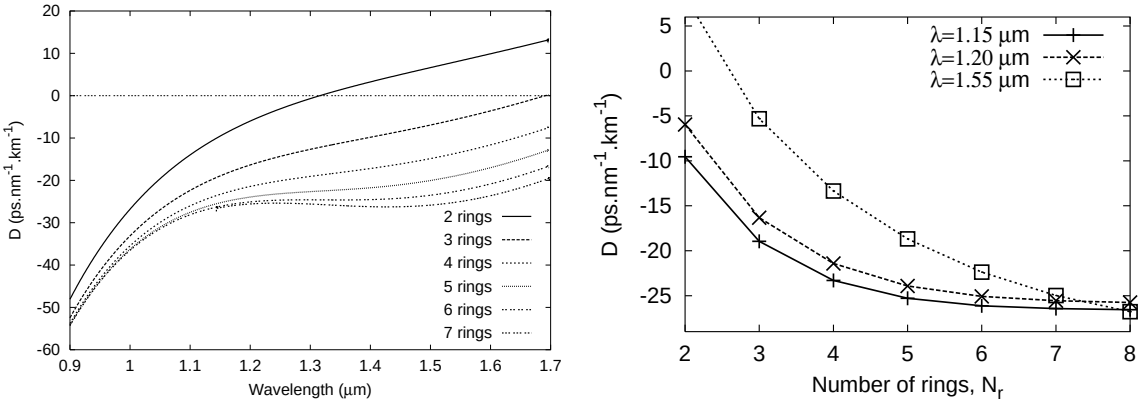

(a) Chromatic dispersion as a function of wavelength for several values of N_r

(b) Chromatic dispersion for three different wavelengths as a function of the number of rings N_r for the same MOF. For $\lambda = 1.55\,\mu m$ convergence is not obtained.

FIG. 3.27 – Chromatic dispersion as a function of the number of rings N_r. Pitch $\Lambda = 2.0\,\mu m$; hole diameter $d = 0.5\,\mu m$.

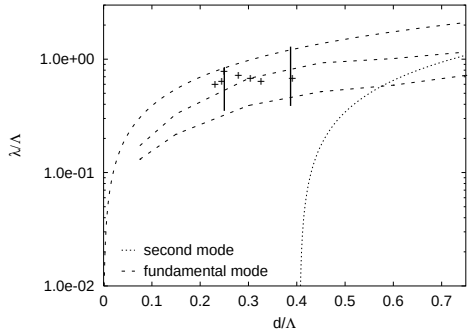

FIG. 3.28 – Positions in the phase-diagram of the MOF parameters used in Fig. 3.27(a) (left black vertical segment). The dashed lines corresponds to the fundamental (see section 3.2.4) and second mode transitions (see formula (3.6)) . The crosses in the transition region correspond to the MOF configurations described in Fig. 3.30.

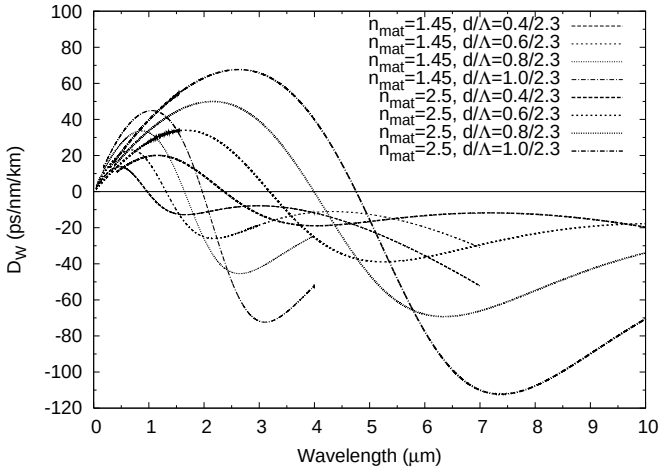

FIG. 3.29 – Waveguide chromatic dispersion curves obtained for a non dispersive matrix with $n_M = 2.5$ (thick curves), the ones computed for $n_M = 1.45$ as given in Fig. 3.24 are also shown (thin curves).

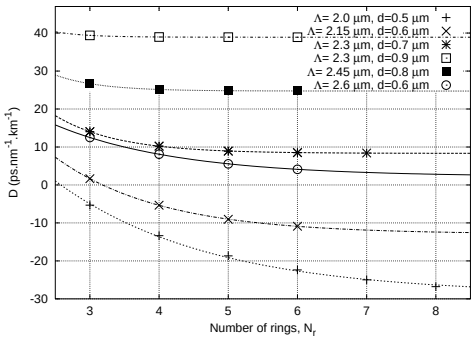

FIG. 3.30 – Dispersion decay at $\lambda = 1.55\,\mu m$ as a function of the total number of hole rings N_r for different MOF structures. Λ is the pitch of the triangular lattice of holes, and d is the hole diameter. The points correspond to the computed numerical dispersion, and the lines to exponential based fits.

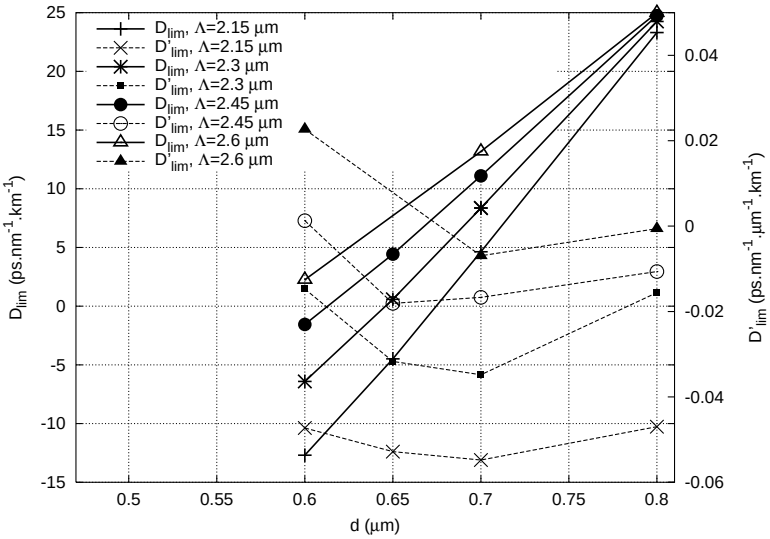

FIG. 3.31 – Limit dispersion (plain thick lines, left y-scale) and limit dispersion slope (dashed lines, right y-scale) at $\lambda = 1.55\,\mu m$ as a function of the hole diameter d for several pitches. The chosen parameter values for Λ and d correspond to the small limit slope region.

3.3 Two examples of hollow core MOFs with air-guided modes

3.3.1 An hollow core MOF made of silica and the band diagram point of view

These fibres represent the second family of MOFs. They are associated with one of the most astonishing property of MOFs : the possibility of guidance in a hollow core[14] [100–103]. This type of structure is realized by a periodic[15] lattice of low index inclusions in a high index matrix with a fibre core associated with a low index inclusion with a possible different size and/or refractive index than that of the microstructured region. This kind of fibre is also called photonic crystal fibres since the cladding region is a photonic crystal, or hollow core MOFs. The basic guiding mechanism relies on the existence of a forbidden bandgap created the cladding that inhibits light propation in this region and consequently confines light in the core region even if it has a lower refractive index than the average one of the cladding. The corresponding schematic band diagram is shown in Figure 3.32.

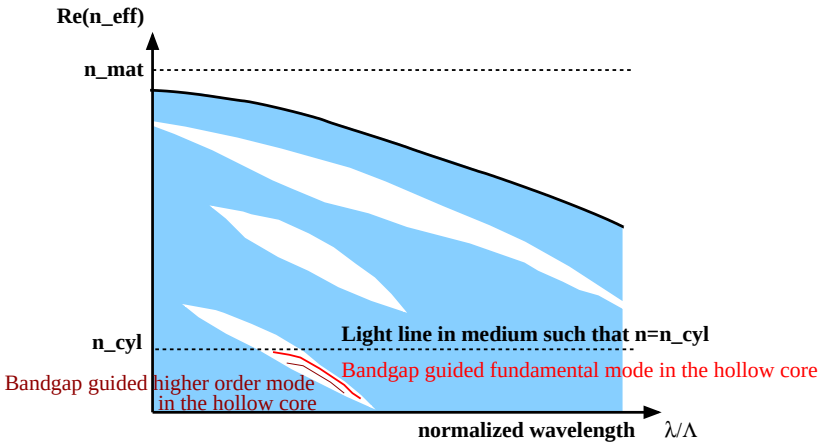

FIG. 3.32 – Schematic band diagram of a periodic array of inclusions of low refractive index n_{cyl} in a high refractive index matrix n_{mat} such that $n_{cyl} < n_{mat}$ together with the dispersion curves of the fundamental mode and a higher order mode of the finite size MOF such that $n_{core} = n_{cyl}$. In this case, the fundamental mode dispersion curve is localized in bandgap below the light line associated with the cylinder medium.

The first MOF described in this section is the same as that used in reference [104]. The pitch Λ is equal to 5.7816 μm, the diameter D_{co} of the center hole is equal to 13.1 μm, the diameter d of the circular inclusion in the cladding region is 4.026 μm, the matrix relative permittivity is equal to 1.9321 (*i.e.* $n_M = 1.39$) irrespective of the wavelength, and the inclusion relative permittivity is 1.0 (*i.e.* $n_i = 1$). We must mention that in our case we do not take into account material losses[16].

The photonic crystal cladding

One way to obtain an air-guided mode in the hollow core MOF is to surround the core with a cladding region of inclusions having a complete photonic bandgap in the transverse direction of the fibre around the desired wavelength. In order to get this full bandgap several rules can be followed [61, 105, 106]. It is worth noting that the dispersion curves must computed in a conical (out-of-plane) propagation configuration in relation to the cylindrical inclusions[107]. These dispersion curves are associated with the Bloch wave of an infinite lattice[105, 106, 108]. Figure 3.33 shows such curves for several values of

[14] Light propagation in hollow core waveguides was already discussed as soon as 1964 by Marcatili in the frame of metallic ones [99].

[15] The term is not exact. We will consider in fact a subset of periodic lattice.

[16] For realistic modeling, both matrix and inclusion material absorption must be taken into account. As will be shown later in this section, the geometrical losses due to the finite number of inclusion rings N_r around the core decrease nearly exponentially with respect to N_r so above a threshold value of N_r, and outside the wavelength associated to surface mode avoided crossings, the main contribution to the losses comes from material absorption.

the propagation constant β for the lattice associated with the cladding region of the hollow core MOF described above. Since for the study of these dispersion curves, we consider only lossless materials and an infinite lattice, β is real for the Bloch waves.

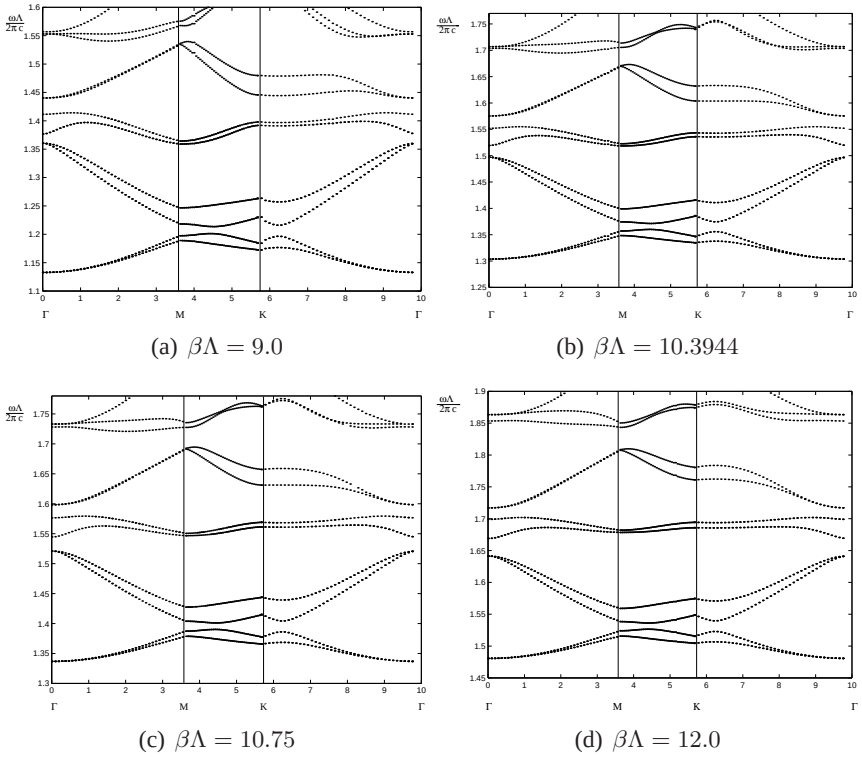

(a) $\beta\Lambda = 9.0$ (b) $\beta\Lambda = 10.3944$

(c) $\beta\Lambda = 10.75$ (d) $\beta\Lambda = 12.0$

FIG. 3.33 – Dispersion curves of the Bloch waves associated with a triangular lattice of circular cylindrical inclusions ($n_i = 1.0$) in an infinite silica matrix ($n_M = 1.39$). The geometrical parameters are : $\Lambda = 5.7816\,\mu m$, inclusion diameter $d = 4.026\,\mu m$. These curves have been obtained for an out-of-plane propagation, *i.e.* $\beta \neq 0$. The x-axis is associated with the route of the transverse wave vector along the edge of the irreducible Brillouin zone (see Appendix B.1.3 page 201). The y-axis represents the normalized frequency $\omega\Lambda/(2\pi c)$ in which ω is the frequency (angular) and c is the speed of light in vacuum.

Computing these diagrams for several values of the normalized wave vector propagation constant $\beta\Lambda$, and determining their putative bandgaps leads to Fig. 3.34 (such bandgap diagrams are often called finger diagrams). As can be seen, several complete photonic bandgaps exist for the studied lattice. Since we are looking for an air-guided mode we must have[17] $\Re e(\beta)/k_0 < 1$. This condition means that the dispersion curve of the air-guided mode of the finite hollow core MOF will be localized in the half-plane above the light line $\beta = k_0$ on the bandgap diagram. This is indeed the case, as can be seen in Fig. 3.34.

One can see in this figure that the dispersion curve of the fundamental mode of the finite MOF crosses the fourth bandgap instead of being inside it. This crossing can be understood from the fact that the modal dispersion curve has been computed for finite structures (N_r=3) while the band diagram comes from an infinite lattice.

To get these band diagrams, we can solve the periodic problem in conical mouning setting the propagation constant *a priori*. The results are the allowed angular frequencies ω associated with the Bloch modes of the periodic structures. This representation $(\beta\Lambda, k_0\Lambda)$ in Fig. 3.33 is similar to the one used in reference [66]. Such representation comes from the way the Bloch modes are obtained. Most of the times, band diagrams are computed with a plane wave method in which the unknown is the frequency and not the propagaton constant β [105]. In our case, since we want to be able to directly take into account the material dispersion, it is more convenient to solve a problem in which the wavelength is fixed and β is unknown. In the appendix B we describe how we solve this problem using a finite element method

[17] We take the real part of β due to the expected leakiness of the mode for the finite MOF.

with periodic boundary conditions. Figures 3.34 has also been obtained with this method but with the formulation in which β is fixed and ω is the unknown like with a conventional plane wave method.

In Fig. 3.35, we give a more complete band diagram corresponding to the same structure but computed directly in the $(\lambda/\Lambda, \Re e(n_{eff}))$ representation with the Finite Element Method.

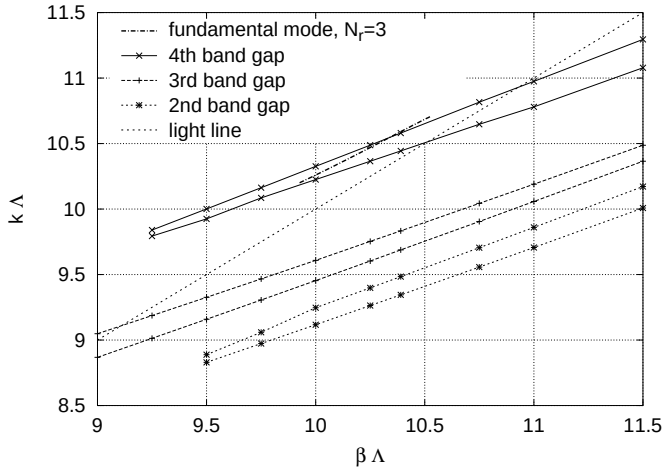

FIG. 3.34 – Bandgap diagrams associated with the dispersion curves of Fig. 3.33 (infinite lattice) and part of the dispersion curve of the fundamental mode for a three-ring finite size MOF. Only the 2^{nd}, 3^{rd}, and 4^{th} bandgaps are shown. Each bandgap is localized between the two curves corresponding to the lower and upper boundaries of the bands (same line style). The thin straight dashed line is the light line $\beta = k_0$.

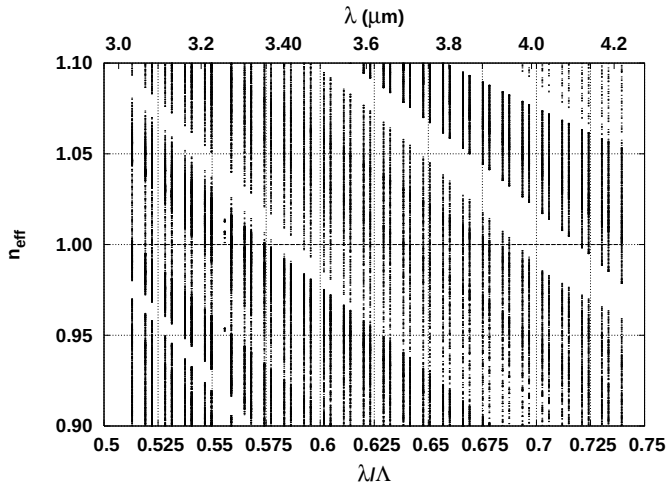

FIG. 3.35 – Computed band diagram in the $(\lambda/\Lambda, \Re e(n_{eff}))$ representation for the same configuration as in Fig. 3.34 but for a wider wavelength range. The modes of the periodic structures are computed for discrete values of the wavelength. They appear as dots forming either a continuum or isolated spots for each wavelength.

The finite structure

A few results concerning finite size effects in hollow core MOF are now described. Due to the large diameter of the central hole we needed to use a fairly large value for the truncation order parameter M (see section 2.2.4 page 23) to ensure a good convergence of the field expansions. Consequently we take M=19 in the multipole method for the numerical computations associated with the finite structures.

The finite MOFs studied in the following have the same parameters (Λ, d) as the infinite lattice used in the previous section. Nevertheless two other parameters are needed to described the finite structure : D_{co}

the diameter of the hollow core which will be kept constant ($D_{co} = 13.1\,\mu m$), and the number of low index inclusions N_r which will be varied. The losses $\Im m(\beta)$ of the fundamental mode of finite size MOFs

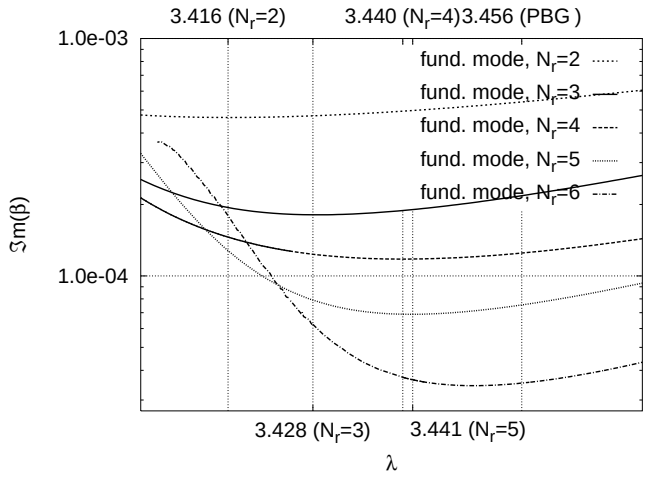

FIG. 3.36 – Losses $\Im m(\beta)$ of the fundamental mode of several finite size MOFs ($N_r = 2, 3, 4,$ and 5) versus the wavelength (note the y log-scale). The wavelengths of the different finite structures associated with the lowest losses λ_{opt} are materialized with vertical lines. The wavelength corresponding to the middle of the photonic bandgap (PBG) of the infinite lattice $\bar{\lambda}_{gap}$ is also shown.

versus the wavelength are shown in Fig. 3.36. These losses are computed for several values of N_r. As can be seen and as expected, the losses decrease with increasing N_r. More interesting is their wavelength dependence : there is an optimal wavelength value λ_{opt} for which the losses are minimal ($\lambda_{opt} = 3.416\,\mu m$ for N_r =2, $\lambda_{opt} = 3.428\,\mu m$ for N_r =3, $\lambda_{opt} = 3.440\,\mu m$ for N_r =4, $\lambda_{opt} = 3.4413\,\mu m$ for N_r =5, and $\lambda_{opt} = 3.4494\,\mu m$ for N_r =6). This behaviour is due to the guidance mechanism in the hollow core : the photonic bandgap effect.

It can also be noticed that the loss minima become sharper as N_r increases. This property is also related to the photonic band gap : the larger the value of N_r, the sharper the resonance.

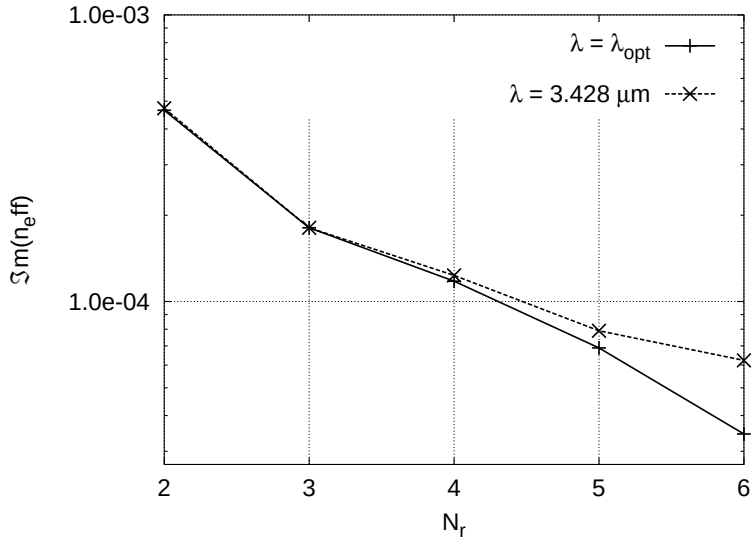

FIG. 3.37 – Losses of the fundamental mode of finite MOFs versus the number of low index inclusion rings N_r for a fixed wavelength $\lambda = 3.428\,\mu m$ and for the optimal wavelength λ_{opt} in each case (see the text).

The losses of the fundamental mode as a function of N_r are shown in Fig. 3.37. For a fixed wavelength, the losses decrease nearly exponentially with N_r. Otherwise if we consider the lowest loss values

found for each N_r, *i.e.* the losses computed at λ_{opt}, the loss decreases is even better fitted by a decaying exponential. The exponential decay of the imaginary part of n_{eff} has already been found for solid core MOF in the CF2 regime (the regime in which the fundamental mode is confined, see section 3.2.4).

We now come back to the band diagram and to the dispersion curves of finite size MOF fundamental modes. Figure 3.38 is a zoom of Fig. 3.34 in which we add the dispersion curves of the fundamental mode computed for $N_r = 2, 3, 4,$ and 5. It can be easily seen that the dispersion curves are very similar and that they cross the bandgap even for $N_r = 5$. If we pick up the optimal value of β denoted by β_{opt} which is associated with λ_{opt} (using the results of the numerical simulations), it can be observed that even for $N_r = 5$, the value of β_{opt} is not yet in the bandgap of the infinite structure. Nevertheless, it seems that as N_r increases, $\Re e(\beta_{opt})$ approaches the middle of the bandgap. This comparison between the infinite lattice properties and those of finite MOFs clearly shows the crucial interest in being able to study finite structures when accurate results are needed as is the case for applications.

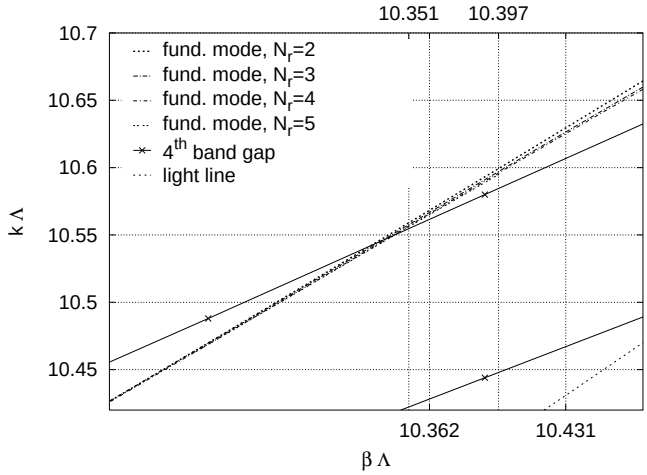

FIG. 3.38 – Crossing of the dispersion curves of the fundamental mode of several finite size MOFs ($N_r = 2, 3, 4,$and 5) with the 4^{th} bandgap of the infinite lattice (See Fig. 3.34). The bandgap is localized between the two plain curves corresponding to the lower and upper boundaries of the band (same line style). The $\Re e(\beta)$ values of the fundamental mode of the finite size MOFs, computed for the wavelength λ_{opt} associated with the lowest losses, are indicated by vertical lines ($N_r = 2$, $\Re e(\beta_{opt}) \simeq 10.431$; $N_r = 3$, $\Re e(\beta_{opt}) \simeq 10.397$; $N_r = 4$, $\Re e(\beta_{opt}) \simeq 10.362$; $N_r = 5$, $\Re e(\beta_{opt}) \simeq 10.3515$). The thin straight dashed line is the light line $\beta = k_0$.

We now describe in more detail the field properties obtained for the finite MOF fundamental mode at a fixed wavelength $\lambda = 3.428\,\mu m$. The computed effective index $n_{\text{eff}} = \beta/k_0$ is equal to $0.98111152 + i0.18086\,10^{-3}$ for $N_r = 3$ and $n_{\text{eff}} = 0.9808734 + i\,0.4724251\,10^{-3}$ for $N_r = 2$. This structure possesses the C_{6v} symmetry therefore we know that the fundamental mode is two-fold degenerate (see section 2.2.3 page 21). This property is illustrated Figs. 3.39 and 3.40. The vector fields of the fundamental mode are also given in Fig. 3.41 : it can be seen that in the core the fields are nearly linearly polarized.

3.3.2 An optimized hollow core MOF made of high index glass for the far infrared

In the previous section, we described an hollow core MOF with a silica matrix that ensures the propagation in its core around $3.44\,\mu$m. Nevertheless, the loss level is over the 100 dB/m limit eliminating this configuration for any practical applications. In the present section we describe how it is possible to obtain an hollow core MOF operating at 9.3 μm with reasonable losses using a high refractive index glass and specific design. It is worth mentioning that a lot of studies have already been dedicated to the study or the characterization of hollow core MOFs made from a silica matrix with an air hole cladding to guide light around $1.5\,\mu$m[100, 101, 103, 104, 109–112]. In the present section, our goal is to show how we can design a photonic crystal fibre (PCF) in which a far infrared beam ($\lambda = 9.3\,\mu$m) can

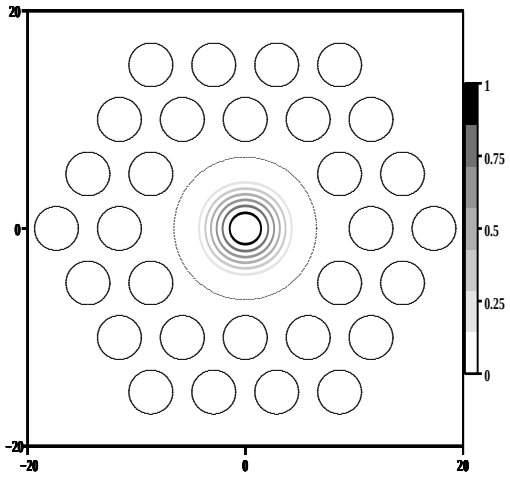

FIG. 3.39 – Modulus of the Poynting vector for the fundamental mode of the hollow core fibre with $N_r = 2$: it is the same for the two symmetry classes p=3 and p=4. The modulus is normalized to unity.

propagate in its hollow core. The guiding of infrared light in hollow core MOFs has already been studied within a silica PCF but this kind of design [113] is limited to wavelength below 3.45 μm due to the huge material losses of silica for larger wavelength. Even if the overall losses of the fundamental mode of these PCFs can be much smaller than the material losses since most of the electromagnetic field propagates in the hollow core, these PCFs still have too important losses. Furthermore, the absorption of the field in the region surrounding the core can heat this region too much or even deteriorate it, knowing that the larger the wavelength the bigger the material losses for silica in the mid or far infrared. Consequently, we decide to find another kind of solution to solve this issue. We chose to investigate the use of high index chalcogenide glasses that are known to have a transparency window in the infrared[68–70, 114]. More recently, it has been shown that these glasses can be used to drawn regular MOFs with several rings of inclusions using the stack and draw process[51]. Consequently, we decide to consider the TAS glass ($Te_2As_3Se_5$) that is transparent from 2 to 12 μm which was used to obtain step-index fibres [115]. Few numerical studies deal with high index MOFs and only some of them are dedicated to high index PCFs[61, 62, 116]. Nevertheless, none of these works consider refractive indices as high as the one of TAS glass around 9.3 μm as studied in this section.

Getting the bandgap at the sought wavelength

To ensure the propagation in the hollow core, we need to find a bandgap generated by the cladding that spans over the wavelength of interest. This wavelength must be located below the light line in air. To obtain this result we compute several band diagrams with a refractive index for the matrix fixed to the value of the TAS glass at 9.3 μm, *i.e.* 2.9095 [115, 117]. Fig. 3.42 shows such diagrams computed for four different values of the d/Λ ratio. The bandgap that fulfills the above requirements is the shaded one. In order to define the more useful bandgap that is to say the one that will provide the lowest losses for the finite structures, we must study the relative width of this bandgap according to the d/Λ ratio. The results are given in Fig. 3.43. We choose $d/\Lambda = 0.775$ because this ratio ensures a large relative width. We take this value, located on the right side of the relative width maximum plateau, to avoid the rapid decrease observed on the left part of the relative width curve so as to optimize the parameters according to drawing constraints.

For this d/Λ ratio, the centre of the bandgap of interest is located at $\lambda/\Lambda = 0.6925$. Consequently, for $\lambda = 9.3\,\mu$m, the pitch Λ must be set to 6.44 μm. The diameter of the air holes must be equal to 4.991

μm to get the optimal d/Λ ratio[18].

Finite structures : influence of the core diameter

It is well known from previous studies [112, 113, 116, 118] based on silica PCFs that the core size and shape are key parameters for the modal properties of the finite structures due to the impact of surface modes [119]. In order to illustrate this issue and to determine the optimal value of the core diameter D_{core}, we compute the dispersion curves for several core sizes (see Fig. 3.44). We clearly see the strong influence of the core size. As can be seen on this figure, for $D_{core} = 12.58\mu$m, we obtain fundamental mode losses that are nearly four times smaller than the ones from other configurations. We note that the real part of the effective index is also higher for this optimal core diameter. To complete these curves, we give in Fig. 3.45, the modulus of the z-component of the Poynting vector for the fundamental mode of the PCFs with $N_r = 4$ for three core diameters D_{core}. We see that the shape of the field map also depends strongly on the core diameter. At least for the optimal D_{core} value, these results can be explained quantitatively using the ARROW model (AntiResonant Reflecting Optical Waveguides) [120]. The generalized application of such a guiding mechanism leads to the third kind of MOFs that is studied in section 3.4. In the present structure this mechanism allows a better confinement of the core modes that are already confined by the cladding due to the existing photonic bandgap.

Indeed, if one consider a slab of thickness e with a low refractive index denoted by n_{low} that will be the waveguide, covered by a layer of thickness t with an high refrative index n_{high} then the anti-resonant condition for a guided wave with wavelength λ in the low index layer determines the t^* values ensuring the confinement of the mode [120] :

$$t^* = \frac{\lambda(2N+1)}{4n_{high}\sqrt{1-\frac{n_{low}^2}{n_{high}^2}+\frac{\lambda^2}{4n_{high}^2e^2}}} \text{ with } N = 0, 1, 2, 3, \ldots \tag{3.15}$$

To adapt this mode to a circular hollow core MOF, we can consider that the thickness e is equal to $D_{core}/2$. The high index ring around the core will acts as the antiresonant layer. Consequently, for a PCF with a fixed d/Λ ratio, the core diameter sets the thickness of the high index ring through the relation :

$$t = 2\Lambda - \frac{d}{2} - \frac{D_{core}}{2} \tag{3.16}$$

Combining eqs. (3.15) and (3.16), we get a nonlinear equation that allows us to compute the core diameters fulfilling the antiresonant condition. For the optogeometric parameters used for Fig. 3.44, we get $D_{core} = 15.66\,\mu$m $(N = 1)$ and $D_{core} = 12.3\,\mu$m $(N = 2)$. As can be seen, the ARROW approximate model gives valid quantitative results in spite of the crude approximations made to move from the PCF to the slab.

This antiresonant phenomenon is also reponsible for the elliptic shape of the field map observed on Fig. 3.45 (one can note that the bi-lobe shape field map corresponds to an increase of the field in the core near the border of the high index region as can be seen in the original ARROW model [120]).

To complete the results, we can also compute the dispersion curves of the fundamental mode in order to find the minimal losses and its respective wavelength (see Fig. 3.46). This figure confirms that the influence of the core diameter is crucial : both the loss minimum and its wavelength are very sensitive to its value. It also shows that the core diameter range in which both low losses and a wavelength around the targeted 9.3 μm is small : between 12.58 μm and 13.08 μm. The other interesting interval for the core diameter is around 15.33 μm (see Fig.3.46) would require to modify again the pitch of the structure to get the wanted wavelength for the bandgap.

Using the losses from dispersion curves (see Fig. 3.44), we can compute the spectral width of the PCF transmission as a function of the core diameter. Two definitions of the width are used : a relative one defined as an increase of 10% of the losses compared to the minimum and an absolute one defined

[18] We must emphasize that the values are much more accurate than that can be reached during the fabrication process of such high index chalcogenide MOFs.

as an increase of 10dB. These results clearly show the advantage to use an optimized value for the core diameter.

An optimized structure

We now set the core diameter to the central value of the above interval, *i.e.* 12.83 μm. To optimize further the guiding properties of the fibre, we need to readjust the other structure parameters Λ and d so as to get the losses minimum exactly around 9.3 μm. To realize this we must diminish Λ keeeping the d/Λ ratio equal to 0.775. A simple rule of three gives $\Lambda = 6.41\,\mu$m and finally we get $d = 4.968\,\mu$m[19].

With this structure, the fundamental mode field map is elliptical as can be seen in Fig. 3.48, and we obtain the fundamental mode dispersion curves shown Fig. 3.49. The losses of this mode at 9.3 μm for several N_r values are given in in the left part of table 3.1 for a lossless matrix. As soon as $N_r > 6$ the losses are below 1 dB/m. This level is nearly three times below the ones measured at 3.14 μm with a silica based PCFs [113]. Nevertheless, in order to improve our fibre model, we can take into account the material losses of the TAS glass [117]. The measured material attenuation is 1.5 dB/m at $9.3\,\mu$m which provides a relative electric permittivity equal to 1.4910^{-6}. The corresponding results are given in the right part of table 3.1. We see that the global losses of the fundamental mode are below the material losses for $N_r \geq 6$ since most of the electromagnetic fields are confined on the hollow core and not in the glass matrix. For $N_r = 7$, these losses are nearly five times smaller than the ones of the silica PCF mentioned in ref. [113].

N_r	Re[n_{eff}]	Im[n_{eff}]	Pertes (dB/m)	Re[n_{eff}]	Im[n_{eff}]	Pertes (dB/m)
3	0.91950645	0.99669946E-04	584.89	0.91950645	0.99763273E-04	585.439
4	0.91956213	0.83702342E-05	49.115	0.91956213	0.84636519E-05	49.667
5	0.91956602	0.10102266E-05	5.928	0.91956602	0.11036755E-05	6.476
6	0.91956664	0.927366E-07	0.544	0.91956664	0.18618142E-06	1.092
7	0.9195667	0.100995e-07	0.059	0.9195667	0.1035440e-06	0.607

TAB. 3.1 – Losses of the fundamental mode of the PCF at $9.3\,\mu$m for several values of the number of hole rings N_r ($\Lambda = 6.41\,\mu$m, $d = 4.968\,\mu$m, and $D_{core} = 12.83\,\mu$m). In the left part of the table, no material losses are taken into account. In the right part, the material losses (1.5 dB/m) are taken into account through a relative electric permittivity fixed to 1.49e-6.

[19] Actually, the core diameter should be adapted due to the Λ dependency in formula 3.16, but we neglect it in this first approach

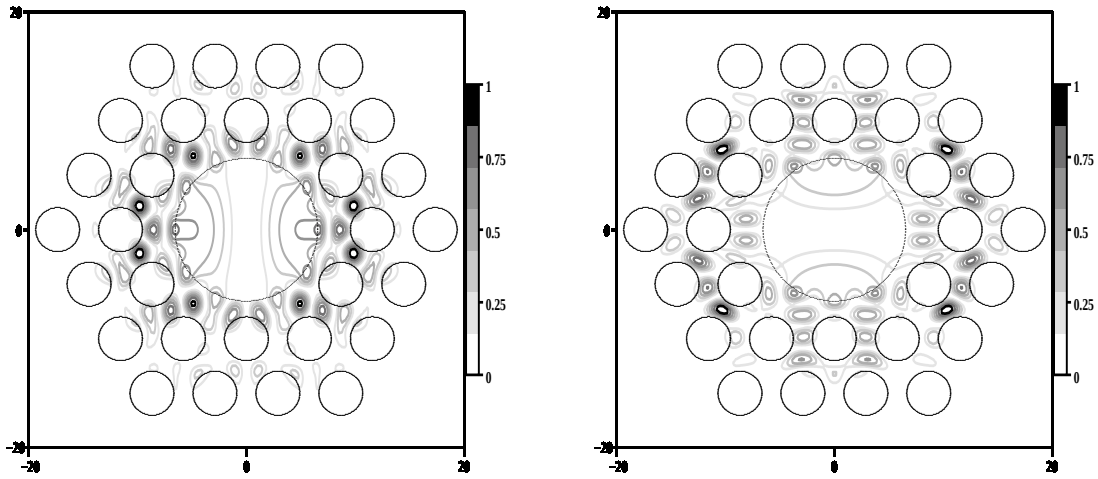

(a) $|E_z|$ for p=3

(b) $|K_z|$ for p=3

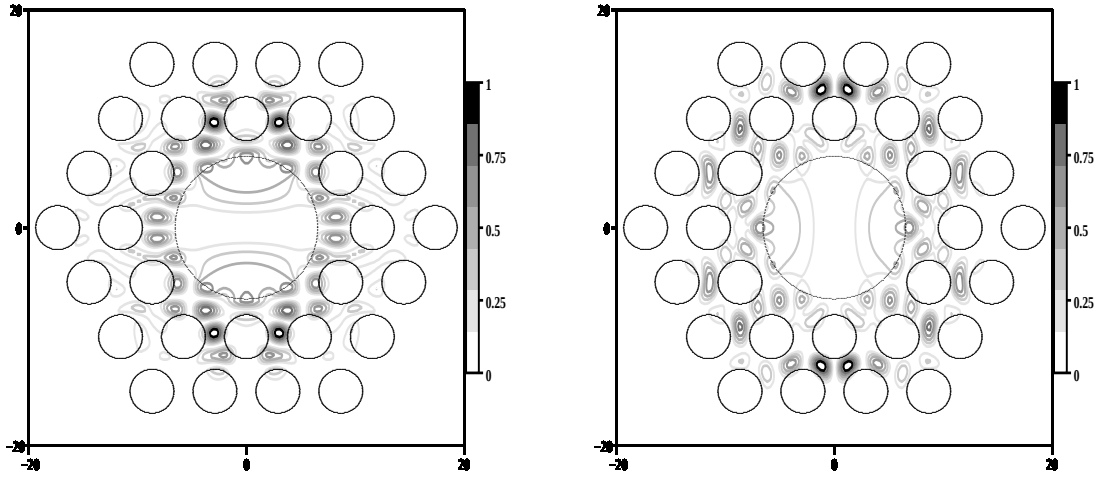

(c) $|E_z|$ for p=4

(d) $|K_z|$ for p=4

FIG. 3.40 – Moduli of electromagnetic field longitudinal components, for the air-guided mode in the hollow core MOF ($N_r = 2$), this mode belongs to the symmetry classes p=3 and p=4. The field moduli are normalized to unity.

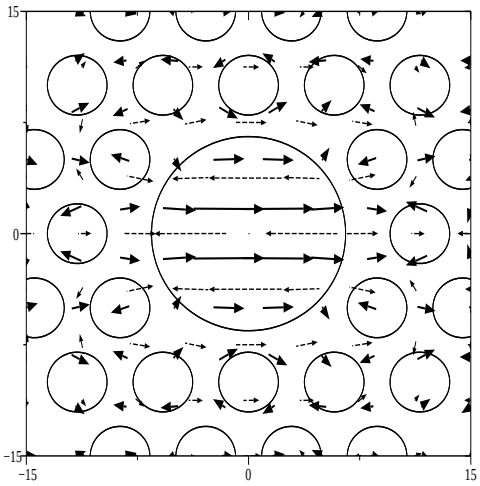

(a) Transverse E vector field for p=3

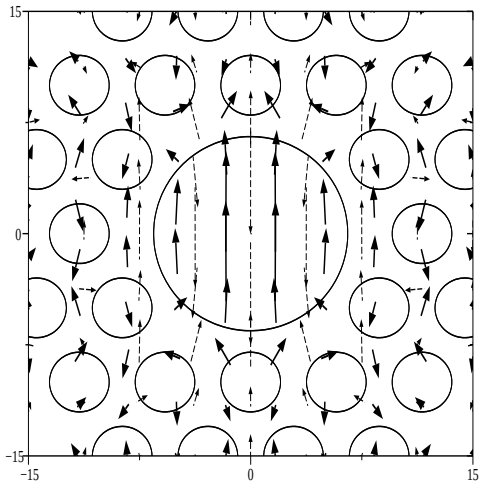

(b) Transverse K vector field for p=3

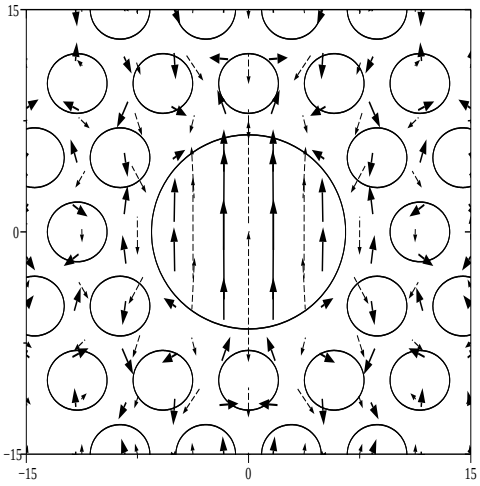

(c) Transver se E vector field for p=4

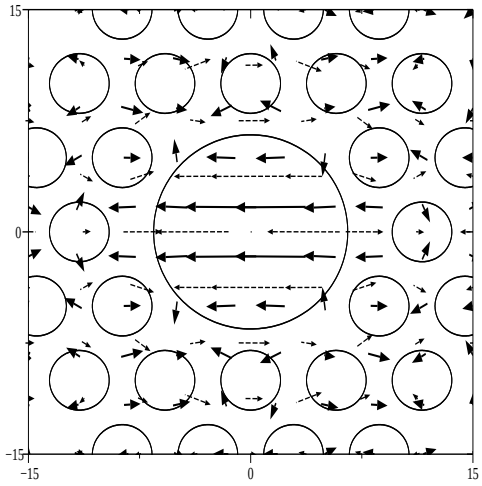

(d) Transverse K vector field for p=4

FIG. 3.41 – Transverse electromagnetic vector field for the degenerate air-guided mode of the hollow core MOF ($N_r = 2$). The real part of the field is represented by plain thick vectors and the imaginary part is represented by dashed thin vectors.

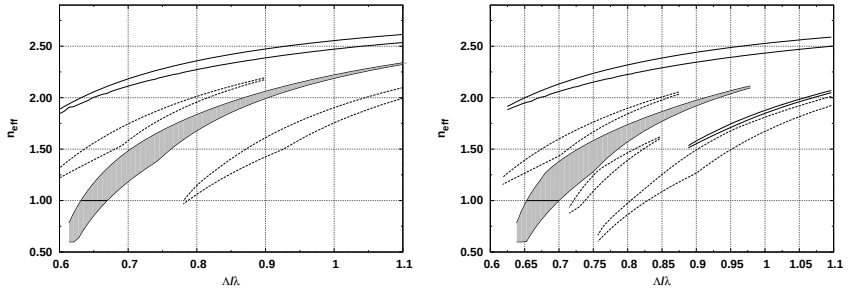

(a) $d/\Lambda = 0.7375$ (b) $d/\Lambda = 0.7625$

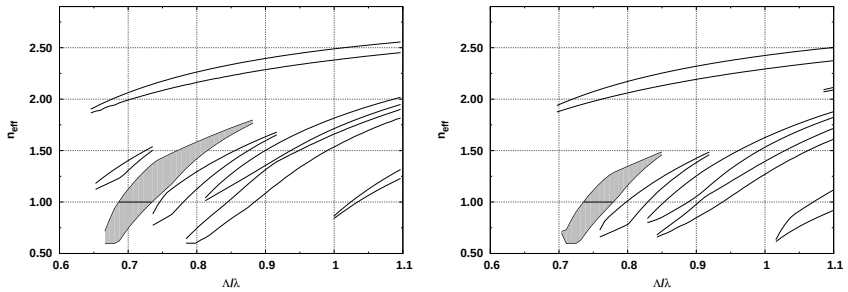

(c) $d/\Lambda = 0.79$ (d) $d/\Lambda = 0.825$

FIG. 3.42 – Band diagrams obtained for several triangular lattices of circular air holes in a TAS matrix such that $n_{mat} = 2.9095$. The shaded region is the bandgap of interest.

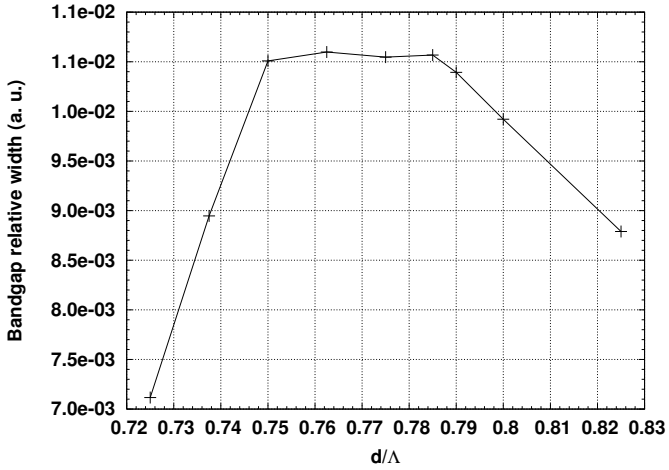

FIG. 3.43 – Relative width of the main bandgap around $n_{eff} = 1$ as a function of the normalized air hole diameter.

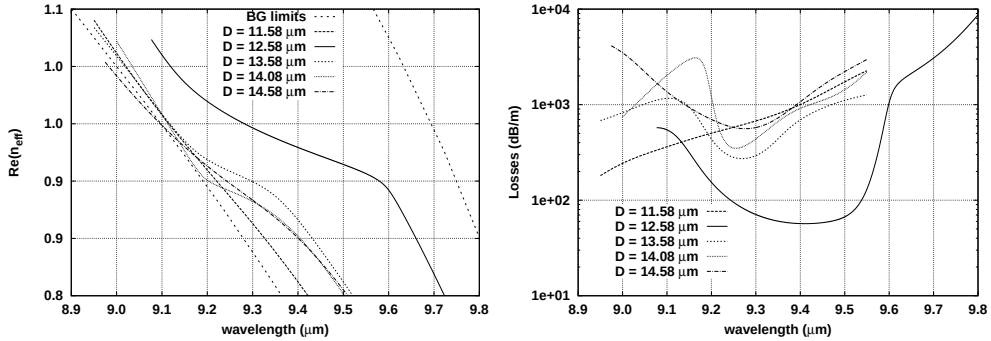

(a) $\Re e(n_{eff})$ (b) $Losses(dB/m)$

FIG. 3.44 – Dispersion curves of the fundamental mode of the PCF for 5 different diameters D_{core} of the hollow core. $\Lambda = 6.44\,\mu$m, $d = 4.991\,\mu$m, $N_r = 4$. The two thin dashed curves represent the boundaries of the main photonic bandgap obtained in Fig. 3.42.

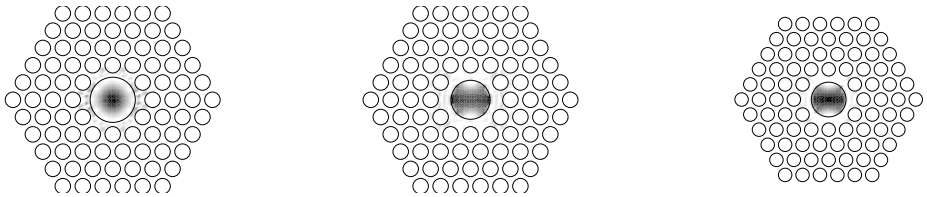

(a) D = 14.58 μm (b) D = 12.83 μm (c) D = 12.58 μm

FIG. 3.45 – Modulus of the z-component of the Poynting vector for the fundamental mode of the PCFs $N_r = 4$ for three core diameters D_{core}. The modulus is normalized to unity.

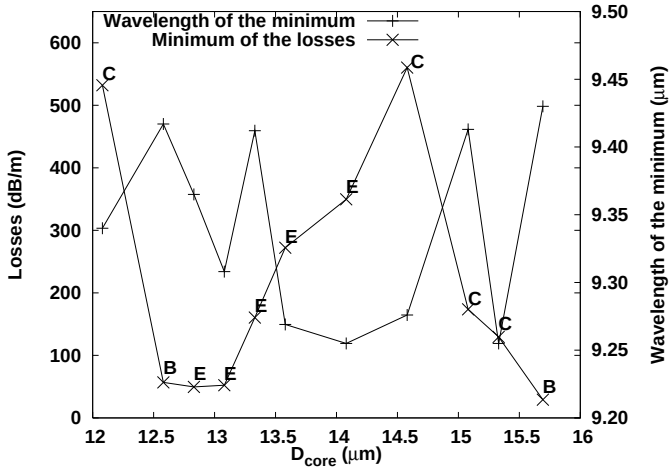

FIG. 3.46 – Guiding losses (left axis) as a function of the core diameter D_{core} for PCFs with $N_r = 4$, $\Lambda = 6.44\,\mu$m, $d = 4.991\,\mu$m. The letters B, C, and E describe the shape of the modulus of the z-component of the Poynting vector for the fundamental mode : B fo a bi-lobe shape, C for a centro-symmetrical one and E for an elliptical one. The wavelength of the minimal losses as a function of D_{core} are given on the right axis.

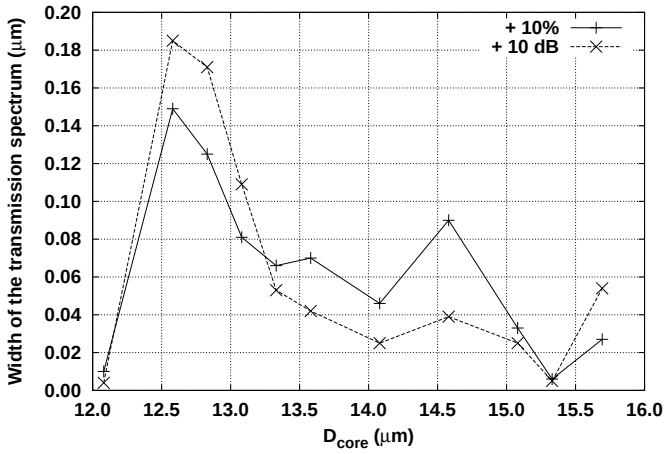

FIG. 3.47 – Width of the transmission (μm) of the PCF as a function of the core diameter. Two definitions of the width are used : a relative one defined as an increase of 10% of the losses compared to the minimum and an absolute one defined as an increase of 10dB.

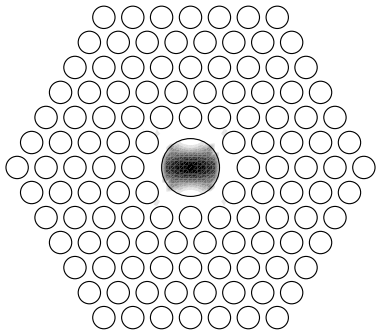

FIG. 3.48 – Modulus of the z-component of the Poynting vector for the fundamental mode of the PCFs $N_r = 5$ for $D_{core} = 12.83\,\mu$m. The modulus is normalized to unity.

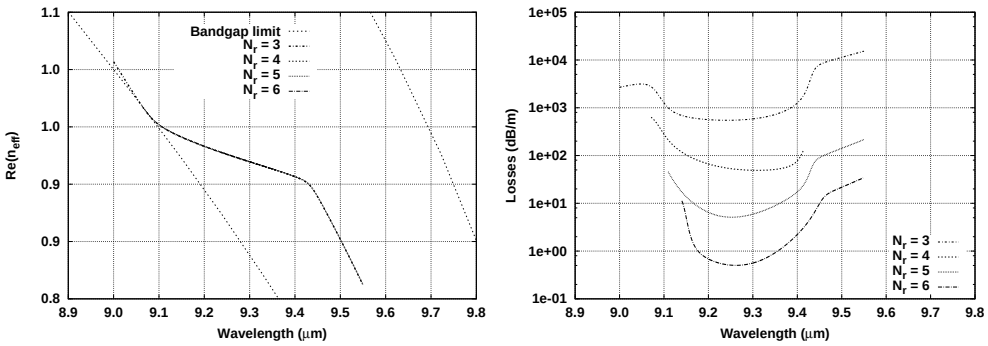

(a) $\Re e(n_{eff})$ (b) $Losses(dB/m)$

FIG. 3.49 – Dispersion curves of the fundamental mode of the PCF for several number of hole rings N_r. $\Lambda = 6.41\,\mu$m, $d = 4.968\,\mu$m. The two thin dashed curves on the left graph represent the boundaries of the main photonic bandgap obtained in Fig. 3.42.

3.4 One detailed example of ARROW MOF to understand their properties

3.4.1 ARROW microstructured optical fibres and its interpretations

This third type of MOFs is similar to the second in the sense that the propagation is made possible in a core with a lower refractive index than the average one of the surrounding region[20]. Nevertheless in the contradistinction to this previous case, the refractive index contrast is reversed : the inclusions have an higher index than the matrix that contains these inclusions and forms the fibre core. To interpret the physical mechanism behind the propagation in the low index core three complementary points of view are useful : the AntiResonant Reflecting Optical Waveguide model (acronym ARROW)[120, 121], the band diagram one, and the analysis based on the avoided crossings of leaky modes. We find again an issue already tackled in section 3.2.1. We had concluded that even if the different simplified models were useful to understand the key properties of the considered structures with much less computational effort, and to bring more physical insights than the *"ab initio"* Maxwell equation problem, they could nevertheless hide some of the properties of the structure.

3.4.2 The ARROW model and its application to MOFs

We briefly presented this model[120] in the previous section to study the influence of the core size diameter on the fundamental mode of an hollow core MOF. In the present section, the high index region is no longer the ring made of the matrix glass but the high index inclusions [122–124]. To propagate a beam in a core made of matrix with a refractive index n_{mat} such that $n_{mat} < n_{cyl}$, the effective index of the mode must fulfill the inequality $n_{eff} < n_{mat}$. If in order to simplify the analysis we consider only grazing beam then $n_{eff} \simeq n_{mat}$. The corresponding mode will leak from the core to the inclusion region when its effective index corresponds to that of the high index inclusions. This phenomenon can occur at the cutoff of the inclusions modes. Consequently, in this first approach, the edges of the transmission bands are defined by the cutoff wavelengths of the high index inclusion modes [123, 125].

It is worth insisting that in the frame of this approach, we actually get the high loss region of the spectrum determined by isolated high index inclusions and not by the lattice of these inclusions. Furthermore, the model gives no clear explanation for the guiding mechanism between these high loss edges.

To illustrate these properties, we chose an ARROW MOF described in reference [123]. It is a one ring C_{6v} MOF with circular inclusions with diameters d equal to 3.315 μm, cylinder refractive index $n_{cyl} = 1.8$, matrix refractive index $n_{mat} = 1.44$, and the pitch Λ being set to 5.64 μm. The dispersion curves and the losses of the fundamental mode (core localized) are given in Fig. 3.50. As can be seen on the right graph, the high losses regions that determine the edges of the transmission bandgaps are nearly the same[21] for several high index inclusion rings N_r and for two values of the pitch Λ. We can note on this figure some irregularities on the dispersion curves and on the losses that will be explained at the end of this section dedicated to ARROW MOFs. In Fig. 3.51 we show the same dispersion curves of the ARROW MOF fundamental mode together with the ones of single high index cylinder, with the same diameter as the one of the MOF, in the same matrix. We can note that the cutoff wavelengths of the single cylinder correspond only approximately to the edges of the transmission band of the ARROW MOF. The exact behaviour will be described after the next subsection. The fact that no modes of the isolated cylinder of the ARROW MOF exists between the edges of the observed transmission band is not sufficient to explain the propagation of the fundamental in the fibre core. To do this we must study the ARROW MOF cladding, this is detailed in the following section.

3.4.3 ARROW MOFs and band diagrams

To take into account the lattice and consequently the coupling between the inclusions, we simply have to compute the band diagram associated with the inclusion region (see Appendix B) [125]. We note

[20] The used average is not the key issue of this assertion.
[21] This assertion will be detailed and slightly modified later.

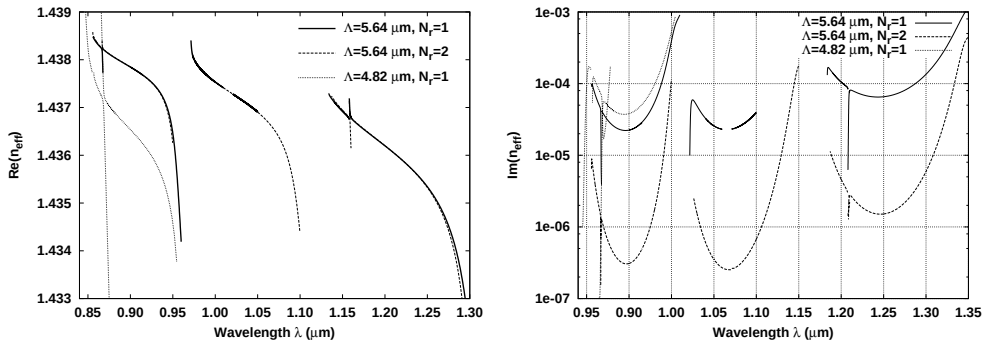

(a) Real part of n_{eff} (b) Imaginary part of n_{eff}

FIG. 3.50 – Real and imaginary parts of the effective index of the fundamental mode of the studied ARROW MOF for several MOFs geometries (see the text of section 3.4.2). For $\Lambda = 5.64\,\mu$m : $N_r = 1, 2$ (thick curves). For $\Lambda = 4.82\,\mu$m : $N_r = 1$ (below $1\,\mu$m thin curve computed on the leftmost part of the two graphs only).

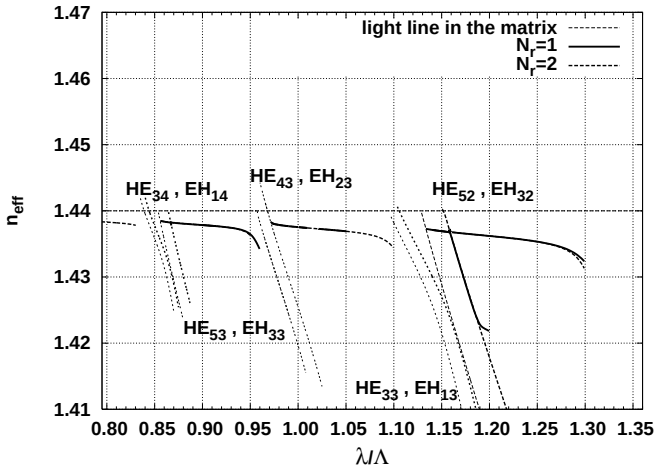

FIG. 3.51 – Real parts of the effective indices of the fundamental mode of the studied ARROW MOF and of several leaky modes of a single high index cylinder with the same diameter in the same matrix as the ones of the ARROW MOF cladding.

that in this case a new parameter is introduced in the model : the lattice pitch Λ which was absent in the ARROW model. As shown by Fig. 3.52 and as expected, the dispersion curves of the fundamental mode are approximately within the bandgap of the band diagram associated with the inclusion region. The long wavelength parts of fundamental mode dispersion curves go beyond the limits of the bandgaps, this may be due to finite size effects. The differences between the dispersion curves obtained for different values of N_r are more important in the long wavelength part of these regions. It is worth mentionning that these parts of the dispersion curves have a more negative slope than the ones in the middle of the bandgaps. Actually, the fundamental core localized mode starts to delocalize towards the cladding region for these wavelengths. We can notice that both the width and the height of the bandgaps, just below the $n_{\text{eff}} = 1$ limit, increase with the wavelength for such structure but the losses of the fundamental mode decrease with the wavelength as can be seen in Fig. 3.50(b) (see also Fig.2 in ref. [123]). This behaviour is different from the one observed for hollow core PCFs.

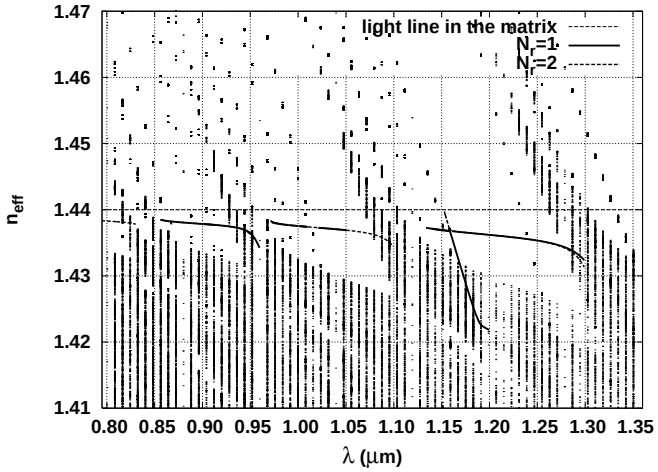

FIG. 3.52 – Real parts of the effective indices of the fundamental mode of the finite studied ARROW MOF (for $N_r = 1, 2$) together with the band diagram corresponding to the elementary cell of the ARROW MOF cladding. The modes of the periodic structures are computed for discrete values of the wavelength. They appear as dots forming either a continuum or isolated spots for each wavelength. Some regions do not contain any mode of the periodic structure : they represent the bandgaps.

3.4.4 ARROW MOFs and avoided crossings

In the two previous subsection, we have described two models that help to understand the main properties of ARROW MOFs. Nevertheless, some of these properties are not given by the models. Actually, as can be seen in Fig. 3.50(a), the dispersion curve of the fundamental mode show several discontinuities. One such discontinuity is shown more clearly in Fig. 3.53. These observed discontinuities are not computational artefacts since we obtain them with two fully different modal methods (see chapter 2). We can also notice that the discontinuities occur at the same wavelengths for the one ring MOF ($N_r = 1$) and the two ring MOF ($N_r = 2$).

Figure 3.54 shows the z-component of the Poynting vector modulus for several increasing wavelengths around the observed transition in the core mode dispersion curve shown in Fig. 3.53. We clearly see that the core mode undergoes a spatial transition from the core fibre to the high-index inclusions. In the present case, we can note that this transition is abrupt, the typical wavelength scale being approximately 1.0 10^{-3} μm. In the vicinity of the transition wavelength and for neighbouring values of the effective index real part, one can check that there are no guided modes of a single high index cylinder in a infinite matrix undergoing a cut-off[1]. Nevertheless, it is possible to find leaky modes for such an isolated cylinder *i.e.*, mode with a non null effective index imaginary part.

Consequently, we can analyze the core mode transition associated with the observed discontinuities in Fig. 3.53 as an avoided crossing between the ARROW MOF core localized leaky mode and a defect

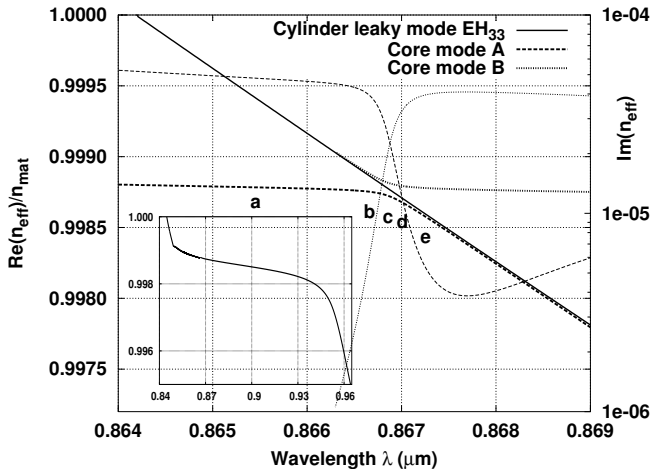

FIG. 3.53 – Normalized real part of the effective index, $\Re e(n_{\text{eff}})$, of the ARROW MOF core mode versus the wavelength around the transition. The asymptot for the core mode curves A and B is the real part of n_{eff} for a leaky mode of one isolated high index cylinder. The imaginary part, $\Im m(n_{\text{eff}})$, of the core modes A and B is also given (thin curves, right y-scale). Inset : overall view of the dispersion curve (without the discontinuities) in the corresponding transmission band.

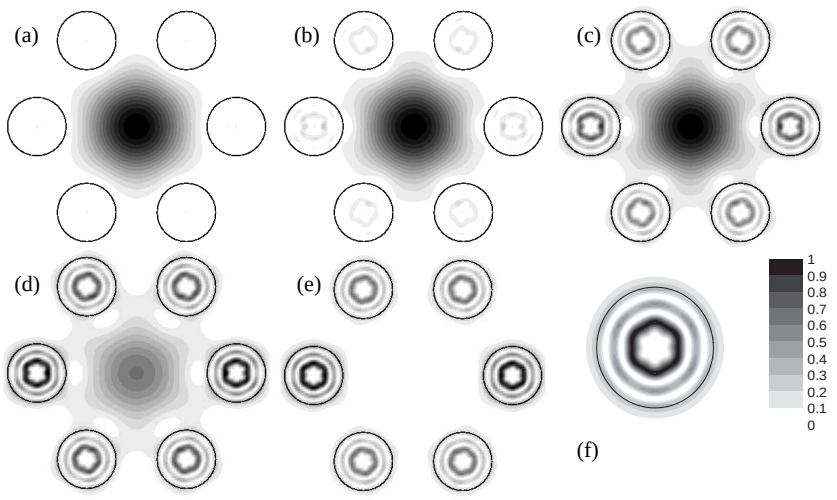

FIG. 3.54 – Modulus distribution of the z-component of the Poynting vector across the transition of core mode A. (a) λ=0.8654 μm, (b) λ=0.8666 μm, (c) λ=0.8668 μm, (d) λ=0.8669 μm, (e) λ=0.8672 μm (see Fig. 3.53 for their respective positions in the $\Re e(n_{\text{eff}})(\lambda)$ dispersion curve), (f) Modulus distribution of the z-component of the Poynting vector for the leaky mode EH_{33} of an isolated high-index inclusion (border shown by the black circle), n_{eff}= 1.438142 + i 9.121 10^{-7} and λ=0.867μm.

leaky mode generated by the set of high-index cylinders.

Some general properties of avoided crossings in ARROW MOFs

Avoided crossings between defect and core modes have already been oberved and studied in Bragg MOFs [126] or in hollow core band-gap MOFs [118]. Since the observed defect modes are linked to the isolated cylinder leaky modes, the avoided crossings will occur in ARROW MOFs whatever the cylinder optogeometrical parameters are (including the ones associated with the single guided mode regime). We can also note that both the observed avoided crossings with the isolated cylinder leaky modes and the behaviour of the core modes in ARROW band gap lower edges (short wavelength) are similar phenomena : a structure core mode transition induced by the coupling with the existing leaky modes of the confining elements *i.e.* the high refractive index cylinders. To illustrate these properties, we give in Fig. 3.55 the dispersion curves showing two other avoided crossings, one associated with the isolated cylinder leaky mode HE_{53} and another one associated with the EH_{14} cylinder leaky mode.

The dispersion curves concerning the lower transition of the core mode is associated with the avoided crossing with the isolated cylinder leaky mode EH_{14}. The EH_{14} leaky mode has much higher losses than the two others leaky modes (HE_{53} and EH_{33}) below the common cut-off limit given by the matrix refractive index. For the upper edges (long wavelength) of ARROW band gaps (see as an example the

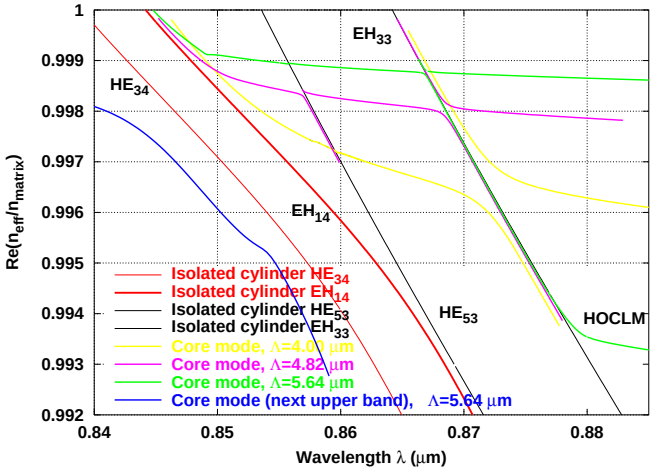

FIG. 3.55 – Avoided crossings between the structure core mode and leaky modes of high refractive index cylinder (EH_{14}, HE_{53}, EH_{33}) ; the cylinder parameters and the refractive indices are the same as the ones used previously. Dispersion curves for two smaller values of the pitch Λ are also given. HOCLM means higher order core localized mode.

leftmost curve entitled *Core mode (next upper band)* in Fig. 3.55), we observe that the involved modes in the avoided crossings are usually multiple cylinder leaky modes coming from the coupling between some modes of the isolated high refractive index cylinders. Such modes are more clearly defined on ARROW MOFs with several rings of high index inclusions since the proportion of cylinders on the external border decreases which induces an increase of the homogeneity of the pertubative coupling terms.

In order to quantify the avoided crossing properties we introduce the quantity $\mathcal{R} = \partial^2 \Re e(n_{eff})/\partial\lambda^2$. As can be seen in Fig. 3.55 and more precisely in Fig. 3.56, the spectral sharpness of the transition decreases with the pitch for a fixed d value (even if a factor $1/\Lambda^2$ is taken into account to compensate for the core size change). In the same way, the strength of the transition (quantified by $max(|\mathcal{R}|)$) decreases with the pitch. The product of the two quantities stays nearly constant in the studied range of parameters. These properties can be explained as follows in terms of coupling between the high refractive index cylinder modes and the core localized mode : a decrease of the pitch induces a stronger coupling between these modes, and consequently the coupling spreads over a greater spectral range and its maximum intensity decreases. This kind of behaviour for the modal interaction is similar to the one already described by Engeness *et al.*[126] in Bragg MOF. We have also studied the influence of the refractive index contrast

on the transition (see Fig. 3.56), and as expected, a contrast decrease induces a decrease of its strength and an increase of its relative spectral range. In Bragg MOF avoided crossings may occur for all the core

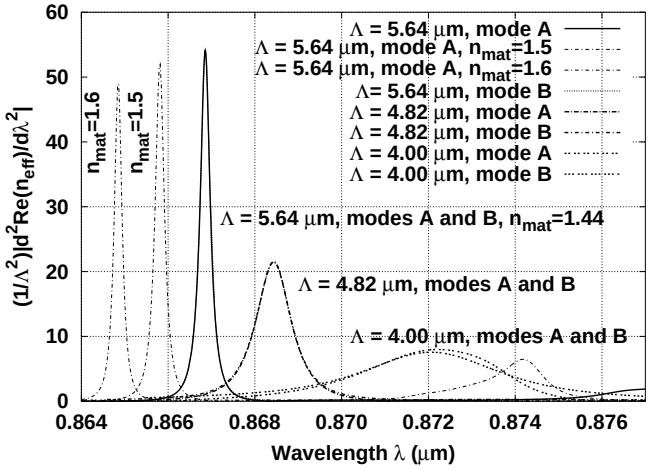

FIG. 3.56 – $|\mathcal{R}|/\Lambda^2$ (as defined in the text) versus the wavelength for core modes A and B for three pitch values around the avoided crossing with leaky mode EH_{33} (d is kept constant). The influence of the refractive index contrast is also given. The curves for n_{mat}= 1.5 and 1.6 have been translated along the x-axis to make them visible.

modes that have the same azimuthal symmetry and polarization as the defect mode[126]. Consequently, some symmetry selection rules may be applied to select the avoided crossings. On the contrary, in AR-ROW MOFs since the modes are expressed as a Fourier-Bessel series a single azimuthal number of the mode is not defined[6] therefore one can't expect the kind of selection rules mentionned above (other selection rules exist due to the fibre C_{6v} symmetry).

3.5 Conclusion

In this Chapter, we have explained some of the main properties of solid and hollow core MOFs even though only linear phenomena were considered. The single-mode property of solid core MOF is now clearly defined, together with their operation regimes. We have focused on MOF based on subsets of triangular lattices but other kind of structures can be studied based on honeycomb [127] or square [128] lattices nevertheless the qualitative conclusions drawn in this chapter should applied for these structures. We have considered circular inclusions but elliptical inclusions [52, 129] or inclusions with even more complicated shapes could in principle be studied with the Multipole Method as long as these inclusions can be included in non overlapping circles, or with the differential method in more general cases. These specific properties of MOFs with a solid or an hollow core have made these fibres truly useful for several applications like supercontinuum generation[54, 88, 130–135], sensing[136, 137], fibre laser[138–141], high power or infrared waveguides[142, 143].

Conclusion

Je pense que la terminologie "*nouveaux guides d'onde*" pour désigner les fibres optiques microstructurées est complétement justifée même si les modes à pertes que l'on rencontre si souvent dans ces dernières étaient déjà présents dans les fibres conventionnelles. Mais ils étaient alors peu étudiés, sauf dans les fibres à profil en W, du fait de leur non utilité pratique.

Ces nouvelles fibres changent le nombre de dimensions de l'espace des paramètres caractérisant le guide d'onde et donc augmentent de manière considérable les caractéristiques possibles des propriétés du guidage (c'est ce qui permet notamment d'obtenir la propagation "*infiniment*" monomode des fibres optiques microstructurées à cœur plein). Nous pouvons désormais accéder à des contrastes d'indices de plus de 50 % avec les fibres air/silice et de 200 % avec les fibres air/verres de chalcogénures au lieu de moins de 1% dans les fibres conventionnelles. Nous avons aussi la possibilité de jouer sur le profil géométrique de la section du guide, via les inclusions, et non plus uniquement sur le diamètre du cœur et sur la couche qui l'entoure comme dans les fibres à profil en W.

La contrepartie de cette grande variété des structures possibles est qu'il faut disposer d'outils de simulation numérique performants afin d'obtenir et d'étudier les propriétés physiques de ces fibres optiques microstructurées. J'ai co-développé deux méthodes rigoureuses de type vectorielle au cours des huit dernières années (la méthode multipolaire et la méthode différentielle avec factorisation rapide de Fourier en tant que méthode modale), et j'en maîtrise complétement une troisième (la méthode de type élements finis appliquée à la recherche des modes que cela soit en configuration scalaire ou en vectorielle, pour des structures finies ou périodiques). Avec pour chacune des trois méthodes, des programmes sources modifiables en fonction des nouveaux besoins qui se présentent.

Les caractériques remarquables du guidage de la lumière par ces fibres optiques microstructurées font qu'elles sont utilisées dans de nombreuses applications : génération de supercontinuum, guidage de laser de puissance, laser fibré, capteurs, compensation de dispersion chromatique, ….. Tous ces dévelopements théoriques et expérimentaux ont eu lieu en douze ans, ce qui est remarquable et ont déjà donné lieu indirectement à un prix Nobel de Physique, celui de 2005[22].

De nouvelles structures de fibres microstructurées ont déjà été proposées pour élargir encore la maîtrise du guidage en leur sein. Il s'agit de fibres où les inclusions sont recouvertes d'une couche métallique. Ceci entraîne alors qu'en plus des propriétés usuelles on peut éventuellement avoir de nouveaux phénomènes comme les plasmons qui entrent en jeu pour modifier les propriétés des fibres. Par ailleurs, les progrès réalisés dans la fabrication des fibres microstructurées en verres de haut indice ayant des coefficients nonlinéaires de 100 à 1000 fois plus élevés que celui de la silice sont désormais suffisants pour affirmer que de telles fibres vont pouvoir être utilisées pour l'optique nonlinéaire. A la vue de ces deux constatations, je compte bien poursuivre mes recherches dans le domaine des fibres optiques microstructurées en développant les outils numériques nécessaires et en étudiant leurs propriétés linéaires et nonlinéaires. J'ai déjà publié très récemment quelques travaux exploratoires concernant l'effet Kerr optique.

[22] Le prix Nobel de physique 2005 a été attribué (la moitié du prix) à John L. Hall et à Theodor W. Hänsch "for their contributions to the development of laser-based precision spectroscopy, including the optical frequency comb technique". L'autre partie a été attribué à Roy J. Glauber "for his contribution to the quantum theory of optical coherence".

Deuxième partie

Sélection d’articles

On trouvera dans cette partie une sélection d’articles dont le contenu est soit partiellement décrit dans ce mémoire soit absent de ce dernier.

Table des matières

Microstructured optical fibers: where's the edge?

Boris T. Kuhlmey

School of Physics, University of Sydney, NSW 2006, Australia
and Institut Fresnel, Unité Mixte de Recherche du Centre National pour la Recherche Scientifique 6133, Faculté des Sciences et Techniques de St Jérôme, 13397 Marseille Cedex 20, France
borisk@physics.usyd.edu.au

Ross C. McPhedran, C. Martijn de Sterke and Peter A. Robinson

School of Physics, University of Sydney, NSW 2006, Australia
ross@physics.usyd.edu.au, desterke@physics.usyd.edu.au, p.robinson@physics.usyd.edu.au

Gilles Renversez and Daniel Maystre

Institut Fresnel, Unité Mixte de Recherche du Centre National pour la Recherche Scientifique 6133, Faculté des Sciences et Techniques de St Jérôme, 13397 Marseille Cedex 20, France
gilles.renversez@fresnel.fr, daniel.maystre@fresnel.fr

Abstract: We establish that Microstructured Optical Fibers (MOFs) have a fundamental mode cutoff, marking the transition between modal confinement and non-confinement, and give insight into the nature of this transition through two asymptotic models that provide a mapping to conventional fibers. A small parameter space region where neither of these asymptotic models holds exists for the fundamental mode but not for the second mode; we show that designs exploiting unique MOF characteristics tend to concentrate in this preferred region.

OCIS codes: (060.2430) Fibers, single-mode; (060.2270) Fiber characterization; (060.2280) Fiber design and fabrication; (230.3990) Microstructure devices

References and Links

1. R. F. Cregan, B. J. Mangan, J. C. Knight, T. A. Birks, P.S. Russel, P. J. Roberts, D. C. Allan, "Single-mode photonic band gap guidance of light in air," Science **285**, 1537-1539 (1999).
2. T. M. Monro, D. J. Richardson, N. G. R. Broderick, P. J. Bennett, "Holey optical fibers: An efficient modal model," J. Lightwave Technol. **17**, 1093-1102 (1999).
3. J. K. Ranka, R. S. Windeler, A. J. Stentz, "Visible continuum generation in air-silica microstructure optical fibers with anomalous dispersion at 800 nm," Opt. Lett. **25**, 25-27 (2000).
4. A. Ferrando, E. Silvestre, J. J. Miret, P. Andrés, "Nearly zero ultraflattened dispersion in photonic crystal fibers," Opt. Lett. **25**, 790-792 (2000).
5. J. C. Knight, J. Arriaga, T. A. Birks, A. Ortigosa-Blanch, W. J. Wadsworth, P. S. Russell, "Anomalous dispersion in photonic crystal fiber," IEEE Photonic Tech. Lett. **12**, 807-809 (2000).
6. W. H. Reeves, J. C. Knight, P. St. J. Russell,"Demonstration of ultra-flattened dispersion in photonic crystal fibers," Opt. Express **10**, 609-613 (2002), http://www.opticsexpress.org/abstract.cfm?URI=OPEX-10-14-609.
7. B. Kuhlmey, G. Renversez, D. Maystre, "Chromatic dispersion and losses of microstructured optical fibers," Appl. Optics OT, in press.
8. T. A. Birks, J. C. Knight, P. St. Russell, "Endlessly single-mode photonic crystal fiber," Opt. Lett. **22**, 961-963 (1997).
9. J. C. Knight, T. A. Birks, R. F. Cregan, P. St. Russell, J. P. de Sandro, "Large mode area photonic crystal fibre," Electron. Lett. **34**, 1347-1348 (1998).
10. R. Holzwarth, M. Zimmermann, Th. Udem, T. W. Hänsch, P. Russbüldt, K. Gäbel, R. Poprawe, J. C. Knight, W. J. Wadsworth, P. St. J. Russell, "White-light frequency comb generation with a diode-pumped Cr:LiSAF laser," Opt. Lett. **26**, 1376-1378 (2001)

#1676 - $15.00 US Received September 28, 2002; Revised October 25, 2002

11. A. V. Husakou, J. Herrmann, "Supercontinuum Generation of Higher-Order Solitons by Fission in Photonic Crystal Fibers," Phys. Rev. Lett. **87**, 203901 (2001).
12. J. P. Dudley, L. Provino, N. Grossard, H. Maillotte, R. S. Windeler B. J. Eggleton, S. Coen, "Supercontinuum generation in air–silica microstructured fibers with nanosecond and femtosecond pulse pumping," J. Opt. Soc. Am. B **19**, 765-771 (2002).
13. T. P. White, B. T. Kuhlmey, R. C. McPhedran, D. Maystre, G. Renversez, C. M. de Sterke, L. C. Botten, "Multipole method for microstructured optical fibers. I. Formulation," J. Opt. Soc. Am. B **19**, 2322-2330 (2002).
14. B. T. Kuhlmey, T. P. White, R. C. McPhedran, D. Maystre, G. Renversez, C. M. de Sterke, L. C. Botten, "Multipole method for microstructured optical fibers. II. Implementation and results," J. Opt. Soc. Am. B **19**, 2331-2340 (2002).
15. T. P. White, R. C. McPhedran, C. M. de Sterke, M. J. Steel, "Confinement losses in microstructured optical fibers," Opt. Lett. **26**, 1660-1662 (2001).
16. N. A. Mortensen, "Effective area of photonic crystal fibers," Opt. Express **10**, 341-348 (2002), http://www.opticsexpress.org/abstract.cfm?URI=OPEX-10-7-341.
17. B. T. Kuhlmey, R. C. McPhedran, C. M. de Sterke, "Modal 'cutoff' in Microstructured Optical Fibers," Opt. Lett. **27**, 1684-1686 (2002).
18. G. W. Milton, *The Theory of Composites* (Cambridge University Press, 2002).
19. A. W. Snyder, J. D. Love, *Optical Waveguide Theory* (Chapman & Hall, London, 1996).
20. J. C. Knight, T. A. Birks, P. St. Russell, J. P. de Sandro, "Properties of photonic crystal fiber and the effective index model," J. Opt. Soc. Am. B **15**, 748-752 (1998).
21. F. Brechet, J. Marcou, D. Pagnoux, P. Roy, "Complete analysis of the characteristics of propagation into photonic crystal fibers, by the finite element method," Opt. Fiber Technol. **6**, 181-191 (2000).
22. T. Monro, P. J. Bennett, N. G. Broderick, D. J. Richardson, "Holey fibers with random cladding distributions," Opt. Lett. **25**, 206-208 (2000).

Microstructured Optical Fibers (MOFs) have received considerable attention since pioneering work demonstrated some of their remarkable properties, such as guidance in hollow cores [1], unprecedented dispersion characteristics [2-7], "endlessly" single-modedness [8], and the support of modes with extremely low or high effective area [2,9]. These unique properties have far-reaching consequences in fundamental and applied areas as diverse as frequency comb generation [10], supercontinuum generation [3,11,12] and dispersion management [5].

One of the most important MOF configurations consists of a silica fiber with a solid core surrounded by a silica cladding pierced by rings of air holes, that are typically hexagonally packed (Fig. 1, lower right inset). These holes can be thought of as acting to depress the average cladding refractive index, so that light escaping the core has to tunnel through an equivalent low-index layer. An intriguing difference between such MOFs and conventional fibers is associated with the distinction between guided and non-guided modes. In conventional fibers the distinction is clear-cut: guided modes are lossless and thus have real propagation constants β, related to a real effective index n_{eff} by $n_{\mathrm{eff}}= \beta/k_0 =2\pi\beta/\lambda$, where λ and k_0 are the light's wavelength and vacuum wavenumber, respectively. For non-guided modes β and n_{eff} are complex, where the imaginary part of n_{eff} is linearly related to the loss coefficient at fixed wavelength. In MOFs with a finite number N_r of rings of confining holes, all modes can tunnel through the confinement region to some extent and are consequently lossy; thus all modes have complex values of β and n_{eff} [13-15].

In two recent papers [16,17] criteria were established for recognizing the transition of the second mode[1] from being unconfined to confined, which we identify with cutoff. Mortensen [16] used the rapid decrease in the mode's effective area at the transition, whereas Kuhlmey *et al.* [17] used effective area and four other criteria to pinpoint the transition. Curve 3 in Fig. 1 shows the locus of the transition of the second mode as a function of wavelength normalized to hole spacing Λ, for MOFs of various hole diameters d in silica. Note that this curve crosses the horizontal axis at d/Λ=0.406. Though the transition is gradual for MOFs with only a few rings of air holes, it becomes sharper when the number of air holes increases [17].

[1] The second mode is defined as the mode having, for a given fiber geometry, the second largest real part of n_{eff}. It usually has the second lowest loss, and its field distribution is similar to the TE_1 mode of conventional fibers.

#1676 - $15.00 US Received September 28, 2002; Revised October 25, 2002

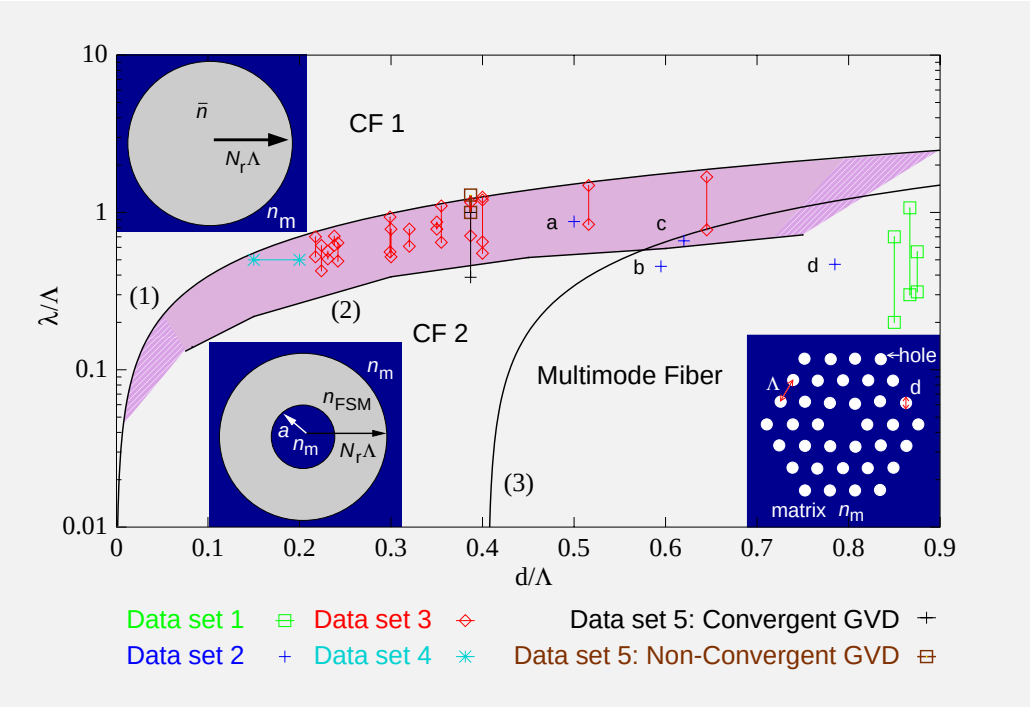

Fig. 1. Operation regimes of MOFs. Lower right inset: cross section of a MOF with 3 rings of holes. Other insets: asymptotic models for large (CF1) and small (CF2) wavelengths. The shaded transition region represents the parameter subspace where MOFs cannot be described by either asymptotic model and therefore behave most unlike conventional optical fibers. Data sets are described in the text.

Using the same criteria as in [17], it appears that the fundamental mode[2] also undergoes a cutoff transition between confined and non-confined states. For long wavelengths, the fundamental mode fills the entire fiber cross-section, whereas for small wavelength it becomes confined in the core. However, instead of having the sharp transition between those states exhibited by the second mode, the transition is characterized by two loci, with a transition region of finite width in between. This was established for structures of up to N_r=10 rings of holes, with conclusions for larger structures following by extrapolation . Above the highest of these loci [curve (1)], in the region denoted by CF1, the fundamental mode fills the entire fiber cross section, and its properties can be accurately predicted on the basis of a conventional fiber model (CF1, using the same symbol for the model and the region of parameter space in which it is valid) that we describe below. Below the second locus [curve (2)], in the region denoted by CF2, the fundamental mode is tightly confined in the core, with its properties given by a second conventional fiber model (CF2). In the transition region between CF1 and CF2, the fundamental mode changes its character and its behavior is thus not only sensitive to the MOF design (*i.e.*, to d/Λ and N_r), but is also unlike that of the modes of conventional fibers. We stress that, as we decrease the wavelength from large values, the fiber at first shows no localized modes (region CF1), but that one of its extended modes undergoes a smooth transition to emerge as a localized mode in region CF2.

We established the mode boundaries of Fig. 1 using a multipole method [13,14], which can calculate MOF modes and their losses accurately over a wide parameter range. We studied the comportment of MOFs at the telecommunications wavelength of λ=1.55 μm, and varied the hole spacing Λ, while keeping the hole diameter to spacing ratio d/Λ constant. The

[2] The fundamental mode is defined as the mode having, for a given fiber geometry, the largest real part of n_{eff}. It is the mode with the lowest losses and for the fibers studied here is doubly degenerate. It is most similar in terms of field distribution to the $HE_{1,1}$ mode of conventional fibers.

#1676 - $15.00 US Received September 28, 2002; Revised October 25, 2002

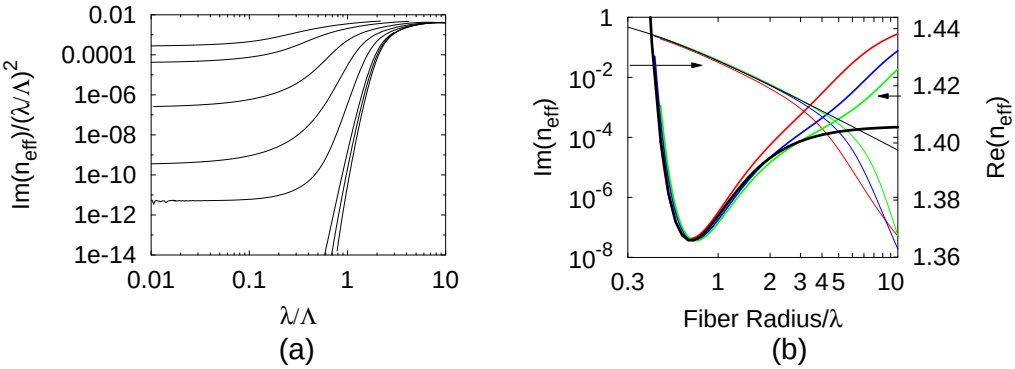

Fig. 2. **A**: Imaginary part of n_{eff} as a function of wavelength on pitch, rescaled by $(\lambda/\Lambda)^2$, for a silica structure with 3 layers of holes, with d/Λ taking the values 0.075 (top curve), 0.15, 0.3, 0.45, 0.6, 0.75, 0.8 and 0.85. **B**: Imaginary (thin curves) and real (thick curves) part of n_{eff} as a function of fiber radius $N_r\Lambda$ divided by λ for MOFs with d/Λ=0.3, for 4 (red), 6 (blue) and 8 (green) rings of holes, and for the corresponding homogenized fiber (black). All calculations in this report were done for varying pitch at fixed λ=1.55μm, where the losses in dB/m are given by $3.52\text{x}10^7\text{Im}(n_{eff})$.

MOFs were taken to consist of air holes (refractive index unity) in a matrix with refractive index n_m=1.44402362. For given d/Λ, we studied the variation of the loss [Im(n_{eff})] as a function of normalized wavelength λ/Λ. At small λ/Λ, the loss increases gently, before rising very steeply in the transition region, and then increasing slowly once again in the second conventional fiber region (see Fig. 2.A). To locate the boundaries of regions accurately, we used the second derivative of the log-log plot of the losses, a function which peaks at the boundaries between regions [17]. Carrying out this procedure for various hole diameters, we established the two boundary curves for the fundamental mode, shown for the first time in Fig. 1. These curves tend to approach one another for decreasing hole size, and reach λ=0 for hole sizes d/Λ somewhere between 0 and 0.06 inclusive. Counting only modes confined to the core, MOFs in silica can be said to be "endlessly" single-moded in the region below the CF1 area of Fig. 1, and to the left of d/Λ = 0.406, where the second mode boundary drops to zero [17]. This observation corroborates and somewhat sharpens the prediction of endless single mode behavior made by Birks *et al.* [8].

In the CF1 region of Fig.1, the fundamental mode fills the entire confining region. Its behavior is modeled accurately by using homogenization arguments [18] to establish effective dielectric constants and thereby refractive indices for the cladding region. Homogenization theory predicts an effective dielectric constant given by the mean of the dielectric constants of air and silica for the electric field parallel to the fiber axis. In contrast, for small d/Λ the Maxwell-Garnett formula can be used to derive effective constants for the transverse electric field component [18]. With f being the air filling fraction of the fiber we have:

$$\bar{n}_z = \left[f\, n_{air}^2 + (1-f)\, n_m^2\right]^{1/2}, \qquad \text{(Extraordinary index)} \qquad (1)$$

$$\bar{n}_\perp \cong n_m\left[(T-f)/(T+f)\right]^{1/2}, \qquad \text{(Ordinary index)} \qquad (2)$$

$$\text{where } T = (n_m^2 + n_{air}^2)/(n_m^2 - n_{air}^2).$$

The effective modal index is then calculated using the theory [19] of propagation in an optical fiber with core of radius $N_r\Lambda$ constituting a uniaxial material, and a silica jacket. Fig. 2.B shows the real and imaginary parts of the effective index of a MOF for different numbers of rings as a function of the fiber size $N_r\Lambda$ and the results given by the homogenized model outlined above. The agreement is excellent for $\lambda/\Lambda \geq 0.5$. Thus in this regime the mode properties remarkably only depend on the total fiber size $N_r\Lambda$, regardless of N_r. MOF modes

#1676 - $15.00 US Received September 28, 2002; Revised October 25, 2002

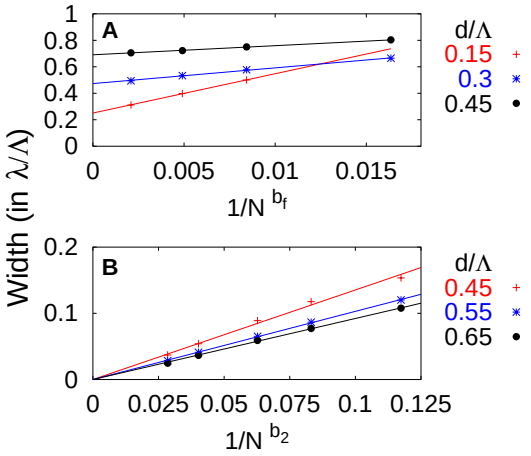

Figure 3: Width of the transition between the large wavelength asymptotic regime (CF1) and the intermediate regime as a function of N_r^{-b}, for the fundamental mode (A, $b_f \approx 2.97$) and the second mode (B, $b_2 \approx 1.55$). For the second mode the width of the intermediate regime tends to zero with increasing number of rings, whereas a finite transition region remains for the fundamental mode, even for $N_r \to \infty$.

tend to be quite lossy here, since the effective indices in the core region are smaller than n_m. Note that the losses do decrease as the number N_r of layers of confining air holes increases, but do so following a power law. Consequently, N_r generally has to be impractically large to generate MOFs with sufficiently low loss for technological applications, and key quantities like the modal dispersion depend sensitively on N_r, even when this number is large. Therefore, practical applications of MOFs are unlikely for designs in the CF1 region of Fig. 1.

For short wavelengths, MOFs have already been successfully modeled by several authors as step index fibers with varying cladding index [5,8,11,12,20,21]. In the model CF2 shown in Fig. 1 the refractive index of the cladding is given by the effective index of the fundamental space-filling mode (FSM) [8]. Best agreement was found for a core radius of approximately $a=0.64\Lambda$ [21]. Based on an asymptotic analysis of this model, it appears that at short wavelengths n_{FSM} can be approximated by

$$n_{FSM} = n_m - n_2(\lambda/\Lambda)^2 \qquad (3)$$

where n_2 can be obtained from a transcendental equation derived from the framework established by Birks *et al.* [8]. It is then readily shown that the imaginary part of the effective index varies as $(\lambda/\Lambda)^2$ for a fixed number N_r of rings of air holes, and decays exponentially with N_r at fixed $k_0\Lambda$, as expected for tunneling losses. Fig. 2.A shows the imaginary part of n_{eff} divided by $(\lambda/\Lambda)^2$ as a function of λ/Λ, for several d/Λ ratios. The curves tend to a constant for approximately $\lambda/\Lambda \leq 0.3$, indicating clearly that the asymptotic dependence becomes valid for reasonable wavelength to pitch ratios. In this regime, and contrary to the behavior in the CF1 regime, the real part of n_{eff}, and derived characteristics such as modal dispersion converge with increasing N_r.[3]

It is thus clear that the region CF2 of Fig. 1 is appropriate for practical MOF designs: Confinement of the fundamental mode improves exponentially as more rings are added, and characteristics such as modal dispersion converge with an increasing number of rings. However, the further the CF2 region is penetrated, the closer the analogy becomes between the MOF and conventional fibers. Thus, the new design possibilities offered by MOFs are essentially available only in the transition region and its border with the region CF2.

[3] Note that n_{FSM} also has importance in relation to the boundary of CF1, which appears to occur when $n_{eff} = n_{FSM}$.

#1676 - $15.00 US Received September 28, 2002; Revised October 25, 2002

As mentioned earlier, the sharpness of the transition region with increasing N_r evolves differently for the fundamental and the second mode. This is illustrated in Fig. 3, where we plot the width of the transition region (more precisely the width of the peak of the second derivatives of the curves in Fig. 1.A) versus $1/N_r^b$, where b is adjusted to give the best straight-line behavior of all datasets in each frame. As the number of confining rings N_r increases, the width of the transition region tends to zero for the second mode (Fig. 3.B), whereas for the fundamental mode this width remains finite (Fig. 3.A). Thus, in an infinite system, the transition region for the second mode disappears, whereas for the fundamental mode there is always a parameter region in which this mode behaves fundamentally differently than the modes of a conventional fiber. Note the linearity of the data for different hole diameters in Fig. 3, showing that the power law exponents for both modes are independent of d/Λ.

The points in Fig. 1 indicate experimental and theoretical data from recent publications of MOF designs with unconventional properties. The first data set concerns MOFs used experimentally for supercontinuum generation, taken from Refs. [3,11-12]. They all lie in the CF2 regime, and indeed the key property for supercontinuum generation – highly shifted zero dispersion wavelength and small core size – can be delivered by the CF2 model, already known to be successful for such MOFs [11,12]. Data set 2 shows the location of experimental zero-dispersion wavelength measures, which were compared to theoretical values from a CF2 model in the original publication [5]. For the two lower points (b and d) which lie in the CF2 region, comparison with the CF2 model gave good agreement, for point c agreement was approximate and for point a, lying in the transition region, the agreement was unsatisfactory.

The third data set consists of regions of observed or predicted flat or oscillating dispersion, taken from Refs. [2,4,6,7,21]. All data points herein are located exactly in the transition region, using the increased and highly configurable wavelength dependence of structural dispersion to compensate material dispersion. The consequences of being in the transition region, and therefore close to cutoff, are that confinement losses are highly wavelength dependent, and that the waveguide dispersion is sensitive to the actual fiber geometry. Such high sensitivity to structural imperfections was observed by Monro *et al.* [22], and indeed the fiber parameters used by these authors are in the transition region (data line 4).

In studying the influence of the number of rings on dispersion [7], we observed that the dispersion does not necessarily converge with the ring number. Data set 5 shows the location of an example where the dispersion converges with N_r in a limited wavelength range before diverging with N_r. The divergent wavelength range crosses the transition line from the intermediate to the homogenized regime CF1, where we have seen N_r dictates mode properties.

Although we tried to map as many published MOF designs as possible onto Fig. 1, a few were omitted: some were overlapping the transition region and the CF2 region and had more conventional dispersion properties, while others were beyond the scope of this study (*e.g.* grossly non-circular holes). One theoretical study by Monro *et al.* [2] had two examples of MOFs lying in the CF1 region, with both displaying conventional dispersion. It should be emphasized that no experimental MOF has been published with parameters in the CF1 region.

In conclusion, we find that the fundamental MOF mode exhibits a transition between being confined around the core region, and filling the entire (finite) fiber cross-section. Thereby, we have shown that MOFs have an edge in the sense of offering modal characteristics unlike those achievable with conventional fibers when operated in the transition region, shown in Fig. 1. They may deliver useful (albeit conventional) design characteristics in the region CF2, but are unlikely to deliver low-loss and stable secondary characteristics such as dispersion in the region CF1. We have shown that these theoretical insights are in keeping with successful MOF designs from the literature, and we are confident they will prove useful in guiding further innovative applications of this exciting new class of optical fiber.

#1676 - $15.00 US Received September 28, 2002; Revised October 25, 2002

Chromatic dispersion and losses of microstructured optical fibers

Boris Kuhlmey, Gilles Renversez, and Daniel Maystre

Using a rigorous and vector multipole method, we compute both losses and dispersion properties of microstructured optical fibers with finite cross sections. We restrict our study to triangular lattices of air-hole inclusions in a silica matrix, taking into account material dispersion. The fiber core is modeled by a missing inclusion. The influence of pitch, hole diameter, and number of hole rings on chromatic dispersion is described, and physical insights are given to explain the behavior observed. It is shown that flattened dispersion curves obtained for certain microstructured fiber configurations are unsuitable for applications because of the fibers' high losses and that they cannot be improved by a simple increase of the number of air-hole rings. © 2003 Optical Society of America

OCIS codes: 060.2270, 060.2280, 060.2400, 060.2430.

1. Introduction and Background

Microstructured optical fibers (MOFs) are generally made from regular lattices of cylindrical inclusions, for example, air holes, in a dielectric matrix. MOF cores usually consist of a defect of the lattice, which can be an inclusion of a different type or size or, in bulk core MOFs, a missing inclusion. In recent publications,[1,2] attention was drawn to the peculiar and interesting dispersion properties that MOFs can exhibit and that indicate that MOFs may be good candidates for dispersion management in optical communication systems. In this paper we use a fully vector and rigorous multipole method[3,4] that was recently developed by the present authors and by Mc Phedran and Botten[5] in Sydney to explore the dependence of chromatic dispersion on wavelength and MOF geometry. We concentrate here on a silica bulk core MOF with a triangular lattice of air holes (see Fig. 1). The most important point in which the research reported here contrasts with that on MOF dispersion published previously is that the multipole method described herein is able to deal with finite cross-section MOFs. We could therefore study the influence of the extent of the confining air-hole region on dispersion and on its associated losses.

Our multipole method is a standard multipole method extended to conical mounts. It is based on local expansions of the vector fields in Fourier Bessel series and uses addition theorems to link these local expansions. Boundary conditions are implemented analytically for circular inclusions, so the only approximations are the truncation of the Fourier Bessel series (see Refs. 4 and 6 for a complete study) as well as the fundamental hypothesis of the invariance of the fiber along its axis. If the inclusions overlap, our method is not appropriate. With the MOF geometry and the wavelength as inputs, the method gives the modes of the MOF as an output. Material dispersion can thus be included in a natural way in the MOF geometry, for example by use of Sellmeier expansions.[7,8]

A mode of a MOF is characterized by its field pattern and propagation constant β (or, equivalently, by its effective index $n_{\mathrm{eff}} = \beta/k_0$, where k_0 is the free-space wave number). Because of the losses that result from the finite transverse extent of the confining structure, the effective index is a complex value; its imaginary part $\Im(n_{\mathrm{eff}})$ is related to the losses $\mathcal{L}$ in decibels per meter through the relation

$$\mathcal{L} = \frac{20}{\ln(10)} \frac{2\pi}{\lambda} \Im(n_{\mathrm{eff}}) \times 10^6, \qquad (1)$$

When this research was performed the authors were with the Institut Fresnel, Unité Mixte de Recherche 6133, Centre National de la Recherche Scientifique, Faculté des Sciences et Techniques de St Jérôme, Avenue Escadrille Normandie-Niémen, 13397 Marseille Cedex 20, France. B. Kuhlmey is now with the School of Physics, University of Sydney, Sydney, NSW 2006, Australia. G. Renversez's e-mail address is gilles.renversez@fresnel.fr.

Received 26 July 2002.
0003-6935/03/040634-06$15.00/0

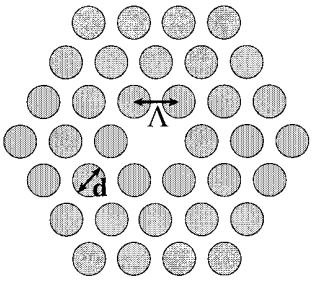

Fig. 1. Cross section of the model MOF with three rings of holes (the holes are shown colored gray); $N_r = 3$. Λ is the pitch of the triangular lattice, and d is a holes diameter. The solid core consists of one missing hole in the center of the structure.

where λ is given in micrometers. Dispersion parameter D is computed through the usual formula from the real part of effective index $\Re(n_{\text{eff}})$ (Ref. 8):

$$D = -\frac{\lambda}{c}\frac{\partial^2 \Re(n_{\text{eff}})}{\partial \lambda^2}. \quad (2)$$

As in ordinary waveguides, the dispersion of guided modes results from both material and waveguide dispersion. The remarkable feature of MOFs is that the waveguide dispersion can be modified significantly by means of a wide range of geometrical parameters, namely, the positions and sizes of the different holes. The behavior of waveguide dispersion can be understood from heuristic considerations of effective media: At short wavelengths, light can distinguish the details of the structure, resulting in a greater concentration in the high-index region (i.e., the core whose index is that of the matrix). In this situation the effective index is smaller than the refractive index of the matrix. At longer wavelengths the structure tends to a homogeneous one, and the effective index of the mode will consequently be upper-bounded by the homogenized refractive index of the structure, which is much lower than the refractive index of the matrix as a result of the air inclusions. These heuristic considerations are unable to predict MOF chromatic dispersion precisely: A precise numerical study is required. Moreover, in practical applications the losses have a vital importance. Detailed studies of losses in MOFs versus pitch of the air-hole lattice, the hole diameter, and the hole ring number have already been carried out by the multipole method.[4,9] A vector method that uses periodic boundary conditions[10] has already been used to study dispersion in MOFs,[11] but in this model the influence of the number of hole rings cannot be investigated, and, above all, the losses cannot be computed.

2. Validation

The method has been checked thoroughly by comparison with other numerical methods, namely; a fictitious source[12] and other multipole methods[13,14] (more details of these comparisons can be found in an earlier paper by the present authors and others.[4]

The symmetry properties of fibers are accurately satisfied[6]: For a MOF with a rotational symmetry of order 6, the fundamental mode is twofold degenerate, as expected from Mc Isaac's theory.[15]

The method that we codeveloped and its numerical implementation have also been compared with a plane-wave method for a microstructured optical fiber with a ring of six air holes of diameter $d = 5$ μm with pitch $\Lambda = 6.75$ μm and a fixed background index $n = 1.45$ at $\lambda = 1.55$ μm; the computed value $\Re(n_{\text{eff}})$ of the fundamental mode is 1.4447672.[6]

With respect to chromatic dispersion, our results are in good agreement (see Table 1) both with the dispersion and with its slope as measured by Gander and his colleagues and with the dispersion calculated by the same authors,[16] who used an expansion of the fields in terms of Hermite–Gaussian functions[1] for a microstructured optical fiber ($d = 0.621$ μm, with a pitch $\Lambda = 2.3$ μm) at $\lambda = 0.813$ μm. Our results are also in good agreement (see Table 1) with the dispersion and the slope dispersion calculated by Brechet *et al.* for the same structure by a finite-element method.[17]

3. Results

In the examples given in what follows, we simulate a MOF made from a subset of triangular array of cylindrical air inclusions ($n_i = 1$) of lattice pitch Λ. The inclusions have identical circular cross sections of diameter d; the core is formed by a missing inclu-

Table 1. Comparison of Dispersion D and Its Slope Measured and Calculated at $\lambda = 0.813$ μm by Gander *et al.*[a]

Dispersion		Dispersion Slope	
Measured	Calculated	Measured	Calculated
-77.7[b]	-77[b]	0.464[a]	
	-78.6[c]		0.450[c]
	-76.95 ($N_r = 4$)[d]		0.455 ($N_r = 4$)[d]
	-76.78 ($N_r = 3$)[d]		0.458 ($N_r = 3$)[d]

[a]They did not compute the dispersion slope, and the N_r value is not given in their text, so only an estimated value can be deduced from the scanning-electron micrograph of the MOF that they show as Fig. 2 of their paper[16]; the results by Brechet *et al.*[17] with a finite-element method at $\lambda = 0.813$ μm and the results with our multipole method for two values of N_r at the same wavelength are also shown here. Unit for dispersion, ps nm^{-1} km^{-1}; unit for the dispersion slope, ps nm^{-2} km^{-1}.
[b]Results of Gander *et al.*[16]
[c]Results of Brechet *et al.*[17]
[d]Results of our multipole method for two values of N_r.

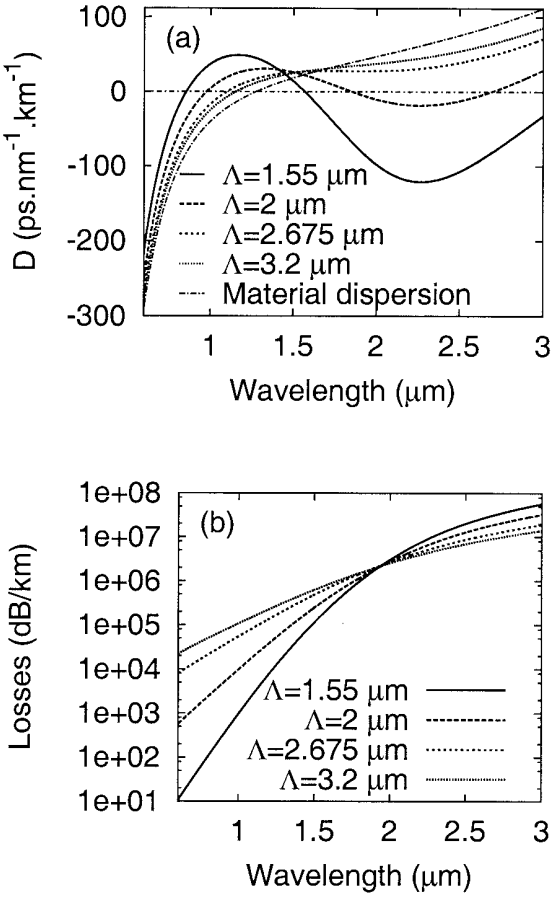

Fig. 2. (a) Dispersion and (b) losses for a three-ring MOF as a function of wavelength and pitch Λ. The material dispersion is also shown. Hole diameter d, 0.8 μm.

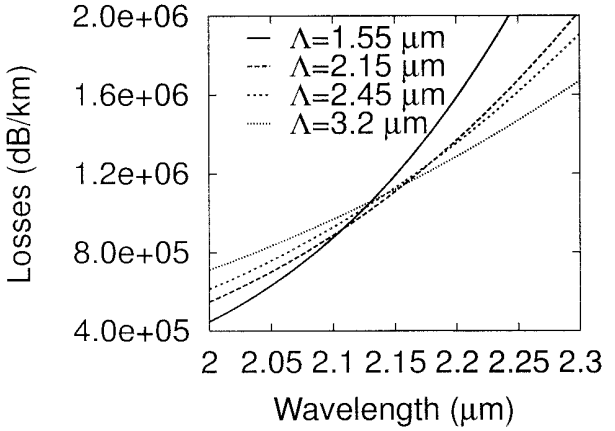

Fig. 3. Losses for a four-ring MOF as a function of wavelength and pitch Λ. Hole diameter d, 0.8 μm. The y scale is linear, unlike for Fig. 2(b).

sion (see Fig. 1). The finite thickness of the hole region about the core can be described by the number of rings of holes N_r. The matrix and the jacket are made from silica, so the guiding structure is formed by a finite number of low-index inclusions in infinite silica bulk (the Sellmeier expansion is taken from Ref. 8). Because the hole region surrounding the core is bounded, it is clear that propagating modes are leaky.

We limit our study to the properties of fundamental mode dispersion, and the wavelengths that we consider here are included in the range 0.6–3 μm. As shown in Fig. 2 for a fixed hole diameter, a small pitch generates oscillations of the dispersion, and several zero-dispersion wavelengths can be found. With a larger pitch, the dispersion increases monotonically with wavelength. This property can be understood as follows: For large pitch, the MOF core is large too, the waveguide effects on dispersion are therefore weak; thus the material dispersion dominates. Conversely, for smaller pitches the waveguide dispersion takes over, and we observe oscillations of the dispersion curve; the amplitude of these oscillations increases as the pitch decreases. In the short-wavelength limit, material dispersion is so negative that waveguide dispersion cannot compensate for its effect. This remark explains why, for submicrometric wavelengths, all the dispersions tend toward material dispersion.

From Fig. 2 it can be noticed that there is a pitch value (Λ = 2.675 μm) for which the dispersion curve is flat over a large range of wavelengths when the average value is taken as 27.9 ps nm^{-1} km^{-1} near 1.85 μm, with the amplitude of dispersion oscillation equal to 0.2 ps nm^{-1} km^{-1} in a wavelength interval of 0.3 μm. For the same pitch but with $N_r = 4$ (data not shown) the dispersion curve is much less flat than with $N_r = 3$, and the average level of the dispersion has decreased; it is 23.7 ps nm^{-1} km^{-1} near 1.85 μm, with an amplitude of oscillation of 3.8 ps nm^{-1} km^{-1} in a wavelength interval of 0.5 μm. Notice that in both cases the corresponding losses (5.9×10^5 dB km^{-1} for $N_r = 3$ and 6.1×10^4 dB km^{-1} for $N_r = 4$) prohibit the use of these MOFs for practical applications. One can try to overcome this drawback by again increasing the number of rings, but this change entails a new change of the dispersion curve, as we show in detail in what follows. This example clearly shows the necessity for studying both losses and dispersion to achieve realistic dispersion engineering.

Another conclusion to draw from Fig. 2 is the existence of a wavelength, $\lambda_{cross} \simeq 1.93$ μm, for which the losses are almost independent of pitch Λ, at least in the range of Λ from 1.55 to 3.2 μm. This phenomenon occurs for other values of N_r: For $N_r = 4$, λ_{cross} is ~2.15 μm (see Fig. 3); for $N_r = 2$, λ_{cross} is ~1.63 μm (data not shown). The value of λ_{cross} increases slowly with N_r. A straight scale-law argument cannot be used because the hole's diameter is kept constant for the various structures. Besides, in as much as material dispersion depends on the actual wavelength, one must take care in using scaling arguments to try to explain this behavior. Material dispersion could also have an influence on the extent of the crossing region. Currently, the crossing region is approximately 0.1 μm large. From a math-

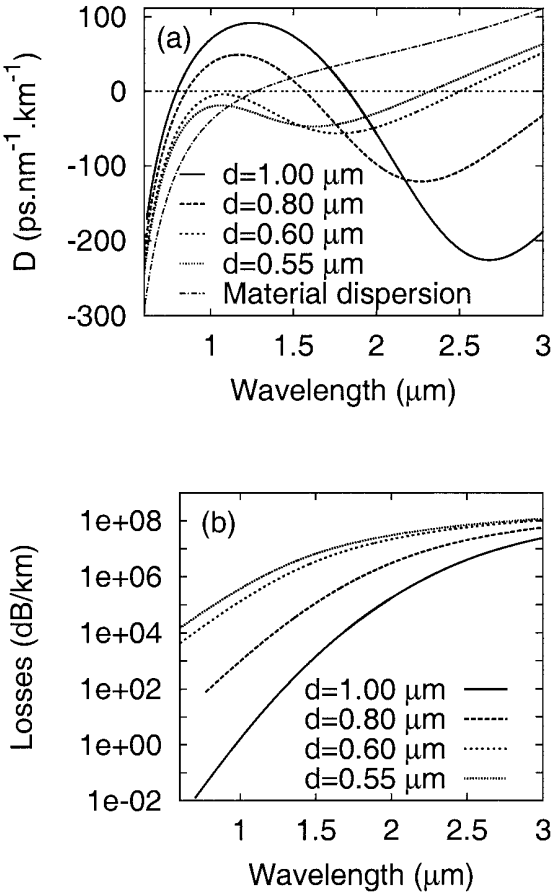

Fig. 4. (a) Dispersion and (b) losses for a three-ring MOF as a function of wavelength and hole diameter d. The material dispersion is also shown. Pitch Λ, 1.55 μm.

ematical point of view, for a fixed value of N_r the crossing phenomenon corresponds to point (λ_{cross}, Λ_{cross}) of surface $\mathcal{L}(\lambda, \Lambda)$ where the curve defined by $\partial\mathcal{L}/\partial\Lambda = 0$ crosses the curve given by $\partial^2\mathcal{L}/\partial\Lambda^2 = 0$. It seems more difficult to give the physical meaning of this phenomenon.

It can be seen from Fig. 4 that the oscillation amplitudes in dispersion curves increase with hole diameter (for d = 1.00 μm, i.e., d/Λ = 0.645, the oscillation amplitude (becomes 300 ps nm^{-1} km^{-1}). This behavior can be explained by consideration of MOF core size and by a competition between material dispersion and waveguide dispersion, similar to that given above for the influence of the pitch. It is worth noting that the value D_{max} of the dispersion's local maximum increases with hole diameter for all dispersion curves that we have computed. For three-ring MOFs with a fixed pitch Λ = 1.55 μm, the wavelength $\lambda_{D_{max}}$ associated with the local maximum D_{max} of dispersion increases with the diameter of the holes. One can use this property to shift the dispersion curves efficiently to obtain the required $\lambda_{D_{max}}$.

One can try to reduce the huge losses [more than 1.0×10^2 dB km^{-1} near λ = 1.3 μm for all the curves plotted in Fig. 4(a)] by increasing the number of hole

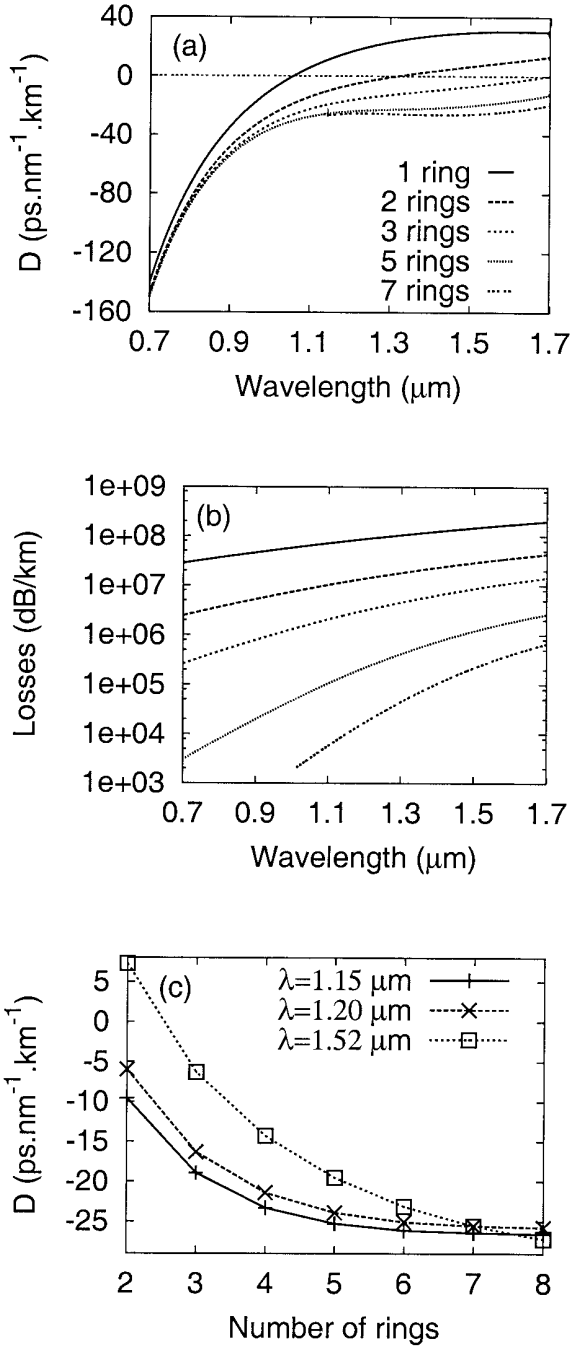

Fig. 5. (a) Dispersion and (b) losses as a function of the wavelength, and number of rings N_r [the types of curves have the same values for (a) and (b)]. Pitch Λ 2.0 μm; hole diameter d, 0.5 μm. (c) Dispersion for three wavelengths as a function of the number of rings N_r for the same MOF.

rings N_r, but once again dispersion profiles are modified. We now describe the influence of this crucial parameter. As shown in Fig. 5(a), when there is no local maximum of dispersion for MOFs with few rings, the dispersion decreases as the number of rings is increased. The difference between successive dispersion curves of two MOFs decreases as the number

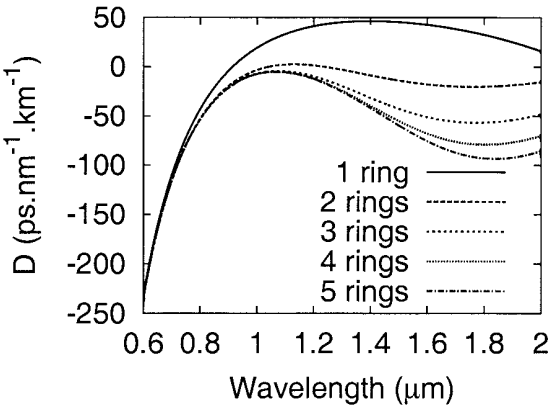

Fig. 6. Dispersion as a function of wavelength and number of rings N_r. Pitch Λ, 1.55 μm; hole diameter d, 0.6 μm.

of rings increases, as shown in Fig. 5(c). This figure clearly shows that the dispersion converges to a limit when the number of rings is increased. The convergence speed depends on the wavelength: The larger the wavelength, the slower the convergence [in Fig. 5(c) for $\lambda = 1.52$ μm the limit is not yet reached with eight rings]. It is worth noting that the losses associated with the flattened dispersion curve obtained with the seven-ring MOF of Fig. 5(a) are still large (more than 1.0×10^4 dB km^{-1} near $\lambda = 1.3$ μm). This influence of N_r on dispersion can be understood in the following way: When losses are weak, a supplementary ring will not change the mode drastically. In contrast, when the mode is not well confined in the core, a supplementary ring will modify the mode significantly. We can thus assume that the field pattern associated with the mode converges with increasing N_r; the convergence is slower for larger wavelengths because modes are less confined for these wavelengths. As opposed to the example in Fig. 5(a), for structures whose dispersion does exhibit oscillatory behavior [e.g., structures of small pitch in Fig. 2(a), which have a high diameter/pitch ratio], an increase of N_r results in amplification of the oscillation amplitude (see Fig. 6).

4. Conclusion and Discussion

As was shown in Section 3, one cannot keep the flattened dispersion with a fixed D value obtained for certain MOFs and at the same time reduce the MOFs' losses through a simple increase of their number of air-hole rings.

It must also be pointed out that an increase of the number of rings can reduce the losses of higher-order modes. As a consequence, a monomode fiber may become multimode for some configurations. Nevertheless, if large differences between the real parts of n_{eff} for the modes are found, mode coupling between the fundamental mode and the higher-order mode should be suppressed. We continue to study these effects and the influence of the jacket on dispersion.

The high loss figures that we have reported throughout this paper might give the wrong impression that low losses are not feasible in microstructured fibers, but low-loss MOFs are possible with appropriate geometric parameters[9] [see also the loss curve at small wavelengths for $d = 1.0$ μm in Fig. 4(b)]. For example, with $\Lambda = 2.26$ μm, d = 1.51 μm, and $N_r = 3$ the losses that we compute are below 1×10^{-4} dB km^{-1} at a wavelength of 0.76 μm. The same structure with $N_r = 7$ corresponds to that studied experimentally by Kubota and his colleagues.[18] The measured global losses at a wavelength of 0.85 μm are 7.1 dB km^{-1}, which clearly shows that the losses in MOFs can be limited by Rayleigh scattering, structural imperfections, and absorption and not by the geometrical losses. But interesting dispersion properties seem to imply geometrical parameters that are not necessarily compatible with low losses and few air-hole rings.

The issue for dispersion engineering applications is to find MOF parameters that produce both ultraflattened dispersion curves (negative, positive, or nearly zero) about the specified wavelength (for example, 1.3 or 1.55 μm) and low losses (near or below 1 dB km^{-1}). Consequently, for such engineering the finite size of the fiber cross section must be considered. Accurate design of such MOFs is currently under study.[19]

This research benefited from travel support from the French and Australian governments.

References and Notes

1. D. Mogilevstev, T. A. Birks, and P. St. J. Russell, "Group-velocity dispersion in photonic crystal fibers," Opt. Lett. **23,** 1662–1664 (1998).
2. J. C. Knight, J. Arriaga, T. A. Birks, A. Ortisaga-Blanch, W. J. Wadsworth, and P. St. J. Russell, "Anomalous dispersion in photonic crystal fibers," IEEE Photon. Technol. Lett. **12,** 807–809 (2000).
3. T. P. White, B. Kuhlmey, R. C. McPhedran, D. Maystre, G. Renversez, C. M. de Sterke, and L. C. Botten, "Multipole method for microstructured optical fibers. I. Formulation," J. Opt. Soc. Am. B **19,** 2322–2330 (2002).
4. B. Kuhlmey, T. P. White, G. Renversez, D. Maystre, L. C. Botten, C. M. de Sterke, and R. C. McPhedran, "Multipole method for microstructured optical fibers. II. Implementation and results," J. Opt. Soc. Am. B **19,** 2331–2340 (2002).
5. R. C. McPhedran and L. C. Botten, Department of Mathematical Sciences, University of Technology, Sydney, New South Wales 2007, Australia.
6. M. J. Steel, T. P. White, C. M. de Sterke, R. C. McPhedran, and L. C. Botten, "Symmetry and degeneracy in microstrutured optical fibers," Opt. Lett. **26,** 488–490 (2001).
7. J. W. Fleming, "Material dispersion in lightguide glasses," Electron. Lett. **14,** 326–328 (1978).
8. G. P. Agrawal, *Nonlinear Fiber Optics* (Academic, San Diego, Calif., 1989).
9. T. P. White, R. C. McPhedran, C. M. de Sterke, L. C. Botten, and M. J. Steel, "Confinement losses in microstructured optical fibers," Opt. Lett. **26,** 1660–1662 (2001).
10. A. Ferrando, E. Silvestre, J.-J. Miret, P. Andrés, and M. V. Andrés, "Vector description of higher-order modes in photonic crystal fibers," J. Opt. Soc. Am. A **17,** 1333–1340 (2000).
11. A. Ferrando, E. Silvestre, J.-J. Miret, and P. Andrés, "Nearly zero ultraflattened dispersion in photonic crystal fibers," Opt. Lett. **25,** 790–792 (2000).
12. F. Zolla and R. Petit, "Method of fictitious sources as applied

to the electromagnetic diffraction of a plane wave by a grating in conical mounts," J. Opt. Soc. Am. A **13,** 1087–1096 (1996).
13. D. Felbacq, G. Tayeb, and D. Maystre, "Scattering by a random set of parallel cylinders," J. Opt. Soc. Am. A **9,** 2526–2538 (1994).
14. E. Centeno and D. Felbacq, "Scattering by a random set of parallel cylinders," J. Opt. Soc. Am. A **17,** 320–327 (2000).
15. P. R. Mc Isaac, "Symmetry-induced modal characteristics of uniform waveguides. I. Summary of results," IEEE Trans. Microwave Theory Tech. **23,** 421–433 (1975).
16. M. J. Gander, R. McBride, J. C. D. Jones, D. Mogilevtsev, T. A. Birks, J. C. Knight, and P. St. J. Russell, "Experimental measurement of group velocity dispersion in photonic crystal fibre, Electron. Lett. **35,** 63–64 (1999).
17. F. Brechet, J. Marcou, D. Pagnoux, and P. Roy, "Complete analysis of the characteristics of propagation into photonic crystal fibers by the finite element method," Opt. Fiber Technol. **6,** 181–191 (2000).
18. H. Kubota, S. Suzuki, S. Kawanishi, M. Nakazawa, and M. Takana. "Low-loss, 2 km-long photonic crystal fiber with zero GVD in the near IR suitable for picosecond pulse propagation at 800 nm band," in *Conference on Lasers and Electro-Optics* (*CLEO*), Vol. 56 of OSP Trends in Optics and Photonics (Optical Society of America, Washington, D. C., 2001), pp. CPD3–1–CPD3–2.
19. G. Renversez, B. Kuhlmey, and R. C. McPhedran are preparing the following paper for publication, "Dispersion management with microstructured optical fibers: ultra-flattened chromatic dispersion with low losses."

June 15, 2003 / Vol. 28, No. 12 / OPTICS LETTERS 989

Dispersion management with microstructured optical fibers: ultraflattened chromatic dispersion with low losses

G. Renversez and B. Kuhlmey

Institut Fresnel (Unité Mixte de Recherche 6133, Centre National de la Recherche Scientifique), Faculté des Sciences et Techniques de St. Jérôme, Avenue Escadrille Normandie-Niémen, 13397 Marseille Cedex 20, France

R. McPhedran

School of Physics, University of Sydney, Sydney, NSW 2006, Australia

Received January 7, 2003

We numerically demonstrate ultraflattened chromatic dispersion with low losses in microstructured optical fibers (MOFs). We propose using two different MOF structures to get this result. Both structures are based on a subset of a triangular array of cylindrical air holes; the cross sections of these inclusions are circular, and a missing hole in the fiber's middle forms the core. In this MOF structure the diameters of the inclusions increase with distance from the fiber axis until the diameters reach a maximum. With this new design and with three different hole diameters, it requires only seven rings to reach the 0.2-dB/km level at $\lambda = 1.55\ \mu$m with a variation amplitude of dispersion below 3.0×10^{-2} ps nm^{-1} km^{-1} of $\lambda = 1.5-1.6\ \mu$m. With the usual MOF (made from holes of identical diameter), we show that at least 18 hole rings are required for losses to decrease to <1 dB/km at $\lambda = 1.55\ \mu$m.

OCIS codes: 060.2270, 060.2280, 060.2400, 060.2430.

Microstructured optical fibers (MOFs) were quite recently proposed as new tools for dispersion management in optical communication systems.[1] Several studies[2,3] in which a vector method with periodic boundary conditions was used[4] were made to design such MOFs; nevertheless, as was recently shown,[5] one must take the finite cross sections of MOFs into account to describe accurately the chromatic dispersion properties of such fibers and to compute the losses. Moreover, comparison of the computed dispersion curves and the experimental results remains difficult.[6]

A mode of a MOF is characterized by the mode's field pattern and its effective indices $n_{\mathrm{eff}} = \beta/k_0$, where β is its propagation constant and $k_0 = 2\pi/\lambda$ is the free-space wave number. Because of the finite transverse extent of the confining structure, the effective index is a complex value; its imaginary part $\Im(n_{\mathrm{eff}})$ is related to losses $\mathcal{L}$ (in decibels per meter) through the relation $\mathcal{L} = 40\pi\ \Im(n_{\mathrm{eff}}) \times 10^6/[\lambda \ln(10)]$, where λ is given in micrometers. Dispersion parameter D is computed through the usual formula from the real part of effective index $\Re(n_{\mathrm{eff}})$ (Ref. 7): $D = -(\lambda/c)\partial^2\ \Re(n_{\mathrm{eff}})/\partial\lambda^2$. We have developed a multipole method[8] that allows us to compute accurately the complex effective index of the modes of a wide variety of MOFs. Our method has been verified by comparison with other numerical methods.[5,9,10]

In what follows, we simulate plain core MOFs made from a subset of a triangular array of cylindrical air inclusions ($n_i = 1$). The inclusion spacing, or pitch, is denoted Λ. The inclusions are circular, possibly with various diameters, and lie about a core that is in fact a missing central inclusion. The matrix and the jacket are made from silica, so the guiding structure is formed by a finite number N_r of rings of air holes in infinite bulk silica whose Sellmeier expansion (which does not include material losses) is taken from Ref. 7. Our aim in this study is to establish MOF designs that combine ultraflattened chromatic dispersion together with low losses near the telecommunication wavelength $\lambda = 1.55\ \mu$m. We exhibit two designs that achieve this objective. The first contains air holes of one diameter and requires 18 rings of holes for losses smaller than 1 dB/km. The second utilizes air holes with three different diameters, which yield ultraflat dispersion and even lower loss levels with only seven rings.

Chromatic dispersion in MOFs arises from that of the silica (D_{mat}) and also from the waveguide dispersion (D_W) associated with the structure of the confining region. Note that our multipole method provides directly the total dispersion (D), so we deduce D_W from the relation $D_W \simeq D - D_{\mathrm{mat}}$. As was pointed out by Ferrando *et al.*,[2] it is convenient to achieve a specific total dispersion by controlling D_W to make it follow a trajectory parallel to that of $-D_{\mathrm{mat}}$ in the target wavelength interval. The parameters with which one can achieve this are hole diameter d, pitch Λ, and number of rings N_r.[5]

From a previous theoretical work,[11] we choose $d/\Lambda < 0.406$ to guarantee single-mode operation of the MOF design.

In Fig. 1 we show the variation of total dispersion D with the number of rings of six normal MOF geometries, all located in the region of stable dispersion. All curves show a simple variation with N_r, which can be modeled accurately by an exponential form $D_1 \exp(-\kappa N_r) + D_{\mathrm{lim}}$. Such a fitting form has three parameters (D_1, κ, D_{lim}), which can be determined accurately from the results of $N_r = 3-6$. This procedure has important advantages because MOFs with relatively small numbers of rings are relatively quickly modeled; yet we have established that the exponential fit thereafter accurately describes the dispersion of much larger structures and even limiting parameter D_{lim}, the dispersion of a mode pinned by a single defect in an infinite lattice. In fact, using the limit dispersion D_{lim} determined numerically for a

0146-9592/03/120989-03$15.00/0

990 OPTICS LETTERS / Vol. 28, No. 12 / June 15, 2003

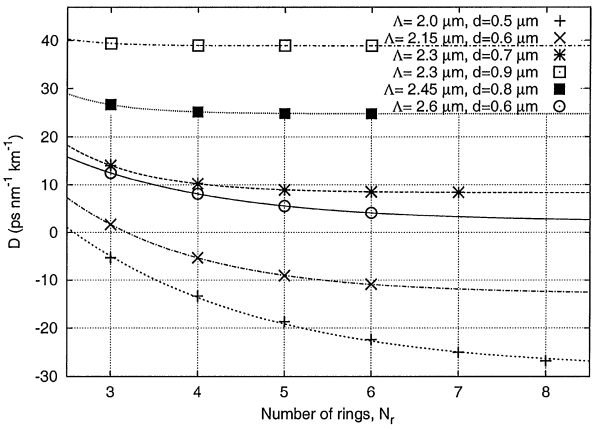

Fig. 1. Dispersion decay at $\lambda = 1.55$ μm as a function of the total number of hole rings N_r for several MOF structures. Λ is the hole spacing, and d is the hole diameter. The points correspond to the computed numerical dispersion; the curves, to exponential based fits.

set of values of wavelength λ, we can also determine $S_{\text{lim}} = \partial D_{\text{lim}}/\partial\lambda$, the limit dispersion slope.

In Fig. 2 we show the variations of these important parameters D_{lim} and S_{lim} as a function of hole diameter d for several pitches Λ. This figure illustrates well how one can isolate a MOF that exhibits a target dispersion value for a sufficiently large number of rings N_r, which is flat over a range about the chosen wavelength value. Indeed, such a MOF will have the desired value of D_{lim} and simultaneously a value of S_{lim} close to zero. Note that the pitches exhibited in Fig. 2 were chosen carefully to exemplify this desirable behavior. We have also shown that, for the data of Fig. 2, the minima of S_{lim} as a function of d occur in the same diameter interval (0.65; 0.7 μm) for all MOFs that have $N_r \geq 6$. From Fig. 2, if one requires a positive nearly zero flat chromatic dispersion, then, using these curves, one should start the dispersion engineering with a MOF such that $\Lambda = 2.45$ μm and $d = 0.6$ μm. Of course, Fig. 2 can be used to isolate MOF geometries that have different characteristics, such as a prescribed slope with a fixed average value of dispersion over a wavelength range.

In Fig. 3 we show dispersion characteristics for three MOF designs. At the top, the total dispersion is linear with negative slope [$D(a)$], constant near zero [$D(b)$], and nearly constant near -5 ps nm^{-1} km^{-1} [$D(c)$]. These curves arise because of the balance between waveguide dispersion D_W curves and that of $-D_{\text{mat}}$ shown in the bottom part of the figure. Note that, whereas these designs have appropriate dispersion characteristics for $N_r \geq 6$, their geometric losses impose much more stringent requirements on the number of rings, and the effective area of the fundamental mode A_{eff} is $\sim$36.5 μm^2 for $N_r = 6$. For example, for the MOF with ultraflat dispersion close to zero, $N_r \geq 18$ (1026 holes) is required for losses to be kept below 1 dB/km at $\lambda = 1.55$ μm. Some laboratories have already drawn 11-ring fibers[6] (around 396 holes), there is clearly a technological interest in investigating designs that can deliver tailored dispersion characteristics with many fewer MOF rings.

To provide MOF designs that display a desirable combination of ultraflat dispersion, low-loss and quasi-single-mode operation, and a practical value of N_r, a natural strategy is to allow the hole diameter to differ from one ring to another (see Fig. 2, inset) with exterior rings that have large holes to lower the losses. We start the design process with a three-ring MOF; d_1 is arbitrarily set to $d_1 = 0.5$ μm. In pursuing designs of this sort it is advantageous to employ the following scaling relation for waveguide dispersion (this is a generalization of a result given in Ref. 2):

$$D_W(\lambda, \Lambda/\Lambda_{\text{ref}}, f_1, f_2, \ldots, f_n) \simeq \frac{\Lambda_{\text{ref}}}{\Lambda} D_W(\lambda\Lambda_{\text{ref}}/\Lambda, 1, f_1, f_2, \ldots, f_n), \quad (1)$$

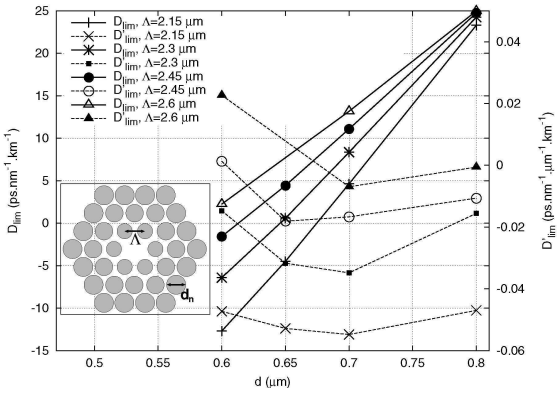

Fig. 2. Limit dispersion (solid lines, left y scale) and limit dispersion slope (dashed lines, right y scale) at $\lambda = 1.55$ μm as a function of hole diameter d only, for several pitches. The chosen parameter values for Λ and d correspond to the small limit slope region. Inset, cross section of the modeled MOF with three rings of holes (holes are shown shaded), $N_r = 3$. Λ is the hole spacing and d_n is the hole diameter of the nth ring. The solid core consists of one missing hole in the center of the structure.

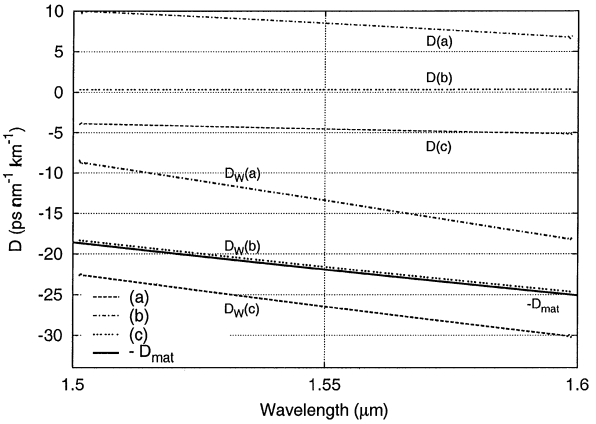

Fig. 3. Waveguide dispersion D_W, dispersion D, and sign-changed material dispersion $-D_{\text{mat}}$ for three six-ring MOF structures. The line style of a MOF structure is identical for D_W and D. Λ and the diameters are given in micrometers. (a) $\Lambda = 2.3$, $d = 0.7$; (b) $\Lambda = 2.45$, $d = 0.6$; (c) $\Lambda = 2.3$, $d = 0.6$.

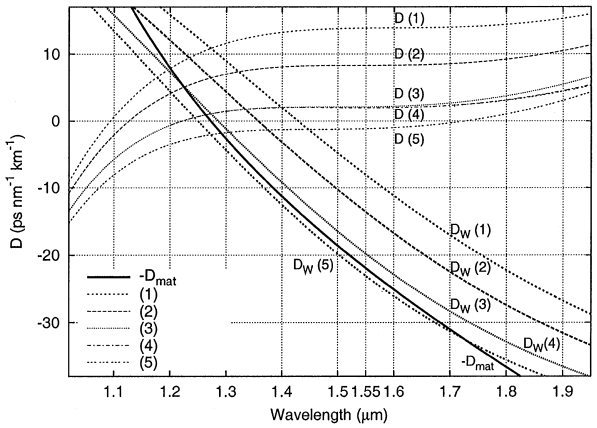

Fig. 4. Waveguide dispersion D_W, dispersion D for the MOF structures that we proposed, and sign-changed material dispersion $-D_{\mathrm{mat}}$. Unless stated, the total number of rings N_r in the MOF is three. The line style of a MOF structure is identical for D_W and D. Λ and the diameters are given in micrometers. d_n is the hole diameter of the nth ring, and $d_{n_1-n_2}$ denotes the hole diameter of the n_1th to n_2th rings. (1) $\Lambda = 1.9$, $d_1 = 0.559$, $d_2 = 0.782$, $d_3 = 0.894$; (2) $\Lambda = 1.8$, $d_1 = 0.529$, $d_2 = 0.741$, $d_3 = 0.847$; (3) $\Lambda = 1.7$, $d_1 = 0.5$, $d_2 = 0.7$, $d_3 = 0.8$; (4) $N_r = 4-7$, $\Lambda = 1.7$, $d_1 = 0.5$, $d_2 = 0.7$, $d_{3-7} = 0.8$; (5) $\Lambda = 1.65$, $d_1 = 0.485$, $d_2 = 0.679$, $d_3 = 0.776$.

where Λ_{ref} is the pitch of a reference lattice and f_n is the ratio d_n/Λ. Using the above scaling law and a rough optimization process on d_2, d_3, and Λ, we found an ultraflat dispersion over a long wavelength interval (approximately [1.45, 1.65] μm) for $d_2 = 0.7$ μm, $d_3 = 0.8$ μm, and $\Lambda = 1.7$ μm [$D(3)$ in Fig. 4]. It must be pointed out that the MOF design can be started from other values of d_1: For example, with $d_1 = 0.6$ μm we found $d_2 = 0.8$ μm, $d_3 = 1.0$ μm, and $\Lambda = 2.0$ μm (data not shown).

Using the scaling law [expression (1)], we can easily derive other structures that have ultraflattened chromatic dispersion but near a different value of D. Three examples of such structures, derived from the reference configuration ($d_1 = 0.5$ μm, $d_2 = 0.7$ μm, $d_3 = 0.8$ μm, $\Lambda = 1.7$ μm), are given in Fig. 4 {$\Lambda = 1.65$ μm [$D(5)$], 1.8 μm [$D(2)$], 1.9 μm [$D(1)$]}. Note that varying the pitch too far results in structures that no longer exhibit ultraflat dispersion; this is so because of the finite length of the ultraflat region in the chosen reference MOF design (data not shown).

We now control losses by adding further rings of holes with fixed diameter 0.8 μm. As can be seen from Fig. 4, adding rings 4–7 has almost no effect on the dispersion properties of the MOF [$D(4)$] but results in acceptably low values of geometric loss for technological applications: With $N_r = 6$, the losses are below 10 dB km^{-1}, and with $N_r = 7$ the losses are below 0.2 dB km^{-1}. For $N_r = 6$, the amplitude of dispersion variation is less than 3.0×10^{-2} ps nm^{-1} km^{-1} in the wavelength interval [1.5; 1.6] μm. These designs thus attain our goal of achieving ultraflat dispersion combined with low geometric loss in a MOF feasible by use of current fabrication technology. Note that one can use designs in which the outer boundary of the confining region is either hexagonal or circular. For the well-confined modes that we deal with here ($A_{\mathrm{eff}} \simeq 10.5$ μm^2 for $N_r = 6$), this difference has no practical effect on dispersion (data not shown). One interesting consequence of using three different hole diameters is that the possibility arises of having modes higher than the fundamental confined between rings of holes with different diameters. Indeed, the second mode in the seven-ring structure of Fig. 4 is confined between the first and second rings of holes and has losses approximately ten thousand times larger than that of the fundamental. This mode would not couple readily to the fundamental mode in the design, because mode energy is concentrated in different regions for the two modes and the real parts of their effective indices are quite different.

In conclusion, we have numerically demonstrated that nearly zero or nonzero ultraflattened chromatic dispersion with low loss can be achieved by use of either of two types of MOF design. The more complex design, proposed in this Letter, which has three different hole diameters, allows us to achieve low losses with many fewer air holes than with the conventional design. The design principles introduced here, together with the powerful control of dispersion given by the MOF geometry, should facilitate effective chromatic dispersion management over a wide spectral range in optical fibers.

This work benefited from travel support from the French and Australian governments.

References

1. D. Mogilevstev, T. Birks, and P. St. J. Russell, Opt. Lett. **23,** 1662 (1998).
2. A. Ferrando, E. Silvestre, J. Miret, and P. Andrés, Opt. Lett. **25,** 790 (2000).
3. A. Ferrando, E. Silvestre, P. Andrés, J. Miret, and M. Andrés, Opt. Express **9,** 687 (2001), http://www.opticsexpress.org.
4. A. Ferrando, E. Silvestre, J. Miret, P. Andrés, and M. Andrés, J. Opt. Soc. Am. A **17,** 1333 (2000).
5. B. Kuhlmey, G. Renversez, and D. Maystre, Appl. Opt. **42,** 634 (2003).
6. W. Reeves, J. Knight, and P. St. J. Russell, Opt. Express **10,** 609 (2002), http://www.optics.express.org.
7. G. P. Agrawal, *Nonlinear Fiber Optics* (Academic, San Diego, Calif., 1989).
8. T. White, B. Kuhlmey, R. McPhedran, D. Maystre, G. Renversez, C. de Sterke, and L. Botten, J. Opt. Soc. Am. B **10,** 2322 (2002).
9. M. Steel, T. White, C. de Sterke, R. McPhedran, and L. Botten, Opt. Lett. **26,** 488 (2001).
10. B. Kuhlmey, T. White, G. Renversez, D. Maystre, L. Botten, C. de Sterke, and R. McPhedran, J. Opt. Soc. Am. B **10,** 2331 (2002).
11. B. Kuhlmey, M. de Sterke, R. McPhedran, P. Robinson, G. Renversez, and D. Maystre, Opt. Express **10,** 1285 (2002), http://www.opticsexpress.org.

1264 OPTICS LETTERS / Vol. 30, No. 11 / June 1, 2005

Second mode transition in microstructured optical fibers: determination of the critical geometrical parameter and study of the matrix refractive index and effects of cladding size

Gilles Renversez and Frédéric Bordas

Université Paul Cézanne Aix-Marseille III and Institut Fresnel (Unité Mixte de Recherche 6133, Centre National de la Recherche Scientifique), Faculté des Sciences et Techniques de St Jérôme, Avenue Escadrille Normandie-Niémen, 13397 Marseille Cedex 20, France

Boris T. Kuhlmey

Centre for Ultrahigh-Bandwidth Devices for Optical Systems and School of Physics, University of Sydney, Sydney, NSW 2006, Australia

Received November 17, 2004

We carried out a numerical study of the second mode transition in finite-sized, microstructured optical fibers (MOFs) for several values of the matrix refractive index. We determined a unique critical geometrical parameter for the second mode cutoff that is valid for all the matrix refractive indices studied. Finite size effects and extrapolated results for infinite structures are described. Using scaling laws, we provide a generalized phase diagram for solid-core MOFs that is valid for all refractive indices, including those of the promising chalcogenide MOFs. © 2005 Optical Society of America

OCIS codes: 060.2270, 060.2280, 060.2400, 060.2430.

Arguably, the most striking property of microstructured optical fibers (MOFs) is that they can be endlessly single mode.[1] In conventional step-index fibers there exist a finite number of modes that are strictly guided, characterized by the fact that their propagation constants β are real. All other modes are leaky, with propagation constants that have nonzero imaginary parts. The number of guided modes increases with decreasing wavelength, and it is only at wavelengths longer than the cutoff wavelength that the fiber is single mode.[2,3] In contrast, ideal (or infinite) solid-core MOFs, which consist of single defects in infinite two-dimensional photonic crystals, can remain single mode at all wavelengths if the holes are sufficiently small.[4,5] Those fibers are said to be endlessly single mode.

Previous studies of the second mode cutoff in MOFs have led to a so-called phase diagram that partitions the parameter space into three regions, depending on whether the MOF is single mode, multimode, or endlessly single mode. However, this phase diagram was established solely for silica MOFs.[4,6] Given that MOFs can be made from a variety of dielectrics and that some of the most promising MOF applications, notably nonlinear ones, rely on high-refractive-index materials such as chalcogenides,[7] it is important to know whether high-index solid-core MOFs can exhibit the endlessly single-mode property within a realistic range of fiber parameters and wavelengths. We numerically investigate the effect of matrix refractive index n_{mat} of the MOF's matrix material on the phase diagram by using the multipole method.[6,8] We accurately determine the critical relative hole size that delimits the endlessly single-mode region, which is independent of n_{mat}.

Our studies also highlight finite size effects, which were ignored in previous studies and have an effect on the precise value of the critical relative hole size that delimits the endlessly single-mode region. Finally, using approximate scaling laws for binary step-index structures, we derive a generalized phase diagram that is valid for a large range of refractive-index contrasts.

We consider solid-core MOFs consisting of a finite number N_r of rings of triangularly arranged holes with circular cross sections (diameter d, refractive index n_i) in an infinite matrix (refractive index, n_{mat}); the core is a missing hole at the center. The center-to-center distance between holes (the pitch) is denoted Λ and is fixed at a value of 2.3 μm, and the effective index of modes is defined as $n_{\mathrm{eff}}=\beta/k_0$, in which $k_0=2\pi/\lambda$ is the free-space wave number and λ denotes the wavelength. We study the second mode cutoff of such MOFs to define their phase diagram in parameter space $(d/\Lambda, \lambda/\Lambda)$.

For such MOFs with finite N_r, the cutoff is not so clearly defined as for infinite MOFs. Indeed, in that case all modes are leaky; their propagation constants have nonzero imaginary parts. For these fibers the cutoff is a transition between two states of the same mode, one localized in the core and the other extending into the cladding. This transition has been studied, e.g., in terms of the sudden expansion of the second mode's effective area[5] or, equivalently, in terms of

0146-9592/05/111264-3/$15.00

a qualitative change of behavior of losses as a function of wavelength.[4] Here we use the latter definition of the cutoff, relying on peaks of quantity Q, defined here as

$$Q = \frac{\partial^2[\log \Im m(n_{\mathrm{eff}})]}{\partial[\log \lambda]^2}, \tag{1}$$

in which $\Im m(n_{\mathrm{eff}})$ is the imaginary part of n_{eff}. Quantity Q is related to the curvature in a log–log plot of the losses as a function of wavelength, and its peaks are associated with qualitative changes in the nature of the mode. For a detailed discussion of the meaning of Q we refer the reader to Refs. 4, 6, 9, and 10. n_{eff} is the effective index of the second mode and was computed by the multipole method.[6,8,11]

First, we concentrate on MOFs with a high matrix refractive index, $n_{\mathrm{mat}}=2.5$. Figure 1 shows Q as a function of normalized wavelength λ/Λ for various diameter-to-pitch ratios; $N_r=7$. The minimum of those curves precisely defines the normalized cutoff wavelength $(\lambda/\Lambda)_{\mathrm{S.M.}}$.[4] Further, as the Q peaks reflect the change of slope of $\Im m(n_{\mathrm{eff}})$, the larger and narrower the peaks are, the sharper the transition between confined and unconfined modes is. Whereas in the research reported in Ref. 4 the Q minima were studied at fixed N_r, it appears that the behavior of the Q curves depends on N_r, as shown in Figs. 2 and 3. Figure 2 shows Q as a function of the normalized wavelength for two values of d/Λ, N_r ranging from 7 to 12, and $n_{\mathrm{mat}}=2.5$. For the same matrix index the magnitude of the Q minima $|Q_{\mathrm{min}}|$ as a function of N_r is shown in Fig. 3 for four d/Λ ratios.

Depending on the value of d/Λ, two different behaviors can be distinguished: for d/Λ ratios greater than or equal to 0.425 the minimum of Q becomes narrower (complete study not shown) and deeper with increasing N_r. Figure 3 shows that, in that case, $|Q_{\mathrm{min}}|$ diverges with N_r and, as can be seen from the curve for $d/\Lambda=0.43$, the rate at which $|Q_{\mathrm{min}}|$ diverges increases quickly with d/Λ. The divergence of $|Q_{\mathrm{min}}|$ implies that the cutoff transition becomes sharper

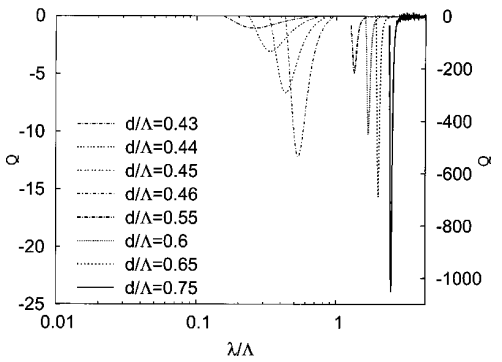

Fig. 1. Q as a function of normalized wavelength λ/Λ for eight d/Λ ratios for a seven-ring MOF made from a high—index matrix ($n_{\mathrm{mat}}=2.5$) with $\Lambda=2.3$ μm. Thinner curves (left) are associated with the left-hand y scale (lowest d/Λ and $|Q|$ values); the thicker curves use the right-hand y scale.

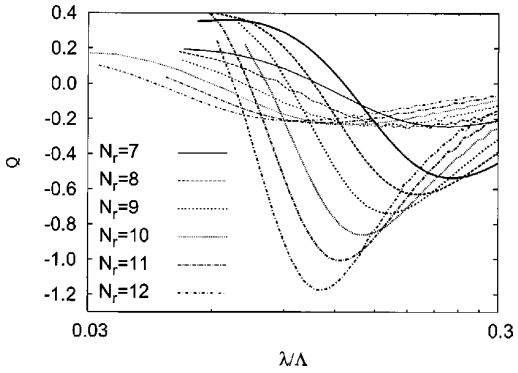

Fig. 2. Q as a function of λ/Λ for $d/\Lambda=0.42$ (thinner curves) and for $d/\Lambda=0.425$ (thicker curves) for several values of N_r.

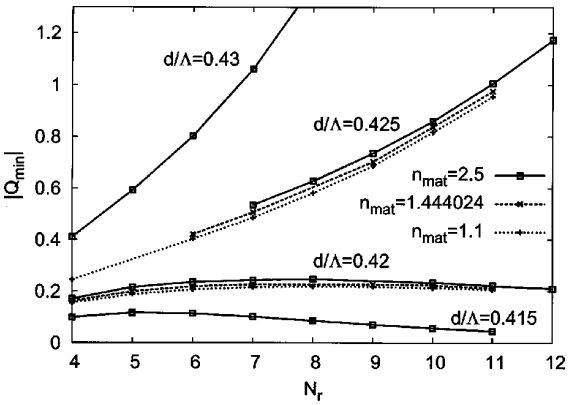

Fig. 3. $|Q_{\mathrm{min}}|$ as a function of N_r for three values of matrix index n_{mat} for several close d/Λ values.

with increasing numbers of rings, consistent with the fact that the cutoff should be infinitely sharp for infinite N_r.[9] Consequently the second mode does undergo a cutoff at finite wavelength for infinite MOFs with $d/\Lambda \geqslant 0.425$.

For $d/\Lambda=0.420$ and d/Λ ratios below this value, however; the minimum of Q vanishes slowly with increasing N_r. This behavior indicates that no transition should occur for the infinite MOF and therefore that the infinite MOF is endlessly single mode for $d/\Lambda \leqslant 0.420$. The critical value $(d/\Lambda)_{\mathrm{S.M.}}$ below which the MOF is endlessly single mode must therefore lie in the interval [0.420, 0.425].

Second, we investigate the effect of n_{mat} on the second mode transition. We repeat the above analysis of Q behavior for $n_{\mathrm{mat}}=1.1$ and $n_{\mathrm{mat}}=1.444024$ (Fig. 3). In all cases $(d/\Lambda)_{\mathrm{S.M.}}$ is strictly bounded by 0.420 and 0.425. Hence, from a numerical point of view, $(d/\Lambda)_{\mathrm{S.M.}}$ can depend only weakly on the matrix index; the theoretical aspects of this critical value are briefly discussed at the end of this Letter. $(d/\Lambda)_{\mathrm{S.M.}}$ can be considered a critical geometrical parameter associated with the second mode cutoff or similarly with the endlessly single-mode behavior of MOFs. Note that $n_{\mathrm{mat}}=1.444024$ was used in Ref. 4, in which $(d/\Lambda)_{\mathrm{S.M.}}$ was found to be 0.406. However, in that Letter a different criterion to establish the endlessly

1266 OPTICS LETTERS / Vol. 30, No. 11 / June 1, 2005

single-mode limit was used, based on a study at fixed N_r. The fact that the Q minima disappear with increasing N_r at values close to but greater than 0.406 had been overlooked.

Third, we sum all our numerical results in the MOF parameter space $(d/\Lambda, \lambda/\Lambda)$. Figure 4 shows a phase diagram of the second mode [i.e., $(\lambda/\Lambda)_{\mathrm{S.M.}}$ as a function of d/Λ] for the three matrix indices studied, obtained for $N_r=7$, along with the extrapolated phase diagram for the infinite MOF with $n_{\mathrm{mat}}=2.5$ that results from an extrapolation of the $(\lambda/\Lambda)_{\mathrm{S.M.}}$ data computed for several values of N_r by use of a nonlinear least-squares algorithm. Note that for values of d/Λ close to $(d/\Lambda)_{\mathrm{S.M.}}$ the cutoff curves for finite and infinite N_r differ substantially. One must keep in mind that $(\lambda/\Lambda)_{\mathrm{S.M.}}$ is defined by the Q minimum and not directly by $\Im\mathrm{m}(n_{\mathrm{eff}})$. The nontrivial behavior of $(\lambda/\Lambda)_{\mathrm{S.M.}}$ with N_r should be studied by use of a W-profile fiber model, for example.

Increasing the index contrast shifts the cutoff curve toward longer wavelengths; however, the limit of the endlessly single-mode regime is conserved. Birks's analysis of scaling laws of photonic states with refractive-index contrast[12] shows that if λ, Λ, n_{mat}, or n_i varies, photonic states change, such that quantity $\nu=2\pi\Lambda(n_{\mathrm{mat}}^2-n_i^2)^{1/2}/\lambda$ remains invariant within the scalar approximation: For two structures with fixed d/Λ but different n_{mat} and n_i (say, n_{mat} and n_i and n'_{mat} and n'_i, respectively), the cutoff will occur at different wavelengths λ and λ' to keep ν constant at a value of $\nu_{\mathrm{S.M.}}$. Following this argument, we have

$$(\lambda/\Lambda)_{\mathrm{S.M.}}' = (\lambda/\Lambda)_{\mathrm{S.M.}}\left(\frac{n_{\mathrm{mat}}'^2 - n_i'^2}{n_{\mathrm{mat}}^2 - n_i^2}\right)^{1/2}. \qquad (2)$$

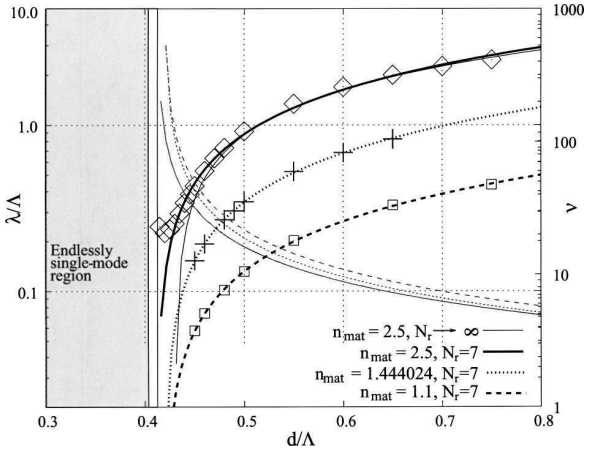

Fig. 4. Phase diagram for the second mode. The points correspond to the computed values of $(\lambda/\Lambda)_{\mathrm{S.M.}}$ for the three matrix indices for $N_r=7$; the thicker curves, to the fits. The thinner, solid curve is associated with the fit of the extrapolated results for $N_r\to\infty$ computed for $n_{\mathrm{mat}}=2.5$. The shaded region is the approximate endlessly single-mode region valid for the three matrix indices for $N_r\geqslant 7$. Lighter curves (right-hand scale) show the value of ν at cutoff for the same refractive indices as the corresponding darker curves.

We can hence draw a unified phase diagram by using quantity ν instead of λ/Λ (Fig. 4, lighter curves): MOFs with ν values that lie above the $\nu_{\mathrm{S.M.}}$ curve are multimode, whereas MOFs with ν values below the $\nu_{\mathrm{S.M.}}$ curve are single mode. As can be seen from Fig. 4, the $\nu_{\mathrm{S.M.}}$ curves for different n_{mat} are surprisingly consistent. (Keep in mind that the scaling laws used are valid only within the scalar approximation.) Furthermore, in the limit $\lambda\to 0$, the scalar approximation applied to the MOF becomes exact, and Eq. (2) is exactly verified. Consequently, the critical geometrical ratio $(\lambda/\Lambda)_{\mathrm{S.M.}}$ associated with the limit case $\lambda\to 0$ is necessarily the same for all the indices studied (see Refs. 1, 2, and 12 for the details of the scalar approximation).

In conclusion, we have explicitly shown that the ratio $(d/\Lambda)_{\mathrm{S.M.}}$ that delimits the endlessly single-mode regime in solid-core MOFs is independent of the matrix refractive index and can therefore be considered a critical geometrical parameter for the second mode cutoff. We observed that the differences between the behavior of finite and infinite structures are more pronounced near $(d/\Lambda)_{\mathrm{S.M.}}$. We have derived a generalized phase diagram for solid-core MOFs. In particular, our results demonstrate that the endlessly single-mode region is preserved for the promising chalcogenide MOFs.

This research benefited from travel support from the French and Australian governments and was produced with the assistance of the Australian Research Council. We thank the Free Software Foundation and Scilab consortium for their help. G. Renversez's e-mail address is gilles.renversez@fresnel.fr.

References

1. T. A. Birks, J. C. Knight, and P. St. J. Russell, Opt. Lett. **22**, 961 (1997).
2. A. W. Snyder and J. D. Love, *Optical Waveguide Theory* (Chapman & Hall, New York, 1983).
3. D. Marcuse, *Theory of Dielectric Optical Waveguides*, 2nd ed. (Academic, San Diego, Calif. 1991).
4. B. T. Kuhlmey, R. C. McPhedran, and C. M. de Sterke, Opt. Lett. **27**, 1684 (2002).
5. N. A. Mortensen, Opt. Express **10**, 341 (2002).
6. F. Zolla, G. Renversez, A. Nicolet, B. Kuhlmey, S. Guenneau, and D. Felbacq, *Foundations of Photonic Crystal Fibres* (Imperial College Press, London, 2005).
7. T. M. Monro, Y. D. West, D. W. Hewak, N. G. R. Broderick, and D. J. Richardson, Electron. Lett. **36**, 1998 (2000).
8. B. T. Kuhlmey, T. P. White, G. Renversez, D. Maystre, L. C. Botten, C. Martijn de Sterke, and R. C. McPhedran, J. Opt. Soc. Am. B **10**, 2331 (2002).
9. B. T. Kuhlmey, "Theoretical and numerical investigation of the physics of microstructured optical fibres," Ph.D. dissertation (Université Aix-Marseille III and University of Sydney, 2003), http://www.physics.usyd.edu.au/~borisk/physics/thesis.pdf.
10. B. T. Kuhlmey, R. C. McPhedran, C. M. de Sterke, P. A. Robinson, G. Renversez, and D. Maystre, Opt. Express **10**, 1285 (2002).
11. A free implementation of the multipole method is available at http://www.physics.usyd.edu.au/cudos/mofsoftware/.
12. T. A. Birks, D. M. Bird, T. D. Hedley, J. M. Pottage, and P. St. J. Russell, Opt. Express **12**, 69 (2003).

1146 J. Opt. Soc. Am. A/Vol. 23, No. 5/May 2006 Boyer *et al.*

Diffraction theory: application of the fast Fourier factorization to cylindrical devices with arbitrary cross section lighted in conical mounting

Philippe Boyer, Evgeny Popov, Michel Nevière, and Gilles Renversez

Institut Fresnel, Case 161, Unité Mixte de Recherche Associée au Centre National de la Recherche Scientifique (UMR 6133), Université Paul Cézanne Aix-Marseille III, et Université de Provence, Faculté des Sciences et Techniques de St. Jérôme, Avenue Escadrille Normandie Niémen, 13397 Marseille Cedex 20, France

Received May 2, 2005; revised October 7, 2005; accepted October 10, 2005; posted November 16, 2005 (Doc. ID 61886)

The differential theory of diffraction by arbitrary cross-section cylindrical objects is developed for the most general case of an incident field with a wave vector outside the cross-section plane of the object. The fast Fourier factorization technique recently developed for studying gratings is generalized to anisotropic and/or inhomogeneous media described in cylindrical coordinates; thus the Maxwell equations are reduced to a first-order differential set well suited for numerical computation. The resolution of the boundary-value problem, including an adapted S-matrix propagation algorithm, is explained in detail for the case of an isotropic medium. Numerical applications show the capabilities of the method for resolving complex diffraction problems. The method and its numerical implementation are validated through comparisons with the well-established multipole method.

OCIS codes: 050.1960, 060.0060.

1. INTRODUCTION

Cylindrical devices commonly appear in diffraction and propagation theory, and their interest has recently increased with the advent of microstructured optical fibers (MOFs).[1] An efficient method called the multipole method (MM) has already been developed to study devices composed of cylindrical inclusions.[1–3] Nevertheless, it has at least two major limitations: All the inclusions must be included in nonoverlapping circles and the refractive index of the matrix containing the inclusions must be homogeneous. In addition, the reflection matrix relating the incident and the scattered field for each individual inclusion must be obtained by other means in the case of a noncircular inclusion or inhomogeneous circular inclusion. In what follows, we present the application of the fast Fourier factorization (FFF) method to diffraction theory. This new method has none of the known limitations of the MM. Briefly, the FFF method rewrites the Maxwell equations through the use of a Fourier series. Although an isolated cylindrical object is *a priori* nonperiodic, it becomes 2π periodic with respect to the polar angle θ when it is described in cylindrical coordinates. This periodicity allows us to describe both the electromagnetic field and the diffracting object in terms of a Fourier series. As was previously done in grating theory,[4] it is now possible to reduce the Maxwell equations to a first-order differential set that must be numerically integrated. Of course the numerical treatment requires truncating the Fourier series of the field, a process that has created great numerical problems for decades but recently received a solution through what is now called the FFF method. In a recent paper[5] we proved that such a method was able to give fast converging results when a cylindrical object was illuminated under TM polarization. The aim of the present paper is to extend the theory to the most general case in which the diffraction device is illuminated with a field propagating outside the cross-section plane of the device, which leads to a full vectorial problem that does not reduce to the two classical TE and TM cases of polarizations. Moreover, the propagation equations will be derived in anisotropic media to open a way to resolve the diffraction problem of a wave by an arbitrary cylinder made of an arbitrary (lossy or lossless) anisotropic medium. In Sections 2 and 3 we present the FFF principles to obtain the set of differential equations defined in the area where the diffracting device locates. In Section 4 we discuss the complete solution of the diffracting problem in the case of an isotropic medium. In some cases, the diffracting object is invariant by a rotation of angle $T=2\pi/N_T$ (N_T is the number of subperiods of the 2π range). In Section 5 the numerical theory is adapted to take into account this subperiodicity on the T range of the polar angle coordinate θ. Finally, we validate the numerical implementation of our method with the well-established MM (Refs. 2 and 3) through several examples including the excitation of the fundamental mode of a six-hole MOF; we also discuss some aspects of the numerical efficiency and accuracy of the FFF method.

2. PRESENTATION OF THE PROBLEM

We consider a cylindrical object described in both a Cartesian coordinate system $Oxyz$ with $(\mathbf{e}_x,\mathbf{e}_y,\mathbf{e}_z)$ unit vectors and in cylindrical coordinates r,θ,z with $(\mathbf{e}_r,\mathbf{e}_\theta,\mathbf{e}_z)$ as

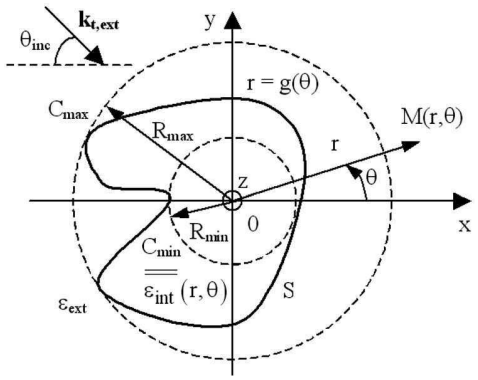

Fig. 1. Cross section of an arbitrary shaped cylindrical object filled with an anisotropic and inhomogeneous media and described by a directrix $r=g(\theta)$ containing the origin in the Oxy plane and generatrices parallel to the z axis.

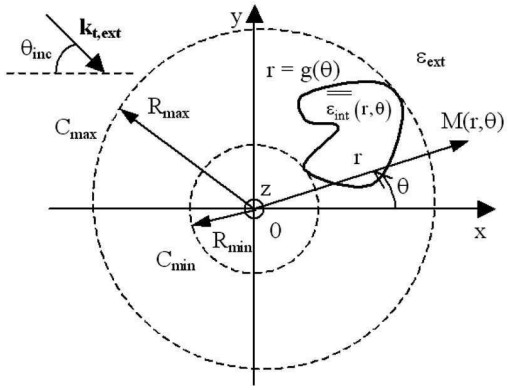

Fig. 2. Same kind of arbitrary cross section as in Fig. 1 with the origin outside the directrix.

unit vectors. Its surface (S) is defined by an arbitrary directrix located in the cross-section plane (Oxy) containing the origin as shown in Fig. 1 or outside the origin (see Fig. 2). Generatrices are straight lines parallel to the z axis. The equation of the directrix is $f(r,\theta)=0$ or $r=g(\theta)$, in which f and g are given functions. The surface (S) divides the space into two regions. The first one, the internal region denoted int, is contained inside the surface and is filled with a linear, inhomogeneous and anisotropic medium, dielectric or conducting (nonmagnetic), and its complex permittivity tensor is denoted $\overline{\overline{\epsilon}}_{\text{int}}(r,\theta)$. The second region, denoted ext, is the outside region and is filled with a homogeneous exterior medium, and its real permittivity is denoted ϵ_{ext}. The present method requires that we introduce three areas defined by two circular cylinders with directrix $C_{\min}$ and $C_{\max}$. The directrix $C_{\min}$ is the inscribed circle of the directrix of surface (S), and $C_{\max}$ is the circumscribed circle (see Fig. 1). The area included between both circular cylinders is called the modulated area. Inside this area the permittivity is described by a 2π periodic with respect to θ tensor $\bar{\bar{\epsilon}}(r,\theta)$. Unless defined otherwise, both lower-case and capital letters in bold represent vectors.

An incident plane wave with wave vector $\mathbf{k}_{\text{ext}}$ with transverse component $\mathbf{k}_{t,\text{ext}}$ and z component γ_0 falls on the device (Fig. 3). We introduce two angles: $\theta_{\text{inc}}=(-\mathbf{e}_x,\mathbf{k}_{t,\text{ext}})$ and $\varphi=(\mathbf{k}_{t,\text{ext}},\mathbf{k}_{\text{ext}})\in[-\pi/2,\pi/2]$. We assume that the plane-wave components have a harmonic $\exp(-i\omega t)$ time dependence. Thus the incident vector field of $\mathbf{E}$ and $\mathbf{H}$ reads

$$\begin{cases} \mathbf{E}^{(\text{inc})}(r,\theta,z,t)=\mathbf{A}_e\exp[i(\gamma_0 z-\omega t)] \\ \quad\times\exp[ik_{t,\text{ext}}r\cos(\theta-\theta_{\text{inc}}-\pi)] \\ \mathbf{H}^{(\text{inc})}(r,\theta,z,t)=\mathbf{A}_h\exp[i(\gamma_0 z-\omega t)] \\ \quad\times\exp[ik_{t,\text{ext}}r\cos(\theta-\theta_{\text{inc}}-\pi)] \end{cases}, \tag{1}$$

in which $\omega=2\pi/\lambda_0\sqrt{\mu_0\epsilon_0}$, $\gamma_0=-k_{\text{ext}}\sin(\varphi)$, $k_{t,\text{ext}}=\sqrt{{k_{\text{ext}}}^2-{\gamma_0}^2}$ with $k_{\text{ext}}=(2\pi/\lambda_0)\sqrt{\epsilon_{\text{ext}}/\epsilon_0}$ where λ_0 is the wavelength in vacuum. Moreover, the polarization of the incident electric field is defined by the azimuthal angle ϕ contained in the plane perpendicular to the wave vector $\mathbf{k}_{\text{ext}}$ and with basic vectors $(\mathbf{p}_1,\mathbf{p}_2)$ [$\mathbf{p}_1$ is chosen to be included in the plane $(\mathbf{k}_{\text{ext}},\mathbf{e}_z)$, see Fig. 4]. The relation between the $\mathbf{E}^{(\text{inc})}$ amplitude noted as $\mathbf{A}_e$ and the $\mathbf{H}^{(\text{inc})}$ amplitude noted as $\mathbf{A}_h$ with the incident wave vector reads thanks to the Maxwell equations in homogeneous regions:

$$\begin{cases} \mathbf{A}_e=[\cos(\phi)\mathbf{p}_1+\sin(\phi)\mathbf{p}_2]|\mathbf{E}^{(\text{inc})}| \\ \mathbf{A}_h=-\dfrac{1}{Z}\dfrac{\mathbf{k}_{\text{ext}}}{|\mathbf{k}_{\text{ext}}|}\times\mathbf{A}_e \end{cases} \quad \text{with } Z=\frac{1}{n_{\text{ext}}}\sqrt{\frac{\mu_0}{\epsilon_0}}, \tag{2}$$

in which $|\mathbf{E}^{(\text{inc})}|$ and $|\mathbf{k}_{\text{ext}}|$ are the norms of their respective vectors $\mathbf{E}^{(\text{inc})}$ and $\mathbf{k}_{\text{ext}}$. If the permittivity is a complex number, the cut of the square root $n_{\text{ext}}=\sqrt{\epsilon_{\text{ext}}}$ is then chosen as the second bisector as explained in Ref. 6. The total field has the same time dependence as the incident wave, and the invariance of the device with respect to z leads to an $\exp(i\gamma_0 z)$ dependence. Moreover, the cylindrical coordi-

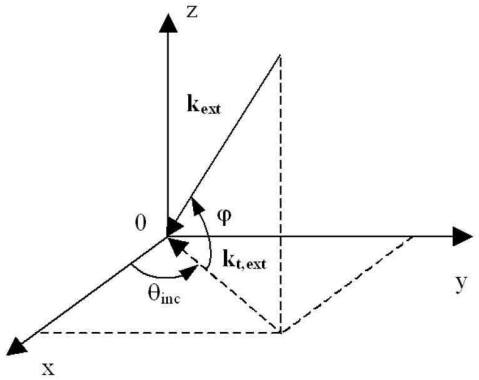

Fig. 3. Incident wave vector in the exterior homogeneous region and notations.

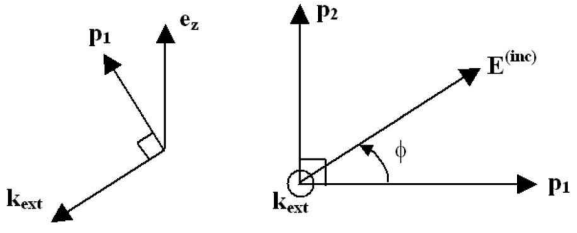

Fig. 4. Definitions and notations for the azimuthal angle ϕ of the incident electric field ($\mathbf{p}_1$ belongs to the plane defined by $\mathbf{e}_z$ and $\mathbf{k}_{\text{ext}}$).

nate system naturally implies a 2π periodicity with respect to θ. In view of a numerical implementation of the theory, an electromagnetic and geometric quantity $u(r,\theta,z,t)$ will be represented by its Fourier series truncated to the Nth order:

$$u(r,\theta,z,t) = \exp[i(\gamma_0 z - \omega t)] \sum_{n=-N}^{+N} u_n(r)\exp(in\theta) \text{ with } u_n(r)$$

$$= \frac{1}{2\pi}\int_0^{2\pi} u(r,\theta)\exp[-in\theta]\mathrm{d}\theta. \quad (3)$$

3. FAST FOURIER FACTORIZATION METHOD IN CYLINDRICAL COORDINATES EXTENDED TO A CONICAL MOUNTING

The aim of this work is to establish, in cylindrical coordinates, a set of equations satisfied by the electromagnetic field suitable for numerical computations. We make use of the recent progress in grating theory published under the name of fast Fourier factorization (FFF), but the case of cylindrical coordinates is not treated in the book describing the method.[4] The FFF method starts from the classical differential method[7] with efficient improvements in the factorizations rule concerning Fourier developments. In fact, we have to consider new factorization rules that take into account the Fourier truncation of developments and the discontinuities of any optogeometric quantities (across the diffracting surface). One of the key steps of the FFF method is to find the correct formulation in the Fourier space of the product between $\bar{\bar{\epsilon}}$ and $\mathbf{E}$ in the constitutive relation that must be injected into the Maxwell equations. Doing so, the Maxwell equations are restated in the Fourier space to obtain a set of coupled linear ordinary differential equations.

A. Formulation of the Linear Relation between E and D in a Truncated Fourier Space

1. Factorization Rules

As has been already treated in the paper concerning TM polarization,[5] the FFF method consists in finding the best formulation in a truncated Fourier space of the product between the tensor $\bar{\bar{\epsilon}}(r,\theta)$ and $\mathbf{E}$ in the modulated region when we want to calculate $\mathbf{D}$ given by

$$\mathbf{D} = \bar{\bar{\epsilon}}(\mathbf{r},\theta)\mathbf{E}. \quad (4)$$

In fact, the function $\bar{\bar{\epsilon}}(r,\theta)$ is discontinuous across the surface (S). The mathematical basis of the FFF method was established by Li[8] with factorization rules that allow one to obtain a solution of this problem. The first rule states that the Fourier components $\tilde{h}_n$ of the product $\tilde{h}(x)$ of two periodic, piecewise-smooth bounded functions $\tilde{f}(x)$ and $\tilde{g}(x)$ that are not discontinuous at the same value of x are given by Laurent's rule:

$$\tilde{h}_n = (\tilde{f}\tilde{g})_n = \sum_{m=-N}^{+N} \tilde{f}_{n-m}\tilde{g}_m. \quad (5)$$

To simplify the equations that follow, we introduce the Toeplitz matrix $[\![\tilde{f}]\!]$ defined by $([\![\tilde{f}]\!])_{n,m}=\tilde{f}_{n-m}$ and the column vector $[\tilde{g}]$ with elements $\tilde{g}_m$. Thus the last equation reads in matrix notation:

$$[\tilde{f}\tilde{g}] = [\![\tilde{f}]\!][\tilde{g}]. \quad (6)$$

The second rule given by Li[8] states that a product of two piecewise-smooth, bounded periodic functions that have only pairwise-complementary jump discontinuities (i.e., that have a continuous product) cannot be factorized by Laurent's rule, but it can be factorized by the inverse rule:

$$[\tilde{f}\tilde{g}]_n = \sum_{m=-N}^{+N} \left(\left[\!\!\left[\frac{1}{\tilde{f}} \right]\!\!\right]^{-1} \right)_{n,m} \tilde{g}_m. \quad (7)$$

Or in matrix notation,

$$[\tilde{f}\tilde{g}] = \left[\!\!\left[\frac{1}{\tilde{f}} \right]\!\!\right]^{-1} [\tilde{g}]. \quad (8)$$

Finally, the most general situation concerns a product of two piecewise-smooth, bounded periodic functions that have discontinuities at the same value of x with noncomplementary jump discontinuities. Such a product can be correctly factorized neither by Laurent's rule nor by the inverse rule. This last case occurs in Eq. (4).

2. Intermediate Notations

The basic idea of the FFF method is to use the first two rules to write a new formulation of Eq. (4), thanks to a suitable continuation of the concept of normal vector. We consider at each point of the surface (S) the normal vector of (S) noted as $\mathbf{N}$ whose components are N_r, N_θ, N_z, and two orthogonal tangential vectors of (S) denoted $\mathbf{T}_1$ with components $(T_{1r}, T_{1\theta}, T_{1z})$ and $\mathbf{T}_2$ with components $(T_{2r}, T_{2\theta}, T_{2z})$ such that $\mathbf{N}=\mathbf{T}_2\times\mathbf{T}_1$ (see Fig. 5). The projections of the fields $\mathbf{E}$ and $\mathbf{D}$ on $\mathbf{T}_1$, $\mathbf{N}$, and $\mathbf{T}_2$ define three field components continuous across the surface (S): $\mathbf{E}_{T_1}$, $\mathbf{D}_N$, and $\mathbf{E}_{T_2}$; they permit us to create a column denoted $\mathbf{F}_\epsilon$ respectively made with these components, whose size is $3(2N+1)$. If we define a generalization of the scalar product applied to a vector $\tilde{\mathbf{v}}$ and a matrix $\mathbf{P}$ by

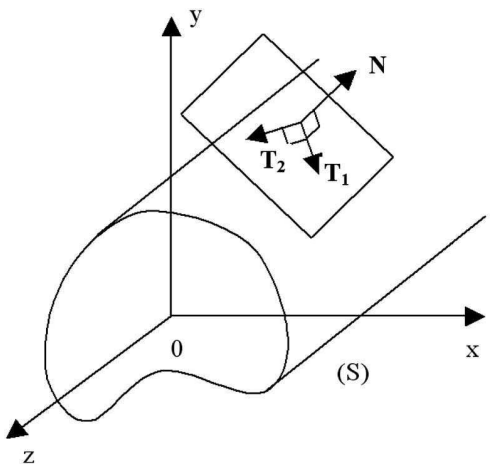

Fig. 5. Tangential and normal vectors of a cylindrical object.

$$\mathbf{v}\cdot\mathbf{P}=\begin{bmatrix}v_r\\v_\theta\\v_z\end{bmatrix}\cdot\begin{bmatrix}P_{rr}&P_{r\theta}&P_{rz}\\P_{\theta r}&P_{\theta\theta}&P_{\theta z}\\P_{zr}&P_{z\theta}&P_{zz}\end{bmatrix}=\begin{bmatrix}v_rP_{rr}+v_\theta P_{\theta r}+v_zP_{zr}\\v_rP_{r\theta}+v_\theta P_{\theta\theta}+v_zP_{z\theta}\\v_rP_{rz}+v_\theta P_{\theta z}+v_zP_{zz}\end{bmatrix}, \tag{9}$$

we obtain

$$\mathbf{F}_\epsilon = O_\epsilon \mathbf{E} \tag{10}$$

with

$$O_\epsilon=\begin{bmatrix}T_{1r}&T_{1\theta}&T_{1z}\\(\mathbf{N}\cdot\bar{\bar{\epsilon}})_r&(\mathbf{N}\cdot\bar{\bar{\epsilon}})_\theta&(\mathbf{N}\cdot\bar{\bar{\epsilon}})_z\\T_{2r}&T_{2\theta}&T_{2z}\end{bmatrix}. \tag{11}$$

Thus for the electric field we can write $\mathbf{E}=C_\epsilon\mathbf{F}_\epsilon$ with $C_\epsilon=O_\epsilon^{-1}$. Tedious algebraic calculations lead to

$$C_\epsilon=\frac{1}{\mathbf{N}\cdot\bar{\bar{\epsilon}}\cdot\mathbf{N}}\begin{bmatrix}((\mathbf{N}\cdot\bar{\bar{\epsilon}})&\mathbf{T}_2)_r&N_r&-((\mathbf{N}\cdot\bar{\bar{\epsilon}})&\mathbf{T}_1)_r\\((\mathbf{N}\cdot\bar{\bar{\epsilon}})&\mathbf{T}_2)_\theta&N_\theta&-((\mathbf{N}\cdot\bar{\bar{\epsilon}})&\mathbf{T}_1)_\theta\\((\mathbf{N}\cdot\bar{\bar{\epsilon}})&\mathbf{T}_2)_z&N_z&-((\mathbf{N}\cdot\bar{\bar{\epsilon}})&\mathbf{T}_1)_z\end{bmatrix}. \tag{12}$$

Then $\mathbf{D}=\bar{\bar{\epsilon}}\mathbf{E}=\bar{\bar{\epsilon}}C_\epsilon\mathbf{F}_\epsilon$, and finally,

$$\mathbf{D}=\bar{\bar{\epsilon}}C_\epsilon O_\epsilon\mathbf{E}. \tag{13}$$

3. New Relation between [**D**] *and* [**E**]

We will write this last equation in the truncated Fourier space using the factorization rules mentioned above. Since $\bar{\bar{\epsilon}}C_\epsilon$ is discontinuous and $\mathbf{F}_\epsilon$ is continuous, we apply Laurent's rule for these two factors. Introducing the column [**D**] made of three blocks $[D_r]$, $[D_\theta]$, and $[D_z]$, each block containing the Fourier coefficients of the corresponding vector component, we write $[\mathbf{D}]=[\![\bar{\bar{\epsilon}}C_\epsilon]\!][\mathbf{F}_\epsilon]$. Then the inverse rule is used since $\mathbf{F}_\epsilon=O_\epsilon\mathbf{E}$ is continuous while O_ϵ and **E** are discontinuous: $[O_\epsilon\mathbf{E}]=[\![O_\epsilon^{-1}]\!]^{-1}[\mathbf{E}]=[\![C_\epsilon]\!]^{-1}[\mathbf{E}]$. Finally, we find

$$[\mathbf{D}]=Q_\epsilon(\mathbf{r})[\mathbf{E}], \tag{14}$$

with

$$Q_\epsilon(r)=[\![\bar{\bar{\epsilon}}C_\epsilon]\!][\![C_\epsilon]\!]^{-1}. \tag{15}$$

B. Maxwell Equations in a Truncated Fourier Space

Differentiating the series in Eq. (3) with respect to θ results in multiplying the nth term by "in". Thus introducing a diagonal matrix α such that $(\alpha)_{nm}=n\delta_{nm}$, the derivation reads in matrix notation as

$$\frac{\partial[U]}{\partial\theta}=i\alpha[U]. \tag{16}$$

According to the z and t dependence of the total fields, the Maxwell equations written in the cylindrical coordinate system become

$$\frac{1}{r}\alpha[E_z]-\gamma_0[E_\theta]-\omega[B_r]=0, \tag{17}$$

$$i\gamma_0[E_r]-\frac{d[E_z]}{dr}-i\omega[B_\theta]=0, \tag{18}$$

$$\frac{1}{r}\left([E_\theta]+r\frac{d[E_\theta]}{dr}-i\alpha[E_r]\right)-i\omega[B_z]=0, \tag{19}$$

$$\frac{1}{r}\alpha[H_z]-\gamma_0[H_\theta]+\omega[D_r]=0, \tag{20}$$

$$i\gamma_0[H_r]-\frac{d[H_z]}{dr}+i\omega[D_\theta]=0, \tag{21}$$

$$\frac{1}{r}\left([H_\theta]+r\frac{d[H_\theta]}{dr}-i\alpha[H_r]\right)+i\omega[D_z]=0. \tag{22}$$

From Eq. (14) we obtain the expression of each block of [**D**] in the cylindrical coordinate system in terms of the **E** blocks. We introduce the following notation for the Q_ϵ matrix:

$$Q_\epsilon=\begin{bmatrix}Q_{\epsilon,rr}&Q_{\epsilon,r\theta}&Q_{\epsilon,rz}\\Q_{\epsilon,\theta r}&Q_{\epsilon,\theta\theta}&Q_{\epsilon,\theta z}\\Q_{\epsilon,zr}&Q_{\epsilon,z\theta}&Q_{\epsilon,zz}\end{bmatrix}. \tag{23}$$

Equation (20) leads to

$$[E_r(r)]=Q_{\epsilon,rr}^{-1}\left(\frac{\gamma_0}{\omega}[H_\theta(r)]-\frac{\alpha}{r\omega}[H_z(r)]-Q_{\epsilon,r\theta}[E_\theta(r)]-Q_{\epsilon,rz}[E_z(r)]\right), \tag{24}$$

and Eq. (17) becomes

$$[H_r(r)]=\frac{1}{\mu_0\omega}\left(\frac{\alpha}{r}[E_z(r)]-\gamma_0[E_\theta(r)]\right). \tag{25}$$

These two last equations and Eq. (23) permit us to rewrite Eqs. (18), (19), (21), and (22). Finally, we obtain a set of first-order differential equations written in a four-block matrix form:

$$\frac{d}{dr}\begin{bmatrix}[E_\theta]\\[E_z]\\[H_\theta]\\[H_z]\end{bmatrix}=iM(r)\begin{bmatrix}[E_\theta]\\[E_z]\\[H_\theta]\\[H_z]\end{bmatrix}, \tag{26}$$

with

$$M(r)=\begin{bmatrix} -\frac{1}{r}\alpha Q_{\epsilon,rr}{}^{-1}Q_{\epsilon,r\theta}+\frac{i}{r}I_d & -\frac{1}{r}\alpha Q_{\epsilon,rr}{}^{-1}Q_{\epsilon,rz} & \frac{\gamma_0}{\omega r}\alpha Q_{\epsilon,rr}{}^{-1} & \omega\mu_0 I_d-\frac{\alpha}{\omega r^2}Q_{\epsilon,rr}{}^{-1}\alpha \\ -\gamma_0 Q_{\epsilon,rr}{}^{-1}Q_{\epsilon,r\theta} & -\gamma_0 Q_{\epsilon,rr}{}^{-1}Q_{\epsilon,rz} & \frac{\gamma_0{}^2}{\omega}Q_{\epsilon,rr}{}^{-1}-\omega\mu_0 I_d & -\frac{\gamma_0}{r\omega}Q_{\epsilon,rr}{}^{-1}\alpha \\ \omega(Q_{\epsilon,zr}Q_{\epsilon,rr}{}^{-1}Q_{\epsilon,r\theta}-Q_{\epsilon,z\theta})-\frac{\gamma_0}{\mu_0\omega r}\alpha & \frac{\alpha^2}{\omega\mu_0 r^2}+\omega(Q_{\epsilon,zr}Q_{\epsilon,rr}{}^{-1}Q_{\epsilon,rz}-Q_{\epsilon,zz}) & \frac{i}{r}I_d-\gamma_0 Q_{\epsilon,zr}Q_{\epsilon,rr}{}^{-1} & Q_{\epsilon,zr}Q_{\epsilon,rr}{}^{-1}\frac{\alpha}{r} \\ \omega(Q_{\epsilon,\theta\theta}-Q_{\epsilon,\theta r}Q_{\epsilon,rr}{}^{-1}Q_{\epsilon,r\theta})-\frac{\gamma_0{}^2}{\mu_0\omega}I_d & \frac{\gamma_0}{\mu_0\omega r}\alpha+\omega(Q_{\epsilon,\theta z}-Q_{\epsilon,\theta r}Q_{\epsilon,rr}{}^{-1}Q_{\epsilon,rz}) & Q_{\epsilon,\theta r}Q_{\epsilon,rr}{}^{-1}\gamma_0 & -Q_{\epsilon,\theta r}Q_{\epsilon,rr}{}^{-1}\frac{\alpha}{r} \end{bmatrix}, \tag{27}$$

where I_d is the identity matrix. It is important to notice that the $M(r)$ matrix depends only on the r coordinate and that its size is $4(2N+1)\times 4(2N+1)$. In brief, Eq. (26) is a new formulation of the Maxwell equations in cylindrical coordinates in a truncated Fourier space, which is valid in any lossless or lossy, anisotropic and/or inhomogeneous medium.

4. RESOLUTION OF THE DIFFRACTION PROBLEM IN THE CASE OF AN ISOTROPIC AND HOMOGENEOUS MEDIUM

The resolution of the diffraction problem is much simpler if the diffracting object is made of an isotropic and homogeneous material, since the field in such a region can then be expressed in terms of Bessel functions. Thus, from now on, we consider that the region (int) is filled with an isotropic and homogeneous medium. Its permittivity tensor is reduced to a complex number ϵ_{int} (see Fig. 1).

A. Linear Relation between E and D in the Case of an Isotropic Medium

In the present case, the tensor $\bar{\bar{\epsilon}}$ in Eq. (4) (defined in the modulated area) becomes a function $\epsilon(r,\theta)$. So we have $\mathbf{N}\cdot\bar{\bar{\epsilon}}\cdot\mathbf{N}=\epsilon(r,\theta)(\mathbf{N}\cdot I_d)\cdot\mathbf{N}=\epsilon(r,\theta)$. Moreover, $(\mathbf{N}\cdot\bar{\bar{\epsilon}})\ \mathbf{T}_2=\epsilon(r,\theta)\mathbf{N}\ \ \mathbf{T}_2=\epsilon(r,\theta)\mathbf{T}_1$ and $(\mathbf{N}\cdot\bar{\bar{\epsilon}})\ \mathbf{T}_1=\epsilon(r,\theta)\mathbf{N}\ \ \mathbf{T}_1=-\epsilon(r,\theta)\mathbf{T}_2$. Thus the term $\bar{\bar{\epsilon}}C_\epsilon$ reduces to

$$\begin{bmatrix} \epsilon N_\theta & N_r & 0 \\ -\epsilon N_r & N_\theta & 0 \\ 0 & 0 & 1 \end{bmatrix}.$$

Considering $\tilde{f}(x)$ and $\tilde{g}(x)$ as 2π periodic functions discontinuous at different values of x and using the first factorization rule, we obtain the following results: $[\![\tilde{f}\tilde{g}]\!]=[\![\tilde{f}]\!][\![\tilde{g}]\!]$. By the use of this property into the Toeplitz matrices $[\![C_\epsilon]\!]$ and $[\![\epsilon C_\epsilon]\!]$ in Eq. (14), we obtain the same formula as in the work on the TM case[5]:

$$Q_\epsilon=\begin{bmatrix} [\![\epsilon]\!][\![N_\theta{}^2]\!]+\left[\!\left[\frac{1}{\epsilon}\right]\!\right]^{-1}[\![N_r{}^2]\!] & -\left([\![\epsilon]\!]-\left[\!\left[\frac{1}{\epsilon}\right]\!\right]^{-1}\right)[\![N_rN_\theta]\!] & 0 \\ -\left([\![\epsilon]\!]-\left[\!\left[\frac{1}{\epsilon}\right]\!\right]^{-1}\right)[\![N_rN_\theta]\!] & [\![\epsilon]\!][\![N_r{}^2]\!]+\left[\!\left[\frac{1}{\epsilon}\right]\!\right]^{-1}[\![N_\theta{}^2]\!] & 0 \\ 0 & 0 & [\![\epsilon]\!] \end{bmatrix}. \tag{28}$$

Since $[\mathbf{D}]$ and $[\mathbf{E}]$ have dimension $3(2N+1)$, the size of this matrix is $3(2N+1)\times 3(2N+1)$. Moreover, we notice that the matrix Q_ϵ contains the Toeplitz matrices $[\![N_r{}^2]\!]$, $[\![N_\theta{}^2]\!]$, and $[\![N_rN_\theta]\!]$. But N_r and N_θ are defined only on the surface (S); that is why we need to extend their definition inside the whole modulated area. The extension can be done in different ways. If the surface is well defined along the interval $[0,2\pi]$ of θ (g is continuous on $[0,2\pi]$), the unit vector normal to the surface (S) can read as

$$\mathbf{N}[r=g(\theta),\theta]=\left.\frac{\mathbf{grad}(f)}{|\mathbf{grad}(f)|}\right|_{r=g(\theta)} \quad \text{with } f(r,\theta)=r-g(\theta)$$
$$=0. \tag{29}$$

From its definition, $\mathbf{N}$ depends only on θ and is defined on (S) only. But we extend its definition to the entire modulated area ($R_{\min}<r<R_{\max}$) by introducing a new vector continuous across the diffracting surface (S) and defined by

$$r\in[R_{\min},R_{\max}],\quad \mathbf{N}(r,\theta)=\left.\frac{\mathbf{grad}(f)}{|\mathbf{grad}(f)|}\right|_{r=g(\theta)}. \tag{30}$$

A second way to extend the normal vector consists in considering only the value of $\mathbf{N}$ at the intersection points between the surface (S) and the circle in the cross section of radius r, and taking an arbitrary vector elsewhere, providing that we avoid discontinuities and strong variations to avoid the Gibbs phenomenon. The main disadvantage of the second method is the longer needed computation time related to the fact that the normal vector now depends on r and θ, which requires computing the Fourier coefficients of its three components at any integration

step that will occur in the numerical resolution of the boundary-value problem.

B. Field Expressions in the Homogeneous Regions

According to the r dependence of the $M(r)$ matrix, no explicit expression of the field in the modulated area can be found. On the other hand, the Maxwell equations in the homogeneous regions (j=int or ext) permit us to obtain a set of independent second-order differential equations governing the Fourier coefficients of the z component of the magnetic and electric field $G_{z,n}$ depending on $k_{t,j}r$:

$$(k_{t,j}r)^2\frac{\mathrm{d}^2G_{z,n}}{\mathrm{d}(k_{t,j}r)^2}+k_{t,j}r\frac{\mathrm{d}G_{z,n}}{\mathrm{d}(k_{t,j}r)}+[(k_{t,j}r)^2-n^2]G_{z,n}=0$$
$$\text{with } G_{z,n}\in\{E_{z,n},H_{z,n}\}, \tag{31}$$

the solutions of which are

$$H_{z,n}=A_{h,n}^{(j)}J_n(k_{t,j}r)+B_{h,n}^{(j)}H_n^+(k_{t,j}r),$$
$$E_{z,n}=A_{e,n}^{(j)}J_n(k_{t,j}r)+B_{e,n}^{(j)}H_n^+(k_{t,j}r). \tag{32}$$

with $k_{t,j}{}^2=k_j{}^2-\gamma_0{}^2$ and $k_j{}^2=\omega^2\mu_0\epsilon_j$. The others components of the field are given by

$$H_r=\frac{1}{k_{t,j}{}^2}\left(i\gamma_0\frac{\partial H_z}{\partial r}-\frac{i\omega\epsilon_j}{r}\frac{\partial E_z}{\partial\theta}\right),$$
$$H_\theta=\frac{1}{k_{t,j}{}^2}\left(\frac{i\gamma_0}{r}\frac{\partial H_z}{\partial_\theta}+i\omega\epsilon_j\frac{\partial E_z}{\partial r}\right),$$
$$E_r=\frac{1}{k_{t,j}{}^2}\left(i\gamma_0\frac{\partial E_z}{\partial r}+\frac{i\omega\mu_0}{r}\frac{\partial H_z}{\partial\theta}\right),$$
$$E_\theta=\frac{1}{k_{t,j}{}^2}\left(\frac{i\gamma_0}{r}\frac{\partial E_z}{\partial_\theta}-i\omega\mu_0\frac{\partial H_z}{\partial r}\right). \tag{33}$$

Equations (32) and (33), which allow us to find the components of the field developments, can be written in a matrix form. Thus we define a matrix $\Psi^{(j)}(r)$ made of 4×4 blocks, each block size being $(2N+1)$. This matrix links the vector $[F(r)]$ containing the components of successively E_θ, E_z, H_θ, and H_z with the vector $[V^{(j)}(r)]$ containing the components $A_{e,n}^{(j)}J_n(k_{t,j}r)$, $A_{h,n}^{(j)}J_n(k_{t,j}r)$, $B_{e,n}^{(j)}H_n^+(k_{t,j}r)$, and $B_{h,n}^{(j)}H_n^+(k_{t,j}r)$ by

$$[F(r)]=\Psi^{(j)}(r)[V^{(j)}(r)] \text{ with } \Psi^{(j)}(r)$$
$$=\begin{bmatrix}\frac{1}{r}p^{(j)} & q_e^{(j)} & \frac{1}{r}p^{(j)} & q_h^{(j)}\\ I_d & 0 & I_d & 0\\ -\frac{\epsilon_j}{\mu_0}q_e^{(j)} & \frac{1}{r}p^{(j)} & -\frac{\epsilon_j}{\mu_0}q_h^{(j)} & \frac{1}{r}p^{(j)}\\ 0 & I_d & 0 & I_d\end{bmatrix}, \tag{34}$$

in which

$$(p^{(j)})_{nm}=-\frac{\gamma_0}{k_{t,j}{}^2}n\delta_{nm}, \tag{35}$$

$$(q_e^{(j)})_{nm}=-\frac{i\omega\mu_0}{k_{t,j}{}^2}\left(\frac{n}{r}-k_{t,j}\frac{J_{n+1}(k_{t,j}r)}{J_n(k_{t,j}r)}\right)\delta_{nm}, \tag{36}$$

$$(q_h^{(j)})_{nm}=-\frac{i\omega\mu_0}{k_{t,j}{}^2}\left(\frac{n}{r}-k_{t,j}\frac{H_{n+1}^+(k_{t,j}r)}{H_n^+(k_{t,j}r)}\right)\delta_{nm}. \tag{37}$$

We notice that the size of vectors $[F(r)]$ and $[V^{(j)}(r)]$ is $4(2N+1)$.

C. Integration of the Differential Set with the *S*-matrix Propagation Algorithm

A basic integration with a shooting method through the modulus area gives the transmission matrix T of the diffracting device. However, the T matrix may be ill-conditioned because of numerical contaminations. Important index gap or strong growth of the function $f(r,\theta)$ increases such numerical contaminations. To improve the convergence of the results, the S-matrix propagation algorithm is used.[4,9] In this subsection, this algorithm is presented in a matrix formulation. The modulated area is divided into L slices of which the circular boundary cylinders have radius r_s, $s\in[1,L+1]$ ($r_1=R_{\min}$ and $r_{L+1}=R_{\max}$). We introduce a infinitely thin homogeneous layer with a permittivity of ϵ_{ext} between each slice except at $R_{\min}$ (see Fig. 6). The resolution of the diffraction problem uses a shooting method that consists of turning the boundary-value problem into an initial-value problem. At the sth slice, we take $4(2N+1)$ independent initial column vectors noted as $[V_p]:([V_p])_i=\delta_{pi}$ with $i\in[1,4(2N+1)]$. In what follows, the sign will denote a matrix, used in the integration process, built from a list of column vectors. These columns form the identity matrix

$$\hat{V}(r_s)=(\ldots,[V_p],\ldots)=I_d, \tag{38}$$

and the corresponding fields read $\hat{F}(r_s)=\Psi^{(\text{ext})}(r_s)I_d=\Psi^{(\text{ext})}(r_s)$ at r_s [if $s=1$ we take $\Psi^{(\text{int})}(r_1)$]. The matrix $\hat{F}(r_s)$

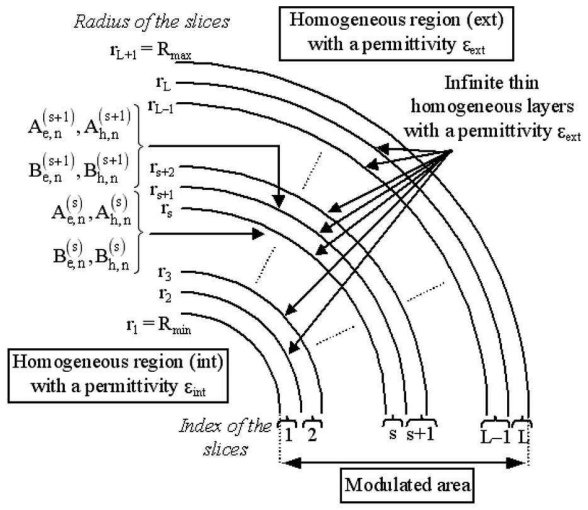

Fig. 6. Notations of the splitting of the modulated area for the S-propagation algorithm (the coefficients $A_{f,n}^{(s)}$ and $B_{f,n}^{(s)}$ with $f=e$ or h are amplitudes of the field in the infinite thin homogeneous layer at $r=r_s$).

contains the column vectors $([F(r_s)])_i$ with $i \in [1,4(2N+1)]$, used as initial values of the field, and we integrate the differential set of Eq. (26) using a suitable algorithm (combining Runge–Kutta and Adams–Moulton algorithms). Compared with Ref. 3, the notations of the $\Psi^{(j)}$ matrix are changed [see Eqs. (31) and (42) in Ref. 3]: The $\Psi^{(j)}$ matrices are normalized by the Bessel and the Hankel functions so as to inject well-conditioned matrices as an initial value in the integration process. This new notation induces that the vector $[V^{(j)}]$ contains the Bessel and the Hankel functions. At the end of the integration, the result is a matrix noted as $\hat{F}_{\text{integ}}(r_{s+1})$ giving the field at r_{s+1}, from which we derived from Eq. (34) the matrix

$$\hat{V}(r_{s+1}) = \{\Psi^{(\text{ext})}(r_{s+1})\}^{-1}\hat{F}_{\text{integ}}(r_{s+1});$$

using Eq. (38), we obtain

$$\hat{V}(r_{s+1}) = \{\Psi^{(\text{ext})}(r_{s+1})\}^{-1}\hat{F}_{\text{integ}}(r_{s+1})\hat{V}(r_s).$$

This last equation shows that the transmission matrix $T^{(s)}$ that links the coefficients of the developments of the field at r_s to the coefficients of the development of the field at r_{s+1} is given by

$$T^{(s)} = \{\Psi^{(\text{ext})}(r_{s+1})\}^{-1}\hat{F}_{\text{integ}}(r_{s+1}). \tag{39}$$

The integration through each slice provides a $T^{(s)}$ matrix that links the field at r_{s+1} to the field at r_s. From this matrix, we deduce a $S^{(s)}$ matrix that links the fields at r_s and r_1, defined by

$$s \in [1,L+1], \quad \begin{bmatrix} \vdots \\ B_{e,n}^{(s)}H_n^+(k_{t,\text{ext}}r_s) \\ \vdots \\ B_{h,n}^{(s)}H_n^+(k_{t,\text{ext}}r_s) \\ \vdots \\ A_{e,n}^{(1)}J_n(k_{t,\text{int}}r_1) \\ \vdots \\ A_{h,n}^{(1)}J_n(k_{t,\text{int}}r_1) \\ \vdots \end{bmatrix} = \begin{bmatrix} S_{11}^{(s)} & S_{12}^{(s)} \\ S_{21}^{(s)} & S_{22}^{(s)} \end{bmatrix} \begin{bmatrix} \vdots \\ B_{e,n}^{(1)}H_n^+(k_{t,\text{int}}r_1) \\ \vdots \\ B_{h,n}^{(1)}H_n^+(k_{t,\text{int}}r_1) \\ \vdots \\ A_{e,n}^{(s)}J_n(k_{t,\text{ext}}r_s) \\ \vdots \\ A_{h,n}^{(s)}J_n(k_{t,\text{ext}}r_s) \\ \vdots \end{bmatrix}. \tag{40}$$

Here the index (s) of the amplitudes $A_{e,n}^{(s)}$, $A_{h,n}^{(s)}$, $B_{e,n}^{(s)}$, and $B_{h,n}^{(s)}$ can be replaced by (int) when $s=1$ and (ext) when $s=L+1$. For the particular case of $s=1$, the $S^{(s)}$ matrix becomes the identical matrix and $k_{t,\text{ext}}$ becomes equal to $k_{t,\text{int}}$. We have checked that all blocks of this matrix are well conditioned (see also Ref. 4). Briefly, the $T^{(s)}$ matrix links the fields at layer (s) and the fields at layer $(s+1)$ while the $S^{(s)}$ matrix links the scattered fields and the incident fields. The $S^{(s)}$ matrix blocks of the $(s+1)$th interface are expressed according to those of the sth interface and to the $T^{(s)}$ matrix blocks $T_{mn}^{(s)}$ of the sth slice:

$$\begin{aligned} S_{22}^{(s+1)} &= S_{22}^{(s)}[T_{11}^{(s)} + T_{12}^{(s)}S_{12}^{(s)}]^{-1}, \\ S_{12}^{(s+1)} &= [T_{21}^{(s)} + T_{22}^{(s)}S_{12}^{(s)}][T_{11}^{(s)} + T_{12}^{(s)}S_{12}^{(s)}]^{-1}, \\ S_{21}^{(s+1)} &= S_{21}^{(s)} - S_{22}^{(s+1)}T_{12}^{(s)}S_{11}^{(s)}, \\ S_{11}^{(s+1)} &= T_{22}^{(s)}S_{11}^{(s)} - S_{12}^{(s+1)}T_{12}^{(s)}S_{11}^{(s)}. \end{aligned} \tag{41}$$

At the end of the integration across the modulated area, we obtain the S matrix of the whole scattering device, which depends only on the surface (S) and on the optical parameters of the media. This matrix links the diffracted field at $R_{\max}$ and $R_{\min}$ to the incident field at $R_{\max}$ and $R_{\min}$. In fact, expressing the exponential function in Eq. (1) in terms of Bessel functions,[10] the incident field can be defined in the form

$$\begin{cases} H_z^{(\text{inc})} = \exp(i\gamma_0 z)\displaystyle\sum_{n-\infty}^{+\infty} A_{h,z}\exp(-in\theta_{\text{inc}})i^n J_n(k_{t,\text{ext}}r)\exp(in\theta) \\ E_z^{(\text{inc})} = \exp(i\gamma_0 z)\displaystyle\sum_{n-\infty}^{+\infty} A_{e,z}\exp(-in\theta_{\text{inc}})i^n J_n(k_{t,\text{ext}}r)\exp(in\theta) \end{cases}. \tag{42}$$

Inside the internal region containing the origin of coordinates, we must state $B_{e,n}^{(\text{int})} = B_{h,n}^{(\text{int})} = 0 \quad n$ to avoid a divergence of the field $(H_n^+(0) \to \infty \quad n)$. This condition allows us to derive through Eq. (40)

$$\begin{bmatrix} \vdots \\ A_{e,n}^{(\text{int})} \\ \vdots \\ A_{h,n}^{(\text{int})} \\ \vdots \end{bmatrix} = S_{22}\begin{bmatrix} \vdots \\ A_{e,z}i^n\exp(-in\theta_{\text{inc}}) \\ \vdots \\ A_{h,z}i^n\exp(-in\theta_{\text{inc}}) \\ \vdots \end{bmatrix},$$

$$\begin{bmatrix} \vdots \\ B_{e,n}^{(\text{ext})} \\ \vdots \\ B_{h,n}^{(\text{ext})} \\ \vdots \end{bmatrix} = S_{12}\begin{bmatrix} \vdots \\ A_{e,z}i^n\exp(-in\theta_{\text{inc}}) \\ \vdots \\ A_{h,z}i^n\exp(-in\theta_{\text{inc}}) \\ \vdots \end{bmatrix}. \tag{43}$$

5. NUMERICAL APPLICATION ON PARTICULAR CASES

A. First Validation Study

The present theory has been implemented using the FORTRAN programming language. It is worth noticing that the results of the TM and TE polarization studied

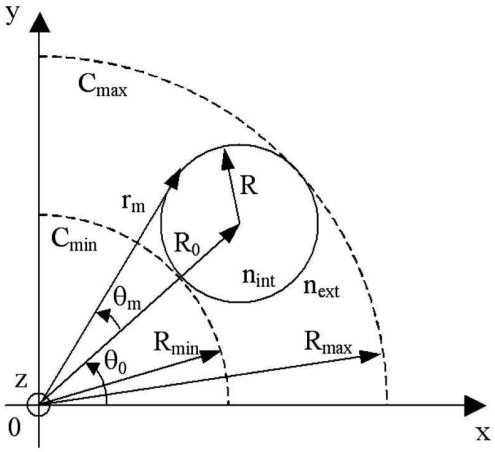

Fig. 7. Cross section of a circular cylinder centered outside the origin and filled with isotropic and homogeneous media with $R=1\ \mu$m, $R_0=2\ \mu$m, $\theta_0=0°$, $n_{\text{int}}=1.6+0.2i$, and $n_{\text{ext}}=1$, and notations.

previously[5] are associated with the particular case of conical diffraction with $\gamma_0=0$. In this case, the current numerical implementation written for conical diffraction gives the same results as the ones computed previously in Ref. 5. To validate and illustrate in more detail the FFF method applied to cylindrical coordinates, we first study the simple case of one circular cylinder centered outside the origin with a radius R and the center with (R_0,θ_0) polar coordinates (see Fig. 7). The r coordinate defined on the circle and related to the maximal angle θ_m defined is noted as $r_m=\sqrt{{R_0}^2-R^2}$. On the θ range where the circle is defined in the cross section ($[\theta_0-\theta_m,\theta_0+\theta_m]$), the diffracting surface directrix equation is given by

$$r(\theta)=R_0\cos(\theta)\pm\sqrt{R^2-{R_0}^2\sin^2(\theta)},$$

$$\theta(r)=\cos^{-1}\left(\frac{r^2+{r_0}^2-R^2}{2r_0r}\right), \tag{44}$$

where the + sign is related to $r\in[R_0-R,r_m]$ and the − sign is related to $r\in[r_m,R_0+R]$. In the modulated area, the permittivity is described by a step function $\epsilon(r,\theta)$ with respect to θ; thus obtaining its Fourier development and the Toeplitz matrix $[\![\epsilon]\!]$ remains easy. The $N_\theta(\theta)$ function is given by

$$N_\theta(\theta)=\frac{r_0}{R}\sin(\theta-\theta_0). \tag{45}$$

We mention that the r component of the surface's normal vector is deduced by $N_r=\pm\sqrt{1-{N_\theta}^2}$. Outside $[\theta_0-\theta_m,\theta_0+\theta_m]$ we could state that the ${N_\theta}^2$ function is extended to unity. In this case, the ${N_\theta}^2$, ${N_r}^2$, and N_rN_θ functions would have the advantages of the continuity and of the r independency. Since these functions would be r independent, their Toeplitz matrices would be calculated once before the integration process. However, it is interesting to point out that, along a circle with radius r included in the modulated area, the ${N_\theta}^2(r,\theta)$ is defined only by one or two points with the same $|{N_\theta}^2|$ value. Then we have chosen a straight extension of a ${N_\theta}^2(r,\theta)$ function with a constant value of ${N_\theta}^2$ evaluated at $\theta(r)$. The main advantage of such an extension is the simplicity of the calculation of its developments: $[{N_\theta}^2]_0={N_\theta}^2[\theta(r)]$ and $[{N_\theta}^2]_n=0,\quad n\neq 0$. On the other hand, the $N_rN_\theta(r,\theta)$ function becomes discontinuous, which leaves the determination of its Fourier coefficients easy but increases the Gibbs phenomena. The numerical results show that the two extensions lead to similar convergence when the order of the Fourier developments is increased.

The differential cross section (DCS) that is determined with the asymptotic form of the Hankel functions of the diffracted field for $r\to\infty$ is given by

$$\sigma(\theta)=2\pi\frac{{k_0}^2}{{k_{t,\text{ext}}}^2}\left[\left|\sqrt{\frac{2}{\pi k_{t,\text{ext}}}}\sum_{n=-\infty}^{+\infty}(-i)^nB_{e,n}^{(\text{ext})}e^{in\theta}\right|^2+\frac{\mu_0}{\epsilon_{\text{ext}}}\left|\sqrt{\frac{2}{\pi k_{t,\text{ext}}}}\sum_{n=-\infty}^{+\infty}(-i)^nB_{h,n}^{(\text{ext})}e^{in\theta}\right|^2\right]. \tag{46}$$

To validate our theory and its numerical implementation, we compare the FFF method results with the ones obtained with the MM.[1,3] We study the scattering by a single cylinder (see Fig. 7) and compute the DCS with the two methods. Figure 8 shows the results of the DCS for $\lambda_0=1\ \mu$m and $\lambda_0=0.5\ \mu$m with a logarithmic scale for the Y axis; as can be seen, the FFF method results agree

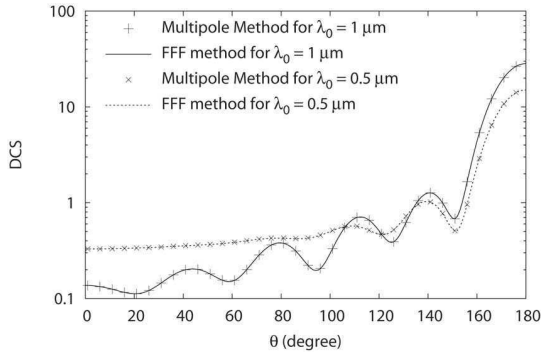

Fig. 8. DCS ($\theta=0°$ to 180°) for the circular cylinder in Fig. 7 with $\theta_{\text{inc}}=0°$, $\varphi=30°$, $\phi=0°$, and $N=50$; comparison of the FFF method and MM for $\lambda_0=1\ \mu$m and $\lambda_0=0.5\ \mu$m.

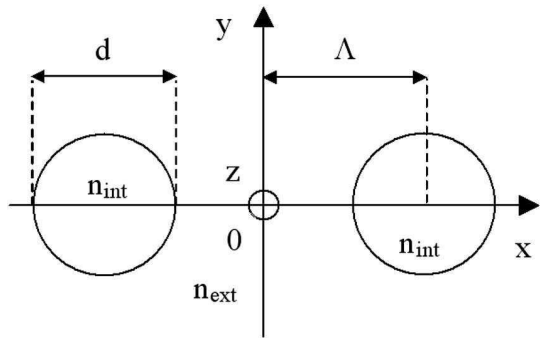

Fig. 9. Cross section of two identical circular cylinders on the X axis centered outside the origin with $d=1\ \mu$m, $\Lambda=1.5\ \mu$m, $n_{\text{int}}=1.4$, and $n_{\text{ext}}=1$.

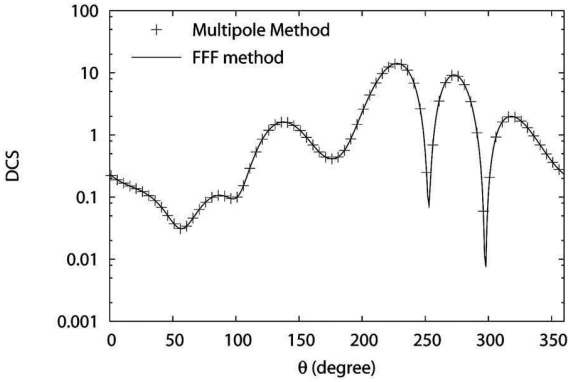

Fig. 10. DCS (θ=0° to 360°) for the two identical circular cylinders on the X axis shown in Fig. 9 with λ_0=2 μm, θ_{inc}=45°, φ=30°, ϕ=0°, and N=60; comparison between the FFF method and the MM.

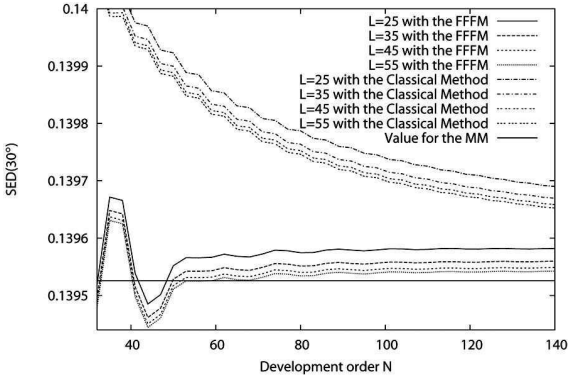

Fig. 11. Convergence test according to the order of the truncated Fourier series (N) of the point at 30° in the DCS of the FFF method (FFFM) (illustrated by Fig. 8) and of the classical differential method with λ_0=1 μm and with different values of L (number of slices for the S algorithm) compared with the MM value.

fairly well with the MM ones. Then we consider the DCS of two identical circular cylinders located on the X axis as shown in Fig. 9; we obtain the results shown in Fig. 10, and again the agreement between the two methods is excellent.

B. Numerical Efficiency and Accuracy of the Fast Fourier Factorization Method

In this subsection we discuss in more detail the numerical efficiency of the FFF method. For the structures already studied (Figs. 7 and 9), the single-cylinder case is in fact more difficult to model than the two-cylinder case. Consequently, we focus on this demanding structure for our convergence tests. In Fig. 11 we show the DCS of the single cylinder for θ=30° versus the development order N for several values of the number of S-algorithm slices. We give both the classical differential method[7] and the FFF method results. We clearly see that the FFF method is more accurate than the classical differential method. For this angle of 30° and for both methods, we also see that an increase of the number of slices in the S algorithm improves the results. In Fig. 12 we give the same study but for θ=150°. Once again, the FFF method converges more quickly than the classical method. Note that, as for θ=30°, the possible crossings between the line corresponding to the value computed with the MM and the convergence curves for small N values are not meaningful. Only the global behavior of these convergence curves are useful. To avoid such putative crossings in our convergence study, we give in Fig. 13 the average relative errors between the computed DCS values and the MM one for all the angles in the range [0°, 360°]. The improvement brought by the FFF method is evident (note the log scale on the Y axis). We finally obtain a relative difference of 2.10^{-4} between the FFF method results and the MM ones for N=140 and L=55. The results obtained with the FFF method are less accurate than the ones obtained with the MM for the different examples of DCS shown in Figs. 11 and 12. Nevertheless, the relative discrepancies between the two methods are fully acceptable. One can ask why such differences can still be observed whereas both the FFF method and the MM are rigorous methods, in which the unique approximations are the truncations of the used series. For the FFF method, we need to truncate the Fourier series of the electromagnetic fields (four components are needed to describe them in a conical mounting) and the ones of the permittivity of the diffracting device. In the case of the MM, we have to truncate only the

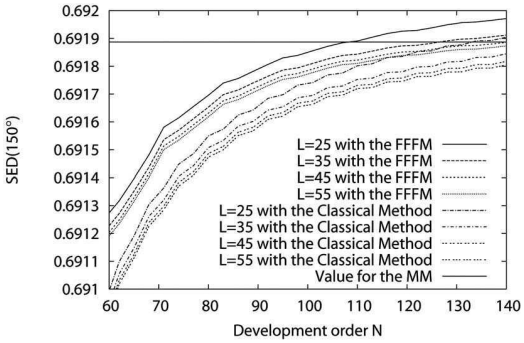

Fig. 12. Convergence test according to the order of the truncated Fourier series (N) of the point at 150° in the DCS of the FFF method (FFFM) (illustrated by Fig. 8) and of the classical differential method with λ_0=1 μm and with different values of L (number of slices for the S algorithm) compared with the MM value.

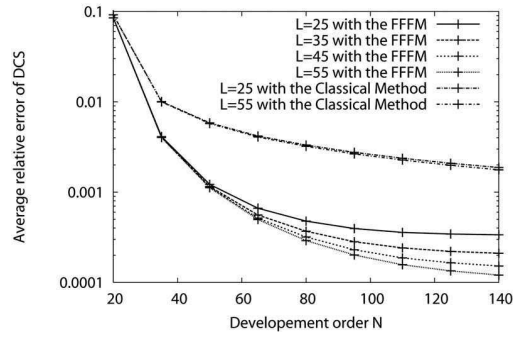

Fig. 13. Average relative error between the DCS of the FFF method (FFFM) (illustrated by Fig. 8) and of the classical differential method and the DCS of the MM according to the order of the truncated Fourier series (N) with λ_0=1 μm and with different values of L (number of slices for the S algorithm).

Fourier–Bessel series of two field components (E_z and H_z are needed in conical mounting) since any series are needed of the permittivity. There are at least two other reasons explaining the better accuracy of the MM for the examples shown here. First, for homogeneous and circular inclusions, the reflection matrix relating the incident and the scattered field in the MM are known analytically. On the contrary, in the framework of the FFF, the inclusions are described through the permittivity tensor $\bar{\bar{\epsilon}}$ (more precisely by its Fourier components) in the modulated area. Second, there is a crucial difference between the two methods: for the MM no numerical integration is necessary, while resolution such as the one associated with Eq. (26) of the FFF method requires such an integration; only analytical changes of basis using Graf's theorem[2,10] are used for the rewriting of the Fourier–Bessel series, which lead to an explicit linear problem.

All these reasons also explain why the MM is much faster than the FFF method for the homogeneous and circular examples treated in this study, even if all the numerical computations can still be achieved on a single PC. It is worth considering how the MM accuracy evolves when noncircular inclusions are considered, and hence when a numerical integration is required. The results given in Ref. 11 concerning homogeneous and elliptical inclusions can give us a first evaluation since a numerical integration is required to compute the reflection matrix of the ellipses. The final results obtained by the MM lose approximately three significant digits when these noncircular inclusions are studied. We do not observe such worsening of the accuracy within the FFF method when similar ellipses are considered instead of circular inclusions since the circles are not treated differently than the ellipses.

To conclude this subsection, we remind the reader that circular and homogeneous inclusions are a special case in which the Multipole Method is certainly the best possible numerical method since several steps are done analytically. The purpose of the FFF method is not to study such simple, but more complicated structures; a trade-off is obtained between the accuracy speed and the generality of the studied structures.

C. Devices with Subperiodicity According to θ

As with MOFs, any device may present a cross section with a subperiodicity according to θ. This property can be taken into account in the integration process to reduce the computation time. Let us assume that the device presents a subperiod T such that $N_T T = 2\pi$ where N_T is the number of periodicity. Thus the spectra of the functions $\epsilon(r,\theta)$ and $N_\theta^2(r,\theta)$ are wider than those obtained without subperiodicity. More precisely, we consider a function $\tilde{f}(\theta)$ (ϵ, ${N_\theta}^2$ or $N_r N_\theta$) subperiodic with period T. The Fourier coefficients of $\tilde{f}$ on the 2π range $\tilde{f}_n$ ($n \in \mathbb{N}$) and the Fourier coefficients of $\tilde{f}$ on the T range $\tilde{f}'_n$ ($n \in \mathbb{N}$) are linked by the following relations: if $n = kN_T$ ($k \in \mathbb{N}$), then $\tilde{f}_n = \tilde{f}'_k$ and $\tilde{f}_n = 0$ otherwise. Consequently, the Toeplitz matrix of the function $\tilde{f}$ is made of nonnull diagonals regularly separated by $N_T - 1$ null diagonals. For instance, if $N=4$ and $N_T=3$, the Toeplitz matrix of the function $\tilde{f}$ is

$$[\![\tilde{f}]\!] = \begin{bmatrix} \tilde{f}'_0 & 0 & 0 & \tilde{f}'_1 & 0 & 0 & \tilde{f}'_2 & 0 & 0 \\ 0 & \tilde{f}'_0 & 0 & 0 & \tilde{f}'_1 & 0 & 0 & \tilde{f}'_2 & 0 \\ 0 & 0 & \tilde{f}'_0 & 0 & 0 & \tilde{f}'_1 & 0 & 0 & \tilde{f}'_2 \\ \tilde{f}'_{-1} & 0 & 0 & \tilde{f}'_0 & 0 & 0 & \tilde{f}'_1 & 0 & 0 \\ 0 & \tilde{f}'_{-1} & 0 & 0 & \tilde{f}'_0 & 0 & 0 & \tilde{f}'_1 & 0 \\ 0 & 0 & \tilde{f}'_{-1} & 0 & 0 & \tilde{f}'_0 & 0 & 0 & \tilde{f}'_1 \\ \tilde{f}'_{-2} & 0 & 0 & \tilde{f}'_{-1} & 0 & 0 & \tilde{f}'_0 & 0 & 0 \\ 0 & \tilde{f}'_{-2} & 0 & 0 & \tilde{f}'_{-1} & 0 & 0 & \tilde{f}'_0 & 0 \\ 0 & 0 & \tilde{f}'_{-2} & 0 & 0 & \tilde{f}'_{-1} & 0 & 0 & \tilde{f}'_0 \end{bmatrix}. \quad (47)$$

We notice that the matrix $[\![\tilde{f}]\!]$ is block diagonalizable. This matrix structure is preserved when such a matrix is reversed or when two such matrices are multiplied; that is why every block of the integration matrix $M(r)$ given by Eq. (26) has this matrix structure. Finally, we conclude that Eq. (26) is split into N_T independent differential sets with matrix sizes equal to $4(2N+1)/N_T$ or less. Since the integration computation time depends roughly on the cube of the matrix integration size, the time of a successive integration of each differential subset scales as $N_T(4(2N+1)/N_T)^3 = (4(2N+1))^3/{N_T}^2$, while the time of the global differential set [Eq. (26)] scales as $(4(2N+1))^3$. It means that taking into account the subperiodicity according to θ of the diffracting surface permits us to gain a factor of ${N_T}^2$ on the computation time. Moreover, each differential subset depends on the reduced Toeplitz matrix:

$$[\![\tilde{f}]\!] = \begin{bmatrix} \tilde{f}'_0 & \tilde{f}'_1 & \tilde{f}'_2 \\ \tilde{f}'_{-1} & \tilde{f}'_0 & \tilde{f}'_1 \\ \tilde{f}'_{-2} & \tilde{f}'_{-1} & \tilde{f}'_0 \end{bmatrix},$$

which simplifies the calculation of the Fourier developments of ϵ, ${N_\theta}^2$, and $N_r N_\theta$ functions defined only on the T period. The subperiodicity according to θ was first successfully implemented on an elliptical cross-section surface centered to the origin since it is π periodic ($N_T=2$) and then on the circular cylinder defined on a period T (data not shown). We note that this study on subperiodicity can be linked to the seminal work of McIsaac[12] concerning waveguide symmetry properties and with the paper written by Bai and Li.[13] The authors of Ref. 13 have explicitly shown how the use of group theory permits one to fairly reduce the computation time on crossed grating analysis. More recently, Fini[14] has revisited McIsaac's work to improve the efficiency of several numerical methods if rotational symmetry properties are present in the device.

D. Excitation of the Fundamental Leaky Mode of a Microstructured Optical Fiber

The subperiodicity of the diffracting device is particularly useful in the case of MOFs. These fibers are usually made of several rings of circular cylinders (filled with vacuum) regularly distributed according to the angular coordinate θ in a infinite matrix. We thus consider a solid core MOF (Fig. 14) composed of six identical circular cylinders with

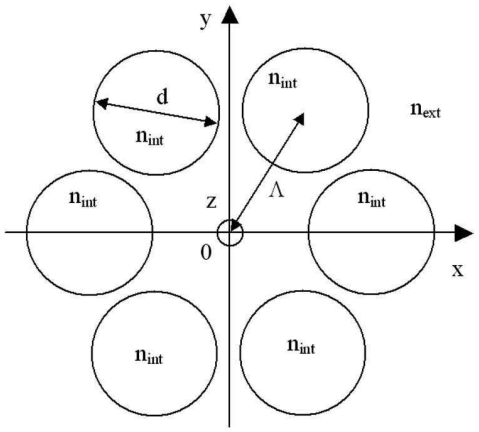

Fig. 14. Cross section of a MOF composed of six identical circular cylinders with $d=1$ μm, $\Lambda=2.3$ μm, $n_{int}=1$, and $n_{ext}=1.4439$.

a diameter $d=1$ μm and the same distance to the origin (pitch) $R_0=\Lambda=2.3$ μm ($\theta_0=0°$); it means that the subperiod is $2\pi/6$ ($N_T=6$). In addition, the whole structure has symmetry planes, so in the formulation used in waveguide theory,[12] this fiber follows the C_{6v} symmetries. The cylinder index is $n_{int}=1$ and the matrix index is $n_{ext}=1.44390356$. In our notation [Eq. (3)], the parameter γ_0 becomes the studied propagation constant usually noted as β. The effective index is defined by $n_{eff}=\beta/k_0$. The well-established MM[1–3] can also be formulated as a modal method, and consequently it can find the modes of MOFs composed with arbitrary inclusions contained in disjoined circular cylinders. It gives a complex effective index equal to $n_{eff}=1.420784+i7.20952\times10^{-4}$ with $\lambda_0=1.56$ μm for the fundamental mode, i.e., this mode is a leaky mode (even if the optical indices of the inclusions and the matrix are purely real). In addition, we know that the fundamental mode is twice degenerated.[1,12] Its component fields E_z belong either to the C4 symmetry class [symmetric according to the Y axis, $u(\pi-\theta)=u(\theta)$, and antisymmetric according to the X axis, $u(-\theta)=-u(\theta)$] or to the C3 symmetry class (antisymmetric according to the Y axis and symmetric according to the X axis). This classification of symmetry is more precisely explained in the work of McIsaac.[12] We search now to apply these symmetry properties on the diffracting problem. The mode that belongs to the C3 symmetry class is excited when $\theta_{inc}=90°$ and the second one (C4 symmetry class) when $\theta_{inc}=0°$.

In the framework of our diffraction method, we have first tried to excite the fundamental mode described above with suitable incident wave parameters [Eq. (1)]. We know that the real parameter γ_0 is equal to $-k_{ext}\sin(\varphi)$ in which $k_{ext}=k_0 n_{ext}$; hence we have searched the angle parameter φ such that $\gamma_0=k_0\,\mathrm{Re}(n_{eff})$, and we have approximately found $\varphi=-79.73°$ about $[\varphi=-\arcsin(\mathrm{Re}(n_{eff})/n_{ext})]$. Doing so, we have neglected the imaginary part of n_{eff}. Consequently, the fundamental mode is only partially excited. Figure 15 shows the computation time versus N for both the six circular cylinder MOFs defined on the 2π period and for the one defined on the $T=2\pi/6$ period. These results clearly illustrate the improvement brought about by the subperiodicity concerning the computation time. Figure 16 illustrates the normalized $|E_z|$ map associated with the partial excitations of the fundamental mode belonging to the C3 symmetry class and Fig. 17 to the C4 symmetric class ($N=60$ and $\phi=0°$). The fields seem well located around the circular cylinders and the similarity with the MM[1] field maps is already clear even if the result

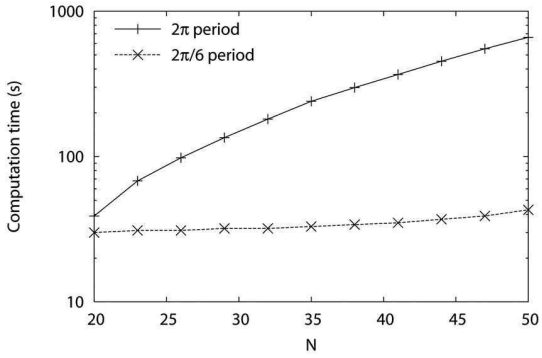

Fig. 15. Computation time for the six circular cylinders as a function of the order of the truncated Fourier series (N), with and without taking advantage of the symmetry.

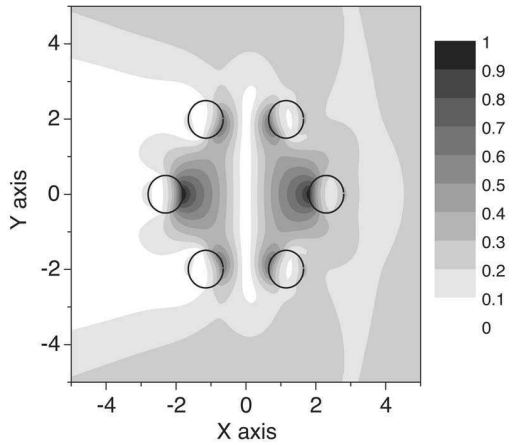

Fig. 16. Normalized $|E_z|$ field map obtained thanks to the partial excitation (see Fig. 18 for the complete excitation) of the MOF fundamental mode belonging to the C3 symmetry class [$\theta_{inc}=90°$, $\phi=0°$, $\lambda_0=1.56$ μm, $N=60$, and $\gamma_0=k_0\,\mathrm{Re}(n_{eff})=1.420784$]. The studied fiber is the same as in Fig. 14.

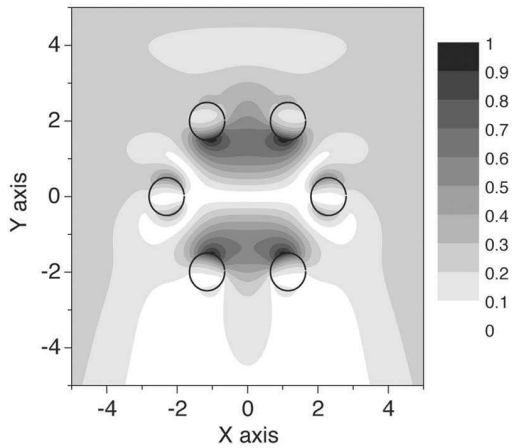

Fig. 17. Normalized $|E_z|$ field map obtained thanks to the partial excitation (see Fig. 19 for the complete excitation) of the MOF fundamental mode belonging to the C4 symmetry class ($\theta_{inc}=0°$). The studied fiber is the same as in Fig. 14.

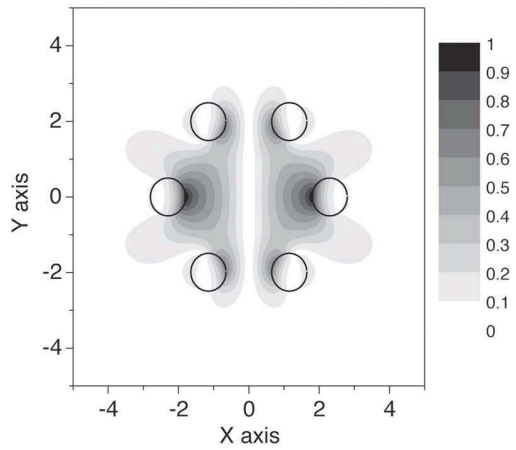

Fig. 18. Normalized $|E_z|$ field map obtained thanks to the complete excitation (see Fig. 16 for the partial excitation) of the MOF fundamental mode belonging to the C3 symmetry class ($\theta_{\text{inc}}=90°$, $\phi=0°$, $\lambda_0=1.56\ \mu$m, $N=60$, and $\gamma_0=k_0 n_{\text{eff}}=1.420784+i7.20952\times10^{-4}$). The studied fiber is the same as in Fig. 14.

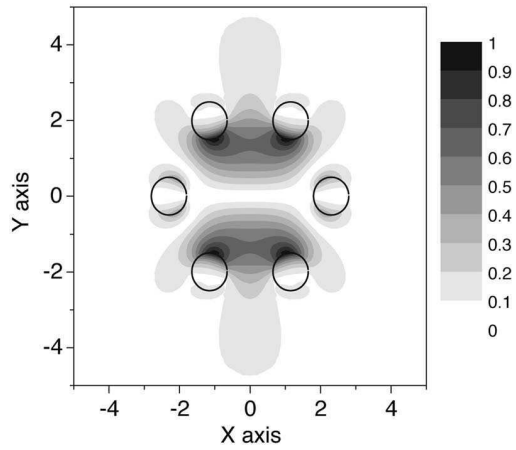

Fig. 19. Normalized $|E_z|$ field map obtained thanks to the complete excitation (see Fig. 17 for the partial excitation) of the MOF fundamental mode belonging to the C4 symmetry class ($\theta_{\text{inc}}=0°$; other parameters are identical to the ones of Fig. 18) of the fundamental mode. The studied fiber is the same as in Fig. 14.

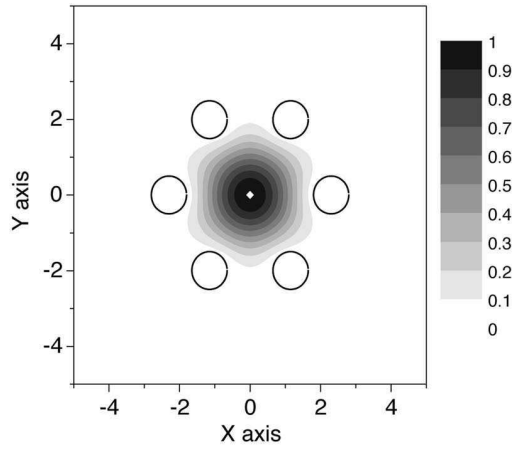

Fig. 20. Normalized $|S_z|$ field map computed from the electromagnetic fields associated with Fig. 18 (the result is similar when the results associated with Fig. 19 are considered).

shown in Fig. 16 is a diffraction phenomenon and not a true mode.

To excite completely the fundamental mode by a incident wave, we now take into account the imaginary part of n_{eff}. The complex number $\gamma_0=k_0 n_{\text{eff}}$ implies that φ also becomes a complex number. However, this implies that all the components of the incident fields are proportional to the same complex number $\cos(\varphi)$. In this case, the field amplitudes $A_{e,z}$ and $A_{h,z}$ deduced from Eq. (2) also become complex numbers proportional to $\cos(\varphi)$:

$$A_{e,z}=\cos(\varphi)\cos(\phi)|\mathbf{E}^{(\text{inc})}|, \tag{48}$$

$$A_{h,z}=\frac{1}{Z}\cos(\varphi)\sin(\phi)|\mathbf{E}^{(\text{inc})}|. \tag{49}$$

Since all the other incident field components are proportional to $A_{e,z}$ and $A_{h,z}$, they are also proportional to $\cos(\varphi)$. Consequently, it is not even necessary to determine the $\cos(\varphi)$ factor if we are only interested in normalized fields. In our example, we choose $\gamma_0=k_0 n_{\text{eff}}$. Figures 18 and 19 show the normalized $|E_z|$ maps associated with the accurate excitation of the C3 (and C4) symmetry class mode, respectively. Figure 20 illustrates the modulus of the z component of the Poynting vector noted as S_z for both electromagnetic field maps ($N=60$). We recognize the same field maps as the ones obtained with the MM used in its mode-searching operation.[1]

6. CONCLUSION

The described FFF method introduces Toeplitz matrices for permittivity $[\![\epsilon]\!]$ and $[\![1/\epsilon]\!]$ and also Toeplitz matrices for geometric quantities such as the normal vector components of the diffracting surface: $[\![N_\theta^2]\!]$, $[\![N_r^2]\!]$, and $[\![N_\theta N_r]\!]$. The convergence results depend directly on these matrix conditions. The numerical implementation on the circle case in which the $\epsilon(r,\theta)$ and $N_\theta{}^2(r,\theta)$ functions present important variations according to θ shows satisfying results for $N=50$. Moreover, the integration of the differential set in the modulated area fairly simplifies when the possible subperiodicity of the diffracting device is taken into account. We apply the FFF method to simple structures made of circular inclusions so as to be able to compare it with a known method. However, the FFF method described here in cylindrical coordinates can compute the fields diffracted by more complex structures than the ones shown in this present work: Some other different diffracting surfaces have been successfully studied (elliptical cylinder, rectangular cylinder, etc.), and the most general case of anisotropic and/or inhomogeneous media can also be analyzed. An association between the FFF method in the homogeneous and isotropic case and the MM has already been used to study a MOF with elliptical inclusions.[11] Our future work will deal with the adaptation of the FFF method applied to light diffraction to the search of modes into arbitrary cross-section MOFs to overcome the known limitations of the MM[1] (inclusions must be inscribed in nonoverlapping circles, the matrix

permittivity must be homogeneous). In this case, the diffraction problem becomes an homogeneous problem, i.e., an eigenvalue problem.

ACKNOWLEDGMENTS

The support of the European Community-funded project PHOREMOST (FP6/2003/IST/2-511616) is gratefully acknowledged. The content of this work is the sole responsibility of the authors. We thank the Free Software Foundation and the Scilab Consortium for their help.

REFERENCES

1. F. Zolla, G. Renversez, A. Nicolet, B. Kuhlmey, S. Guenneau, and D. Felbacq, *Foundations of Photonic Crystal Fibers* (Imperial College Press, 2005).
2. T. P. White, B. T. Kuhlmey, R. C. McPhedran, D. Maystre, G. Renversez, C. M. de Sterke, and L. C. Botten, "Multiple method for microstructured optical fibers. I. Formulation," J. Opt. Soc. Am. B **19**, 2322–2330 (2002).
3. B. T. Kuhlmey, T. P. White, G. Renversez, D. Maystre, L. C. Botten, C. M. de Sterke, and R. C. McPhedran, "Multipole method for microstructured optical fibers. II. Implementation and results," J. Opt. Soc. Am. B **19**, 2331–2340 (2002).
4. M. Nevière and E. Popov, *Light Propagation in Periodic Media: Differential Theory and Design* (Marcel Dekker, 2003).
5. P. Boyer, E. Popov, M. Nevière, and G. Tayeb, "Diffracting theory in TM polarization: application of the fast Fourier factorization method to cylindrical devices with arbitrary cross section," J. Opt. Soc. Am. A **21**, 2146–2153 (2004).
6. M. Nevière, "The homogeneous problem," in *Electromagnetic Theory of Gratings*, R. Petit ed. (Springer-Verlag, 1980).
7. P. Vincent and R. Petit, "Sur la diffraction d'une onde plane par un cylindre diélectrique," Opt. Commun. **5**, 261–266 (1972).
8. L. Li, "Use of Fourier series in the analysis of discontinuous periodic structures," J. Opt. Soc. Am. A **13**, 1870–1876 (1996).
9. L. Li, "Formulation and comparison of two recursive matrix algorithms for modeling layered diffraction gratings," J. Opt. Soc. Am. A **13**, 1024–1035 (1996).
10. M. Abramowitz and L. E. Stegun, eds., *Handbook of Mathematical Functions with Formulas, Graphs, and Mathematical Tables* (National Bureau of Standards, 1972).
11. S. Campbell, R. C. McPhedran, C. M. de Sterke, and L. C. Botten, "Differential multipole method for microstructured optical fibers," J. Opt. Soc. Am. B **21**, 1919–1928 (2004).
12. P. R. McIsaac, "Symmetry-induced modal characteristics of uniform waveguides. I. Summary of results," IEEE Trans. Microwave Theory Tech. **MTT-23**, 421–429 (1975).
13. B. Bai and L. Li, "Reduction of computation time for crossed-grating problems: a group-theoretic approach," J. Opt. Soc. Am. A **21**, 1886–1894 (2004).
14. J. M. Fini, "Improved symmetry analysis of many-moded microstructure optical fibers," J. Opt. Soc. Am. B **21**, 1431–1436 (2004).

Fabrication of complex structures of Holey Fibers in Chalcogenide glass

Laurent Brilland[1], Fréderic Smektala[2], Gilles Renversez[3], Thierry Chartier[4], Johan Troles [2],Thanh Nam Nguyen[4], Nicholas Traynor[1] , Achille Monteville[1]

[1] PERFOS (Plateforme d'Etudes et de Recherche sur les Fibres Optiques Spéciales) ; 11 rue Louis de Broglie 22300 Lannion, France,
[2] Laboratoire Verres et Céramiques; UMR CNRS 6512, Université Rennes 1, Rennes, France
[3] Institut Fresnel ; UMR CNRS 6133, Universite Paul Cézanne Aix-Marseille 3, Marseille, France
[4] Laboratoire d'Optronique de l'ENSSAT ; UMR CNRS FOTON 6082, Université Rennes, Lannion, France
lbrilland@perfos.com

Abstract: We report recent progress on fabrication of solid core microstructured fibers in chalcogenide glass. Several complex and regular holey fibers from $Ga_5Ge_{20}Sb_{10}S_{65}$ chalcogenide glass have been realized. We demonstrate that the "Stack & Draw" procedure is a powerful tool against crystallisation when used with a very stable chalcogenide glass. For a 3 ring multimode Holey Fiber, we measure the mode field diameter of the fundamental mode and compare it successfully with calculations using the multipole method. We also investigate, via numerical simulations, the behaviour of fundamental mode guiding losses of microstructured fibers as a function of the matrix refractive index, and quantify the advantage obtained by using a high refractive index glass such as chalcogenide instead of low index glass.

OCIS codes: (160.2750) Glass and other amorphous materials; (060.2310) Fiber optics

References and links

1. F. Smektala, C. Quemard, V. Couderc, and A. Barthelemy, "Non-linear optical properties of chalcogenide glasses measured by Z-scan," J. Non-Cryst. Solids **274**, 232-237 (2000).
2. J. Troles, F. Smektala, G. Boudebs, A. Monteil, B. Bureau, and J. Lucas, "Chalcogenide glasses as solid state optical limiters at 1.064µm," Opt. Mater. **25**, 231-237 (2004.)
3. R. E. Slusher, Gadi Lenz, Juan Hodelin, Jasbinder Sanghera, L. Brandon Shaw and Ishwar D. Aggarwal, "Large Raman gain and nonlinear phase shifts in high purity As_2Se_3 chalcogenide fibers," J. Opt. Soc. Am. B **21**, 1146-1155 (2004).
4. K. Michel, B. Bureau, C. Boussard-Plédel, T. Jouan, J. L. Adam, K. Staubmann and T. Bauman, "Monitoring of pollutant in waste water by infrared spectroscopy using chalcogenide glass optical fibers," Sens. Actuators B **101**, 252-259 (2004).
5. M. F. Churbanov, I. V. Scripachev, V. S. Shiryaev, V. G. Plotnichenko, S. V. Smetanin, E. B. Kryukova, Yu. N. Pyrkov, and B. I. Glagan, "Chalcogenide glasses doped with Tb, Dy and Pr ions," J. Non-Cryst. Solids **326&327**, 301-305 (2003).
6. J. Nishii, T. Yamashita, and T. Yamagishi, "Chalcogenide glass fiber with a core-cladding structure," Appl. Opt. **28**, 5122 (1989).
7. T. A. Birks, P. J. Roberts, P. St. J. Russel, D. M. Atkin, and T. J. Sheperd, "Full 2D photonic bandgap in silica/air structures," Electron. Lett. **31**, 1941-1943 (1995).
8. T. M. Monro, and D. J. Richardson, "Holey optical fibres: Fundamental properties and device applications," Contemp. R. Phys. **4**, 175-186 (2003).
9. G. Renversez, B. Kuhlmey and R. McPhedran, "Dispersion management with microstructured optical fibers: ultraflattened chromatic dispersion with low losses," Opt. Lett. **28**, 989-991 (2003).
10. T. A. Birks, J. C. Knight, P. St. J. Russel, "Endlessly single mode photonic crystal fiber," Opt. Lett. **22**, 961-963 (1997).
11. T. M. Monro, Y. D. West, D. W. Hewak, N. G. R. Broderick, and D. J. Richardson, "Chalcogenide Holey Fibres," Electron. Lett. **36**, 1998-2000 (2000).

#9841 - $15.00 USD Received 1 December 2005; revised 20 January 2006; accepted 20 January 2006

12. L. B. Shaw, P. A. Thielen, F. H. Kunk, V. Q. Nguyen, J. S. Sanghera, and I. D. Aggarwal, "IR supercontinuum generation in As-Se Photonic Crystal Fiber," in Advanced Solid State Photonics., Vol. 98 of OSA Proceedings Series (Optical Society of America, Washington, DC., 2005), pp. 864-868.
13. Y. Guimond, J. L. Adam, A. M. Jurdyc, H. L. Ma, J. Mugnier, and B. Jacquier,"Optical properties of antimony-stabilised sulphide glasses doped with Dy and Er ions," J. Non-Cryst. Solids, **256 & 257**, 378-382 (1999).
14. G. Renversez, F. Bordas and B. T. Kuhlmey, "Second mode transition in microstructured optical fibers : determination of the critical geometrical parameter and study of the matrice refractive index and effects of cladding size," Opt. Lett. **30**, 1264-1266 (2005).
15. T. P. White, B. T. Kuhlmey, R. C. McPhedran, D. Maystre, G. Renversez, C. Martijn de Sterke, and L. C. Botten, «Multipole method for microstructured optical fibers. I Formulation," J. Opt. Soc. Am. B **19**, 2322-2330 (2002).
16. B. Kuhlmey, T. P. White, G. Renversez, D. Maystre, L. C. Botten, C. Martijn de Sterke, and R. C. McPhedran, "Multipole method for microstructured optical fibers II: Implementation and results," J. Opt. Soc. Am. B **10**, 2331-2340 (2002).
17. F. Bordas, L. Provino, and G. Renversez, " Fibres optiques microstructurées de haut indice : pertes et dispersion chromatique du fondamental et cutoff du second mode, comparaison avec la silice," Journées Nationales Optique Guidée, Société Française d'Optique, Paris, France, 230-232 (2004).

1. Introduction

Chalcogenide glasses offer several interesting optical properties including a large wavelength transparency window (from about 1 µm to above 10 µm) and a high refractive index (greater than 2). Depending on composition, the nonlinear coefficient n_2 has been measured to be between 100 to 1000 times larger than for silica glass [1]. Theses high values are very attractive for applications such as all optical signal processing, optical demultiplexing, raman amplification, and broad band spectrum generation [2], [3]. Chalcogenide glass based optical fibers are also attractive as a transport medium for high power infrared (IR) lasers such as CO_2 lasers and are currently actively studied in optical sensor systems using IR optical detection [4]. Furthermore, several chalcogenide based glasses offer the possibility of relatively high concentration rare earth doping for amplification and lasing applications [5].

For many applications, single mode guiding is required. In the recent past, single mode guiding in chalcogenide glass fibers in a step index configuration has been demonstrated, using, in general, rod in tube or double crucible processes [6]. Theses methods require significant care and expertise in order to prevent crystallisation effects, bubbles, contaminations at the core/cladding interface and ellipticity of the core. Moreover, great precision in the index of refraction is needed in order to ensure single mode guiding.

For single mode fibers in a step index configuration, very small or very large mode field diameters (MFD) are difficult to obtain since the precision required for the core and clad refractive index are incompatible with the bulk glass forming techniques used. Nevertheless, large MFDs are useful to minimise the risks of glass damage during the transport high power laser beams and small MFDs enable the enhancement of nonlinear effects.

A solution to the above problem may be found in Holey Fibers (HF) also named microstructured fibers [7]. These fibers exhibit remarkable optical properties: very small or very large mode areas [8]; widely tuneable dispersion [9]; endlessly single mode operation [10]. These fibers consist of a periodic lattice of low index inclusions (very often simple holes) arranged around a solid core that run along the fiber length. In silica glass, the most common fabrication method is the "Stack & Draw" technique. Glass capillaries are stacked in a hexagonal lattice of several rings, and surrounded by a glass jacket to form the fiber preform. This process enables the realisation of complex structures and it is reproducible.

So far, in the case of chalcogenide glass, there are few articles dealing with holey fibers [11, 12]. In [11], a first holey fiber based on the Gallium Lanthanum Sulphide glasses system was realized with one ring of non regularly arranged holes. In [12], a section of As-Se holey fiber is presented, here the pre-form was fabricated by stacking one ring of tubes and 7 rings of rods around a central rod with no outer glass jacket, giving one ring of "guiding" holes and 7 rings of very small interstitial holes formed from the gaps between the glass rods. In the

#9841 - $15.00 USD Received 1 December 2005; revised 20 January 2006; accepted 20 January 2006

present paper, we report recent progress on the fabrication of holey fibers with GaGeSbS chalcogenide glass using the "Stack & Draw" procedure. The fabricated fibres present multiple hole rings formed by stacking multiple capillary layers, as is required to offer control over modal and dispersion properties while ensuring low propagation loss. We measure the mode field diameter and compare it with calculations using the well established multipole method.

2. Glass fabrication

The nominal glass composition is $Ga_5Ge_{20}Sb_{10}S_{65}$ (2S2G) [13]. High purity raw materials (5N) are placed in a sealed silica tube under vacuum (10^{-5} mb), heated at 800°C for 12h and then quenched in water. The index of refraction is 2.25 at 1550 nm and the nonlinear coefficient, n_2, is measured to be 120 times greater than that of silica. This particular glass is transparent from 0.6 µm to 10 µm (low loss fiber fabrication is possible from 1 to 6 µm). The glass transition temperature, Tg, was measured with a differential scanning calorimeter (DSC). Tg is measured to be at 305 °C as indicated by Fig. 1 which shows the thermal flux versus temperature. Between 305 °C and 500°C, this composition exhibits no crystallisation peak in the DSC curve when heated at a rate of 10°C/min.

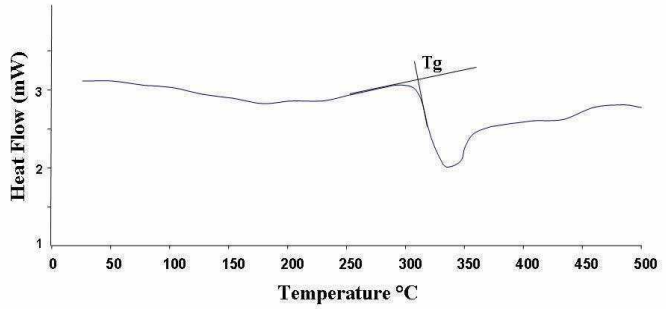

Fig. 1. determination of transition temperature Tg by DSC measurement for 2S2G glass

Furthermore, there is shallow variation of viscosity with temperature allowing stable fiber draw over a range of several tens of °C. These properties make this glass an ideal candidate for the "Stack and Draw" technique.

To make the core rod, the glass is quenched in water and then annealed near the glass transition temperature for 30 min and cooled down to room temperature. For tube fabrication, a glass melt at 700°C is spun at 3000 rpm at ambient temperature during several minutes [Fig. 2(a)]. During cooling, the viscosity increases and after a few minutes the vitrified tube is formed Fig. 2(b). The tube size used here is typically 12cm*12mm*5mm (length*outer diameter*inner diameter).

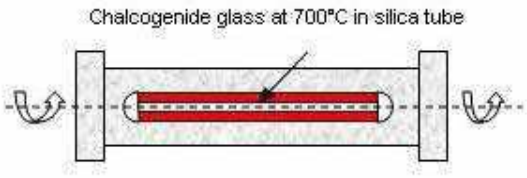

Fig. 2. (a) rotational casting set up

Fig. 2. (b) chalcogenide tube formed by rotational casting

3. Holey fiber fabrication and characterization

A chalcogenide (2S2G) tube, placed in a suitable furnace in a drawing tower is drawn down to form capillaries with an outer diameter typically of 665 µm. These tubes are stacked in

#9841 - $15.00 USD Received 1 December 2005; revised 20 January 2006; accepted 20 January 2006

hexagonal lattice, with a rod of identical diameter in the central region, and placed in a larger jacket tube to create the pre-form. The jacket tube is then collapsed around the microstructure via an initial rapid descent through the furnace of the drawing tower, with very little deformation of the capillary tubes. The fiber is then drawn at a rate of 5 m/min at a temperature of around 480 °C. A variable gas pressure system enables precise control of hole size during the draw.

Figure 3(a) shows the cross section of the solid core chalcogenide HF, which is based on the subset of a triangular lattice. The fiber consists of 3 rings of holes (Nr=3). The outer diameter, Φ_{ext}, of the HF is 147µm, the distance between hole centers (pitch) is Λ=8 µm, the average hole diameter is d=3.2 µm and the ratio d/ Λ is estimated at 0.4. In the upper right region the holes are larger than in the other regions. This is almost certainly due to the pre-form being off centre in the furnace, creating a non uniform viscosity. The higher temperature region experiences lower viscosity and presents less resistance to the pressure inside the capillaries/holes.

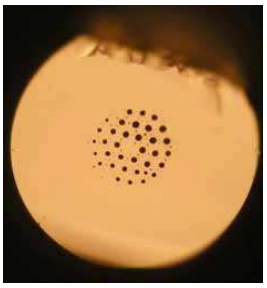

Fig. 3. (a) cross section of 3 rings HF; Φ_{ext}=147 µm

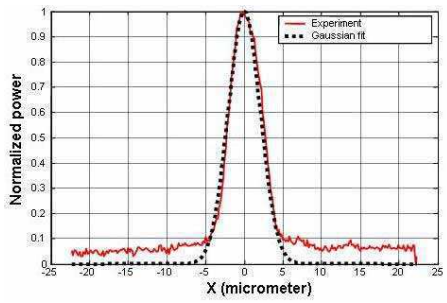

Fig. 3. (b) experimental Mode Field Diameter measurement

The output profile of the guided mode near to 1550 nm was investigated using a near field measurement. An indium metal coating was applied to inhibit cladding mode guidance. Light from a broadband source at 1550 nm was injected into the chalcogenide HF via a standard single mode fiber and the output from the fiber end was imaged onto an infrared camera. As shown in Fig. 3(b), the output profile can be accurately fitted with a Gaussian function. The mode field diameter (MFD) at $1/e^2$ of maximum intensity was measured to be 8.3 µm, comparable to the MFD of conventional single mode fiber. Using the well-established multipole method [15,16], we compute the MFD for this irregular profile. We obtain a MFD of 10.75 µm on the x axis (see Fig. 4(b) for the axis definition) and 11.45 µm on the y axis, for a perfect C_{6v} (*i.e.* a structure invariant by $2\pi/6$ rotations and by plane symmetries) microstructured fiber defined by the average geometrical parameters defined above. The relative error between the experimental result and the numerical simulations is about 25% which is larger than the estimated measurement error. If we consider several irregular profiles with circular holes mimicking the measured profile, the computed MFD are still in the range [10.4, 11.8] µm. Consequently, we must assume other hypothesis to explain the MFD relative error. This important relative error may be due to small longitudinal variations along the fiber of this imperfect structured profile. It may also result from slight variations of the matrix refractive index in the core and cladding regions since the capillaries and the central rod come from two different batches of 2S2G glass. If this hypothesis is right and since we have observed a MFD smaller than the computed one, we may assume that the central rod refractive index is slightly higher than for the capillaries. Concerning the single-modedness of the fabricated fiber, since the average hole diameter over pitch ratio is equal to 0.4, the fiber is near the upper border of the endlessly single-mode region defined for solid core C_{6v} microstructured fiber with an infinite number of hole rings (see Fig. 4 in Ref. [14]). As demonstrated in this reference, we can't neglect the cladding size effect for the single-mode behaviour of the considered fiber in which the number Nr is equal to three. Therefore the

#9841 - $15.00 USD Received 1 December 2005; revised 20 January 2006; accepted 20 January 2006

endlessly single modedness of the fabricated fiber is not guaranteed. Furthermore the imperfect profile and the supposed index difference mentioned above may also modify the single mode properties compared to the perfect C_{6v} microstructured fiber used in the above numerical study.

Another 3 rings Holey Fiber was realized under the same experimental conditions, but with a better control of the hole diameter and with capillaries and central rod from the same batch. Figure 4(a) shows a picture of the fiber. The step Λ is about 7.7 µm and the diameter d of the holes is 4.85 µm. The ratio d/Λ of 0.63 indicates multimode guiding at 1550 nm even with only three hole rings [13]. About 10 centimetres of the holey fiber, held straight, was used in the previous injection set up, with only the fundamental mode excited. Figure 4(b) shows the near field intensity distribution of the microstructure with a guiding beam at 1550 nm.

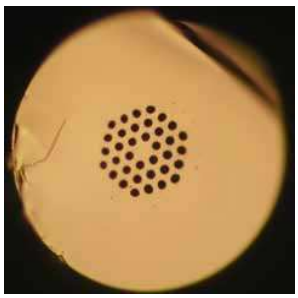

Fig. 4. (a) cross section of 3 rings HF; Φ_{ext}=137 µm

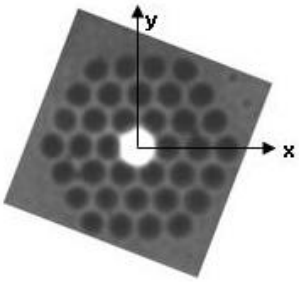

Fig. 4. (b) Near field intensity distribution in the Holey Fiber

The regular structure enabled us to compare more accurately the experimental and the theoretical mode field diameter measurements. Following a Gaussian approximation experimental measurements give the MFD at 9.3 µm on the x-axis and 9.66 µm on the y-axis. Calculation results with the multipole method gives a MFD of 8.64 µm on the x axis and 9.03 on the y axis. The agreement between experiment and theory is much better for this fiber, with an average error of 7%.

4. Discussion

In this work, we have presented a single mode and a multimode holey fiber with 3 rings. The profile of the second fiber is, to the best of our knowledge, the first demonstration of a regular (regular d and Λ) multi-hole layer index guiding fibre based on chalcogenide glass. Here we have focused on the fabrication of HF with a MFD near that of standard single mode silica fiber in order to facilitate coupling. We believe that this work can be extended to produce very small MFDs with only 3 or 4 rings of holes. Indeed, the high index of refraction of chalcogenide glasses enables a better confinement of the light. In paper [17], for an index of refraction of 2.5, d/Λ=0.4, Λ=2.3 µm, λ=1550nm and 4 rings, calculations show that guiding losses are less than 5 dB/km, significantly lower than the 1-2 dB/m $Ga_5Ge_{20}Sb_{10}S_{65}$ material losses around 1550 nm. Such a structure could be of significant interest for the realization of compact non linear devices. The demonstration of the advantage obtained with respect to guiding losses with the high refractive index of chalcogenide glasses is made below, using numerical simulations. It is well known that an increase of the number of hole rings, Nr, induces a decrease in the fundamental mode loss, L [16]. In the considered wavelength range, L decreases geometrically with Nr. We introduce the ratio of the fundamental mode guiding losses L(m+1) for a microstructured fiber made of Nr=m+1 hole rings over the fundamental mode losses L(m) for a Nr=m fiber. Slight variations of this ratio L(m+1)/L(m) occur for different and small m values. In order to give an unique but meaningful value for this ratio, we compute its average, denoted $\langle L(m+1)/L(m) \rangle$ for $m \in [1, 4]$. In Fig. 5, we show this average ratio as a function of d/Λ for two matrix refractive indices. A lower loss ratio denotes a fiber with more efficient confining capacity. As can be seen in Fig. 5 (note the y axis logarithmic scale), a matrix refractive index of n=2.25 ensures much stronger confinement than

#9841 - $15.00 USD Received 1 December 2005; revised 20 January 2006; accepted 20 January 2006

n=1.444024. Consequently, fewer rings of holes are needed to obtain the same guiding losses even for small values of d/Λ. It is worth mentioning that no material losses are taken into account in these numerical results. For the fabricated structures, the overall losses are set by the high intrinsic material losses.

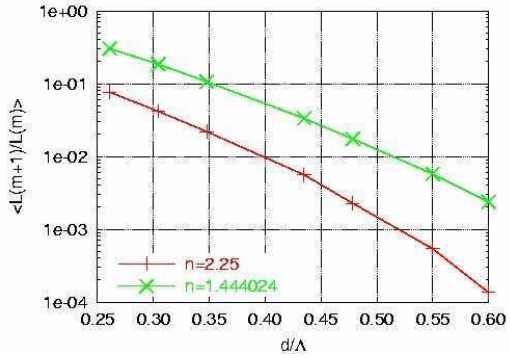

Fig. 5. Average ratio of the losses of a Nr=m+1 microstructured fiber $\langle L(m+1)\rangle$ over the losses of a Nr=m fiber $\langle L(m)\rangle$ for the fundamental mode as a function of d/Λ for two matrix refractive indices n=1.444024 and n=2.25 (Λ= 2.3 µm and λ=1.55 µm), see the text for the definition of the average.

Furthermore, compared to a step index single mode fiber in chalcogenide glasses, HFs offer more tolerance for the realization of single mode guiding. Actually, numerical and theoretical results [14] demonstrate that the critical ratio $(d/\Lambda)_{s.m}$ delimiting the endlessly single mode regime in C_{6v} solid core microstructured fibers with an infinite number of hole rings Nr is in the interval [0.42, 0.425]. For finite size HF this critical ratio $(d/\Lambda)_{s.m}$ depends on Nr, and it converges towards the infinite cladding critical ratio as Nr increases. Using the multipole method, we obtain that, for a 6 ring microstructured fiber with a pitch equal to 8 µm, a ratio d/Λ =0.35 ensures single mode guiding (in the sense defined in reference [14]) at 1.55 µm. Besides, if we change the matrix refractive index of 1% around 2.25, the single modedness is preserved. In the case of a step index single mode fiber, the composition of core and cladding glasses must be perfectly controlled and many iterations are often necessary to produce the required index of refraction. Accuracy better than 10^{-3} in refractive index for the core and cladding glasses is often required to obtain single mode guiding.

5. Conclusion

The first Holey Fibres in GaGeSbS chalcogenide glass have been manufactured. We have demonstrated the possibility of fabrication of complex structures up to three rings using the "Stack & Draw" technique. The use of a stable glass with excellent thermo-mechanical properties is key in allowing us to use tried and tested fabrication techniques. We believe that the combination of this technique and chalcogenide glass holds great potential for the realization of both small and large effective area fibers, with applications not only around 1550 nm but also in the mid infrared window. The ability to precisely control geometry from preform assembly through to final fibre fabrication opens up the possibility for the fabrication of infrared air guiding photonic band-gap fibres. In this work, we found an experimental mode field diameter in good agreement with calculations. In future work, we plan to improve the purity of our chalcogenide glass and our drawing process in order to reduce the overall losses. We also plan to characterize the single mode behaviour of our HF and their modal properties including losses and chromatic dispersion.

Acknowledgments

We thank the "Délégation Générale pour l'Armement" for financial support for the study (n° 05.34.008).

#9841 - $15.00 USD Received 1 December 2005; revised 20 January 2006; accepted 20 January 2006

IOP Publishing Journal of Optics A: Pure and Applied Optics
J. Opt. A: Pure Appl. Opt. **10** (2008) 125101 (13pp) doi:10.1088/1464-4258/10/12/125101

Spatial Kerr solitons in optical fibres of finite size cross section: beyond the Townes soliton

F Drouart[1], G Renversez[1], A Nicolet[1] and C Geuzaine[2]

[1] Institut Fresnel, UMR CNRS 6133, Université d'Aix-Marseille, 13397 Marseille Cedex 20, France
[2] Department of Electrical Engineering and Computer Science, Institut Montefiore B28, Université de Liège, Sart-Tilman, B-4000 Liège, Belgium

E-mail: fabien.drouart@fresnel.fr and gilles.renversez@fresnel.fr

Received 9 July 2008, accepted for publication 29 September 2008
Published 31 October 2008
Online at stacks.iop.org/JOptA/10/125101

Abstract
We propose a new and efficient numerical method to find spatial solitons in optical fibres with a nonlinear Kerr effect including microstructured ones. A nonlinear non-paraxial scalar model of the electric field in the fibre is used (nonlinear Helmholtz equation) and an iterative algorithm is proposed to obtain the nonlinear solutions using the finite element method. The field is supposed to be harmonic in time and along the direction of invariance of the fibre but inhomogeneous in the cross section. In our approach, we solve a nonlinear eigenvalue problem in which the propagation constant is the eigenvalue. Several examples dealing with step-index fibres and microstructured optical fibres with a finite size cross section are described. In each geometry, a single self-coherent nonlinear solution is obtained. This solution, which also depends on the size of the structure, is different from the Townes soliton—but converges towards it at small wavelengths.

Keywords: spatial solitons, Kerr nonlinearity, microstructured optical fibres, nonlinear optics, self-coherent solutions, Townes solitons

1. Introduction

Rigorous techniques for modelling the *linear* properties of microstructured optical fibres have been available for several years [1], and have been successfully used to study losses and chromatic dispersion of the fundamental mode [2], as well as the second mode cut-off [3]. A detailed review of these techniques with further references can be found in chapter 7 of [4].

Modelling the *nonlinear* properties of fibres (and in particular the optical Kerr effect) is inherently more complex, and while several techniques have been proposed (see e.g. [5, 6]), none is completely satisfactory. On the one hand, there are numerous works based on the nonlinear Schrödinger equation (NLSE), which do not deal with the finite size of the waveguide cross section, but focus on the transient evolution of pulse propagation along the fibre axis. The NLSE and its vector version are derived from Maxwell's equations assuming that the term $\nabla(\nabla \cdot \mathbf{E})$ in $\nabla \times \nabla \times \mathbf{E}$ can be neglected and that the slowly varying envelope approximation (SVEA) can be used [7]. On the other hand, there are (fewer) works based directly on Maxwell equations or their scalar approximation, which take into account the optogeometric profile of the fibre and do not introduce the SVEA. The NLSE and its vector version lead to a parabolic system of equations, whereas methods based directly on Maxwell's equations result in an elliptic system in the harmonic case. The differences between the two approaches have been studied extensively in [7–9]. In spite of many achievements of the NLSE (see [6]), some questions have been asked concerning its validity or its accuracy in several cases. In particular, Karlsson *et al* have shown that the use of the NLSE can give rise to wrong results for the self-phase modulation of a pulse that propagates in a bulk medium with a Kerr nonlinearity [10, 11]. Later, Ciattoni *et al* even show in [12] that several generalizations of the standard NLSE, aimed at describing non-paraxial propagation

in Kerr media, are not able to recover available exact results for TE and TM $(1 + 1)$-D bright spatial solitons. Only few works among the numerous articles published about spatial optical solitons deal with the genuine non-paraxial propagation of solitons. In [13], using a non-paraxial beam propagation method, the time evolution of solitons in a Kerr medium has been studied without introducing the SVEA. For several cases related either to wide angle propagation, fast varying envelope, or large spatial frequencies, it is obtained that the NLSE is not able to predict even quantitatively the time evolution given by the more accurate model based on the scalar nonlinear Helmholtz equation [13]. In [14], the time evolution of spatial solitons is computed in a $(2 + 1)$-D homogeneous Kerr-type nonlinear dielectric for a TM-problem using a finite-difference time-domain (FD-TD) method and the corresponding problem is solved using the NLSE. The FD-TD method shows that co-propagating in-phase spatial solitons diverge to arbitrarily large separations if the ratio of soliton beam width to wavelength is of order one or less. This is not the case for the NLSE for which the two in-phase solitons remain bounded to each other, executing a periodic separation [14]. An even more striking result was obtained by Feit and Fleck in 1988. They have shown that, for a nonlinear medium with a cubic nonlinearity, if the non-paraxiality of the beam propagation is taken into account then a finite size focusing of the optical beam is reached while with the paraxial wave equation a catastrophic collapse occurs [15].

The study presented here belongs to the second group mentioned above: it is based on the direct numerical solution of a non-paraxial scalar approximation of Maxwell's equations with non-saturable Kerr-type nonlinearities. It deals with stationary solutions and not pulse propagation. It uses the finite element method [4, 16]. We improve on previous studies in several ways. First of all, in our approach, we solve a nonlinear eigenvalue problem in which the propagation constant is an unknown of the problem; it is not fixed *a priori* or computed from the field map. Secondly, while the numerical method we propose is closely related to that proposed by Ferrando *et al* [17, 18] (we also choose a scalar nonlinear Helmholtz equation to compute the spatial solitons), we do not artificially periodize the cross section of the fibre. Its symmetry properties are thus fulfilled more easily, since no unit cell must be defined to implement the periodic boundary conditions. Thirdly, and more importantly, we do not use the 'fixed-power' algorithm proposed in [17, 18]. In this algorithm, at each step of the iterative process defined to obtain the nonlinear solution, the power of the intermediate solution is renormalized to the power arbitrarily fixed at the beginning of the algorithm [16]. Our new algorithm determines the power of the solution by itself, relying only on residue minimization. Finally, in contrast to related work by Snyder *et al* [19, 20], our algorithm can deal with inhomogeneous media [21]. As mentioned above, this is achieved by using a finite element method to solve the nonlinear problem. Although other techniques can also deal with the inhomogeneous refractive index of the fibre matrix [22], the finite element method has proved to be very efficient for the determination of propagating modes in microstructured optical fibres [23]. It is also flexible enough to represent the geometry of complex structures, and it permits a natural treatment of inhomogeneous media [21].

So as to focus on the main novel idea of our approach, only the properties of the fundamental nonlinear solutions are studied in the present paper. It is important to note that our numerical method could also deal with both high-order linear modes and higher-order nonlinear solutions.

In order to avoid any misunderstanding of the present study, we clearly state that it is not directly comparable to Bose–Einstein condensate (BEC) ones. Nonlinear optical solitons and matter–wave condensates are sometimes linked together due to the use of the NLSE (see for example [24]). Since the scalar equation we consider is different from the NLSE one, we are not allowed to take advantage of the powerful functional density method which is often used in the BEC field [25, 26]. This remark leads to at least two important consequences. The first concerns the method we have developed. It cannot be easily compared to those developed or improved for the NLSE (see section 5 of [27] and [28]) since the considered equations are different. These equations may share some general common properties but this has not been mathematically proved, at least to the best of our knowledge. Another point related to the method is that one aim of the present study is to set the basis of a non-paraxial method (solving an eigenvalue problem) in the frame of a scalar approach that can be extended to the genuine non-paraxial vector case obtained directly from Maxwell's equations. The second consequence concerns the results we obtain. We do not state that all the results obtained using our method differ from those coming from the NLSE in all cases. It is clear that when the required hypotheses are fulfilled the NLSE and our method must give similar results. But since the nonlinear scalar Helmholtz equation is nearer to Maxwell's equations than the NLSE one, the former must be considered, for stationary solutions with the $\exp(-\mathrm{i}\beta z)$ term, as the reference one.

The paper is organized as follows. In section 2, the first steps of our self-coherent algorithm are described. The nonlinear equation derived from Maxwell's equations is defined, and the treatment of the nonlinear term and the iterative process to solve the nonlinear problem are explained. Section 3 presents how a unique self-coherent nonlinear solution can be obtained. This is explained in detail for a step-index fibre, and then more briefly for a microstructured optical fibre. In the last part of section 3, we study the convergence of the iterative process and the physical properties of the self-coherent solution obtained. A comparison with the 'fixed-power' algorithm is also performed to validate our self-coherent solution. Finally, in section 4, the physical meaning of the self-coherent solution is described. The fibre geometry dependence, including the finite size effect of the microstructured fibres, is demonstrated and a comparison with the Townes soliton [29, 30] is shown so as to prove the originality of our nonlinear solution.

2. Introduction to the new solution technique

The scalar model is considered for the propagating solution obtained under the weak guidance (weak refractive index

contrast) hypothesis [31, 32]. In this case, the electric field $\mathbf{E}$ is supposed to have only a non-vanishing transverse component of known (arbitrary) direction given by the unit vector $\hat{\mathbf{e}}$. Moreover, its divergence is usually neglected, so that $\nabla \cdot \mathbf{E} = 0$ is assumed. In the linear case, the electric field corresponding to a propagation mode is therefore a field of the form

$$\mathbf{E} = \Re\mathfrak{e}\left[\phi(x, y)\mathrm{e}^{-\mathrm{i}(\omega t - \beta z)}\right]\hat{\mathbf{e}} \tag{1}$$

in which $\omega = k_0 c$ is the pulsation, $k_0 = 2\pi/\lambda$ is the wavenumber and β is the propagation constant. The problem reduces to determining the function $\phi(x, y)$ and the constant β for a given value of k_0 by solving the scalar eigenvalue problem

$$\Delta_\mathrm{t}\phi + k_0^2 \varepsilon_\mathrm{r}\phi = \beta^2\phi, \tag{2}$$

where Δ_t is the transverse Laplacian. This equation is obtained from Maxwell's equations with materials of relative permittivity ε_r and using all the hypotheses above. The dispersion curves are the set of pairs (k_0, β) for which a solution of equation (2) exists.

The relative permittivity is itself a function of the field intensity and the following dependence is assumed:

$$\varepsilon_\mathrm{r}(\phi) = n_0^2 + \mathbb{I}_\mathrm{nl} n_\mathrm{Kerr}^2 |\phi|^2 \tag{3}$$

in which $\mathbb{I}_\mathrm{nl}$ is the indicative function equal to one in the nonlinear case (where the fibre is made of an optical Kerr material) and zero elsewhere, and where n_0 (the linear refractive index) and $n_\mathrm{Kerr}^2 = 3\chi^{(3)}/2\epsilon_0 c n_0$ (the Kerr coefficient) are constants characterizing the material [17, 33].

As the nonlinearities depend only on the modulus of the field and not on its instantaneous value, it may be possible to obtain solutions that can be represented by equation (1). This is our fundamental hypothesis. We are therefore looking for solutions (β, ϕ) of the nonlinear equation

$$\Delta_\mathrm{t}\phi + k_0^2(n_0^2 + \mathbb{I}_\mathrm{nl} n_\mathrm{Kerr}^2 |\phi|^2)\phi = \beta^2\phi. \tag{4}$$

When a single Kerr material is used, setting the reduced field

$$\phi_\mathrm{r} = n_\mathrm{Kerr}\phi \tag{5}$$

allows one to reduce equation (4) to

$$\Delta_\mathrm{t}\phi_\mathrm{r} + k_0^2(n_0^2 + \mathbb{I}_\mathrm{nl}|\phi_\mathrm{r}|^2)\phi_\mathrm{r} = \beta^2\phi_\mathrm{r}, \tag{6}$$

which is independent of the Kerr coefficient. Clearly, this means that the refractive index profile leading to the self-coherent solution ϕ_r depends on the linear part of the medium but not on the value of the Kerr coefficient n_Kerr: only the quadratic dependence matters. The physical field $\phi = \phi_\mathrm{r}/n_\mathrm{Kerr}$, however, depends on the coefficient n_Kerr: the smaller n_Kerr, the larger the power injected to produce the self-coherent solution.

We use a finite element method [4] to solve equation (4). As mentioned in section 1, this method is well adapted. This is not the case of the well-known multipole method [1] for which the refractive index of the matrix surrounding the inclusion must be homogeneous. The more recent fast Fourier factorization mode searching method is able to deal with an inhomogeneous medium [22]. Nevertheless, like the multipole method, it has been directly developed in the vector case not in the scalar one. Furthermore, since one of the final goals of our work is to solve the full vector nonlinear problem, it is more convenient for us to use the finite element method for which we already have both the scalar and the vector formulations of the linear problem.

In the present case of a scalar model, we use a classical finite element approximation based on piecewise linear interpolation on a triangular mesh. Moreover, the solutions are supposed to be close to the modes of the linear fibre and therefore the proposed algorithm is a simple Picard iteration, in which a propagation mode is computed in a linear fibre with a refractive index profile determined by the field intensity obtained at the previous iteration.

The starting point of our algorithm is thus the linear fibre; i.e., no nonlinear Kerr effect is considered. For a given k_0, some modes are computed (by solving a matrix eigenvalue problem to find the βs and the corresponding electric fields) and the mode of interest is selected (e.g., the fundamental mode). The corresponding electric field (whose amplitude is arbitrarily fixed in the linear fibre only) is used to compute the new refractive index profile, then new modes are computed with this given refractive index. The mode of interest is selected and used to modify again the refractive index profile that gives a new eigenvalue problem. This process is repeated until the refractive index profile and the β value reaches a fixed point.

This process seems quite simple but there is a fundamental flaw: the amplitude of the eigenmodes is irrelevant and the numerical solutions of the intermediary eigenvalue problems have an uncontrolled amplitude. To the contrary, the nonlinear problem depends fundamentally on the amplitude of the field, and therefore this amplitude has to be determined *a posteriori* for the mode of interest. The chosen solution $\psi(x, y)$ of the numerical eigenvalue problem has thus to be scaled by a scalar factor χ to obtain the reduced field

$$\phi_\mathrm{r} = \chi\psi \tag{7}$$

which corresponds to normalizing the field ψ. A suitable numerical value of χ may be obtained by cancelling a weighted residual of equation (6), with the solution ψ itself taken as the weight factor (so as to minimize the error where the field has the largest values).

In detail, here is how this normalization procedure is applied. First, (ψ_i, β_i) at step i $(i \geqslant 1)$ are computed as particular solutions to the eigenvalue problem

$$\Delta_\mathrm{t}\psi_i + k_0^2(n_0^2 + \mathbb{I}_\mathrm{nl}|\phi_{r,i-1}|^2)\psi_i - \beta_i^2\psi_i = 0, \tag{8}$$

in which, at $i = 1$, $\phi_{r,0}$ is the solution of the linear problem. Then, the value of χ_i is computed so as to optimize the self-coherence of $\phi_{r,i} = \chi_i\psi_i$ by cancelling the residue

$$\int_K \left[\Delta_\mathrm{t}\psi_i + k_0^2(n_0^2 + |\chi_i\psi_i|^2)\psi_i - \beta_i^2\psi_i\right]\overline{\psi_i}\,\mathrm{d}S = 0, \tag{9}$$

where the integral is computed on the cross section K of the Kerr medium region ($\overline{\psi_i}$ represents the complex conjugate of

ψ_i). Using this equation as is would lead to an ill-conditioned expression for χ_i, due to the subtraction of two terms of very similar magnitude. Using the following identity derived from equation (8),

$$\int_K \left[(\Delta_t\psi_i + k_0^2 n_0^2\psi_i - \beta_i^2\psi_i)\overline{\psi_i}\right] \mathrm{d}S = \int_K k_0^2|\phi_{r,i-1}|^2\psi_i\overline{\psi_i}\,\mathrm{d}S, \tag{10}$$

a numerically well-conditioned expression for χ_i can be obtained:

$$\chi_i^2 = \frac{\int_K |\psi_i|^2|\phi_{r,i-1}|^2\,\mathrm{d}S}{\int_K |\psi_i|^4\,\mathrm{d}S}. \tag{11}$$

The whole procedure is summarized in the following algorithm [16]:

begin:

- Set $\psi_0 = 0$ (linear case), $\chi_0 = 1$, $i = 1$
- **repeat**
  - Compute the eigenfunctions ψ_i and the corresponding β_i via the finite element solution of the eigenvalue problem defined by equation (8) and select the one of interest (e.g., the fundamental).
  - Compute χ_i via formula (11).
  - Set $i \leftarrow i + 1$.
- **until** the absolute value of the relative difference between β_i and β_{i-1} denoted by $\delta_i^{\mathrm{relat}}$ is smaller than a prescribed tolerance.
- The $(\chi_{\mathrm{coh}}\psi_{\mathrm{coh}}/n_{\mathrm{Kerr}} = \phi_{\mathrm{coh}}, \beta_{\mathrm{coh}})$ of the last iteration is the self-coherent solution.

end.

Therefore, the proposed algorithm allows us to find a self-coherent solution from an initial solution of the linear problem normalized at one ($\chi_0 = 1$). We call this algorithm the SC_{LinN} algorithm. This process renormalizes the field at each iteration and we can thus deduce the 'self-coherent' power *a posteriori*: it is defined as the integral of $\chi_{\mathrm{coh}}^2\psi_{\mathrm{coh}}^2$.

3. Towards a unique self-coherent solution

Numerical experiments show that the SC_{LinN} algorithm seems sensitive to the amplitude and the shape of the initial field used to start the iteration. To study this feature, a scan of the amplitude and of the shape of the initial solution is performed. To evaluate quantitatively the quality of a solution obtained at the convergence according to the starting point, we propose a criterion: the residue given by the left-hand side of equation (9) is calculated numerically with the finite element approximation of ψ_i.

The numerical tests concern two types of fibre: step-index fibres and microstructured optical fibres. Moreover, we are only interested in the fundamental mode in the linear case. The nonlinear solution associated with this fundamental mode will be referred to as the *nonlinear fundamental 'mode'*. We put 'mode' in between quotation marks, as it is not a mode such as defined in the linear case—there is no superposition principle. Our finite element code has been validated for the computation of modes in linear microstructured fibres, by comparing the results with the well-established multipole method [1, 2] and with the more recent fast Fourier factorization mode searching method which is more versatile [22].

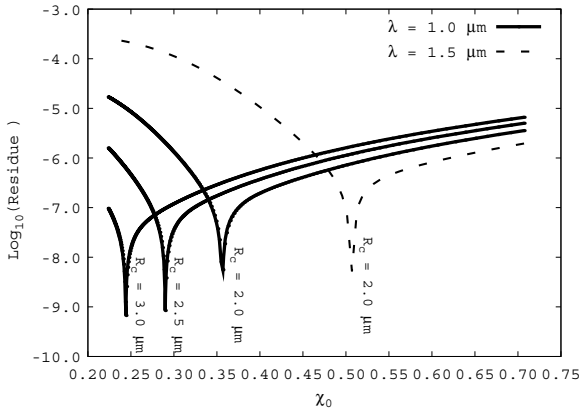

Figure 1. Logarithm of the residue obtained at the convergence, computed using the left-hand side of equation (9), versus the field amplitude χ_0 for two different wavelengths and three different core radii of the step-index fibre.

To correctly describe the field in the fibre and to minimize the computation time, an adaptive mesh refinement is used: the stronger the field, the finer the mesh. In addition, the convergence of the SC_{LinN} algorithm has been shown in [16], and in all the following tests we choose the prescribed tolerance $\delta_i^{\mathrm{relat}} < 10^{-10}$.

3.1. Scanning the amplitude of the linear initial field for the step-index fibre

We start by studying the influence of the amplitude χ_0 of the initial (linear) field $\phi_{r,0}$. For this, we inject $\chi_0\psi_0$ at the first iteration in the nonlinear term in equation (8):

$$\Delta_t\psi_1 + k_0^2(n_0^2 + \mathrm{I\!I}_{\mathrm{nl}}|\chi_0\psi_0|^2)\psi_1 - \beta_1^2\psi_1 = 0, \tag{12}$$

in which the amplitude χ_0 is arbitrarily fixed. Therefore, the initialization of the SC_{LinN} by a unique initial guess is replaced by a one-dimensional scan of the amplitude of the linear initial solution. We denote this process the SC_{Lin1D} algorithm.

In addition, to start the study of SC_{Lin1D}, a cylindrical fibre with a Kerr material ($n_{\mathrm{Kerr}} = 3.2 \times 10^{-20}$ m^2 W^{-1}) in the circular core of radius 2.0 μm is considered. The linear part of the refractive index of this core is $n_0 = 1.45$. The core is embedded in an infinite cladding with a linear refractive index $n = 1.435$ (weak guidance approximation WGA). The Dirichlet condition at the edge of the geometry is also applied (in the present paper we do not address the computation of the leaky modes [1, 4]).

Figure 1 gives the effect of the initial field amplitude on the residual values defined by the left-hand side of equation (9), for different wavelengths and geometries.

Figure 1 shows the minimum residue for the nonlinear solution at the convergence of the iterative process (i.e. when $\delta_i^{\mathrm{relat}} < 10^{-10}$, the fixed point is reached). The influence of

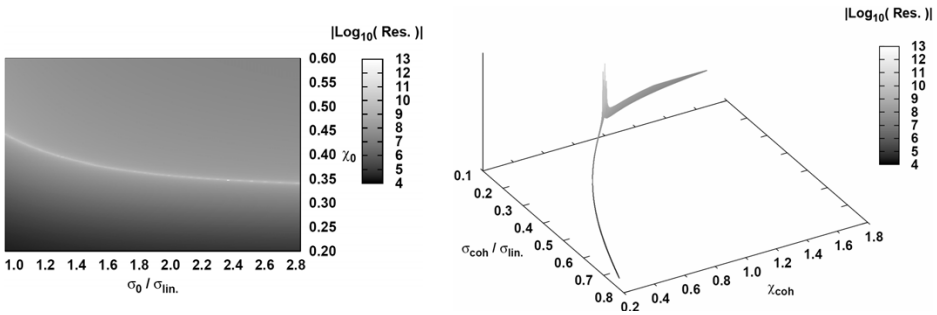

(a) Final residue versus initial parameters χ_0 and $\sigma_0/\sigma_{lin.}$

(b) Final residue versus final parameters χ_{coh} and $\sigma_{coh}/\sigma_{lin.}$ (see the text for a complete description)

Figure 2. Maps of the residue computed for the nonlinear solution as a function of the input parameters characterizing the initial field (a) and as a function of the output parameters characterizing the nonlinear field (b) of the step-index fibre described in the text at $\lambda = 1.0\ \mu$m. σ_{lin} corresponds to the standard deviation of the solution of the linear problem approximated by a Gaussian function.

the mesh has been ruled out by verifying that the minimum corresponds to the same χ_0 for different meshes. It may be deduced that a single nonlinear solution is found for each wavelength: it is *the self-coherent nonlinear solution*. Obviously there exists another minimum residue for $\chi_0 = 0$, corresponding to the solution of the linear problem.

3.2. Scanning both the amplitude and the width of the initial field

In a further investigation, the residue is considered by scanning the initial solution not only in amplitude but also in shape. At the first iteration, instead of the solution of the linear problem, we inject a Gaussian function $\chi_0 e^{-(r/\sigma_0)^2}$, where $r = \sqrt{x^2 + y^2}$ and where σ_0 represents the standard deviation of the function. Therefore, the initialization of the SC_{Lin1D} algorithm is replaced by a two-dimensional scan on χ_0 and σ_0. We call this process the $SC_{Gauss2D}$ algorithm.

The computation is started with one value of σ_0 and the scan in χ_0 is performed, then another value of σ_0 is taken, and so on. Finally, the residue at the convergence of $SC_{Gauss2D}$ is obtained, according to the two parameters χ_0 and σ_0 characterizing the initial field, as shown in figure 2(a).

A narrow valley of minimal residues is observed. This means that for one σ_0 there exists a single χ_0 such that one 'good' final nonlinear solution is obtained: it is the self-coherent solution. Notice that the linear case corresponds to a vertical line in the figure 2(a) at $\sigma_0/\sigma_{\text{lin}} = 1$ when the Gaussian profile closely matches the profile of the fundamental mode as in the WGA. Figure 2(a) suggests that there exists a continuum of solutions depending on the value of σ_0 given for each minimum of the residue. Thus, the question is whether the nonlinear solutions obtained with the solution of the linear problem or each Gaussian function (characterized by σ_0) as the starting point are the same: is the self-coherent solution really unique?

Figure 2(b) shows the absolute value of the logarithm of the residue according to the final solution parameters $(\chi_{\text{coh}}, \sigma_{\text{coh}})$, in which we approximate this nonlinear solution with a Gaussian fit. This figure shows that these final parameters have nearly the same value. Therefore, from a full map of the initial parameters, the $SC_{Gauss2D}$ algorithm provides a localized surface formed by the final parameters characterizing the computed nonlinear solution. In addition, the minimum residues are localized in a small part of this surface. These results allow us to confirm the assumption that the $SC_{Gauss2D}$ algorithm finds a single nonlinear solution: the self-coherent nonlinear solution. This solution is a scalar spatial Kerr soliton in the step-index fibre.

Since for both studied cases (SC_{Lin1D} and $SC_{Gauss2D}$ algorithms) only a unique residue minimum associated to a nonlinear solution (corresponding to the same β value) is found for all the step-index fibres and wavelengths we have tested, we can assume that this observed rule is general for this kind of fibres.

3.3. Results for the microstructured optical fibre

Microstructured optical fibres (MOFs) have more degrees of freedom related to the geometries and index contrasts than step-index fibres [4]. The study of these fibres allows us to extend the domain of validity of our algorithm and to compare our results with those previously published in [17]. The case of a solid core MOF made of four rings of air holes embedded in a Kerr material matrix ($n_{\text{Kerr}} = 3.2 \times 10^{-20}\ \text{m}^2\ \text{W}^{-1}$) is considered here. The linear part of the refractive index in the matrix is $n_0 = 1.45$. The pitch Λ (space between the centre of two adjacent air hole centres) is equal to 10.0 μm and the air hole radius is equal to 2.75 μm.

As for the step-index fibre, the results obtained with SC_{Lin1D} show two minima for the residue: one associated with the solution of the linear problem ($\chi_0 = 0$) and one corresponding to the nonlinear solution. Whatever the amplitude of the solution of the linear problem, a single nonlinear solution—the self-coherent solution—is again found.

For the $SC_{Gauss2D}$ algorithm the Gaussian function is injected only in the matrix and not in air holes since the

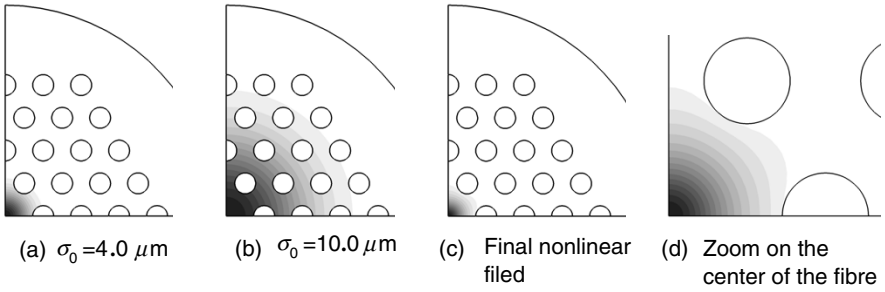

Figure 3. Field distribution in the microstructured optical fibre at $\lambda = 5.0$ μm for two initial Gaussian fields ((a) and (b)) and for the fundamental soliton ((c) and (d)).

field is usually very weak in the air holes due to the index contrast between the matrix and the inclusions. As for the step-index fibre, there is a narrow valley (similar to that of figure 2(a)) corresponding to the minimal values of the residue as a function of the initial parameters χ_0 and $\sigma_0/\sigma_{\text{lin}}$. The map of the final residue versus the final parameters χ_{coh} and $\sigma_{\text{coh}}/\sigma_{\text{lin}}$ obtained is similar to that of figure 2(b).

Figure 3 shows the field distribution when the Gaussian function is used as an initial field, as well as the effect of the nonlinearity when $SC_{Gauss2D}$ has converged. (Using the symmetry properties of the fibre, only a quarter of the geometry needs to be modelled, which significantly reduces the cost of the numerical computations.) These figures illustrate the independence of the final self-coherent nonlinear solution according to the spatial extent of the input initial field.

Therefore both for step-index fibres and for MOFs, SC_{Lin1D} and $SC_{Gauss2D}$ lead to the same solution: the self-coherent solution. Actually, the most natural choice for the physical studies is to use SC_{Lin1D} in which the starting point depends on the solution of the linear problem.

Note that a very fine scan must be performed to obtain the minimum value of the residue equal to the machine accuracy (10^{-15}). Consequently, in practice, the speed and accuracy of the algorithm SC_{Lin1D} are improved by using the golden section search in one dimension [34]. For each wavelength studied, the search is performed on the value of χ_0. The typical shape of the function to be minimized is that in figure 1. Using this improvement, the algorithm is able to reach machine accuracy for the minimal values of the computed residues.

3.4. Physical significance of the self-coherent solution: comparison with the 'fixed-power' method

A 'fixed-power' method was proposed by Ferrando *et al* in [17, 18] to find nonlinear solutions in MOFs with a Kerr term in the matrix refractive index. We call this process, in which the power is given *a priori*, the algorithm FP_{Fer}. Our algorithm SC_{LinN} can be easily modified (to study the 'fixed-power' method) by replacing equation (11) with $\chi_i^2 = P/\int_K |\psi_i|^2 \, \mathrm{d}S$, in which P is the fixed value of the power. We call our finite element method implementation of the 'fixed-power' process the FP_{FEM} algorithm.

To compare the physical properties of the solutions given by FP_{Fer}, FP_{FEM}, and SC_{Lin1D}, we use the quantities

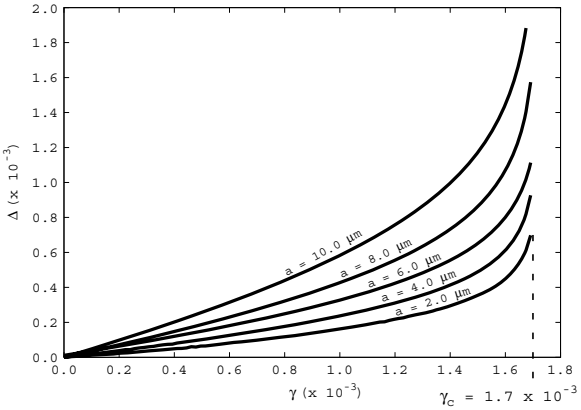

Figure 4. Dependence of the gap function Δ on the nonlinear coefficient γ for various air hole radii a at $\lambda = 1.55$ μm. These results are obtained by using the algorithm FP_{FEM}, and γ_c is defined in the text.

defined in [17]: the dimensionless nonlinear coefficient $\gamma = Pn_{\text{Kerr}}^2/A_0$ and the gap function $\Delta = (\beta_{\text{NL}} - \beta_{\text{lin}})/k_0$, in which P is the total power, and $A_0 = \pi(\Lambda/2)^2$ characterizes the core size (for the step-index fibre, $A_0 = \pi R_{\text{core}}^2$, in which R_{core} is the radius of the core). β_{lin} and β_{NL} are the propagation constants of the solution of the linear and nonlinear problems, respectively.

Our first study consists in comparing the results of the two implementations of the 'fixed-power' method: FP_{Fer} and FP_{FEM}. The computations are provided for a silica microstructured optical fibre with a pitch equal to 23.0 μm, for various air hole radii at $\lambda = 1.55$ μm [17]. The MOF considered in FP_{FEM} has a finite size and is made of four rings of air holes, while the geometry for FP_{Fer} is periodic. The evolution of the gap function Δ according to the nonlinear coefficient γ is computed (see figure 4) for various air hole radii. This figure shows an approximate limit power corresponding to $\gamma_c = 1.7 \times 10^{-3}$. As soon as $\gamma > \gamma_c$ the numerical process is divergent. Figure 4 shows that the value of γ_c found with FP_{FEM} is the same as that obtained with FP_{FEM} (see figure 3(a) in [17]).

The second study consists in understanding the physical significance of the self-coherent solution. To achieve this,

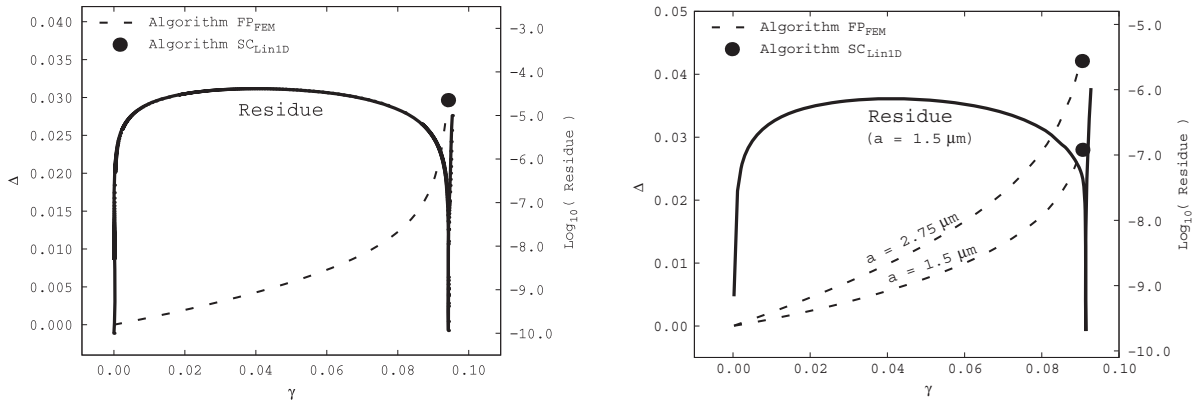

(a) Comparison for the step-index fibre described in section 3.1 at λ = 1.0 μm and the corresponding residue

(b) Comparison for two MOFs with different radii *a* at λ = 5.0 μm and one associated residue for *a* =1.5 μm

Figure 5. Comparison between FP_{FEM} and SC_{Lin1D} for the fundamental 'mode' for different fibres. γ_c corresponds to the critical power; above this value FP_{FEM} diverges.

the physical powers obtained by FP_{FEM} and SC_{Lin1D} are compared. Therefore, this study consists in getting the value of the 'self-coherent power' (i.e., $P_{coh} = \int_F |\chi_{coh}|^2 |\psi_{coh}|^2 \, dS$) obtained using SC_{Lin1D}. Then, the value of the physical power equal to $P_{phys.} = P_{coh}/n_{Kerr}^2$ is deduced. Finally, some ascending values of power are injected as input in FP_{FEM} until the value of the physical power $P_{phys.}$ obtained with SC_{Lin1D} is reached. Figure 5 gives the results of this comparison for several fibres: the step-index one, figure 5(a), and two microstructured optical ones with different air hole sizes, figure 5(b).

Figure 5(a) shows the comparison between FP_{FEM} and SC_{Lin1D} for the step-index fibre described in section 3.1 at $\lambda = 1.0$ μm. The 'fixed-power' algorithm FP_{FEM} diverges for power γ above the critical power γ_c (see figure 4). Contrary to the results provided by FP_{Fer} in [17], the critical γ computed with FP_{FEM} depends slightly on the air hole radius a. As will be shown in the next paragraph, this dependence is confirmed using SC_{Lin1D}. This issue is also discussed in section 4.

The self-coherent algorithm SC_{Lin1D} finds the self-coherent solution at the corresponding critical power directly. As mentioned at the end of section 3.1, two minimal values of the residue are found. The first one corresponds to the linear case $\gamma = 0$ and the second one corresponds to the self-coherent nonlinear solution. This solution is obtained both with SC_{Lin1D} and with $SC_{Gauss2D}$. The other solutions found with the 'fixed-power' method at lower powers are not the self-coherent solution because they do not correspond to a minimal residue.

To complete this observation, the study is repeated for various MOFs (figure 5(b)). The computed results for these two MOF geometries lead to the same conclusion as that already drawn for the step-index fibre: the self-coherent solution obtained with the algorithm SC_{Lin1D} gives directly (and so, much more rapidly) the limit of the highest power solution reachable ($\gamma = \gamma_c$) with the algorithm FP_{FEM}.

Therefore, with our new SC_{Lin1D} algorithm and for each fibre, a single self-coherent solution corresponding to the spatial soliton with the highest possible energy just before the self-focusing instability is easily obtained.

The last study is to compare the convergence of SC_{Lin1D} with the one of the 'fixed-power' method FP_{FEM} (figure 6).

This figure shows the comparison of the convergence for two different powers (represented by the γ coefficient) in the MOF described in section 3.3. Figure 6 proves that SC_{Lin1D} converges much more rapidly than FP_{FEM}. After 50 steps the convergence of FP_{FEM} is not reached, whereas SC_{Lin1D} requires 13 steps to converge. In addition, at the critical power ($\gamma = \gamma_c$), that is to say for the self-coherent solution, the effective index cannot be found with FP_{FEM} because this algorithm does not reach the required accuracy (for $\delta_i^{relat} < 10^{-10}$) unlike the self-coherent algorithm SC_{Lin1D}.

4. Beyond the Townes soliton

As illustrated in figure 5, the self-coherent solution corresponds to the spatial soliton with the highest reachable power before the self-focusing instability. Therefore, we can wonder whether this solution is the solution obtained for a homogeneous silica medium with a nonlinear Kerr term [29]. To analyse this issue, SC_{Lin1D} is implemented for this case and the results are compared with those given by the following fibre geometries (figure 7): the step-index fibres with various core radii in the case of the WGA described in section 3.1, and different solid core microstructured optical fibres with various air hole radii.

Figure 7 shows that the self-coherent solution of the nonlinear step-index fibre depends on the core radius. This means that, even in the nonlinear case, the core/cladding interface is important. The curves given in figure 7 also prove that the nonlinear solution obtained in the step-index fibres differs from that of the homogeneous medium. As

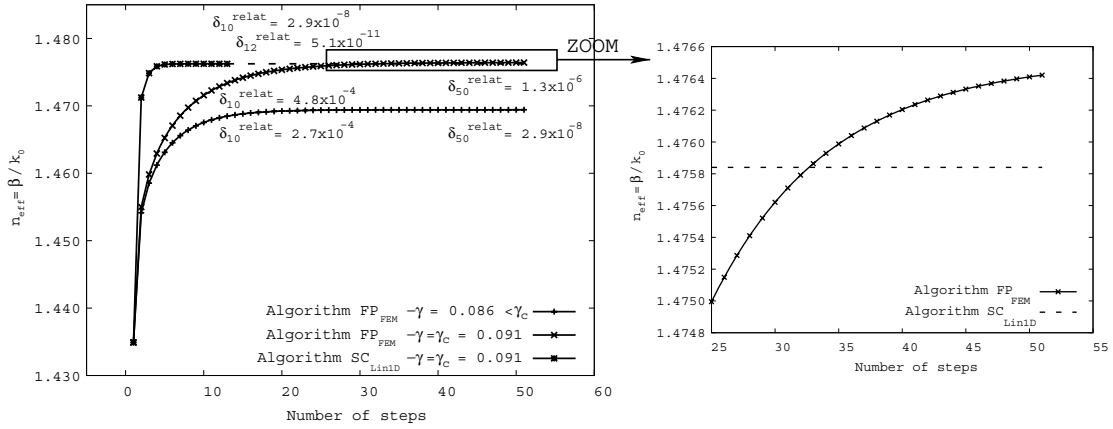

Figure 6. Convergence of SC_{Lin1D} compared with FP_{FEM} for the fundamental 'mode' of the MOF described in section 3.3 at $\lambda = 5.0\ \mu$m. δ_i^{relat} is the absolute value of the relative difference between the values of β at the steps $i-1$ and i. To make the comparison with the FP_{FEM} results easier, the value of n_{eff} for the self-coherent solution at step 13 of the SC_{Lin1D} is extended to step 50.

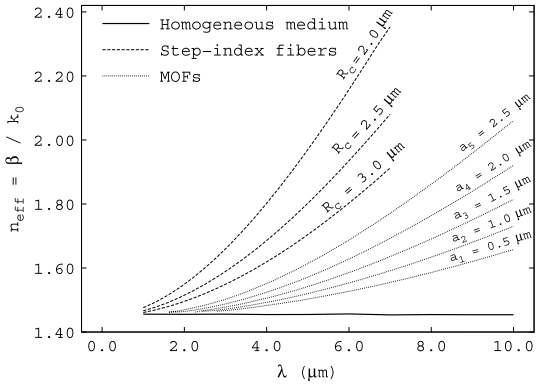

Figure 7. Comparison of the nonlinear effective index of the spatial soliton versus the wavelength in different nonlinear waveguides and in a homogeneous nonlinear medium. The solid core MOFs studied have four rings of air holes with various radii a and $\Lambda = 6.0\ \mu$m. The index contrast of the step-index fibres with various core radii fulfils the WGA.

expected, the higher the core radius (i.e. the structure tends to the homogeneous medium), the smaller the difference with the homogeneous medium. The same phenomenon is observed for the MOFs, where the self-coherent solution does not correspond to that obtained in the homogeneous medium. In addition, the smaller the air hole radius (i.e. the structure tends to the homogeneous medium), the smaller the difference with the homogeneous case. Figure 7 also shows that for smaller wavelengths the role of the air holes decreases, the self-coherent solution being more confined. Notice that, in the 'fixed-power' study [17], the ratio λ/Λ is small. This explains the weak influence of the fibre geometry on the critical nonlinear coefficient γ_c. As a consequence, the diagram of existence of spatial solitons (figure 3(b) in [17]) must be modified so as to take into account the influence of the waveguide geometry. In the parameter space (γ, a) and using the terminology defined in [17], the frontier between the *spatial soliton* region and the *self-focusing* region is not exactly a vertical line defined by a unique critical nonlinear coefficient γ_c. It is rather a line segment such that the lower the nonlinear coefficient the bigger the hole radius. The limit case corresponds to a step-index fibre with nonlinear core surrounded by an air ring with the hole diameter $d = 2a = \Lambda/2$ (see figure 7).

Therefore, the spatial solitons obtained with our algorithm for nonlinear optical waveguides differ from that of a nonlinear homogeneous medium.

The second point concerns the study of the Townes soliton [17, 29, 30]. The Townes soliton corresponds to the solution of a propagation problem in a nonlinear homogeneous medium. It corresponds to the critical solution before the self-focusing instability. We recall that the genuine Townes soliton, as defined in the seminal article written by Chiao *et al*, is obtained without using the SVEA (see equations (5) and (6) in [29]) but the propagation constant of the soliton is computed from the field profile. The problem solved (see the paragraph below equation (6) in [29]) is not an eigenvalue problem. To assert the difference between our self-coherent solution obtained for each structure with the Townes soliton, the power and the profiles of these solutions are studied. The first step is to get the profile $R(r)$ of the Townes soliton as the solution of the one-dimensional (1D) equation:

$$\Delta_t R - R + R^3 = 0, \qquad R'(0) = 0 \qquad \text{and} \qquad R(\infty) = 0. \tag{13}$$

To solve this two-point boundary value problem a shooting method is used [34]. The profile of the solution is obtained and shown in figure 1 of [29]. We have also calculated the critical power coefficient N_{cr} [30] given by

$$N_{\text{cr}} = \int_\Omega |R|^2 r\, \mathrm{d}r \approx 1.862 \tag{14}$$

where Ω corresponds to the 1D domain.

To compare our self-coherent solution with the Townes one, an expression of the self-coherent power N_{coh} associated

with the critical power coefficient N_{cr} is defined. In physical units, the lower bound of the critical power P_{cr}^{lb} is given by [30, 33]

$$N_{cr} = \frac{4\pi n_0 n_2}{\lambda^2} P_{cr}^{lb} \tag{15}$$

where n_2 represents the nonlinear coefficient characterizing the Kerr medium. The scalar optical Kerr effect can be defined as follows: $\varepsilon_r(\phi) = (n_0 + n_2|\phi|^2)^2 \approx n_0^2 + 2n_0 n_2|\phi|^2$, and we have defined $n_{Kerr}^2 = 2n_0 n_2$, in which n_2 is the nonlinear coefficient characterizing the material [5]. However, in our case, an eigenvalue-like problem is solved. Indeed, unlike the Townes soliton studies [29, 30], the propagation constant β is considered so as to describe completely the features of the nonlinear self-coherent solution. To take into account the β_{coh} eigenvalue of our approach, the physical power P_{phys} defined directly from the Poynting theorem is calculated. In this case,

$$P_{phys} = \frac{\beta_{coh}}{\tilde{k}_0} P_{cr}^{lb} = \frac{P_{coh}}{n_{Kerr}^2} = \frac{P_{coh}}{2n_0 n_2}, \tag{16}$$

in which $P_{coh} = \int_\Omega |\chi_{coh}|^2 |\psi_{coh}|^2 \, dS$ is the self-coherent power obtained at the convergence of SC_{Lin1D}, and $\tilde{k}_0 = 2\pi n_0/\lambda$ is defined so as to compare with the critical power coefficient N_{cr} given in [30]. Consequently, we get

$$P_{cr}^{lb} = \frac{\tilde{k}_0}{2n_0 n_2 \beta_{coh}} P_{coh}. \tag{17}$$

Therefore, the coefficient N_{coh} permitting us to compare our scalar spatial Kerr solitons with the Townes soliton can be defined, by using P_{cr}^{lb} of the equation (17) in expression (15), as

$$N_{coh} = \frac{4\pi^2 n_0}{\beta_{coh}\lambda^3} P_{coh}. \tag{18}$$

Figure 8 shows the comparison between the coefficient N_{coh} for step-index fibres with various core radii, for solid core MOFs with various air hole sizes, and for the homogeneous medium with the critical power coefficient N_{cr} of the Townes soliton. These results confirm those obtained in figure 7, and they illustrate the influence of the fibre geometry. In addition, figure 8 shows that the smaller the wavelength (the field is more confined in the MOF core), the smaller the difference between the Townes soliton and the self-coherent solutions.

Figure 8 also gives the evolution of the value of N_{coh} in the homogeneous medium case, with respect to the wavelength. As explained above, our numerical approach SC_{Lin1D} takes into account the β value. Nevertheless, it is very near the constant one of the genuine Townes soliton (1.4555 instead of 1.45). A more detailed wavelength dependence cannot be obtained with the current numerical accuracy of the effective indices. We can recall that it is known from the seminal work of Chiao *et al* that for the Townes soliton this dependence is really weak (see page 480 of [29], second column).

It is interesting to notice that the nonlinear self-coherent solution (obtained with SC_{Lin1D} from equation (6), ϕ and β being unknown) in the homogeneous medium corresponds well to the Townes soliton (obtained from equation (13) with a shooting method).

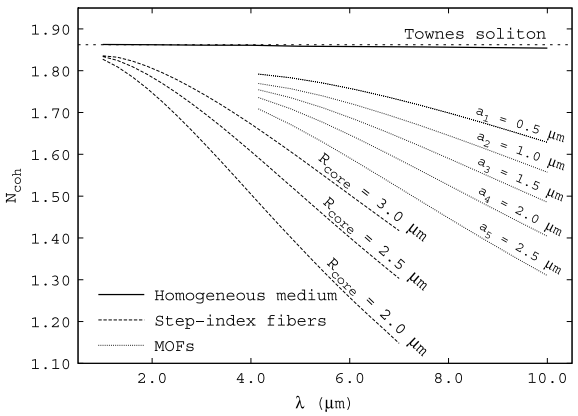

Figure 8. Evolution of the value of the self-coherent power coefficient N_{coh} for various step-index fibres, for different solid core MOFs, and for the homogeneous medium as a function of the wavelength. The horizontal dashed line is the critical power coefficient $N_{cr} = 1.862$ of the Townes soliton.

Figure 9 illustrates the dependence of the nonlinear self-coherent profile as a function of the wavelength and of the fibre geometry. The global shapes of these spatial solitons are similar that of the Townes soliton (see figure 1 in [29] and figure 1 in [30] that show clearly that the Townes soliton can be approximated with a Gaussian curve) but the amplitudes are different. As expected at a fixed wavelength, the spatial width of these spatial solitons decreases with the radius a of the air holes but the maximal amplitude increases. Nevertheless, the ratio P_{coh}/β_{coh} which appears in formula (18) decreases with a, inducing an overall decrease of the critical power coefficient N_{coh} (see also figure 8).

The next point concerns the influence of the finite size of the structure. The solid core MOF considered in figure 10 has the same geometry as that described in section 3.3 but the air hole radius is equal to 1.0 μm. The results are given for several numbers of air hole rings N_r. As can be seen in figure 10, the curve order is reversed between the linear and the nonlinear cases for the MOFs.

In the linear case and at a fixed wavelength, the effective index increases when N_r increases, which is well known [4]. In the nonlinear case, the evolution of N_r is physically coherent with the wavelength dependence already observed in figure 7: the more the structure confines the field, the lower is the nonlinear effective index. Obviously, if the air hole radius increases, the influence of the finite size structure becomes negligible. These results prove that the nonlinear self-coherent solution depends not only on the MOF structure but also on its finite size.

Last, figure 11(a) gives the evolution of the linear and nonlinear effective indices and normalized effective area versus the wavelength obtained with SC_{Lin1D} for a step-index fibre described in section 3.1.

Figure 11(a) shows that the larger the wavelength, the stronger the nonlinear effect. To confirm this observation, figure 11(b) shows that the effective area obtained in the nonlinear case is constant in comparison with the linear case.

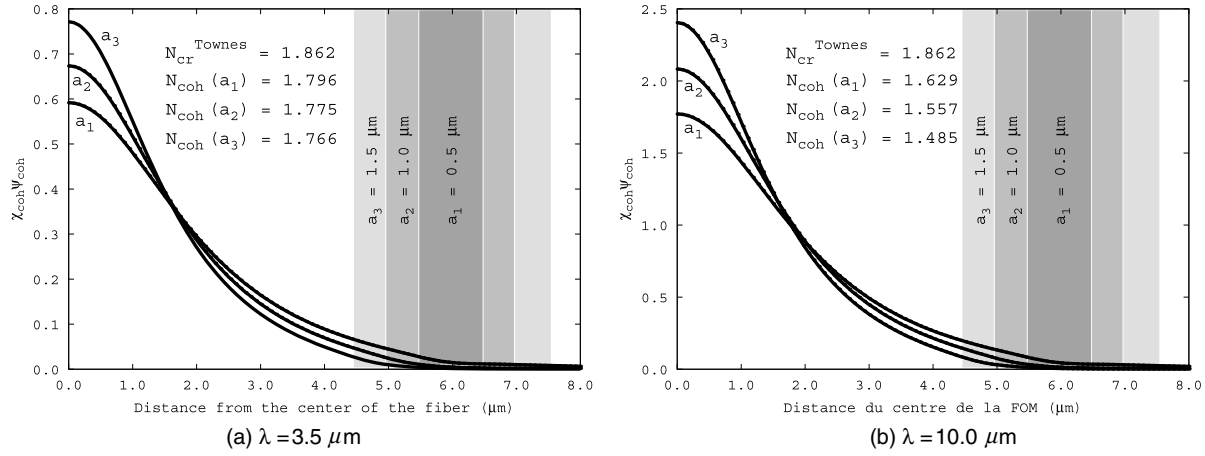

Figure 9. Field profiles for three MOFs with four air hole rings at two wavelengths. The coloured region represents the first air hole of the MOF according to the radius and the associated values of the 'self-coherent power'.

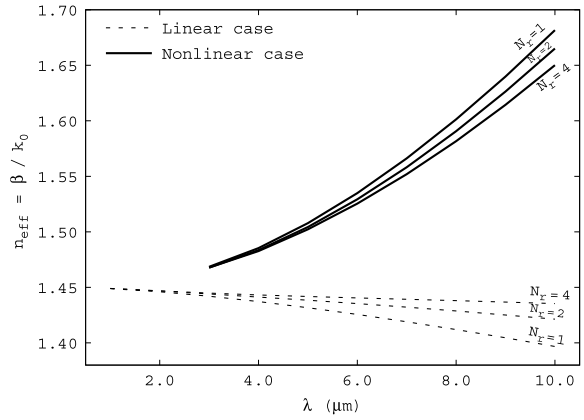

Figure 10. Effect of the number of air hole rings N_r in a solid core MOF ($\Lambda = 6.0\ \mu$m and $a = 1.0\ \mu$m) on the effective index according to the wavelength in the linear and nonlinear cases.

Thus, the field scattering which increases with the wavelength is challenged by the nonlinear effect.

From the results of this section, we can infer that differences from Townes soliton properties will be observed in waveguides in which the ratio of the wavelength over the characteristic size of the nonlinear core is above a constant slightly smaller that unity. Such a ratio is only three times that measured in a nonlinear glass planar waveguide [35] and can be overcome in structures like nanowires [36].

5. Discussion

The self-coherent algorithm SC_{Lin1D} has been presented for the scalar approach within the weak guidance approximation. Neglecting the term $\nabla[\mathbf{E} \cdot \nabla\epsilon_r/\epsilon_r]$, we obtain the equation $\Delta\mathbf{E} + k_0^2\epsilon_r\mathbf{E} = 0$. However, for the step-index fibre, while the weak index contrast is fulfilled in the linear case, as soon as we have considered the Kerr effect the index contrast increases and the WGA is not valid any more (see figure 12(a)). For the microstructured optical fibre, even the linear case does not obey this approximation (see figure 12(b)). Indeed, the WGA is only validated if the relative index variation is negligible on a distance of one wavelength [31]. Consequently, so as to obtain more accurate results, future studies must deal with the full vector problem. Such an extension of the present work is possible since our original numerical method can be formulated in the vector case [4, 23].

The second issue is the value of the physical power $P_{\text{phys.}} = P_{\text{coh}}/n_{\text{Kerr}}^2$ of the nonlinear self-coherent solution. This implies that the stronger the Kerr coefficient n_2 (or $n_{\text{Kerr}}^2 = 2n_0n_2$), the weaker the physical power. Nevertheless, even if we choose chalcogenide glasses which are known to have a high Kerr nonlinearity [37, 38], the power of the self-coherent solution is huge as already computed for the Townes soliton power [29]. With $n_{\text{Kerr}}^2 = 10^{-17}$ m^2 W^{-1}, one gets a soliton power of 2.6×10^4 W at 2 μm for the MOF described in section 3.3 and 7.4×10^5 W at 10 μm. These results suggest that the scalar self-coherent solution cannot easily be validated by experiments. In the scalar approach used in our study, from a practical point of view the induced increase in the refractive index of the core or of the matrix is so important that either other nonlinear effects should be taken into account or the medium is damaged [39]. However, spatial optical solitons have already been observed in planar nonlinear glass waveguides using a 4×10^5 W input at 620 nm using 75 fs pulses [35]. It will be interesting to know if, in the vector case, the physical power of the self-coherent soliton will decrease or not so as to make it more accessible to experimental observation.

The third issue of the discussion concerns the stability of the self-coherent solutions. This is a difficult problem since, in the present cases, it requires one to solve a 3D propagation problem along the waveguide axis. For the fixed-power solutions, Ferrando *et al* [17] have already proved that the spatial solitons are stable under arbitrary perturbations. They also showed that spatial solitons found at fixed power

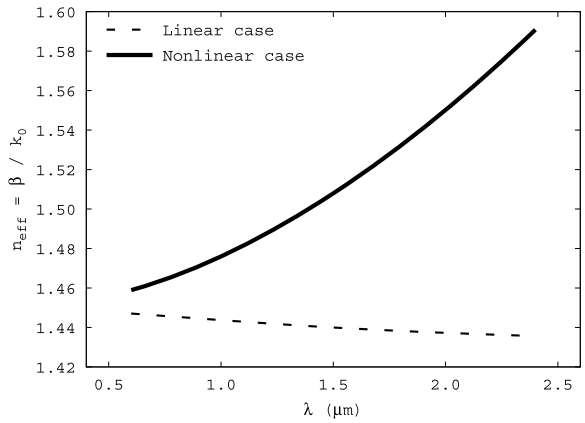

(a) Evolution of the effective indices

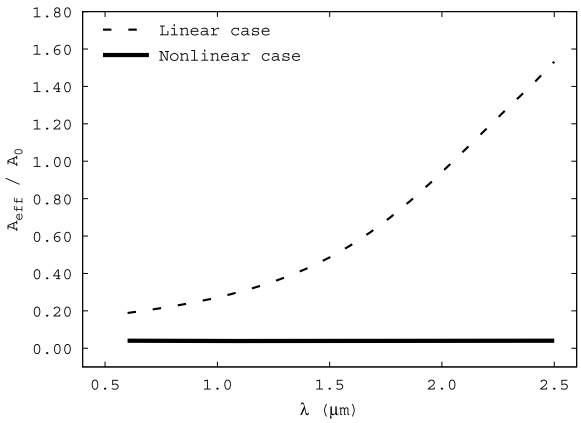

(b) Evolution of the effective area normalized with the core area $A_0 = \pi R^2_{core}$

Figure 11. Evolution of the linear and nonlinear effective indices and normalized effective area versus the wavelength for the step-index fibre described in section 3.1. For the nonlinear case, the SC_{Lin1D} algorithm is used.

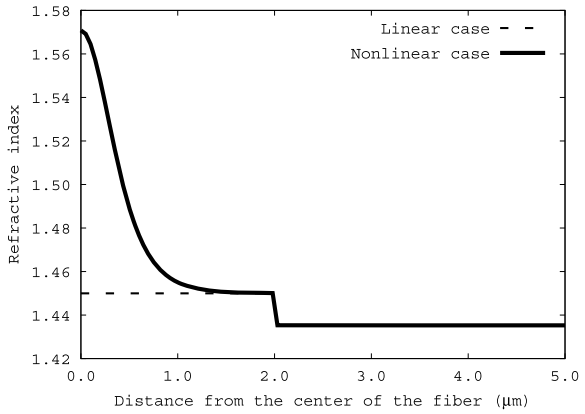

(a) Refractive index profile for the step-index fibre at λ = 1.0 μm (see section 3.1 for a complete description of the structure)

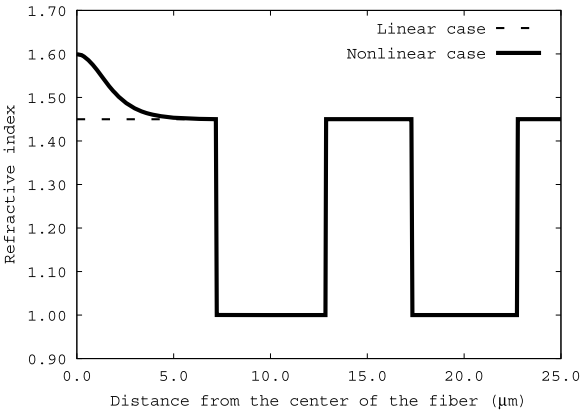

(b) Refractive index profile according to the horizontal axis of the microstructured fibre at λ = 5.0 μm (see section 3.3 for a complete description of the structure)

Figure 12. Effective index profile computed from equation (3) in the linear and nonlinear case for the fundamental 'mode' of the two fibre types described in the text.

are stable under both small transverse displacements relative to the hole cladding and non-perfect launching conditions. In the case of the self-coherent spatial solitons described in the present article, a stability analysis should also be performed. Although this issue is crucial in the case of nonlinear studies, it is beyond the scope of this initial work.

The last issue concerns the comparison with NLSE studies, as already mentioned in section 1. The counterpart of our non-paraxial description of spatial solitons is that the results we obtain are less general than the NLSE ones which can be related to both nonlinear optics and Bose–Einstein condensates [24]. Our results are not obtained with the powerful methods coming from quantum mechanics (like functional density approach) [25, 26] but with a more numerical method well adapted to our non-paraxial problem. Nevertheless, as long as stationary states are considered, our approach, which considers the nonlinear Helmholtz equation as an eigenvalue problem (with the propagation constant as an unknown), is a better model of Maxwell's equations in a nonlinear Kerr-type medium.

6. Conclusions

We have demonstrated that the nonlinear self-coherent solution found in step-index fibres and solid core MOFs, corresponding to the spatial soliton with the highest reachable energy avoiding the self-focusing instability, is different from the Townes soliton. This solution generalizes the Townes soliton within

finite size waveguides. This result, built in the frame of a non-paraxial and scalar approach for stationary solutions, relies on a new algorithm implemented using the finite element method.

To find the nonlinear self-coherent solution, two distinct criteria are defined: the convergence of the algorithm to the required accuracy (the fixed point) and the minimum of the residue at this point. By solving the eigenvalue problem, a single nonlinear solution verifying these criteria is found, for given wavelength and fibre geometry. This single solution of the eigenvalue problem is obtained with various initial guesses: the solution of the associated linear problem (SC_{Lin1D} algorithm) and some Gaussian functions ($SC_{Gauss2D}$ algorithm).

So as to verify the numerical results obtained with the self-coherent algorithm SC_{Lin1D}, several comparisons have been performed. We can adapt our numerical method to obtain a 'fixed-power' algorithm denoted FP_{FEM}. The results computed with FP_{FEM} are in good agreement with already published data for MOFs given in [17], called here FP_{Fer}. The comparison between FP_{FEM} and SC_{Lin1D} has shown that the self-coherent solution is obtained at the critical power just before the self-focusing instability. The SC_{Lin1D} algorithm is shown to be more reliable and more efficient than FP_{FEM} to find the critical power of the spatial solitons.

Then, the physical meaning of the self-coherent nonlinear solution of a step-index fibre with a Kerr material core and of solid core MOFs with Kerr material matrix is discussed. Two comparisons are made: one with the self-coherent solution computed for a homogeneous Kerr material and the second one with the usual Townes soliton computed for the same structure. From the mathematical point of view the former problem is a nonlinear eigenvalue problem while the latter is a two-point boundary value problem (since the dependence on the propagation is not taken into account.) We have shown that the self-coherent spatial solitons found for the step-index fibres and for MOFs are different from those of the homogeneous nonlinear medium and from the genuine Townes soliton. In the various structures considered in the present paper, the dependence of the self-coherent solutions is described as a function of the wavelength. We have observed that, as expected, these self-coherent spatial solitons converge towards the Townes soliton at small wavelengths. We have also observed that the amplitude of the nonlinear self-coherent solution depends on the waveguide geometry: the core size for the step-index fibre, and the air hole radius and number of air hole rings for the solid core MOFs.

Finally, the study of the refractive index induced by the nonlinear self-coherent solution has been performed. The weak guidance approximation and the scalar model are no longer valid if the self-coherent solution is considered. To tackle this problem, a study of the full-vectorial version of the proposed method, including a study of the losses, is under development.

Acknowledgments

We would like to thank Gadi Fibich and Yonatan Sivan from the Department of Applied Mathematics of Tel Aviv University for their help concerning the study of the Townes soliton profile.

References

[1] Kuhlmey B, White T P, Renversez G, Maystre D, Botten L C, de Sterke C M and McPhedran R C 2002 Multipole method for microstructured optical fibers II: implementation and results *J. Opt. Soc. Am.* B **10** 2331–40
[2] Kuhlmey B, Renversez G and Maystre D 2003 Chromatic dispersion and losses of microstructured optical fibers *Appl. Opt.* **42** 634–9
[3] Renversez G, Bordas F and Kuhlmey B T 2005 Second mode transition in microstructured optical fibers: determination of the critical geometrical parameter and study of the matrix refractive index and effects of cladding size *Opt. Lett.* **30** 1264–6
[4] Zolla F, Renversez G, Nicolet A, Kuhlmey B, Guenneau S and Felbacq D 2005 *Foundations of Photonic Crystal Fibres* (London: Imperial College Press)
[5] Agrawal G P 2001 *Nonlinear Fiber Optics* 3rd edn (New York: Academic)
[6] Kivshar Y S and Agrawal G P 2003 *Optical Solitons* (Amsterdam: Academic)
[7] Chen Y and Atai J 1997 Maxwell's equations and the vector nonlinear Schrödinger equation *Phys. Rev.* E **55** 3652–7
[8] Akhmediev N, Ankiewicz A and Soto-Crespo J M 1993 Does the nonlinear Schrödinger equation correctly describe beam propagation? *Opt. Lett.* **18** 411
[9] Ciattoni A, Crossignani B, Di Porto P and Yariv A 2005 Perfect optical solitons: spatial Kerr solitons as exact solutions of Maxwell's equations *J. Opt. Soc. Am.* B **22** 1384–94
[10] Karlsson M, Anderson D, Desaix M and Lisak M 1991 Dynamic effects of Kerr nonlinearity and spatial diffraction on self-phase modulation of optical pulses *Opt. Lett.* **16** 1373
[11] Karlsson M, Anderson D and Desaix M 1992 Dynamics of self-focusing and self-phase modulation in a parabolic index optical fiber *Opt. Lett.* **17** 22
[12] Ciattoni A, Crossignani B, Di Porto P, Scheuer J and Yariv A 2006 On the limit of validity of nonparaxial propagation equations in Kerr media *Opt. Express* **14** 5517–23
[13] Selleri S, Vincenti L and Cucinotta A 1998 Finite element method resolution of non-linear Helmholtz equation *Opt. Quantum Electron.* **30** 457–65
[14] Joseph R M and Taflove A 1994 Spatial soliton deflection mechanism indicated by FD-TD Maxwell's equations modeling *IEEE Photon. Technol. Lett.* **6** 1251–4
[15] Feit M D and Fleck J A Jr 1988 Beam nonparaxiality, filament formation, and beam breakup in the self-focusing of optical beams *J. Opt. Soc. Am.* B **5** 633
[16] Nicolet A, Drouart F, Renversez G and Geuzaine C 2007 A finite element analysis of spatial solitons in optical fibres *COMPEL* **26** 1105–13
[17] Ferrando A, Zacarés M, Fernandez de Cordoba P, Binosi D and Monsoriu J A 2003 Spatial soliton formation in photonic crystal fibers *Opt. Express* **11** 452–9
[18] Ferrando A, Zacares M, Fernandez de Cordoba P and Monsoriu J A 2004 Vortex solitons in photonic crystal fibers *Opt. Lett.* **12** 817–22
[19] Snyder A W, Mitchell D J and Chen Y 1994 Spatial solitons of Maxwell's equations *Opt. Lett.* **19** 524–6
[20] Snyder A W, Hewlett S J and Mitchel D J 1994 Dynamic spatial solitons *Phys. Rev. Lett.* **72** 1012–5
[21] Nicolet A, Guenneau S and Zolla F 2004 Modelling of twisted optical waveguides with edge elements *Eur. Phys. J. Appl. Phys.* **28** 153–7
[22] Boyer P, Renversez G, Popov E and Nevière M 2007 Improved differential method for microstructured optical fibres *J. Opt. A: Pure Appl. Opt.* **9** 728–40

[23] Guenneau S, Nicolet A, Zolla F and Lasquellec S 2002 Modeling of photonic crystal fibers with finite elements *IEEE Trans. Magn.* **38** 1261–4
[24] Alexander T J and Bergé L 2002 Ground states and vortices of matter–wave condensates and optical guided waves *Phys. Rev.* E **65** 026611
[25] Dalfovo F, Renversez G and Treiner J 1992 Vortices with more than one quantum of circulation in He-4 at negative-pressure *J. Low Temp. Phys.* **89** 425–8
[26] Dalfovo F, Giorgini S, Pitaevskii L P and Stringari S 1999 Theory of Bose–Einstein condensation in trapped gases *Rev. Mod. Phys.* **71** 463–512
[27] García-Ripoll J J and Pérez-García V M 2001 Optimizing Schrödinger functionals using Sobolev gradients: applications to quantum mechanics and nonlinear optics *SIAM J. Sci. Comput.* **23** 1315–33
[28] Ablowitz M J, Ilan B, Schonbrun E and Piestun R 2006 Solitons in two-dimensional lattices possessing defects, dislocations, and quasicrystal structures *Phys. Rev.* E **74** 035601
[29] Chiao R Y, Garmire E and Townes C H 1964 Self-trapping of optical beams *Phys. Rev. Lett.* **13** 479–82
[30] Fibich G and Gaeta A L 2000 Critical power for self-focusing in bulk media and in hollow waveguides *Opt. Lett.* **25** 335–7
[31] Marcuse D 1991 *Theory of Dielectric Optical Waveguides* 2nd edn (San Diego, CA: Academic)
[32] Snyder A W and Love J D 1983 *Optical Waveguide Theory* (New York: Chapman and Hall)
[33] Boyd R W 2003 *Nonlinear Optics* 2 edn (New York: Academic)
[34] Press W H, Flannery B P, Teukolsky S A and Vetterling W T 1986 *Numerical Recipes* (Cambridge: Cambridge University Press)
[35] Aitchison J S, Weiner A M, Silberberg Y, Oliver M K, Jackel J L, Leaird D E, Vogel E M and Smith P W E 1990 Observation of spatial optical solitons in a nonlinear glass waveguide *Opt. Lett.* **15** 471–3
[36] El-Ganainy R, Mokhov S, Makris K G, Christodoulides D N and Morandotti R 2006 Solitons in dispersion-inverted AlGaAs nanowires *Opt. Express* **14** 2277–82
[37] Smektala F, Quemard C, Couderc V and Barthélémy A 2000 Non-linear optical properties of chalcogenide glasses measured by *z*-scan *J. Non-Cryst. Solids* **274** 232–7
[38] Brilland L, Smektala F, Renversez G, Chartier T, Troles J, Nguyen T, Traynor N and Monteville A 2006 Fabrication of complex structures of holey fibers in chalcogenide glass *Opt. Express* **14** 1280–5
[39] Stuart B C, Feit M D, Rubenchik A M, Shore B W and Perry M D 1995 Laser-induced damage in dielectrics with nanosecond to subpicosecond pulses *Phys. Rev. Lett.* **12** 2248–51

Small-core chalcogenide microstructured fibers for the infrared

Frédéric Désévédavy,[1,5] Gilles Renversez,[2,*] Laurent Brilland,[3] Patrick Houizot,[1] Johann Troles,[1] Quentin Coulombier,[1] Frédéric Smektala,[4] Nicholas Traynor,[3] and Jean-Luc Adam[1]

[1]Laboratoire Verres et Céramiques, UMR CNRS 6226, Université de Rennes 1, Rennes, France

[2]Institut Fresnel, UMR CNRS 6133, Université d'Aix-Marseille, Marseille, France

[3]PERFOS (plateforme d'Etudes et de Recherche sur les Fibres Optiques Spéciales), 11 rue Louis de Broglie 22300 Lannion, France

[4]Institut Carnot de Bourgogne, ICB UMR CNRS 5209, Université de Bourgogne, Dijon, France

[5]frederic.desevedavy@univ-rennes1.fr

*Corresponding author: gilles.renversez@fresnel.fr

Received 1 August 2008; revised 7 October 2008; accepted 13 October 2008; posted 13 October 2008 (Doc. ID 99575); published 4 November 2008

We report several small-core chalcogenide microstructured fibers fabricated by the "Stack & Draw" technique from $Ge_{15}Sb_{20}S_{65}$ glass with regular profiles. Mode field diameters and losses have been measured at 1.55 μm. For one of the presented fibers, the pitch is 2.5 μm, three times smaller than that already obtained in our previous work, and the corresponding mode field diameter is now as small as 3.5 μm. This fiber, obtained using a two step "Stack & Draw" technique, is single-mode at 1.55 μm from a practical point of view. We also report the first measurement of the attenuation between 1 and 3.5 μm of a chalcogenide microstructured fiber. Experimental data concerning fiber attenuation and mode field diameter are compared with calculations. Finally, the origin of fiber attenuation and the nonlinearity of the fibers are discussed.

OCIS codes: 160.2750, 060.2310, 060.2270, 060.2280.

1. Introduction

To extend the wavelength range available for light guiding in microstructured fibers (MFs) toward the midinfrared is a challenging task, which would allow the extension of techniques successfully used between 0.5 and 1.7 μm to longer wavelengths [1,2]. At least two bands are of particular interest, from 3–5 μm and from 8–12 μm due to low atmospheric absorption, for applications such as light-imaging detection and ranging (LIDAR), or hyperspectral imaging. Other applications, such as supercontinuum generation [3,4] or sensors [5,6], may also be envisaged. To reach such goals, chalcogenide glasses are doubtlessly good candidates due to their low bulk material losses in the midinfrared spectral region and to their high nonlinear coefficient [7,8]. Only a few chalcogenide microstructured fibers have already been reported in the literature because fiber fabrication has proved to be an extremely difficult technical task. The first report concerned an irregular structure obtained by extrusion and made of only one ring of holes [9] and where no optical characterization was given. More recently, we have shown by using the chalcogenide glass 2S2G ($Sb_{10}S_{65}Ge_{20}Ga_5$) that the "Stack & Draw" procedure is a useful tool to build complex and regular MFs made of several rings of holes [10]. In this previous study, no attenuation measurement could be realized due to the strong

0003-6935/08/326014-08$15.00/0

losses of the fibers, and the smallest pitch obtained was 7.7 μm. Furthermore, only a multimode MF was obtained. In the work presented here, we describe the fabrication, characterization, and modeling of MFs made of chalcogenide glasses from the system Sb-S-Ge (2SG). This glass was chosen to allow a reduction in the overall losses of the fabricated MFs. The glass losses are given from 1.5 up to 7.5 μm with a minimum of 0.05 dB/m at 2.3 μm and with a value of 0.39 dB/m at 1.55 μm. To the best of our knowledge, no such results have already been published for this glass. The overall MF losses are measured at 1.55 μm for all three fabricated MFs, and a full attenuation curve is given from 1 to 3.5 μm for one of the fibers. We also describe the first chalcogenide small solid core MF (mode field diameter less than 4 μm) that exhibits single-mode behavior at 1.55 μm. This MF was obtained using a two step drawing technique and its pitch is 2.5 μm, which is more than three times smaller than that previously obtained. Its effective area is measured at 10 μm^2, which is seven times smaller than the one previously reported [10]. The main application of such a MF would be nonlinear based devices such as a supercontinuum sources in the midinfrared [11,12]. In the present study, we also give numerical results concerning mode field diameters and attenuation computed with or without material losses. Good agreement between calculations and experimental data is obtained for the three considered MFs, allowing us to define some practical rules to improve future fabrication. To the best of our knowledge, no such comparisons have already been published previously for chalcogenide MFs. It is worth mentioning that the first two fibers we present are necessary for the present study notably because they enable a better understanding of the origins of the overall losses in chalcogenide MF obtained with the "Stack & Draw" procedure. Loss issues are much more crucial in chalcogenide MF than in silica ones in which the losses are already at the dB/km level [13–15].

The article is organized as follows: in Section 2 glass synthesis is described. The fabrication and characterization of a 2SG monoindex rod are described in Section 3. The description of fiber fabrication and their geometrical characterization is given in Section 4. Section 5 deals with optical characterization of the three MFs with optical losses and mode field diameters compared to numerical simulation results. Finally, the origins of the overall losses are discussed in Section 6, first using numerical simulations and second considering fabrication issues. The single mode behavior of the MF with the smallest core at 1.55 μm is demonstrated using numerical simulations. In Section 6 we also evaluate the effective nonlinearity in this small-core chalcogenide MF.

2. Glass Synthesis

Among the wide variety of chalcogenide glasses, we have selected the 2SG ($Sb_{20}S_{65}Ge_{15}$) glass because it presents a good compromise between its linear and nonlinear properties. The index of refraction is 2.37 at 1.55 μm, and the n_2 is very similar to that of the 2S2G glass (3.2 10–18 m^2/W at 1064 nm, 120 times higher than that of silica glass) [10]. The glass is transparent for bulk samples between 600 nm and 11 μm, giving the glass a red color. The phonon energy of this chalcogenide glass is around 350 cm^{-1} [16]. The partial transparency of this material in the visible is a useful aid for the glass and fiber fabrication process, as eventual defects such as bubbles, crystals, and refractive index variations can be easily visualized. This is not the case when working with selenide or telluride based glasses, which are opaque in the visible wavelength region. In our previous work [10], we have used another sulfide glass from the Sb-S-Ge-Ga system. The current compositional change is mainly due to the purification process for this glass, which enables a decrease of the global fiber loss (see Section 3). The previous glass suffered from the inclusion of gallium, which has a low vapor pressure, meaning that complete distillation of 2S2G glass is not possible. The absence of gallium from the current glass removes this problem. The degree of purity of the final material is determined by the content of impurities in the constituent elements, by introduction of impurities from the apparatus walls and by contamination of the batch components during their loading into the silica tube where the glass is synthesized. The glass is prepared from high purity raw materials (5N: 99.999%): antimony, germanium, and sulfur are supplied by Alfa Aesar, Umicore, and Strem, respectively. However the sulfur used still has high levels of OH, water, and carbon. The required amounts of the different elements are placed in a silica ampoule under vacuum (10^{-5} mbar). Then the sulfur is purified using dehydration and distillation procedures. After sealing, the ampoule is introduced in a rocking furnace and progressively heated up to 800 °C. The ampoule is maintained at this temperature for 12 h, before being quenched in water to allow glass formation and avoid any crystallization process. The vitreous sample is then annealed for several hours at the glass temperature (Tg = 250 °C) to relax the internal mechanical stress induced by quenching, and it is slowly cooled to room temperature. A glass rod is subsequently obtained.

3. Shaping of the Glass and Monoindex Optical Fiber Fabrication

The realization of microstructured optical fibers requires the preparation of glass tubes. One glass tube is used for the fiber jacket and another is used to draw the capillaries that will form the holes of the fiber. Tubes are fabricated by centrifugation of a 700 °C glass melt spinning at 3000 rpm at ambient temperature during several minutes (see Fig. 1). During the rotation cooling occurs, the viscosity increases, and the formation of a vitreous tube is obtained after a few minutes. The glass rod is obtained as described in the Section 2.

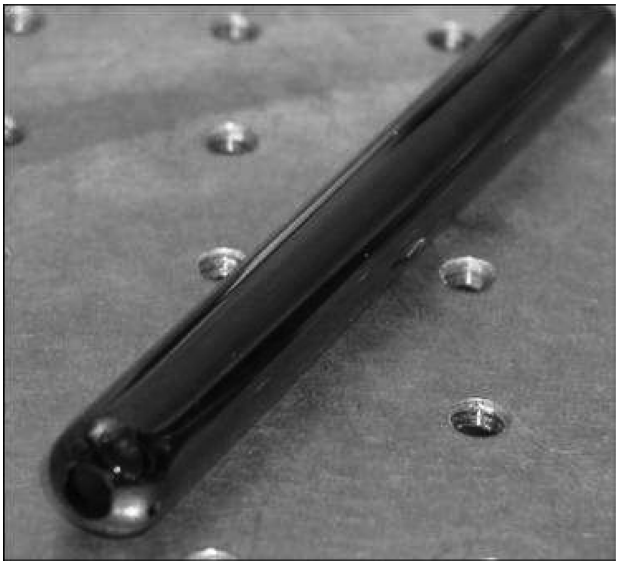

Fig. 1. Chalcogenide glass tube.

Before the fabrication of the MF, we have drawn a single index fiber from the previous glass rod to control its quality by measuring the optical losses. The material losses of the monoindex fiber have been measured using the cutback technique with a Fourier transform infrared spectrometer (Bruker) from 1.5 to 8 μm. Figure 2 shows the typical attenuation curve of 2SG glass single index fiber after purification, obtained via cutback on 20 m of fiber. Several extrinsic absorption bands are present, especially those associated with the S–H vibration at 4 and 3.1 μm, which are due to a reaction between the glass and the remaining water in the batch. The carbon particles and water that are present in the initial sulfur are not completely removed during the purification process. The extinction coefficient of the S–H band is equal to 2.5 dB/m/ppm [17], which means that the quantity of S–H in our glass is below 5 ppm. The presence of remaining carbon particles that induce strong scattering behavior [18] explains the increasing loss observed below 2 μm. The losses above 6 μm are induced by oxides and multiphonon absorptions. The losses at 1.55 μm are equal to 0.39 dB/m. The minimum attenuation is 0.05 dB/m around 2.30 μm. The reduction of the S–H absorption band to a reasonable level opens up significant transmission windows in the 3–5 μm region of interest, notably between 4.5 and 5 μm, as well as between 3 and 3.8 μm, with attenuation below 0.5 dB/m. The low loss level reached for the measured attenuation spectrum justifies the choice of the 2SG glass.

To ensure the refractive index homogeneity of the microstructured area, it is necessary that this zone is made with identical glass. We therefore draw the core rod for the MF from the same 2SG tube used for capillaries, collapsed by drawing in a negative pressure regime. As a consequence, the material losses of a monoindex fiber made from this rod are increased from the intrinsic losses, and are measured to be 4.26 dB/m at 1.55 μm, 2.4 dB/m at 2.5 μm, and 2 dB/m at 5 μm. The origin of this loss increase is the same as the origin of the increased loss observed for the fabricated fibers, as described in Section 6. Each MF presented here is made of capillaries and core rods originating from the same glass batch.

4. Microstructured Fiber Fabrication

The fabrication of the MF is realized through the "Stack & Draw" technique which consists of the fabrication of a preform presenting the required geometrical arrangement of air holes around a solid glass core [10,19,20]. Capillaries are stacked in a triangular lattice around the solid core rod of identical diameter, and placed in a larger jacket tube to create the preform. To exacerbate nonlinear effects a small-core diameter is needed [21,22]. To decrease the core size, a microstructured cane with a diameter of 3 mm is drawn from the previous preform and is then inserted into a second jacket tube of 4 mm inner diameter (see Fig. 3). The jacket tube is collapsed onto the microstructured rod and this preform is drawn again, down to the final optical fiber. In this way the core/clad diameter ratio is reduced without reducing the overall fiber diameter. We call this process the two step "Stack & Draw" technique as opposed to direct fiber draw from the initial preform (one step "Stack & Draw" technique).

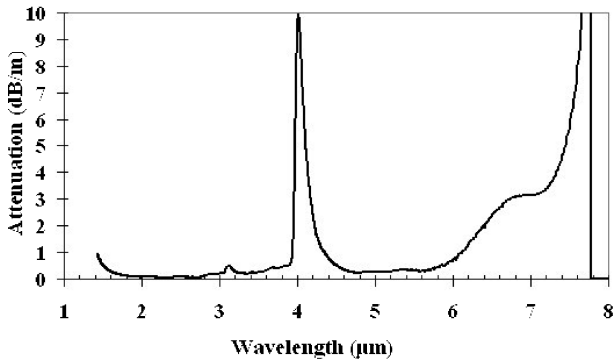

Fig. 2. Typical attenuation curve of 2SG glass monoindex fiber, $\Phi_{ext} = 400\,\mu$m.

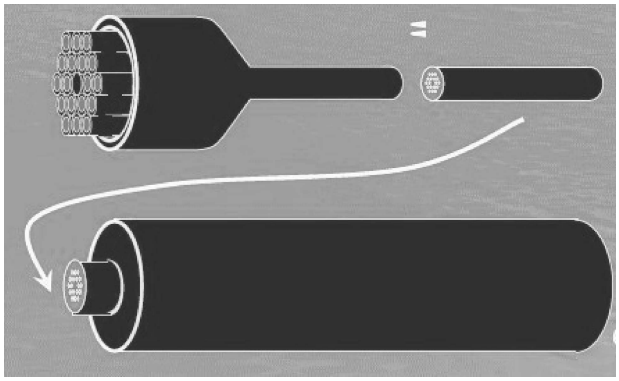

Fig. 3. Jacketing of the stack, drawing and jacketing of the microstructured stick to get small-core MF.

Table 1. Summary of the Different Drawings

Fiber	Process	Φ_{fiber} (μm)[a]	d (μm)	Λ (μm)	Deduced d/Λ ratio	Losses (dB/m) at 1.55 μm
MF1	One step stack and draw technique	150	4.7	11.1	0.423	13
MF2a	One step stack and draw technique	275	6.0	14.0	0.429	15
MF2b [b]	Two step stack and draw technique	150	1.07	2.5	0.429	34

[a] Φ_{fiber} is the fiber outer diameter. The losses are measured with monochromatic light at 1.55 μm.
[b] For fiber MF2b, the value of the hole diameter d has been estimated from the measured pitch and the measured d/Λ ratio of the MF2a, the measured value of the diameter being 1.1 μm (see the text for the details).

It is well known that the high index of refraction of chalcogenide glass enables a better confinement of light in conventional solid core MFs compared to silica. While the number of rings can be reduced for an equivalent core size, several rings are nevertheless necessary to reduce the confinement losses to below the intrinsic glass loss [10,23]. Our previous work [10] shows that, in many cases, three rings of holes are sufficient to ensure guiding losses below material losses of around 1 dB/m. In the present paper we report the fabrication of small-core MFs from 2SG glass with structures based on three rings of holes. Table 1 summarizes the fabrication process and the geometrical specifications of each fiber. Three different fibers have been studied, MF1, MF2a, and MF2b.

Figure 4 shows the cross section of fiber MF1, with three rings of holes (Nr = 3). The outer diameter (Φ_{ext}) is 150 μm, the distance between hole centers (pitch) is $\Lambda = 11.1\,\mu$m, the average hole diameter is 4.7 μm, and the deduced ratio d/Λ is 0.423. The average size of the triangular interstitial holes is 1.2 μm.

One can observe from Fig. 4 that interstitial holes are present across the fiber cross section. These extra holes come from the spaces which exist between the capillaries when they are stacked. The collapse of the external tube was not sufficient in this case to close these holes during the jacketing step of the fabrication of the preform. A second three hole ring MF was realized (MF2a) with an outer diameter Φ_{ext} of 275 μm, a pitch Λ of 14 μm, an average hole diameter of 6 μm, and an estimated ratio of d/Λ at 0.429. The preform used for fiber MF2a was subsequently drawn down to form a cane and jacketed with a second 2SG tube to decrease the core/cladding diameter ratio (Fig. 3). The obtained preform was drawn under the same atmosphere and temperature conditions as MF2a. This fiber (fiber MF2b) is represented in Fig. 5, together with a zoom of the microstructured region. The characteristics are $\Phi_{ext} = 150$, $\Lambda = 2.5\,\mu$m. This pitch is three times smaller than that of fibers obtained in our previous work [10]. The measured hole diameter d is 1.1 μm with a relatively high uncertainty. Other fiber draws with similar structures and using the same draw conditions have shown that the d/Λ ratio is conserved in the process used to draw MF2b from MF2a. Using the d/Λ ration of M2a (0.429), we estimate a d value of 1.07 μm using the measured pitch of 2.5 μm, in agreement with the above value. The measured core size is 4 μm.

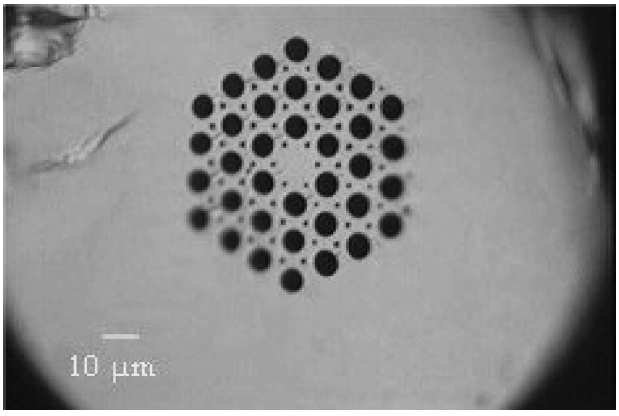

Fig. 4. Picture of the cross section of 2SG fiber MF1.

The two vertical lines at the bottom of Fig. 5 (left) are due to the transversal breaking of the fiber when it was cleaved before analysis. The large hole visible in the lower part of the holey cladding is explained by the presence of an interstitial hole between the stack and the external tube before the jacketing step. The collapse of the external tube was not sufficient in this case to close this hole. Moreover these holes at the edge of the holey region, are the largest of the preform in this kind of stack, and the gas pressure used during the drawing of the fiber leads to their growth. One can note that the third ring is not complete.

5. Optical Characterization and Modeling Results

Optical measurements were made on the fibers using near-field microscopy. An indium metal coating was applied to inhibit cladding mode guidance. Monochromatic light ($\lambda = 1.55\,\mu$m) guided in a single-mode silica optical fiber is butt-coupled to the 2SG MF. The typical fiber length used for the measurements was 50 cm. The image of the fiber output was visualized on an IR camera (Electrophysics) as shown in Figs. 6, 7(a), and 7(b). The output profiles can be accurately fitted with Gaussian functions.

The mode field diameter (MFD) of MF1 at $1/e^2$ of maximum intensity of the fundamental mode is measured using a Gaussian curve fitted to the mode profile [see Fig. 8(a)]. Along the x axis, the measured value is 11.0 μm, while the expected value calculated based on the fiber geometry is 10.7 μm, representing a relative error of 3%. Along the y axis, the measured value is 12.2 μm, versus a calculated value of 11.3 μm, representing a relative error of 8%. We believe that the source of these discrepancies can be at least partially explained by uncertainty in the measured size of the triangular interstitial holes. Attenuation

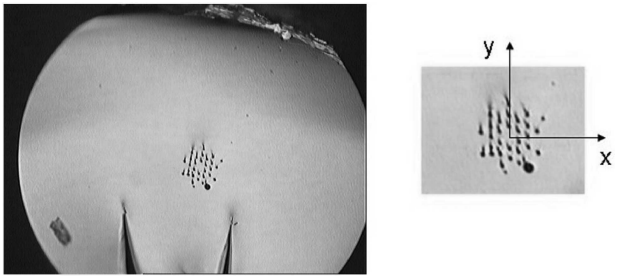

Fig. 5. Picture of the cross section of 2SG fiber MF2b, $\Phi_{core} = 4\,\mu$m.

for this fiber was measured to be 13 dB/m at 1.55 μm using the cutback method on a 50 cm fiber length. For the numerical simulations, it is possible to compute the overall losses with and without taking into account the material losses. For the fundamental mode at 1.55 μm, the computed losses are around 10^{-2} dB/m without material loss and 4.35 dB/m with material loss. The measured loss is 8.5 dB/m above this minimal threshold. We discuss in Section 6 the reasons for this difference.

For the second mode at the same wavelength, the computed losses are approximately equal to 0.14 dB/m (without material losses) whereas they are around 4.57 dB/m with them. The similar level of computed losses of the fundamental mode and of the second mode explains why this higher order mode was easily observed [see Fig. 8(b)]. To the best of our knowledge, this figure represents the first second mode profile observed in a chalcogenide MF.

The measurement of optical attenuation for MF2a at 1.55 μm was made using the same technique as for MF1. The attenuation value at 1.55 μm has been found to be 15 dB/m measured by the cutback method on 50 cm of fiber. The losses have also been recorded between 1 to 3.5 μm using a sensitive FTIR spectrometer (Thermo Electron 5700) adapted to small-core fiber (see Fig. 9). The image of the fiber output is visualized on a thermal camera (FLIR) working from 3 to 5 μm. As for the previous fiber, an indium metal coating was applied to inhibit cladding mode guidance.

The measurement of attenuation on the FTIR spectrometer is made with a shorter length of fiber (≤30 cm) than that realized with monochromatic light

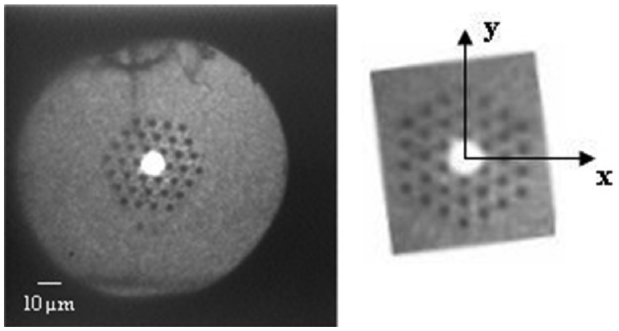

Fig. 6. Near-field observation of the guided beam at 1.55 μm in the MF1

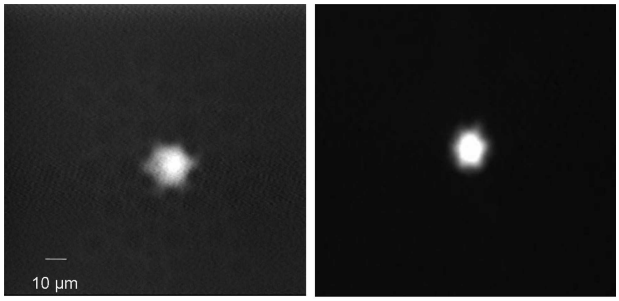

Fig. 7. Near-field observation of the guided beam at 1.55 μm with indium coating.

at 1.55 μm, with a shorter cutback length, perhaps explaining the difference of the attenuation value at 1.55 μm between these two measurements (see Fig. 9). The absorption band centered on 2.9 μm is due to OH absorption. The peaks at 2.05 and 3.1 μm are due to resonances from the main SH absorption peak at 4.1 μm (see Fig. 2). Figure 9 shows that between 2.3 and 2.7 μm the losses are below 12 dB/m.

Figure 10 shows the profile of the output beam at 1.55 μm for the MF2b fiber. Using a Gaussian approximation, experimental measurements give a mode field diameter (MFD) of 3.5 μm for the x axis and 3.3 μm for the y axis. The corresponding computed values are, respectively, 3.7 μm and 3.5 μm, giving a relative error between experimental and computed values of less than 6%. The losses at 1.55 μm for this fiber are 34 dB/m. The computed losses for the fundamental mode at the same wavelength are found to be around 17.5 dB/m without material losses and around 22.3 dB/m with them. We were not able to excite the second mode using the same method as for MF1. We refer to Section 6 for the discussion of these results.

6. Discussion

Here we discuss the origins of the overall losses in the different fibers shown in the previous sections. This issue is crucial since the losses are the current limiting factor of our MF. Next, we briefly compare our results with the ones obtained with soft-glass MFs. We conclude by the determination of the nonlinear parameter of the chalcogenide small-core MF described in the Section 5. The results presented here and previous reports [10] show that the "Stack & Draw" technique is a valid method for the fabrication of chalcogenide MFs of at least up to three rings. Some difficulties must still be overcome to obtain a regular microstructure: homogeneity in hole diameters and control of the interstitial holes. We now control the size of the holes by a gas setup system linked to the preform, but the jacketing step and the use of a glass with excellent thermomechanical properties remain the keys for total control of the profile and of the overall losses.

Measurements show an important difference of loss level between the initial material losses

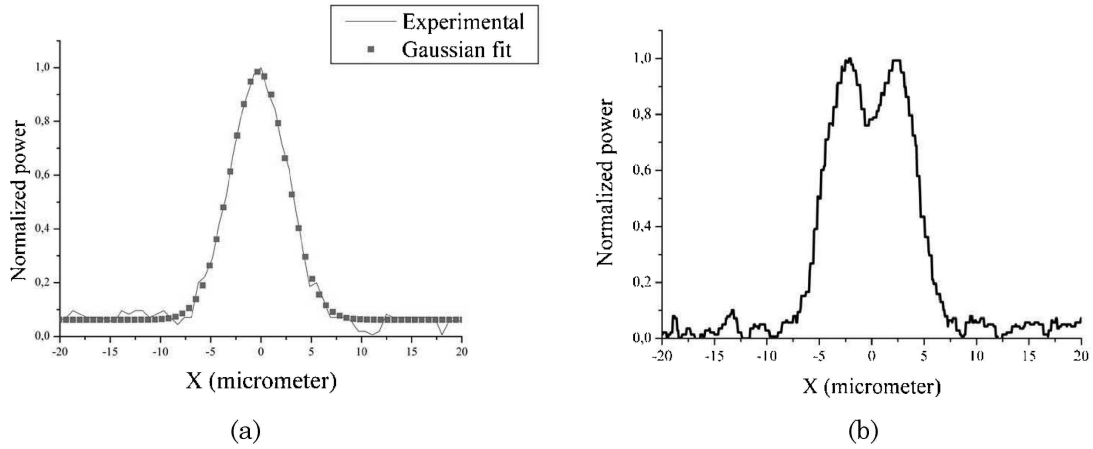

Fig. 8. Experimental profiles at 1.55 μm m in the MF1.

(4.26 dB/m at 1.55 μm, see the last paragraph of Section 3) and the MF ones, 13 dB/m for MF1 and 15 dB/m for MF2a at the same wavelength. The difference is greater for MF2b, 34 dB/m at 1.55 μm. To reduce the losses for future MFs, the results obtained from numerical simulations are useful to understand these discrepancies. They clearly indicate that the limiting factor for the fundamental mode losses of MF1 and MF2a is the material loss. For the second mode of MF1, the scenario is the same: the guiding losses alone are around 0.15 dB/m, and the overall losses reach 4.57 dB/m when material loss is considered. No second mode experimental losses are available but we can expect that they are slightly more important than those of the fundamental mode as suggested by the numerical simulations.

For MF2b, the calculated guiding losses are equal to 17.5 dB/m for the fundamental mode and around 9100 dB/m for the second one. When the material losses are taken into account the fundamental mode, losses are equal to 22.3 dB/m, whereas the measured losses are 34 dB/m. For the second mode, the computed losses with a lossy material are around 9105 dB/m. Consequently, even if the second mode is only starting to delocalize in the microstructured region [23–25], the loss ratio between the two modes explains why the second mode was not found experimentally in MF2b. The MF2b is effectively single-mode for any practical purpose. The easiest way to reduce the fundamental mode losses for future small-core MFs is to decrease the guiding losses. If a similar fiber to MF2b is considered but with a complete third ring of holes (see Fig. 5) then the guiding loss is decreased to 0.11 dB/m. With the material losses taken into account, the overall loss would reach 4.36 dB/m for the fundamental mode, which is equal to the level obtained from the numerical simulation for MF1 and MF2a. For the second mode with the same conditions, the calculated loss is 4000 dB/m. As a result, it should be possible using the same synthesis and drawing processes to get a small-core single-mode chalcogenide MF with overall losses around 15 dB/m found for MF2a at 1.55 μm. Further increase in the number of hole rings is unnecessary since, in this case, the overall loss of the fundamental mode is set by the material loss of 4.35 dB/m, while the addition of a fourth ring of holes would decrease the second mode loss to 2266 dB/m.

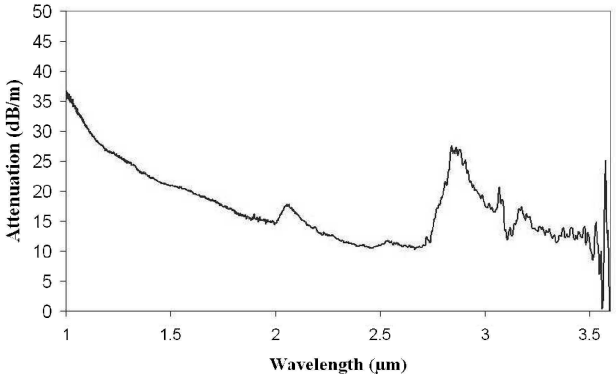

Fig. 9. Attenuation curve of MF2a between 1 and 3.5 μm.

We now discuss the excess loss compared to the computed loss even when homogeneous material loss is considered. This excess is probably due to interface problems between the capillaries during the different drawing steps. These problems are characterized by scattering centers (bubbles or crystals), local glass inhomogeneity, and a non total mixing of the glass at the interfaces that induce diffusion, especially at low wavelengths. Indeed, we observe that when interstitial holes are present in the preform, especially around the core, the losses tend to decrease. This is because the presence of these holes diminishes the surface of glass–glass interfaces. Another source of optical losses can be the photosensitivity of germanium sulphide glasses, including photorefraction and photoinduced anisotropy under sub-bandgap excitation [26].

For soft glasses, the measured losses are 10 dB/m at 1.55 μm for a MF made of the SF-57 Schott glass [27] and slightly above 4 dB/m at the same wavelength for a MF made of the SF-6 Schott glass [28]. Another study on TeO_2-based fibers has shown

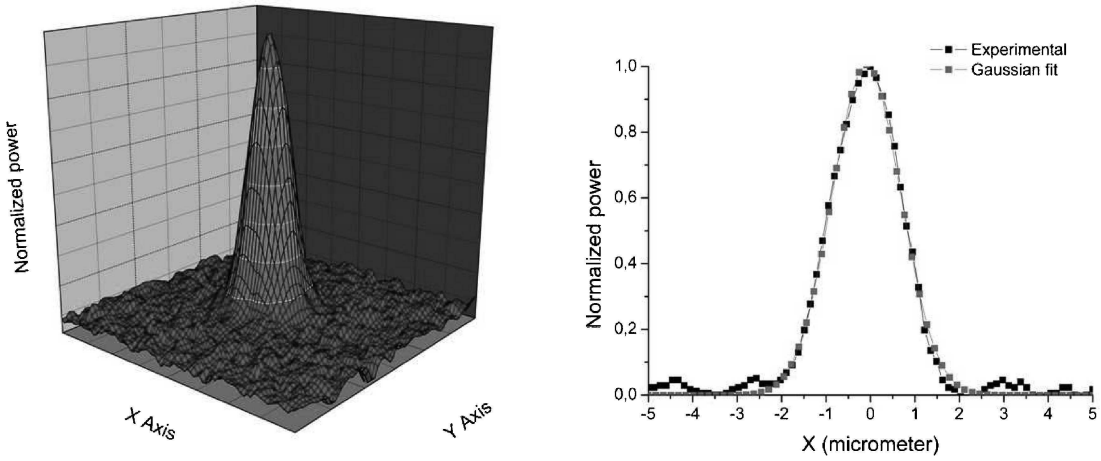

Fig. 10. Experimental profiles of the output beam at 1.55 μm m in the small-core fiber MF2b.

optical losses around 4.5 dB/m at 1.55 μm [29]. These losses are lower than the ones reported in the present study at the same wavelength for the MFs. Nevertheless, the chalcogenide MFs are promising due to their high nonlinear optical properties. Furthermore, these soft glasses have higher losses than the 2SG glass for wavelengths above 2.5 μm. The losses of our 2SG rod are 2.4 dB/m at 2.5 μm and the measured losses of our MF2a fiber are below 12 dB/m bewteen 2.3 and 2.7 μm (see Fig. 9).

To end this discussion, we evaluate the nonlinear parameter of the small-core fiber MF2b. Since the fundamental mode is well confined in the chalcogenide matrix, we can use the formula $\gamma = 2\pi n_2/(\lambda A_{\text{eff}})$ [20]. The effective area A_{eff} is around 10 μm^2. We note that this effective area is seven times smaller than that already obtained in [10]. Since n_2 is around 10^{-18} m^2/W, γ is approximately equal to 1.3 W^{-1} m^{-1}. This value is much smaller than the maximal theoretical γ computed recently for an $As_2 2Se_3$ conventional fiber taper [30]. Nevertheless, if we take into account the lengths L of the devices, the comparison is more favorable. We are able to get meter-long small-core MF, therefore the product $(\gamma L)_{\text{MF}}$ is equal to 1.3 W^{-1}, whereas for the taper length L is around 20 mm, giving a product $(\gamma L)_{\text{taper}}$ equal to 3.3 W^{-1}. For future nonlinear devices, MFs have several advantages. First, the MF can be made polarization-maintaining; as a result the nonlinear parameter can be multiplied by a factor 9/8 as explained in Appendix B of [20]. Second, the MF profile can be designed to manage chromatic dispersion [31,32] to obtain an anomalous dispersion regime at the sought wavelength. Third, several meters of regular and reproducible MF can be obtained using the standard "Stack & Draw" process.

7. Conclusion

Several 2SG chalcogenide MFs with regular profile have been fabricated with the "Stack & Draw" process. For the first time, to the best of our knowledge, a small-core (4 μm) chalcogenide MF with single-mode behavior, at least at 1.55 μm, has been obtained. All the described fibers have been optically characterized. The numerical results concerning the MFD are in good agreement with the experimental data. Concerning optical losses, the numerical results are coherent with the measured results. Comparison between the two has allowed us to optimize the future small-core MF profile to reduce the overall losses. A challenging task will be the further reduction of material loss and the supplementary losses induced by capillary surface problems. Success in these tasks will enable a reduction of the overall loss level for chalcogenide MF to below 3 dB/m, which will open up new opportunities in nonlinear photonics in fibers. Furthermore, due to their infrared transmittance, the chalcogenide MFs will also be studied to observe nonlinear phenomena above 2 μm.

We acknowledge the French Délégation Générale pour l'Armement (contracts 05.34.053 and 05.34.008) and the French ANR (FUTUR contract) for their financial support.

References

1. T. A. Birks, J. C. Knight, and P. J. S. Russell, "Endlessly single-mode photonic crystal fiber," Opt. Lett. **22**, 961–963 (1997).
2. S. Coen, A. H. L. Chau, R. Leonhardt, J. D. Harvey, J. C. Knight, W. J. Wadsworth, and P. St. J. Russell, "White-light supercontinuum generation with 60 ps pump pulses in a photonic crysral fiber," Opt. Lett. **26**, 1356–1358 (2001).
3. J. K. Ranka, R. S. Windeler, and A. J. Stentz, "Visible continuum generation in air-silica microstructure optical fibers with anomalous dispersion at 800 nm," Opt. Lett. **25**, 25–27 (2000).
4. J. M. Dudley, L. Provino, N. Grossard, H. Maillotte, R. Windeler, B. Eggleton, and S. Coen, "Supercontinuum generation in air-silica microstructured fibers with nanosecond

and femtosecond pulse pumping," J. Opt. Soc. Am. B **19**, 765–771 (2002).
5. J. M. Fini, "Microstructure fibres for optical sensing in gases and liquids," Meas. Sci. Technol. **15**, 1120–1128 (2004).
6. A. S. Webb, F. Poletti, D. J. Richardson, and J. K. Sahu, "Suspended-core holey fiber for evanescent-field sensing," Opt Eng. **46**, 010503 (2007).
7. D. Hewak, ed., *Properties, Processing and Applications of Glass and Rare Earth-Doped Glasses for Optical Fibers*, Vol. 22 of EMIS Datarev. Ser. (INSPEC, 1998).
8. F. Smektala, C. Quemard, V. Couderc, and A. Barthélémy, "Non-linear optical properties of chalcogenide glasses measured by z-scan," J. Non-Cryst. Solids **274**, 232–237 (2000).
9. T. M. Monro, Y. D. West, D. W. Hewak, N. G. R. Broderick, and D. J. Richardson, "Chalcogenide holey fibres," Electron. Lett. **36**, 1998–2000 (2000).
10. L. Brilland, F. Smektala, G. Renversez, T. Chartier, J. Troles, T. Nguyen, N. Traynor, and A. Monteville, "Fabrication of complex structures of holey fibers in chalcogenide glass," Opt. Express **14**, 1280–1285 (2006).
11. J. M. Dudley, G. Genty, and S. Coen, "Supercontinuum generation in photonic crystal fiber," Rev. Mod. Phys. **78**, 1135–1184 (2006).
12. J. S. Sanghera, I. D. Aggarwal, L. B. Shaw, C. M. Florea, P. Pureza, V. Q. Nguyen, F. Kung, and I. D. Aggarwal, "Nonlinear properties of chalcogenide glass fibers," J. Optoelectron. Adv. Mater. **8**, 2148–2155 (2006).
13. C. M. Smith, N. Venkataraman, M. T. Gallagher, D. Müller, J. A. West, N. F. Borrelli, D. C. Allan, and K. W. Koch, "Low-loss hollow-core silica/air photonic bandgap fibre," Nature **424**, 657–659 (2003).
14. A. Bétourné, G. Bouwmans, Y. Quiquempois, M. Perrin, and M. Douay, "Improvements of solid-core photonic bandgap fibers by means of interstitial air holes," Opt. Lett. **32**, 1719–1721 (2007).
15. Crystal Fibre, http://www.crystal-fibre.com/.
16. M. Guignard, V. Nazabal, F. Smektala, J. L. Adam, O. Bohnke, C. Duverger, A. Moreac, H. Zeghlache, A. Kudlinski, G. Martinelli, and Y. Quiquempois, "Chalcogenide glasses based on germanium disulfide for second harmonic generation," Adv. Funct. Mater. **17**, 3284–3294 (2007).
17. M. F. Churbanov, I. V. Scripachev, G. E. Snopatin, V. S. Shiryaev, and V. G. Plotnichenko, "High-purity glasses based on arsenic chalcogenides," J. Optoelectron. Adv. Mater. **3**, 341–349 (2001).
18. J. S. Sanghera, L. E. Busse, and I. D. Aggarwal, "Effect of scattering centers on the optical loss of As_2S_3 glass fibers in the infrared," J. Appl. Phys. **75**, 4885–4891 (1994).
19. J. C. Knight, T. A. Birks, P. St. J. Russel, and D. M. Atkin, "All silica single-mode optical fiber with photonic crystal cladding," Opt. Lett. **21**, 1547–1549 (1996).
20. J. C. Knight, T. A. Birks, P. St. J. Russell, and D. M. Atkin, "All-silica single-mode optical fiber with photonic crystal cladding: errata," Opt. Lett. **22**, 484 (1997).
21. G. P. Agrawal, *Nonlinear Fiber Optics*, 3rd ed. (Academic, 2001).
22. T. M. Monro and D. J. Richardson, "Holey optical fibres: Fundamental properties and device applications," C.R. Physique **4**, 175–186 (2003).
23. G. Renversez, F. Bordas, and B. T. Kuhlmey, "Second mode transition in microstructured optical fibers: Determination of the critical geometrical parameter and study of the matrix refractive index and effects of cladding size," Opt. Lett. **30**, 1264–1266 (2005).
24. F. Zolla, G. Renversez, A. Nicolet, B. Kuhlmey, S. Guenneau, and D. Felbacq, *Foundations of Photonic Crystal Fibres* (Imperial College, 2005).
25. L. Labonté, D. Pagnoux, P. Roy, F. Bahloul, M. Zghal, G. Mélin, E. Burov, and G. Renversez, "Accurate measurement of the cutoff wavelength in a microstructured optical fiber by means of an azimuthal filtering technique," Opt. Lett. **31**, 1779–1781 (2006).
26. V. Tikhomirov, G. J. Adriaenssens, and A. J. Faber, "Photoinduced anisotropy and photorefraction in Pr-doped Ge-Ga-S glasses," J. Non-Cryst. Solids **213–214**, 174–178 (1997).
27. K. M. Kiang, K. Frampton, T. Monro, R. Moore, J. Tucknott, D. W. Newak, D. J. Richardson, and H. N. Rutt, "Extruded single-mode non-silica glass holey optical fibres," Electron. Lett. **38**, 546–547 (2002).
28. V. V. Ravi Kanth Kumar, A. K. George, W. H. Reeves, J. C. Knight, P. St. J. Russell, F. G. Omenetto, and A. J. Taylor, "Extruded soft glass photonic crystal fiber for ultrabroad supercontinuum generation," Opt. Express **10**, 1520–1524 (2002).
29. V. V. Ravi Kanth Kumar, A. K. George, J. C. Knight, and P. St. J. Russell, "Tellurite photonic crystal fiber," Opt. Express **11**, 2641–2645 (2003).
30. E. C. Mägi, L. B. Fu, H. C. Nguyen, M. R. Lamont, D. I. Yeom, and B. J. Eggleton, "Enhanced Kerr nonlinearity in subwavelength diameter As_2Se_3 chalcogenide fiber tapers," Opt. Express **15**, 10324–10329 (2007).
31. B. Kuhlmey, G. Renversez, and D. Maystre, "Chromatic dispersion and losses of microstructured optical fibers," Appl. Opt. **42**, 634–639 (2003).
32. G. Renversez, B. Kuhlmey, and R. McPhedran, "Dispersion management with microstructured optical fibers: Ultra-flattened chromatic dispersion with low losses," Opt. Lett. **28**, 989–991 (2003).

Troisième partie

Annexes, bibliographie et index

Table des matières

Annexe A

Some details of the Multipole Method derivation

A.1 Derivation of the Wijngaard identity

To generalize the Wijngaard expansion of the field to MOF, we define a function $U(x,y)$ as

$$U(x,y) = \begin{cases} E_z, & r < R_0, \\ 0, & \text{elsewhere.} \end{cases} \tag{A.1}$$

Thus U is continuous inside the hole region, because of the continuity of the tangential field component, while its normal derivative is discontinuous at the boundaries of the inclusions. Both U and its normal derivative are discontinuous at the jacket boundary C ($r = R_0$). As a consequence, it can be deduced from Eqs. 2.3 and 2.4 that U satisfies, in the sense of distributions [144],

$$\triangle U + k_\perp^2 U = s \tag{A.2}$$

where $k_\perp = k_\perp^i$ in inclusion i, and $k_\perp = k_\perp^e$ elsewhere. Source s is a singular distribution given by

$$s = \sum_{j=1}^{N_c} S_j \delta_{C_j} - T\delta_C - \mathrm{div}(\mathbf{n} Q \delta_C) \tag{A.3}$$

with S_j defined at the boundary C_j of the j-th hole as the jump of the normal derivative of U. Further, Q and T are, respectively, the limits of U and its normal derivative at $r = R_0$, where the normal $\mathbf{n}$ is outwardly oriented. The distribution $A\delta_C$ is defined by [144]

$$\langle A\delta_C, \varphi \rangle = \int_C A(M)\varphi(M) dM \tag{A.4}$$

M being a point of C, dM the length of an elementary segment of C and φ an infinitely differentiable function with bounded support.

Equation A.2 can be rewritten as

$$\triangle U + (k_\perp^e)^2 U = \left[(k_\perp^e)^2 - (k_\perp)^2\right] U + s \tag{A.5}$$

and so in the hole region U follows from the convolution

$$U = G_e \star \left[s + \left((k_\perp^e)^2 - (k_\perp)^2\right) U \right], \tag{A.6}$$

where G_e is the Green function of the Helmholtz equation : $G_e = -iH_0^{(1)}(k_\perp^e r)/4$. From Eqs. A.3 and A.6 U can be reexpressed as

$$U = \sum_{j=1}^{N_c} G_e \star D_j + G_e \star D, \tag{A.7}$$

with

$$D_j = S_j \delta_{C_j} + \left[(k_\perp^e)^2 - (k_\perp^j)^2 \right] U_j \tag{A.8}$$

$$D = -T\delta_C - \mathrm{div}(\mathbf{n} Q \delta_C), \tag{A.9}$$

$$U_j = \begin{cases} U \text{ in the } j\text{-th inclusion} \\ 0 \text{ elsewhere.} \end{cases} \tag{A.10}$$

Each term $V_j = G_e \star D_j$ of the sum on the right-hand side of Eq. A.7 is generated by sources placed inside or at the boundary of the j-th inclusion and satisfies a radiation condition outside this hole. It can be identified at any point outside this inclusion as the field scattered by it. Of course, since it satisfies the homogeneous Helmholtz equation outside the j-th inclusion, in the sense of distributions, it can be represented in the entire matrix region as a Fourier Bessel series

$$V_j = \sum_m B_m^{\mathrm{E}j} H_m^{(1)}(k_\perp^e r_j) e^{im\theta_j}. \tag{A.11}$$

The term $G_e \star D$ on the right-hand member of Eq. A.7 is generated by sources jacket boundary and it thus has no singularity inside this boundary. It can be identified as the incident field generated by the jacket and illuminating the matrix-inclusion region. It can also be represented in a Fourier Bessel expansion

$$V_{\mathrm{inc}} = \sum_m A_m^{\mathrm{E}0} J_m(k_\perp^e r) e^{im\theta}. \tag{A.12}$$

From Eqs. A.7, A.11 and A.12, it can now be shown that in the entire matrix region, the field E_z can be represented by the Wijngaard expansion 2.20. The same argument can be used for the z component of the magnetic field H_z.

A.2 Change of basis

Three changes of basis transformations are required : (i) conversion of outgoing fields sourced on one cylinder to regular fields in the basis of another cylinder ; (ii) conversion of the regular field sourced on the jacket boundary to a regular field in the basis of each cylinder ; and (iii) conversion of outgoing fields sourced at the cylinders to an outgoing field close to the jacket boundary. These are considered separately below.

A.2.1 Cylinder to cylinder conversion

Here we consider an outgoing cylindrical harmonic wave sourced from cylinder j and derive its regular representation in the coordinate system of cylinder l. From Graf's Theorem [22], we derive

$$H_m^{(1)}(k_\perp^e r_j) e^{im \arg(\mathbf{r}_j)} = \sum_{n=-\infty}^{\infty} J_n(k_\perp^e r_l) e^{in \arg(\mathbf{r}_l)} \\ H_{n-m}^{(1)}(k_\perp^e c_{lj}) e^{-i(n-m) \arg(\mathbf{c}_{lj})}, \tag{A.13}$$

so that the total field due to cylinder j is expressed as

$$\sum_{m=-\infty}^{\infty} B_m^j H_m^{(1)}(k_\perp^e r_j) e^{im \arg(\mathbf{r}_j)} = \sum_{n=-\infty}^{\infty} A_n^{lj} J_n(k_\perp^e r_l) e^{in \arg(\mathbf{r}_l)}, \tag{A.14}$$

where A_n^{lj}, defined in Eqs. 2.23 and 2.24, denotes the contribution to the nth multipole coefficient at cylinder l due to cylinder j.

A.2.2 Jacket to cylinder conversion

From Graf's Theorem [22] we now have

$$J_m(k_\perp^e r)e^{im\theta} = \sum_{n=-\infty}^{\infty} J_n(k_\perp^e r_l)e^{in\arg(\mathbf{r}_l)}(-1)^{n-m} J_{n-m}(k_\perp^e c_l)e^{-i(n-m)\arg(\mathbf{c}_l)}, \tag{A.15}$$

and from this, the change of basis transform is

$$\sum_{m=-\infty}^{\infty} A_m^0 J_m(k_\perp^e r)e^{im\theta} = \sum_{n=-\infty}^{\infty} A^{l0} J_n(k_\perp^e r_l)e^{in\arg(\mathbf{r}_l)}, \tag{A.16}$$

where A_n^{l0} denotes the multipole coefficient in the basis of cylinder l due to the regular field radiating from the jacket. Equation 2.27 is the matrix form A.16.

A.2.3 Cylinder to jacket conversion

The relevant transformation from Graf's theorem [22] is now

$$H_m^{(1)}(k_\perp^e r_l)e^{im\arg(\mathbf{r}_l)} = \sum_{n=-\infty}^{\infty} H_n^{(1)}(k_\perp^e r)e^{in\theta} J_{n-m}(k_\perp^e c_l)e^{-i(n-m)\arg(\mathbf{c}_l)}. \tag{A.17}$$

The contribution from cylinder l to the outgoing field near the jacket boundary is

$$\sum_{m=-\infty}^{\infty} B_m^l H_m^{(1)}(k_\perp^e r_l)\, e^{im\arg(\mathbf{r}_l)} = \sum_{n=-\infty}^{\infty} B_n^{0l} H_n^{(1)}(k_\perp^e r)\, e^{in\theta}, \tag{A.18}$$

which can be written in the matrix notation 2.31.

A.3 Boundary conditions : reflection matrices

We consider a cylinder centered at the origin of refractive index n_- and radius a embedded in a medium of refractive index n_+. To derive the reflection matrices of this cylinder we express the E_z and H_z fields in terms of Fourier-Bessel series in the local cylindrical coordinates (r,θ) inside and outside the cylinder,

$$E_z^{\mp}(r,\theta) = \sum_{m=-\infty}^{\infty} \left[A_m^{\mathrm{E}\mp} J_m(k_\perp^{\mp} r) + B_m^{\mathrm{E}\mp} H_m^{(1)}(k_\perp^{\mp} r)\right] e^{im\theta}, \tag{A.19}$$

for $r < a$ $(-)$ and $r > a$ $(+)$, with similar expressions for K_z. Here, $k_\perp^{\pm} = (k^{0^2} n_{\pm}^2 - \beta^2)^{1/2}$ are the transverse wave numbers inside (outside) the cylinder. We introduce the vectors $\mathbf{A}^{\mathrm{E}\pm} = [A_m^{\mathrm{E}\pm}]$ and $\mathbf{B}^{\mathrm{E}\pm} = [B_m^{\mathrm{E}\pm}]$, as well as their K counterparts, and the condensed notation introduced in Eqs. 2.36 and 2.37 for $\tilde{\mathbf{A}}^{\pm}$ and $\tilde{\mathbf{B}}^{\pm}$. The interpretation of the J and H terms was given in Section 2.2.2. At the cylinder boundary, reflection and transmission occurs and the waves mix with each other, which, because of the linearity of the Maxwell equations, can be expressed as a matrix relation between the various coefficients, as

$$\begin{cases} \tilde{\mathbf{A}}^- = \tilde{\mathbf{T}}^- \tilde{\mathbf{A}}^+ + \tilde{\mathbf{R}}^- \tilde{\mathbf{B}}^-, \\ \tilde{\mathbf{B}}^+ = \tilde{\mathbf{R}}^+ \tilde{\mathbf{A}}^+ + \tilde{\mathbf{T}}^+ \tilde{\mathbf{B}}^-. \end{cases} \tag{A.20}$$

Here, $\mathbf{R}^-$ and $\mathbf{R}^+$ are referred to as interior and exterior reflection matrices of the cylinder, over whereas $\mathbf{T}^+$ and $\mathbf{T}^-$ are transmission matrices, which do not matter in the analysis below. Note that the first equation of set (A.20) leads to Eq. 2.38, whereas the second leads to Eq. 2.37.

The $\mathbf{R}^{\pm}$ matrices can be derived from the continuity of the tangential field components at the cylinder boundary. To do this we need the expressions for the θ components of the fields, which can be expressed as a function of the z components as [2]

$$E_\theta(r,\theta) = \frac{i}{k_\perp^2}\left(\frac{\beta}{r}\frac{\partial E_z}{\partial \theta} - k\frac{\partial K_z}{\partial r}\right), \tag{A.21}$$

$$K_\theta(r,\theta) = \frac{i}{k_\perp^2}\left(\frac{\beta}{r}\frac{\partial K_z}{\partial \theta} + kn^2\frac{\partial E_z}{\partial r}\right), \tag{A.22}$$

where n is the refractive index. The partial derivatives that appear straightforwardly follow from Eqs. A.19

We can now write the continuity conditions for the z components by equating Eqs. A.19 on the boundary. Since the resulting equation is valid for all θ, terms with different m decouple and we find for each m

$$A_m^{\mathrm{E}-} J_m^- + B_m^{\mathrm{E}-} H_m^- = A_m^{\mathrm{E}+} J_m^+ + B_m^{\mathrm{E}+} H_m^+, \tag{A.23}$$

with the same result for K_z. Here we introduced the condensed notation $J_m^\pm = J_m(k_\perp^\pm a)$, *etc.*

In the same way we can equate the interior and exterior expressions for E_θ and K_θ. We then obtain two equalities of Fourier series in $e^{im\theta}$, in which, again, terms with different m decouple. These equations, which are not written out here, in combination with Eq. A.23 and its K_z counterpart are sufficient to obtain the $\mathbf{R}$ matrices.

We first concentrate on the interior reflection matrix $\tilde{\mathbf{R}}^-$; we obtain its coefficients by setting the exterior incoming field to zero : $\tilde{\mathbf{A}}^+ = \mathbf{0}$. It is now straightforward to solve, for a given m, the linear set of equation given to express $A_m^{\mathrm{E}-}$ and $A_m^{\mathrm{K}-}$ in terms of $B_m^{\mathrm{E}-}$ and $B_m^{\mathrm{K}-}$ by eliminating $B_m^{\mathrm{E}+}$ and $B_m^{\mathrm{K}+}$. We obtain

$$\begin{cases} A_m^{\mathrm{E}-} &= R_m^{\mathrm{EE}^-} B_m^{\mathrm{E}-} + R_m^{\mathrm{EK}^-} B_m^{\mathrm{K}-}, \\ A_m^{\mathrm{K}-} &= R_m^{\mathrm{KE}^-} B_m^{\mathrm{E}-} + R_m^{\mathrm{KK}^-} B_m^{\mathrm{K}-}, \end{cases} \tag{A.24}$$

with

$$\begin{aligned} R_m^{\mathrm{EE}-} &= \frac{1}{\delta_m}\Big\{ \left(\alpha^+_{J^-H^+} - \alpha^-_{H^+J^-}\right) \times \\ &\quad \left(n_-^2\alpha^+_{H^-H^+} - n_+^2\alpha^-_{H^+H^-}\right) - m^2 J_m^- H_m^- H_m^{+2}\tau^2\Big\}, \\ R_m^{\mathrm{EK}-} &= \frac{1}{\delta_m}\left\{\frac{2m\tau}{\pi ka}\frac{k_\perp^+}{k_\perp^-}H_m^{+2}\right\}, \\ R_m^{\mathrm{KE}-} &= -n_-^2 R_m^{\mathrm{EK}-}, \\ R_m^{\mathrm{KK}-} &= \frac{1}{\delta_m}\Big\{ \left(\alpha^+_{H^-H^+} - \alpha^-_{H^+H^-}\right) \times \\ &\quad \left(n_-^2\alpha^+_{J^-H^+} - n_+^2\alpha^-_{H^+J^-}\right) - m^2 J_m^- H_m^- H_m^{+2}\tau^2\Big\}, \end{aligned} \tag{A.25}$$

where

$$\alpha^\pm_{J^\pm H^\pm} = \frac{k_\perp^\pm}{k} J_m'^\pm H_m^\pm \tag{A.26}$$

with other α coefficients defined analogously. Further

$$\begin{aligned} \delta_m &= \left(\alpha^-_{H^+J^-} - \alpha^+_{J^-H^+}\right)\left(n_-^2\alpha^+_{J^-H^+} - n_+^2\alpha^-_{H^+J^-}\right) \\ &+ \left(mJ_m^- H_m^+\tau\right)^2 \end{aligned} \tag{A.27}$$

and

$$\tau = \frac{\beta}{ak_\perp^- k_\perp^+}\left(n_+^2 - n_-^2\right). \tag{A.28}$$

To obtain the exterior reflection matrix $\tilde{\mathbf{R}}^+$ we set $\tilde{\mathbf{B}}^- = \mathbf{0}$, and eliminate the A_m^- coefficients. This yields

$$
\begin{aligned}
R_m^{\mathrm{EE}+} &= \frac{1}{\delta_m}\Big\{ \left(\alpha^+_{J^-H^+} - \alpha^-_{H^+J^-}\right) \times \\
&\qquad \left(n_-^2\alpha^+_{J^-J^+} - n_+^2\alpha^-_{J^+J^-}\right) - m^2 J_m^+ H_m^+ J_m^{-2}\tau^2 \Big\}, \\
R_m^{\mathrm{EK}+} &= \frac{1}{\delta_m}\left\{ \frac{2m\tau}{\pi ka}\frac{k_\perp^-}{k_\perp^+} J_m^{-2} \right\}, \\
R_m^{\mathrm{KE}+} &= -n_+^2 R_m^{\mathrm{EK}+}, \\
R_m^{\mathrm{KK}+} &= \frac{1}{\delta_m}\Big\{ \left(\alpha^+_{J^-J^+} - \alpha^-_{J^+J^-}\right) \times \\
&\qquad \left(n_-^2\alpha^+_{J^-H^+} - n_+^2\alpha^-_{H^+J^-}\right) - m^2 J_m^+ H_m^+ J_m^{-2}\tau^2 \Big\}.
\end{aligned}
\tag{A.29}
$$

Annexe B

Computing band diagram using the Finite Element Method

B.1 Periodic waveguides

B.1.1 Bloch Modes

Though real structures are finite and one is often interested in the study of defects, the determination of modes in ideal periodic structures is of foremost importance. It allows us to compute band diagrams that are truly useful in MOFs studies (see Chapter 3).

The Floquet-Bloch theory reduces the problem to the study of a single cell as discussed in references [6, 105, 106]. The purpose of this section is to show how to combine this feature with finite element modelling in order to obtain numerical solutions for propagating modes in periodic structures. We consider a structure still invariant along the z-axis but now also periodic in the xy-plane. Given two

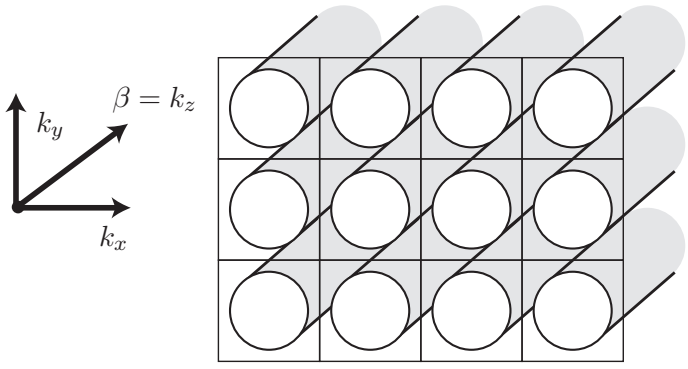

$$\mathbf{U}_\mathbf{k}(x,y,z,t) = \mathbf{U}(x,y)e^{i(k_x x + k_y y + \beta z - \omega t)}$$

FIG. B.1 – A system with a continuous translational invariance along the z-axis together with a two-dimensional periodicity in the xy-plane and the general form of propagating modes $\mathbf{U}_\mathbf{k}(x,y,z,t)$.

linearly independent vectors $\mathbf{a}$ and $\mathbf{b}$ in the xy-plane, the set of points $n\mathbf{a}+m\mathbf{b}$ is called the *lattice*. The *primitive cell* Y is a subset of $\mathbb{R}^2$ such that for any point $\mathbf{r}'$ of $\mathbb{R}^2$ there exist unique $\mathbf{r} = x\mathbf{e}_x + y\mathbf{e}_y \in Y$ and $n, m \in \mathbb{Z}$ such that $\mathbf{r}' = \mathbf{r}+n\mathbf{a}+m\mathbf{b}$. A function $U(\mathbf{r})$ is Y*-periodic* if $U(\mathbf{r}+n\mathbf{a}+m\mathbf{b}) = U(\mathbf{r})$ for any $n, m \in \mathbb{Z}$. The waveguide is Y-periodic if $\varepsilon_r(x,y)$ and $\mu_r(x,y)$ are Y-periodic functions. Possible PEC's and PMW's have boundaries that form a Y-periodic pattern.

The problem reduces to looking for solutions $\mathbf{U}_\mathbf{k}$ that have the form[6, 145] :

$$\mathbf{U}_\mathbf{k}(\mathbf{r}) = e^{i\mathbf{k}\cdot\mathbf{r}}\mathbf{U}(\mathbf{r}) = e^{i(k_x x + k_y y)}\mathbf{U}(x,y)\ ,\ \forall\ (x,y) \text{ in } \mathbb{R}^2 \tag{B.1}$$

where $\mathbf{U}(x,y)$ is a Y-periodic function and $\mathbf{k} = k_x\mathbf{e}^x + k_y\mathbf{e}^y \in Y^* \subset \mathbb{R}^2$ is a parameter (the or quasi-momentum in solid state physics). $Y^* \subset \mathbb{R}^2$ is the *dual cell (first Brillouin zone)* , *i.e.* the primitive cell of the *reciprocal lattice* determined by the two vectors $\mathbf{a}^*$ and $\mathbf{b}^*$ such that $\mathbf{a}^* \cdot \mathbf{a} = 2\pi$, $\mathbf{a}^* \cdot \mathbf{b} = 0$,

$\mathbf{b}^*\cdot\mathbf{a} = 0$, $\mathbf{b}^*\cdot\mathbf{b} = 2\pi$ (it is worth noting that this dot product is in fact a duality product : $\mathbf{k}\cdot\mathbf{r} =< \mathbf{k}, \mathbf{r} >$). Such solutions $\mathbf{U_k}$ are said to be $(\mathbf{k}, Y)$-*periodic* in the sequel (though they are not periodic but almost-periodic).

To specify the class of solutions of our spectral problem, one introduces the Hilbert space

$$[L^2_\sharp(\mathbf{k}, Y)]^3 = \left\{ \mathbf{U_k}|_Y \in [L^2(Y)]^3 \ , \ \mathbf{U_k} \ \text{ is } (\mathbf{k}, Y)\text{-periodic} \right\} \tag{B.2}$$

of $(\mathbf{k}, Y)$-periodic square integrable functions with values in $\mathbb{C}^3$.

The pair $(\mathbf{E_k}, \mathbf{H_k})$ associated with the Bloch vector $\mathbf{k}$ is called an *electromagnetic propagating Bloch mode* if $\mathbf{E_k}$ and $\mathbf{H_k}$ are $(\mathbf{k}, Y)$-periodic fields satisfying the spectral problem :

$$\begin{cases} \mathbf{curl}_\beta \, \mathbf{H_k} = -i\omega\varepsilon_0\varepsilon_r(x,y)\mathbf{E_k} \\ \mathbf{curl}_\beta \, \mathbf{E_k} = i\omega\mu_0\mu_r(x,y)\mathbf{H_k} \end{cases} \tag{B.3}$$

with :

$$\begin{cases} (\beta, \omega, \mathbf{k}) \in \mathbb{R}_+ \times \mathbb{R}_+ \times Y^* \\ (\mathbf{E_k}, \mathbf{H_k}) \neq (\mathbf{0}, \mathbf{0}) \\ \mathbf{E_k}, \mathbf{H_k} \in [L^2_\sharp(\mathbf{k}, Y)]^3 \end{cases} \tag{B.4}$$

Looking for solutions that are Bloch functions in $[L^2_\sharp(\mathbf{k}, Y)]^3$ ensures the well-posedness of this spectral problem, as a replacement for the Sommerfeld radiation condition (or other decaying conditions for the far field) which is usually imposed in the presence of compact obstacles in the medium.

The finite element formulation is completely identical to the non-periodic one. The only difference is that the study is now reduced to the primitive cell Y which is meshed and in which the integrations are performed. Some technique must be found to ensure that the solution is a $(\mathbf{k}, Y)$-periodic Bloch mode. This can be imposed by using special boundary conditions as explained in the next section.

B.1.2 The Bloch conditions

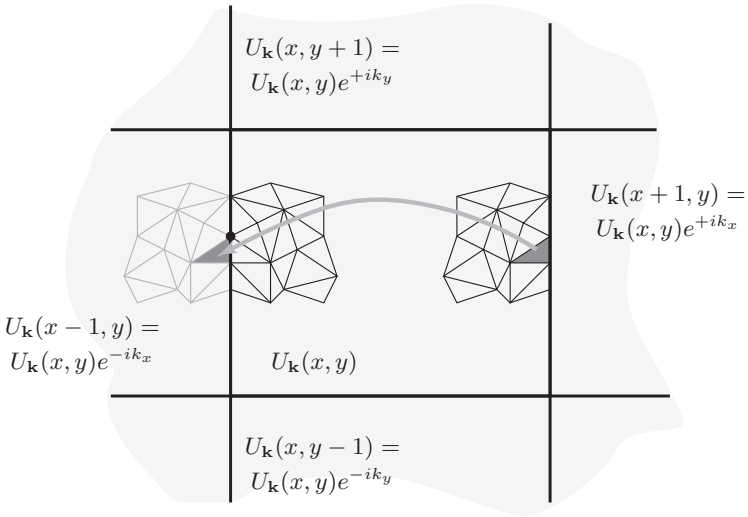

FIG. B.2 – Bloch theorem and virtual periodic mesh with $\Lambda = 1$.

In order to find Bloch modes with the method, some changes have to be made with respect to classical boundary value problems which will be named [146]. For the sake of simplicity, one considers first a square cell $Y =]0,1[\times]0,1[$ as an example. To avoid tedious notation, the case of a scalar field $U_\mathbf{k}(x,y)$ (time and z dependence are irrelevant here and it is no particular problem to extend this method to vector quantities and edge elements) is considered on the square cell Y with Bloch conditions relating the lefthand and the righthand sides (Fig. B.2). The set of nodes is separated into three subsets : the nodes on

the left side, *i.e.* with $x = 0$, corresponding to the column array of unknowns $\mathbf{u_l}$, the nodes on the right side, *i.e.* with $x = 1$, corresponding to the column array of unknowns $\mathbf{u_r}$, and the internal nodes, *i.e.* with $x \in]0,1[$, corresponding to the column array of unknowns $\mathbf{u}$. One has the following structure for the matrix problem (corresponding in fact to natural boundary conditions, *i.e.* Neumann homogeneous boundary conditions, as the degrees of freedom on the boundaries have to be kept as unknowns in the problem) :

$$\mathbf{A} \begin{pmatrix} \mathbf{u} \\ \mathbf{u_l} \\ \mathbf{u_r} \end{pmatrix} = \mathbf{b} \tag{B.5}$$

where $\mathbf{A}$ is the (square Hermitian) matrix of the system and $\mathbf{b}$ is the right hand side. The solution to be approximated by the numerical method is a Bloch function $U_{\mathbf{k}}(x,y) = U(x,y)e^{i(k_x x + k_y y)}$ with U being Y-periodic and in particular $U(x+1,y) = U(x,y)$. Therefore, the relation between the lefthand and the righthand sides is :

$$U_{\mathbf{k}}(1,y) = U(1,y)e^{i(k_x+k_y y)} = U_{\mathbf{k}}(0,y)e^{ik_x} \Rightarrow \mathbf{u_r} = \mathbf{u_l}e^{ik_x} \tag{B.6}$$

The set of unknowns can thus be expressed as a function of the reduced set $\mathbf{u}$ and $\mathbf{u_l}$ via :

$$\begin{pmatrix} \mathbf{u} \\ \mathbf{u_l} \\ \mathbf{u_r} \end{pmatrix} = \mathbf{P} \begin{pmatrix} \mathbf{u} \\ \mathbf{u_l} \end{pmatrix} \text{ with } \mathbf{P} = \begin{pmatrix} \mathbf{1} & \mathbf{0} \\ \mathbf{0} & \mathbf{1} \\ \mathbf{0} & \mathbf{1}e^{ik_x} \end{pmatrix} \tag{B.7}$$

where $\mathbf{1}$ and $\mathbf{0}$ are identity and null matrices respectively with suitable dimensions. The finite element equations related to the eliminated nodes have now to be taken into account. Due to the periodicity of the structure, the elements on the left of the right side correspond to elements on the left of the left side (Fig. B.2). Therefore their contributions (i.e. the equations corresponding to $\mathbf{u_r}$) must be added to the equations corresponding to $\mathbf{u_l}$ with the right phase factor, i.e. e^{-ik_x}, which amounts to multiplying the system matrix by $\mathbf{P}^*$ (the Hermitian of $\mathbf{P}$). Finally, the linear system to be solved is :

$$\mathbf{P}^*\mathbf{A}\mathbf{P} \begin{pmatrix} \mathbf{u} \\ \mathbf{u_l} \end{pmatrix} = \mathbf{P}^*\mathbf{b} \tag{B.8}$$

where it is worth noting that the system matrix is still Hermitian, which is important for numerical computation. Now a generalized eigenvalue problem (with natural boundary conditions) $\mathbf{A}\mathbf{u} = \lambda\mathbf{B}\mathbf{u}$ is transformed to a Bloch mode problem according to $\mathbf{P}^*\mathbf{A}\mathbf{P}\mathbf{u}' = \lambda\mathbf{P}^*\mathbf{B}\mathbf{P}\mathbf{u}'$ which is still a large sparse Hermitian generalized eigenvalue problem.

B.1.3 A first numerical example

As an illustration, the Bloch finite element method will be used to reproduce the results presented in [107], where they were obtained using a plane wave method. The inclusion parameters are $R = 0.48\Lambda$ for the radius and $\varepsilon_r = 1.0$) for the relative permittivity. The matric has $\varepsilon_r = 13.0$.

The basic cell is a rhombus made of two equilateral triangles : the lattice vectors are $\mathbf{a} = \Lambda\mathbf{e}_x$ and $\mathbf{b} = \frac{\Lambda}{2}\mathbf{e}_x + \frac{\Lambda\sqrt{3}}{2}\mathbf{e}_y$ where Λ is the nearest neighbour distance, *i.e.* the length of the sides of the cells. This cell contains a circular air inclusion (radius $R = 0.48\Lambda$, so that the filling fraction $f = 0.8358$, and $\varepsilon_r = 1.0$) surrounded by solid dielectric material ($\varepsilon_r = 13.0$). The vectors of the reciprocal lattice are $\mathbf{a}^* = \frac{2\pi}{\Lambda}\mathbf{e}^x - \frac{2\pi\sqrt{3}}{3\Lambda}\mathbf{e}^y$ and $\mathbf{b}^* = \frac{4\pi\sqrt{3}}{3\Lambda}\mathbf{e}^y$ and the first Brillouin zone is hexagonal. The irreducible part can be represented by the triangle with vertices $\Gamma = (0,0)$, $M = (0, \frac{2\pi}{\sqrt{3}\Lambda})$, and $K = (\frac{2\pi}{3\Lambda}, \frac{2\pi}{\sqrt{3}\Lambda})$. The basic cell is meshed with 4628 triangles. These data are summarised in Figures B.3 and B.4. Note that the circular inclusion is too large to fit as a single piece inside the basic cell hence the splitting into four parts in the corners.

The Bloch boundary conditions connect the degrees of freedom on opposite sides of the rhombus : the degrees of freedom on the lower lefthand side are equal to the corresponding ones on the upper righthand side multiplied by a phase factor equal to $e^{i(-k_x\frac{\Lambda}{2} - k_y\frac{\sqrt{3}\Lambda}{2})}$ and the degrees of freedom on the

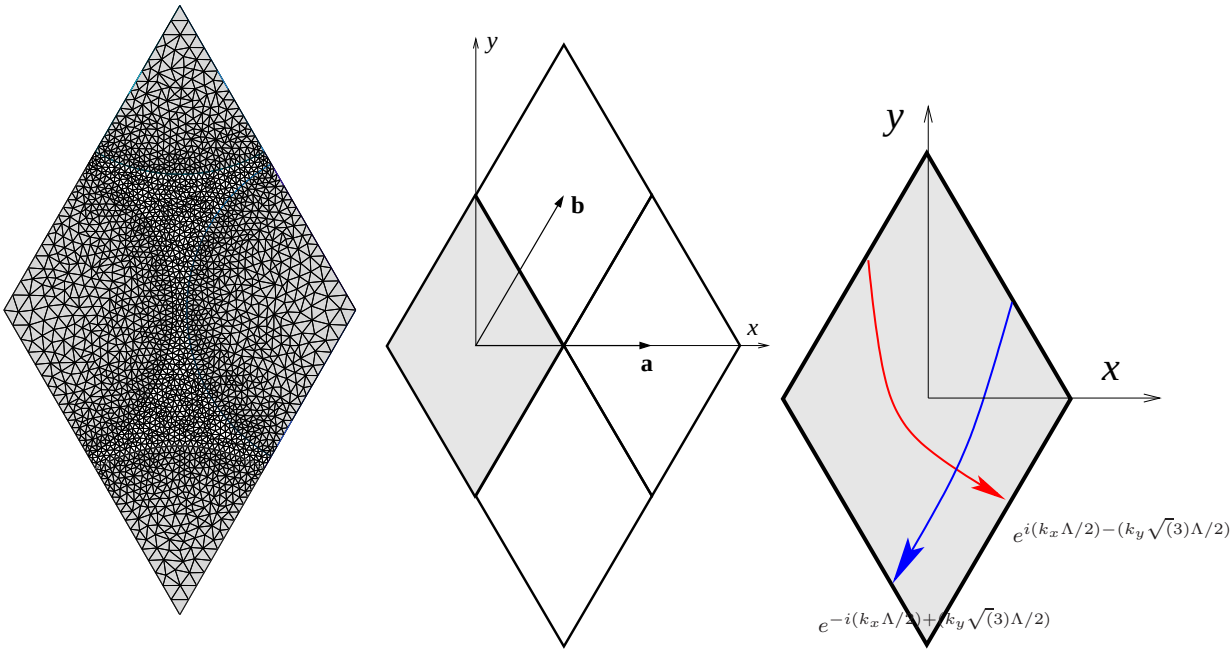

(a) Meshing of a basic rhombic cell with 4628 triangles.

(b) Representation of some lattice cells with the lattice vectors $\mathbf{a} = \Lambda \mathbf{e}_x$ and $\mathbf{b} = \frac{\Lambda}{2}\mathbf{e}_x + \frac{\Lambda\sqrt{3}}{2}\mathbf{e}_y$.

(c) Factors used to set the Bloch conditions on the adjacent borders of the basic cell

FIG. B.3 – Example of two-dimensional periodic structure : the triangular lattice of cicular inclusions. The basic cell is rhombic with a side length Λ with a circular air inclusion with a radius $R = 0.48\Lambda$.

lower righthand side are equal to the corresponding ones on the upper lefthand side multiplied by a phase factor equal to $e^{i(+k_x\frac{\Lambda}{2}-k_y\frac{\sqrt{3}\Lambda}{2})}$.

The dispersion curves shown on Fig. B.5 correspond to pulsations ω (only the ω such that $\omega < \frac{2\pi c}{\Lambda}$ are represented here) of the propagation modes associated with a given value of the propagation constant β ($\beta\Lambda = 0.0, 2.0, 4.$).

The value 1.0 is given to Λ for the numerical computations. The boundary of the irreducible Brillouin zone is sampled with 120 points (40 on each side of the triangle). The results are in good agreement with those of [107].

B.1.4 Band diagram and bandgaps

As can be seen in Fig. B.5, the formulation chosen to solve the system (B.3) fixes the β-value and compute the possible ω. Another way to proceed is avalaible as mentioned in Chapter 3) and can be more useful from the practical point of view for MOF studies : it is to fix ω (or equivalently λ) and to computed the possible β. This approach has at least two advantages. First, it permits to take into account easily the material dispersion since this last depends on λ and not on β. Secondly, the results can be compared directly with the ones obtained for finite size MOFs by the multipole or the FFF-mode searching methods described in chapter 2.

As a result, at a fixed wavelength we compute the propagation constants β of the modes allowed in the periodic structures using the method described in the previous section of this appendix. Actually, we compute only a finite number of these modes in some given range for the propagation constant. We repeat this operation for all the wavelengths of interest in order to get the corresponding *band diagram*.

Since one of the key features is the existence of *bandgap* within these band diagrams, we must not miss some modes of the periodic structures to ensure a valid building of the band diagram. To limit the number of these missing modes, we follow not only the borders of the irreducible Brillouin zone like we did to get Fig. B.5 but we also sample the whole region in a regular way as shown in Fig. B.4(b). Proceeding in this way we obtain band diagram like the one shown in Fig. B.6. The periodic structure

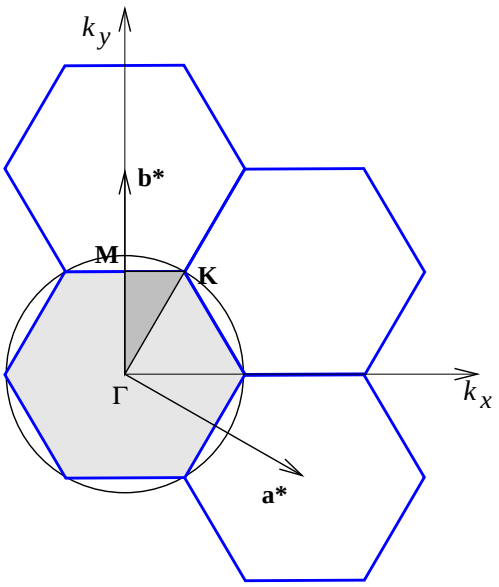

(a) Some cells of the reciprocal lattice with the lattice vectors

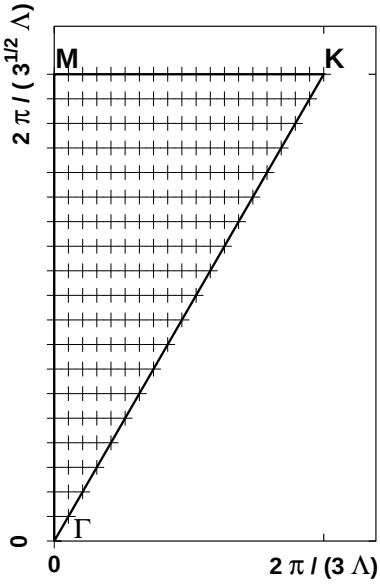

(b) Example of sampling points in the irreducible part of the Brillouin zone (IBZ) for a triangular lattice. 210 points are used in this case to sample in 2D the IBZ. Among them, 57 points are on the three side of the triangle $\Gamma - M - K$.

FIG. B.4 – For the two-dimensional periodic structure of Fig.(B.3, representation of some cells of the reciprocal lattice with the lattice vectors $\mathbf{a}^* = \frac{2\pi}{\Lambda}\mathbf{e}^x - \frac{2\pi\sqrt{3}}{3\Lambda}\mathbf{e}^y$ and $\mathbf{b}^* = \frac{4\pi\sqrt{3}}{3\Lambda}\mathbf{e}^y$ and the irreducible part of the first Brillouin zone represented by the triangle with vertices $\Gamma = (0,0)$, $M = (0, .\frac{2\pi}{\sqrt{3}\Lambda})$, and $K = (\frac{2\pi}{3\Lambda}, \frac{2\pi}{\sqrt{3}\Lambda})$.

modelized is the one used in section 3.3.1. The pitch $\Lambda = 5.7816\,\mu$m, the hole diameter is $4.026\,\mu$m and the refractive index of theses holes is fixed to 1.0, the matrix relative electric permittivity being 1.9321 ($n_{mat} = 1.39$).

From these diagrams built from a finite set of modes, one can extract numerically the limits of the observed bandgaps. We also build such a tool to get automatically the contours of the bandgaps. This tools is able to determine them for all the tested configurations. Several examples are shown in Fig. B.7 : one extracted from the results shown on Fig. B.6 and two others from configuration with higher values of n_{mat}.

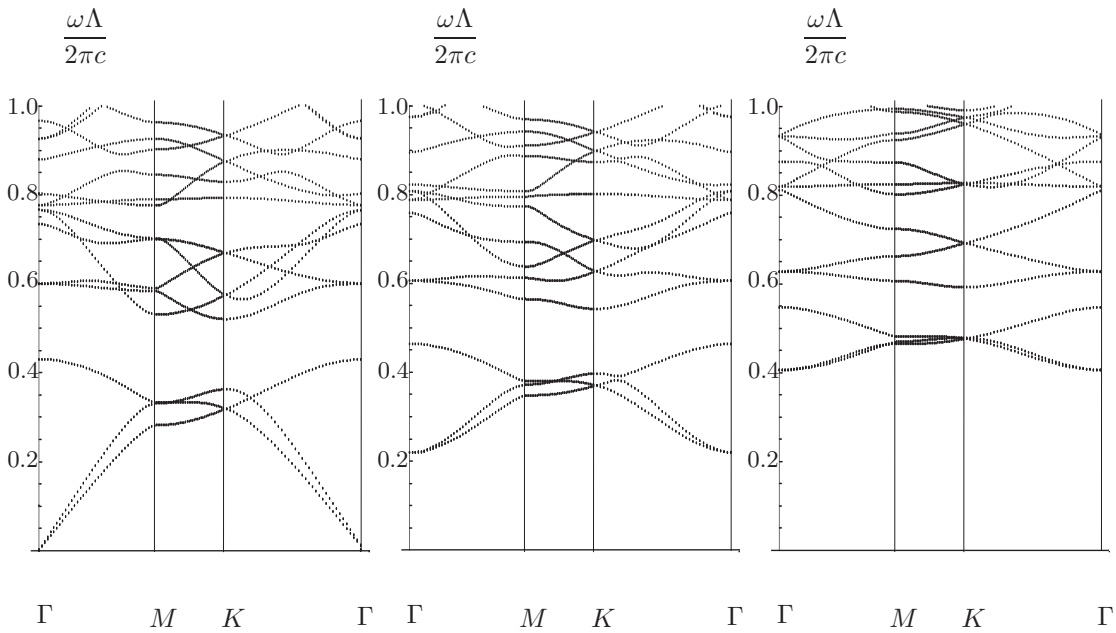

(a) $\beta\Lambda = 0.0$ (b) $\beta\Lambda = 2.0$ (c) $\beta\Lambda = 4.0$

FIG. B.5 – Dispersion curves corresponding to Bloch waves in classical (a) and conical mounting for two values of β (b) and (c) in the lattice of Fig. (B.3). In these examples only the borders $\Gamma - M - K - \Gamma$ of the irreducible Brillouin zone are sampled.

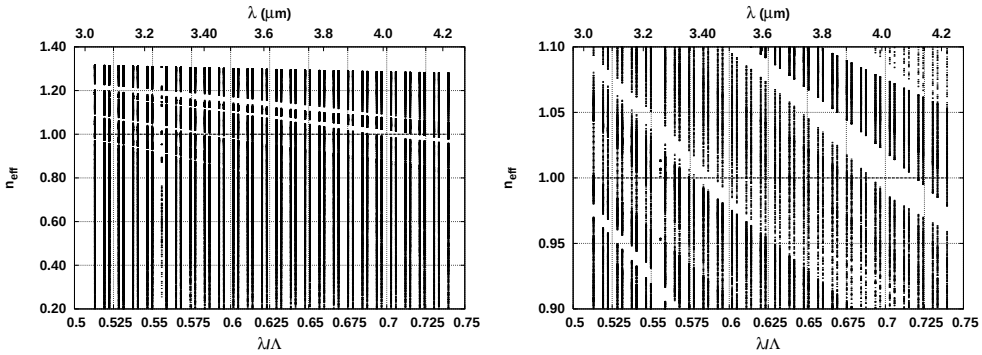

(a) Whole view of the band diagram. (b) Zoom of the band diagram around the light line.

FIG. B.6 – Computed Band diagram of a triangular lattice of circular inclusions of low refractive index $n_{cyl} = 1$ in a high refractive index matrix $n_{mat} = 1.39$. The white region represent the parameter space in which no modes can propagates in the periodic structures, *i.e.* f ull finite photonic bandgaps.

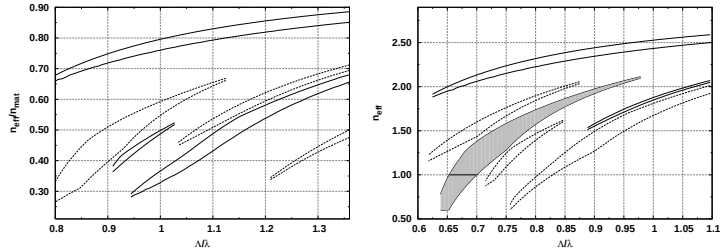

(a) $n_{mat} = 2.4$ and diameter d is $7.9\ \mu$m, and $\Lambda = 10\ \mu$m. (b) $n_{mat} = 2.9095$ and diameter d is $7.625\ \mu$m, and $\Lambda = 10\ \mu$m.

FIG. B.7 – Computed Band diagram of three different triangular lattices of circular inclusions of low refractive index $n_{cyl} = 1$ in high refractive index matrices.

Bibliographie

[1] D. Marcuse. *Theory of Dielectric Optical Waveguides*. Academic Press, San Diego, 2nd edition, 1991.

[2] A. W. Snyder and J. D. Love. *Optical Waveguide Theory*. Chapman & Hall, New York, 1983.

[3] R. Sammut and A. W. Snyder. Leaky modes on a dielectric waveguide : orthogonality and excitation. *Applied Optics*, 15(4) :1040–1044, 1976.

[4] M. Maeda and S. Yamada. Leaky modes on W-fibers : mode structure and attenuation. *Applied Optics*, 16(8) :2198–2203, 1977.

[5] P. L. François and C. Vassallo. Finite cladding effects in W-fibers : a new interpretation of leaky modes. *Applied Optics*, 22(19) :3109–3120, 1983.

[6] F. Zolla, G. Renversez, A. Nicolet, B. Kuhlmey, S. Guenneau, and D. Felbacq. *Foundations of Photonic Crystal Fibres*. Imperial College Press, London, 2005.

[7] P. T. Leung and K. M. Pang. Completeness and time-independent perturbation of morphology-dependent resonances in dielectric spheres. *J. Opt. Soc. Am. B*, 13(5) :805–817, 1996.

[8] P. T. Leung, S. S. Tong, and K. Young. Two-component eigenfunction expansion for open systems described by the wave equation i : completeness of expansion. *J. Phys. A : Math. Gen.*, 30 :2139–2151, 1997.

[9] P. T. Leung, S. S. Tong, and K. Young. Two-component eigenfunction expansion for open systems described by the wave equation ii : linear space structure. *J. Phys. A : Math. Gen.*, 30 :2153–2162, 1997.

[10] P. T. Leung, W. M. Suen, C. P. Sun, and K. Young. Waves in open systems via a biorthogonal basis. *Phys. Rev. E*, 57(5) :6101–6104, 1998.

[11] K. M. Lee, P. T. Leung, and K. M. Pang. Dyadic formulation of morphology-dependent resonances. ii. perturbation theory. *J. Opt. Soc. Am. B*, 16(9) :1418–1430, 1999.

[12] K. M. Lee, P. T. Leung, and K. M. Pang. Dyadic formulation of morphology-dependent resonances. i. completeness relation. *J. Opt. Soc. Am. B*, 16(9) :1409–1417, 1999.

[13] K. C. Ho, P. T. Leung, A. M. van den Brink, and K. Young. Second quantization of open sytems using quasinormal modes. *Phys. Rev. E*, 3 :1409–1417, 1999.

[14] S. W. Ng, P. T. Leung, and K. M. Lee. Dyadic formulation of morphology-dependent resonances. iii. degenerate perturbation theory. *J. Opt. Soc. Am. B*, 19(1) :154–164, 2002.

[15] T. P. White, B. Kuhlmey, R. C. McPhedran, D. Maystre, G. Renversez, C. M. de Sterke, and L.C. Botten. Multipole method for microstructured optical fibers I : formulation. *J. Opt. Soc. Am. B*, 10(19) :2322–2330, 2002.

[16] B. Kuhlmey, T. P. White, G. Renversez, D. Maystre, L.C. Botten, C. M. de Sterke, and R. C. McPhedran. Multipole method for microstructured optical fibers II : implementation and results. *J. Opt. Soc. Am. B*, 10(19) :2331–2340, 2002.

[17] D. Felbacq, G. Tayeb, and D. Maystre. Scattering by a random set of parallel cylinders. *J. Opt. Soc. Am. A*, 9 :2526–2538, 1994.

[18] P. R. Mc Isaac. Symmetry-induced modal characteristics of uniform waveguides-I : Summary of results. *IEEE Trans. on Microwave Theory Tech.*, 23(5) :421–429, 1975.

[19] P. R. Mc Isaac. Symmetry-induced modal characteristics of uniform waveguides-II : Theory. *IEEE Trans. on Microwave Theory Tech.*, 23(5) :429–433, 1975.

[20] B. Kuhlmey. *Theoretical and Numerical Investigation of the Physics of Microstructured Optical Fibers*. PhD thesis, Université Aix-Marseille III and University of Sydney, 2003.

[21] M. Nevière. The Homogeneous Problem. In *Electromagnetic Theory of Gratings*, volume 22 of *Topics in Current Physics*, chapter 5. Springer-Verlag, 1980.

[22] M. Abramowitz and I. A. Stegun. *Handbook of mathematical functions*. Dover Publications, New York, 9th edition, 1965.

[23] D. Maystre and P. Vincent. Diffraction d'une onde électromagnétique plane par un objet cylindrique non-infiniment conducteur de section arbitraire. *Optics Communications*, 5(5) :327–330, 1972.

[24] M. Nevière and E. Popov. *Light propagation in periodic media*, chapter 14. Marcel Dekker, 2003.

[25] W. Wijngaard. Guided normal modes of two parallel circular dielectric rods. *J. Opt. Soc. Amer.*, 63 :944–949, 1973.

[26] K. M. Lo, R. C. McPhedran, and I. M. Bassett ans G. W. Milton. An electromagnetic theory of dielectric waveguides with multiple embedded cylinders. *J. Lightwave Technology*, 12 :396–410, 1994.

[27] C-S Chang and H-C Chang. Theory of the circular harmonics expansion method for multiple-optical-fiber system. *J. Lightwave Technology*, 12 :415–417, 1994.

[28] Lord Rayleigh. On the influence of obstacles arraged in rectangualr order upon the properties of a medium. *Phil. Mag.*, 34 :481–502, 1892.

[29] P. Curie. Sur le symétrie des phénomènes physiques, symétrie d'un champ électrique et d'un champ magnétique. *Journal de Physique*, page 393, 1894.

[30] M. J. Steel, T. P. White, C. Martijn de Sterke, R. C. McPhedran, and L. C. Botten. Symmetry and degeneracy in microstrutured optical fibers. *Opt. Lett.*, 26(8) :488–490, 2001.

[31] W.H. Press, B.P.Flannery, S.A. Teukolsky, and W.T. Vetterling. *Numerical Recipes*. Cambridge University Press, 1986.

[32] P. Kravanja and M. Van Barel. *Computing the Zeros of Analytic Functions*. Springer, Berlin, 2000.

[33] L. C. Botten, M. S. Craig, and R. C. McPhedran. Complex Zeros of Analytic Functions. *Comp. Phys. Comm.*, 29 :245–249, 1983.

[34] C. G. Broyden. A class of methods for solving nonlinear simultaneous equations. *Mathematics of Computation*, 19 :577–593, 1965.

[35] G. P. Agrawal. *Nonlinear fiber optics*. Academic Press, 3rd edition, 2001.

[36] F. Brechet, J. Marcou, D. Pagnoux, and P. Roy. Complete analysis of the characteristics of propagation into photonic crystal fibers by the finite element method. *Opt. Fiber Technol.*, 6(2) :181–191, 2000.

[37] B. Kuhlmey, G. Renversez, and D. Maystre. Chromatic dispersion and losses of microstructured optical fibers. *Appl. Opt.*, 42(4) :634–639, 2003.

[38] T. P. White, R. C. McPhedran, C. M. de Sterke, L. C. Botten, and M. J. Steel. Confinement losses in microstructured optical fibers. *Opt. Lett.*, 26(21) :1660–1662, 2001.

[39] A. Ortigosa-Blanch, J. C. Knight, W. J. Wadsworth, J. Arriaga, B. J. Mangan, T. A. Birks, and P. St. J. Russell. Highly birefringent photonic crystal fibers. *Optics Letters*, 25(18) :1325–1327, 2000.

[40] P. Boyer, M. Nevière, E. Popov, and G. Renversez. Diffraction theory : Application of the fast Fourier factorization method to cylindrical devices with arbitrary cross section lighted in conical mounting. *J. Opt. Soc. Am. A*, 53(5) :1146–1158, 2006.

[41] P. Boyer, G. Renversez, E. Popov, and M. Nevière. A new differential method applied to the study of arbitrary cross section microstructured optical fibers. *Opt. and Quant. Electron.*, 38 :217–230, 2006.

[42] P. Boyer, E. Popov, M. Nevière, and G. Tayeb. Diffraction theory in TM polarization : application of the fast Fourier factorization method to cylindrical devices with arbitrary cross section. *J. Opt. Soc. Am. A*, 21(11) :2146–2153, 2004.

[43] L. Li. Use of Fourier series in the analysis of discontinuous periodic structures. *J. Opt. Soc. Am. A*, 13(9) :1870–1876, 1996.

[44] G. H. Golub and C. F. Van Loan. *Matrix Computations*. the John Hopkins University Press, Baltimore and London, third edition, 1996.

[45] M. Nevière and E. Popov. *Light propagation in periodic media*. Marcel Dekker, 2003.

[46] P. Boyer. *Elaboration d'une méthode diffrérentielle pour l'étude des fibres optiques microstructurées*. PhD thesis, Université Paul Cézanne Aix-Marseille III, 2006.

[47] J. M. Fini. Improved symmetry analysis of many-moded microstructure optical fibers. *J. Opt. Soc. Am. B.*, 21(8) :1431–1436, 2004.

[48] B. Bai and L. Li. Reduction of computation time for crossed-grating problems : a group-theoretic approach. *J. Opt. Soc. Am. A.*, 21(10) :1886–1894, 2004.

[49] B. Bai and L. Li. Group-theoretic approach to the enhancement of the Fourier modal method for crossed gratings : C_2 symmetry case. *J. Opt. Soc. Am. A.*, 22(4) :654–661, 2005.

[50] P. Vincent and R. Petit. Sur la diffraction d'une onde plane par un cylindre diélectrique. *Opt. Commmun.*, 5 :261–266, 1972.

[51] L. Brilland, F. Smektala, G. Renversez, T. Chartier, J. Troles, T. Nguyen, N. Traynor, and A. Monteville. Fabrication of complex structures of holey fibers in chalcogenide glass. *Opt. Express*, 14(3) :1280–1285, 2006.

[52] S. Campbell, R. C. McPhedran, C. Martijn de Sterke, and L. C. Botten. Differential multipole method for microstructured optical fibers. *JOSA B*, 21(11) :1919–1928, 2004.

[53] K. M. Kiang, K. Frampton, T.M. Monro, R. Moore, J. Tucknott, D. W. Newak, D. J. Richardson, and H. N. Rutt. Extruded single-mode non-silica glass holey optical fibres. *Electronics Letters*, 38(12) :546–547, 2002.

[54] V. V. Ravi Kanth Kumar, A. K. George, W. H. Reeves, J. C. Knight, P. St. J. Russell, F. G. Omenetto, and A. J. Taylor. Extruded soft glass photonic crystal fiber for ultrabroad supercontinuum generation. *Optics Express*, 10(25) :1520–1524, 2002.

[55] S. T. Peng, T. Tamir, and H. L. Bertoni. Theory of periodic dielectric waveguides. *IEEE Trans. Microwave Theory and Techn*, MTT-23 :123–133, 1975.

[56] E. Popov, M. Nevière, B. Gralak, and G. Tayeb. Staircase approximation validity for arbitrary shaped gratings. *J. Opt. Soc. Am. A.*, 19 :33–42, 2002.

[57] H. P. Uranus and H. J. W. M. Hoekstra. Modelling of microstructured waveguides using a finite-element-based vectorial mode solver with transparent boundary conditions. *Optics Express*, 12(12), 2004.

[58] N. A. Issa and L. Poladian. Vector wave expansion method for leaky modes of microstructured optical fibers. *Journal of Lightwave Technology*, 21(4) :1005–1012, 2003.

[59] M. Yan and P. Shum. Guidance varieties in photonic crystal fibers. *J. Opt. Soc. Am. B*, 23 :1684–1691, 2006.

[60] B. Kuhlmey, C. M. de Sterke, R. McPhedran, P. Robinson, G. Renversez, and D. Maystre. Microstructured optical fibers : where's the edge. *Opt. Express*, 10(22) :1285–1290, 2002.

[61] J. M. Pottage, D. Bird, T. D. Hedley, J. C. Knight, T. A. Birks, P. St. J. Russell, and P. J. Roberts. Robust photonic band gaps for hollow core guidance in PCF made from high index glass. *Optics Express*, 11(22) :2854–2861, 2003.

[62] G. J. Pearce, J. M. Pottage, D. Bird, P. J. Roberts, J. C. Knight, and P. St. J. Russell. Hollow-core PCF for guidance in the mid-infrared to far infra-red. *Opt. Express*, 13 :6937–6946, 2005.

[63] G. J. Pearce. *Plane-wave modelling methods for modelling photonic crystal fibre*. PhD thesis, University of Bath, 2006.

[64] A. Ferrando, E. Silvestre, J.-J. Miret, P. Andrès, and M. V. Andrès. Donor and acceptor guided modes in photonic crystal fibers. *Optics Letters*, 25(18) :1328–1330, 2000.

[65] J. M. Stone, G. J. Pearce, F. Luan, T. A. Birks, J. C. Knight, A. K. George, and D. Bird. An improved photonic bandgap fiber based on an array of rings. *Opt. Express*, 14 :6291–6296, 2006.

[66] P. St. J. Russell. Photonic crystal fibers. *Science*, 299(5605) :358–362, 2003.

[67] Michele Midrio, Mukesh P. Singh, and Carlo G. Someda. The space filling mode of holey fibers : An analytical vectorial solution. *J. Lightwave Technol.*, 18(7) :1031–1037, 2000.

[68] G. Boudebs, S. Cherukulappurath, M. Guignard, J. Troles, F. Smektala, and F. Sanchez. Linear optical characterization of chalcogenide glasses. *Optics Communications*, 230 :331–336, 2004.

[69] A. R. Hilton. Nonoxide chalcogenide glasses as infrared optical materials. *Applied Optics*, 5(12) :1877–1882, 1966.

[70] J. .A. Savage. Optical properties of chalcogenide glasses. *Journal of Non-Crytalline Solids*, 47(1) :101–116, 1982.

[71] P. Klocek and L. Colombo. Index of refraction and light scattering in geSe and geSbSe glasses. *Journal of Non-Crytalline Solids*, 93 :1–16, 1987.

[72] T. A. Birks, J. C. Knight, and P. St. J. Russell. Endlessly single-mode photonic crystal fiber. *Opt. Lett.*, 22(13) :961–963, 1997.

[73] L. Labonté, D. Pagnoux, P. Roy, F. Bahloul, M. Zghal, G. Mélin, E. Burov, and G. Renversez. Accurate measurement of the cutoff wavelength in a microstructured optical fiber by means of an azimuthal filtering technique. *Opt. Lett.*, 31 :1779–1781, 2006.

[74] B. Kuhlmey, R. C. McPhedran, and C. M. de Sterke. Modal 'cutoff' in microstructured optical fibers. *Optics Letters*, 27(19) :1684–1686, 2002.

[75] B. J. Eggleton, P. S. Westbrook, C. A. White, C. Kerbage, R. S. Windeler, and G. L. Burdge. Cladding-mode-resonnances in Air-Silica. *Journal of Lightwave technology*, 18(8) :1084–1099, 2000.

[76] J. C. Knight, T. A. Birks, and P. St. J. Russell. Properties of photonic crystal fiber and the efective index model. *J. Opt. Soc. Am. A*, 15(4) :746–750, 1998.

[77] N. A. Mortensen. Effective area of photonic crystal fibers. *Optics Express*, 10(7) :341–348, 2002.

[78] J. R. Folkenberg, N. A. Mortensen, K. P. Hansen, T. P. Hansen, H. R. Simonsen, and C. Jacobsen. Experimental investigation of cut-off phenomena in nonlinear photonic crystal fibers. *Optics Letters*, 28(20) :1882–1884, 2003.

[79] N. A. Mortensen, J. R. Folkenberg, M. D. Nielsen, and K. P. Hansen. Modal cutoff and the V parameter in photonic crystal fibers. *Optics Letters*, 28(20) :1879–1881, 2003.

[80] G. Renversez, F. Bordas, and B. T. Kuhlmey. Second mode transition in microstructured optical fibers : determination of the critical geometrical parameter and study of the matrix refractive index and effects of cladding size. *Opt. Lett.*, 30(11) :1264–1266, 2005.

[81] T. A. Birks, D. M. Bird, T. D. Hedley, J. M. Pottage, and P. St. J. Russell. Scaling law and vectors effects in bandgap-guiding fibres. *Opt. Express*, 12(1) :69–74, 2003.

[82] S. Kawakami and N. Nishida. Characteristics of a doubly clad optical fiber with a low-index inner cladding. *J. Quantum Electron.*, 10 :879–887, 1974.

[83] S. Wilcox, L. C. Botten, C. Martijn de Sterke, B. T. Kuhlmey, R. C. McPhedran, D. P. Fussel, and S. Tomljenovic-Hanic. Long wavelength behavior of the fundamental mode of microstructured optical fibers. *Opt. Express*, 13 :1978, 2005.

[84] J. C. Knight, J. Arriaga, T. A. Birks, A. Ortigosa-Blanch, W. J. Wadsworth, and P. St. J. Russell. Anomalous dispersion in photonic crystal fibers. *IEEE Photon. Tech.. Lett.*, 12(7) :807–809, 2000.

[85] C. G. Poulton. *Asymptotics and wave propagation in cylindrical geometries*. PhD thesis, University of Sydney, 1999.

[86] T. Okoshi. *Optical Fibers*. Academic Press, New York, 1982.

[87] J. K. Ranka, R. S. Windeler, and A. J. Stentz. Visible continuum generation in air-silica microstructure optical fibers with anomalous dispersion at 800 nm. *Opt. Lett.*, 25(1) :25–27, 2000.

[88] J. M. Dudley, L. Provino, N. Grossard, H. Maillotte, R. Windeler, B. Eggleton, and S. Coen. Supercontinuum generation in air-silica microstructured fibers with nanosecond and femtosecond pulse pumping. *J. Opt. Soc. Am. B*, 19(4) :765–771, 2002.

[89] A. Ferrando, M. Zacarés, P. Fernandez de Cordoba, D. Binosi, and J. A. Monsoriu. Spatial soliton formation in photonic crystal fibers. *Optics Express*, 11(5) :452–459, 2003.

[90] D. Mogilevstev, T. A. Birks, and P. St. J. Russell. Group-velocity dispersion in photonic crystal fibers. *Opt. Lett.*, 23(21) :1662–1664, 1998.

[91] A. Ferrando, E. Silvestre, J.-J. Miret, and P. Andrés. Nearly zero ultraflattened dispersion in photonic crystal fibers. *Opt. Lett.*, 25(11) :790–792, 2000.

[92] A. Ferrando, E. Silvestre, J.-J. Miret, P. Andrés, and M. V. Andrés. Vector description of higher-order modes in photonic crystal fibers. *J. Opt. Soc. Am. A*, 17(7) :1333–1340, 2000.

[93] A. Ferrando, E. Silvestre, P. Andrés, J.-J. Miret, and M.V. Andrés. Designing the properties of dispersion-flattened photonic crystal fibers. *Optics Express*, 9(13) :687–697, 2001.

[94] G. Renversez, B. Kuhlmey, and R. McPhedran. Dispersion management with microstructured optical fibers : Ultra-flattened chromatic dispersion with low losses. *Opt. Lett.*, 28(12) :989–991, 2003.

[95] J. W. Fleming. Material dispersion in lightguide glasses. *Electron. Lett.*, 14(11) :326–328, 1978.

[96] F. Bordas, L. Provino, and G. Renversez. Fibres optiques microstructurées de haut indice : pertes et dispersion chromatique du fondamental, et cutoff du second mode, comparaison avec la silice. In $XXIII^{èmes}$ *Journées Nationales d'Optique Guidée*, pages 230–232, 2004.

[97] D. Hewak, editor. *Properties, Processing and Applications of Glass and Rare Earth-Doped Glasses for Optical Fibers*, volume 22 of *EMIS Datarev. Ser.* INSPEC, London, 1998.

[98] W. H. Reeves, J. C. Knight, and P. St. J. Russell. Demonstration of ultra-flattened dispersion in photonic crystal fibers. *Optics Express*, 10(14) :609–613, 2002.

[99] E.A.J. Marcatili and R. A. Schmeltzer. Hollow metallic and dielectric waveguides for long distance optical transmission and lasers. *Bell Syst. Tech. J.*, 43 :1783–1809, 1964.

[100] J.C. Knight, J. Broeng, T.A. Birks, and P. S. J. Russel. Photonic Band Gap Guidance in Optical Fibers. *Science*, 282 :1476–1478, 1998.

[101] S. E. Barkou, J. Broeng, and A. Bjarklev. Silica-air photonic crystal fiber design that permits waveguiding by a true photonic bandgap effect. *Optics Letters*, 24(1) :46–48, 1999.

[102] J. Broeng, T. Sondergaard, S. E. Barkou, P. M. Barbeito, and A. Bjarklev. Waveguidance by the photonic bandgap effect in optical fibres. *Journal of Optics A*, 1 :477–482, 1999.

[103] R. F. Cregan, B. J. Mangan, J. C. Knight, T. A. Birks, P. St. J. Russell, P. J. Roberts, and D. C. Allan. Single-mode photonic band gap guidance of light in air. *Science*, 285 :1537–1539, 1999.

[104] T.P. White, R.C. McPhedran, L.C. Botten, G.H. Smith, and C.M. de Sterke. Calculations of air-guided modes in photonic crystal fibers using the multipole method. *Optics Express*, 9(13) :721–732, 2001.

[105] J. D. Joannopoulos, R. Meade, and J. N. Winn. *Photonic Crystals Molding the Flow of Light*. Princeton University Press, 1995.

[106] J.M. Lourtioz, H. Benisty, V. Berger, J.-M. Gérard, D. Maystre, and A. Tchelnokov. *Les cristaux photoniques*. Hermes, Paris, 2003.

[107] A. A. Maradudin and A. R. McGurn. Out of plane propagation of electromagnetic waves in a two-dimensional periodic dielectric medium. *Journal of Modern Optics*, 41(2) :275–284, 1994.

[108] K. Sakoda. *Optical Properties of Photonic Crystals*. Springer, 2001.

[109] T.A. Birks, P.J. Roberts, P. St. J. Russell, D.M. Atkin, and T.J. Shepeerd. Full 2-d photonic bandgaps in silica/air structures. *Electronics Letters*, 31(22) :1941–1943, 1995.

[110] Y. Xu and A. Yariv. Loss analysis of air-core photonic crystal fibers. *Optics Letters*, 28(20) :1885–1887, 2003.

[111] C. M. Smith, N. Venkataraman, M. T. Gallagher, D. Müller, J. A. West, N. F. Borrelli, D. C. Allan, and K. W. Koch. Low-loss hollow-core silica/air photonic bandgap fibre. *Nature*, 424 :657–659, 2003.

[112] K. Saitoh and M. Koshiba. Leakage loss and group velocity dispersion in air-core photonic bandgap fibers. *Optics Express*, 11(23) :3100–3109, 2003.

[113] J. Shephard, W. MacPherson, R. Maier, J. Jones, D. Hand, M. Mohebbi, A. George, P. Roberts, and J. Knight. Single-mode mid-IR guidance in a hollow-core photonic crystal fiber. *Opt. Express*, 13(18) :7139–7144, 2005.

[114] M. F. Churbanov, I. V. Scripachev, G. E. Snopatin, V. S. Shiryaev, and V. G. Plotnichenko. High purity glasses based on arsenic chalcogenides. *Journal of Optoelectronics and Advanced Materials*, 3 :341–349, 2001.

[115] P. Houizot, C. Boussard-Plédel, A. J. Faber, L. K. Cheng, B. Bureau, P. A. Van Nijnatten, W. L. M. Gielesen, J. Pereira do Carmo, and J. Lucas. Infrared single mode chalcogenide glass fiber for space. *Opt. Express*, 15(19) :12529–12538, 2007.

[116] J. Hu and C. R. Menyuk. Leakage loss and bandgap analysis in air-core photonic bandgap fiber for nonsilica glass. *Opt. Express*, 15 :339–349, 2006.

[117] Université de Rennes I Laboratoire Verres et Cérqmiques. private communication. 2007.

[118] K. Saitoh, N. A. Mortensen, and M. Koshiba. Air-core photonic bang-gap fibers : the impact of surface modes. *Opt. Express*, 12(3) :394–400, 2004. http ://www.opticsinfobase.org/abstract.cfm ?URI=oe-12-3-394.

[119] J. West, C. Smith, N. Borrelli, and D. Allan and. Koch. Surface modes in air-core photonic bandgap fibers. *Opt. Express*, 12(8) :1485–1496, 2004.

[120] M.A. Duguay, Y. Kokubun, T. L. Koch, and L. Pfeiffer. Antiresonant reflecting optical waveguides in SiO_2-Si multilayer structures. *Appl. Phys. Lett*, 49 :13–15, 1986.

[121] N. M. Litchinitser, A. K. Abeeluck, C. Headley, and B. J. Eggleton. Antiresonant reflecting photonic crystal optical waveguides. *Opt. Lett.*, 27(18) :1592–1594, 2002.

[122] N. M. Litchinitser, S. C. Dunn, P. E. Steinwuzel, B. J. Eggleton, T. P. White, R. C. McPhedran, and C. M. de Sterke. Application of an ARROW model for designing tunable photonic devices. *Opt. Express*, 12(8) :1540–1550, 2004. http ://www.opticsinfobase.org/abstract.cfm ?URI=oe-12-8-1540.

[123] T. P. White, R. C. McPhedran, C. M. de Sterke, N. M. Litchinitser, and B. J. Eggleton. Resonance and scaterring in microstructured optical fibers. *Opt. Lett.*, 27(22) :1977–1979, 2002.

[124] N. M. Litchinitser, S. C. Dunn, B. Usner, B. J. Eggleton, T. P. White, R. C. McPhedran, and C. M. de Sterke. Resonances in microstructured optical waveguides. *Opt. Express*, 11(10) :1243–1251, 2003.

[125] J. Laegsgaard. Gap formation and guided modes in photonic bandgap fibres with high-index rods. *J. Opt. A : Pure Appl. Opt.*, 6 :798–804, 2004.

[126] T. D. Engeness, M. Ibanescu, S. G. Johnson, O. Weisberg, M. Skorobogatiy, S. Jacobs, and Y. Fink. Dispersion tailoring and compensation by modal interactions in omniguide fibers. *Optics Express*, 11(10) :1175–1196, 2003.

[127] T. Sondergaard, J. Broeng, A. Bjarklev, K. Dridi, and S. E. Barkou. Suppression of spontaneous emission for a two-dimensional honeycomb photonic bandgap structure estimated using a new effective-index model. *IEEE journal of quantum electronics*, 34(12) :2308–2313, 1998.

[128] A. Ferrando and J. J. Miret. Single-polarization single-mode intraband guidance in supersquare photonic crystals fibers. *Applied Physics Letters*, 78(21) :3184–3186, 2001.

[129] M. J. Steel and R. M. Osgood. Elliptical-hole photonic crystal fibers. *Opt. Lett.*, 26(4) :229–231, 2001.

[130] A. V. Husakou and J. Herrmann. Supercontinuum generation of higher-order solitons by fission in photonic crystal fibers. *Phys. Rev. Lett.*, 87(20) :203901, 2001.

[131] S. Coen, A. H. Lun Chau, R. Leonhardt, J. D. Harvey, J. C. Knight, W. J. Wadsworth, and P. St. J. Russell. White-light supercontinuum generation with 60-ps pump pulses in a photonic crysral fiber. *Optics Letters*, 26(17) :1356–1358, 2001.

[132] J. Herrmann, U. Griebner, N. Zhavoronkov, A. Husakou, D. Nickel, J. C. Knight, W. J. Wadsworth, P. S. Russell, and G. Korn. Experimental evidence for supercontinuum generation by fission of higher-order solitons in photonic fibers. *Phys. Rev. Lett.*, 88(17) :173901, 2002.

[133] M.A. Foster, J.M. Dudley, B. Kibler, Q. Cao, D. Lee, R. Trebino, and A.L. Gaeta. Nonlinear pulse propagation and supercontinuum generation in photonic nanowires : experiment and simulation. *Applied Physics B : Lasers and Optics*, pages 363–367, 2005.

[134] J. M. Dudley, G. Genty, and S. Coen. Supercontinuum generation in photonic crystal fiber. *Review of Moderm Physics*, 78 :1135–1184, October–December 2006.

[135] P. Domachuk, N. A. Wolchover, M. Cronin-Golomb, A. Wang, A. K. George, C. M. B. Cordeiro, J. C. Knight, and F. G. Omenetto. Over 4000 nm bandwidth of mid-ir supercontinuum generation in sub-centimeter segments of highly nonlinear tellurite pcfs. *Opt. Express*, 16(10) :7161–7168, 2008.

[136] J. M. Fini. Microstructure fibres for optical sensing in gases and liquids. *Measurement Science and Technology*, 15 :1120–1128, 2004.

[137] A. S. Webb, F. Poletti, D. J. Richardson, and J. K. Sahu. Suspended-core holey fiber for evanescent-field sensing. *Optical Engeneering Letters*, 46(1) :010503–1–010503–3, 2007.

[138] W. J. Wadsworth, J. C. Knight, W. H. Reeves, and P. S. J. Russel. Yb^{3+}-doped photonic crystal fibre laser. *Electron. Lett.*, 36 :1452–1454, 2000.

[139] K. Furusawa, A. N. Malinowski, J. H. Price, T. M. Monro, J. K. Sahu, J. Nilsson, , and D. J. Richardson. Cladding pumped ytterbium-doped fiber laser with holey inner and outer cladding. *Optics Express*, 9(13) :714–720, 2001.

[140] J. Limpert, T. Schreiber, S. Nolte, H. Zellmer, T. Tunnermann, R. Iliew, , F. Lederer, J. Broeng, G. Vienne, A. Petersson, and C. Jakobsen. High-power air-clad large-mode-area photonic crystal fiber laser. *Optics Express*, 11(7) :818–823, 2003.

[141] Sébastien Février, Dmitry D. Gaponov, Philippe Roy, Mikhail E. Likhachev, Sergei L. Semjonov, Mikhail M. Bubnov, Evgeny M. Dianov, Mikhail Yu. Yashkov, Vladimir F. Khopin, Mikhail Yu. Salganskii, and Aleksei N. Guryanov. High-power photonic-bandgap fiber laser. *Opt. Lett.*, 33(9) :989–991, 2008.

[142] B. Temelkuran, S. D. Hart, G. Benoit, J. D. Joannopoulos, and Y. Fink. Wavelength-scalable hollow optical fibres with large photonic bandgaps for co_2 laser transmission. *Nature*, 420 :650–653, 2002.

[143] L. B. Shaw, J. S. Sanghera, I. D. Aggarwal, and F. H. Hung. As-S and As-Se based photonic band gap fiber for IR laser transmission. *Optics Express*, 11(25) :3455–3460, 2003.

[144] L. Schwartz. *Méthodes mathématiques pour les sciences physiques*. Hermann, Paris, 1987 edition, 1965.

[145] Neil W. Ashcroft and N. David Mermin. *Solid State Physics*. Saunders College Publishing, 1 edition, 1976.

[146] A. Nicolet, S. Guenneau, C. Geuzaine, and F. Zolla. Modeling of electromagnetic waves in periodic media with finite elements. *J. of Comp. and Appl. Math.*, 168 :321–329, 2004.

Index